Title
Nanostructured Materials for Fast Charging and High Capacity Energy Storage

Author
Lin, Terri Chai

Publication Date
2019

Peer reviewed|Thesis/dissertation

UNIVERSITY OF CALIFORNIA

Los Angeles

Nanostructured Materials for Fast Charging and High Capacity Energy Storage

A dissertation submitted in partial satisfaction of the requirements for the degree Doctor of Philosophy in Chemistry

by

Terri Chai Lin

2019

ABSTRACT OF THE DISSERTATION

Nanostructured Materials for Fast Charging and High Capacity Energy Storage

by

Terri Chai Lin

Doctor of Philosophy in Chemistry

University of California, Los Angeles, 2019

Professor Sarah H. Tolbert, Chair

The need for energy storage continues to grow due to our increasing use of consumer electronics, and adoption of electrical vehicles and renewable energy sources, which necessitates grid storage. Unfortunately, fast charging capabilities and cycle life remain problematic in current lithium-ion batteries. In this thesis, we aim to: 1) develop novel materials with good rate capability and define design rules for fast charging materials, and 2) use nanoporous metal to hinder degradation and extend the lifetime of high capacity alloying anodes and utilize *operando* X-ray diffraction and imaging studies to understand the mechanisms that underpin the performance of these materials.

Thus far, we have identified a number of key requirements for optimized battery performance. 1) With our highly defected MoS_2 nanocrystal, mesoporous $LiMn_2O_4$ and $LiVPO_4F$, we have found that the key to producing fast charging is nano-structuring a battery material to increase the maximum charge and discharge rate by shortening the diffusion path length for lithium and sodium-ions and in some cases allowing ions to intercalate into the channels or layers of the redox-active material in a

non-diffusion controlled manner. At the root of this behavior is suppression of the phase transition that often occur upon ion intercalation.

For long cycle lifetime, we used nanoporous tin and antimony tin as platforms to show that nanoporous metals, intermetallics and surface coatings are effective in alleviating the volume expansion that causes material degradation and impedes the lifetime of these alloying anodes. *Operando* transmission X-ray microscopy shows that porosity and protective coatings are critical in reducing stress and strengthening the structural integrity during cycling. Through our experimental approaches, we hope to establish a set of materials and architectural guidelines for the next generation electrochemical energy storage.

The dissertation of Terri Chai Lin is approved.

Xiangfeng Duan

Richard Kaner

Bruce Dunn

Sarah H. Tolbert, Committee Chair

University of California, Los Angeles

2019

To my parents, S.T. Lin and Chai-Fong Huang, and my sister, Tina Lin

Table of Contents

List of Figures **xii**

List of Tables **xxiii**

Acknowledgements **xxiv**

Vita **xxvi**

Chapter 1. Introduction **1**

1.1. Reference 6

Chapter 2. Pseudocapacitive Charge Storage in Thick Composite MoS_2 Nanocrystal-Based Electrode **11**

2.1. Introduction 11

2.2. Results and Discussion 16

1.2.1. Materials and Characterization 16

1.2.2. Electrochemistry 19

2.3. Conclusion 33

2.4. Experimental 33

2.4.1. Synthesis 34

2.4.2. Characterization 35

2.4.3. Electrochemistry 35

2.4.4. Full Cells 36

2.4.5. Electrochemical Impedance Spectroscopy 37

2.5. References 38

Chapter 3. Direct Observation of Suppression of Electronically Drive Phase Transition in Nanosized MoS_2 Using *Operando* X-ray Diffraction **44**

3.1. Introduction 44

3.2. Results and Discussion 47

3.2.1. Materials and Characterization 47

3.2.2. Electrochemistry 49

3.2.3. Kinetics Analysis 52

3.2.4. *Operando* X-ray Diffraction Study 55

3.3. Conclusion 59

3.4. Experimental 60

3.4.1. Synthesis 60

3.4.2. Characterization 61

3.4.3. Electrochemistry 61

3.4.4. Data Processing 62

3.5. References 63

Chapter 4. Crossover from Slow Sodium-Ion Storage in MoS_2 to Ultrafast Intercalation Pseudocapacitance in MoS_2 Nanoparticles by Phase Transition Suppression 67

4.1. Introduction 67

4.2. Results and Discussion 69

4.2.1. Electrochemistry 69

4.2.2. *Operando* X-ray Diffraction Study 73

4.2.2. Superior Electrochemical Properties 77

4.3. Conclusion 79

4.4. Experimental 80

4.4.1. Synthesis 80

4.4.2. Characterization 80

4.4.3. Electrode Formulation 81

4.4.4. Electrochemical Measurement 81

4.4.5. *Operando* Synchrotron based X-ray diffraction 82

4.5. References 84

Chapter 5. Suppression of Phase Transition in Nanostructured $LiMn_2O_4$ with Small Crystallite Sizes during Charge and Discharge 88

5.1. Introduction 88

5.2. Results and Discussion 90

5.2.1. Synthesis and Characterization of 15nm and 50 nm $LiMn_2O_4$ Nanostructured Powders 90

5.2.2. Electrochemical Properties of 15 and 50 nm $LiMn_2O_4$ Nanostructured Powders 92

5.2.3. *Operando* X-ray Diffraction of 15 and 50 nm $LiMn_2O_4$ Nanostructured Powders 94

5.3. Conclusion 101

5.4. Experimental 101

5.4.1. Synthesis 102

5.4.2. Characterization 103

5.4.3. Electrode Preparation and Electrochmical Analysis 103

5.4.4. *Operando* Transmission X-ray Diffraction 104

5.5. References 105

Chapter 6. Polymer-templated Nanoporous $LiVPO_4F$ as a Fast Charging Cathode for Lithium-ion Batteries 107

6.1. Introduction 107

6.2. Results and Discussion 109

6.2.1. Materials and Characterization 109

6.2.2. Electrochemical Cycling 114

6.2.3. Charge Storage Mechanism and *Operando* X-ray Diffraction Study 117

6.2.4. Self-Discharge Study 121

6.2.5. Full Cell Device 121

6.3. Conclusion 122

6.4. Experimental 123

6.4.1. Synthesis 123

6.4.2. Characterization 124

6.4.3. Electrochemistry 124

6.4.4. *Operando* X-ray Diffraction Study 125

6.5. References 127

Chapter 7. Using X-ray Microscopy to Understand How Nanoporous Materials can be Used to Reduce the Large Volume Change in Alloy Anodes 132

7.1. Introduction 132

7.2. Result and Discussion 134

7.2.1. Structural Characterization 134

7.2.2. Electrochemistry 137

7.2.3. Transmission X-ray Microscopy 140

7.3. Conclusions 147

7.4. Experimental 148

7.4.1. Synthesis 148

7.4.2. Characterization 149

7.4.3. Electrode Preparation 149

7.4.4. *Operando* Transmission X-ray Microscopy 150

7.4.5. Data Analysis 151

7.5. References 153

Chapter 8. Understanding the Stabilization Mechanism in Nanoporous Intermetallic Alloy Anodes through *Operando* Transmission X-ray Microscopy 157

8.1. Introduction 157

8.2. Results and Discussion 159

8.2.1. Materials and Characterization 159

8.2.2. Electrochemistry 163

8.2.3. *Operando* Transmission X-ray Microscopy Study 165

8.3. Conclusion 169

8.4. Experimental 170

8.4.1. Synthesis 170

8.4.2. Characterization 170

8.4.3. Electrochemical Testing 171

8.4.4. *Operando* Transmission X-ray Microscopy 171

8.4.5. Data Analysis 172

8.5. References 174

Chapter 9. Nanoporous Antimony Tin as a Sodium-ion Battery Anode 179

9.1. Introduction 179

9.2. Results and Discussion 181

9.2.1. Materials and Characterization 181

9.2.2. Electrochemistry 182

9.2.3. *Operando* Transmission X-ray Microscopy Study 184

9.3. Conclusion 187

9.4. Experimental 187

9.4.1. Synthesis 187

9.4.2. Characterization 187

9.4.3. Electrochemistry 188

9.4.4. *Operando* Transmission X-ray Microscopy 188

9.4.5. Data Analysis 189

9.5. References 191

Chapter 10. Improved Cycling Capabilities of Nanoporous Antimony Tin with Atomic-Layer-Deposition Aluminum Oxide for Sodium-ion Batteries 195

10.1. Introduction 195

10.2. Results and Discussion 197

10.2.1. Materials and Characterization 197

10.2.2. Electrochemistry 199

10.2.3. *Operando* Transmission X-ray Microscopy Study 201

10.3. Conclusion 206

10.4. Experimental 206

10.4.1. Synthesis 206

10.4.2. Characterization 206

10.4.3. Atomic Layer Deposition 207

10.4.4. Electrochemistry 207

10.4.5. *Operando* Transmission X-ray Microscopy 208

10.4.6. Data Processing 208

10.5. References 210

Chapter 11. Conclusions 214

List of Figures

Figure 1.1. Schematic diagram of various electrochemical energy storage systems

Figure 2.1. (a) X-ray diffraction of b-MoS_2 and nc-MoS_2 shows that both materials crystalize in the 2H hexagonal crystal structure (JCPDS 037-1492). The nc-MoS_2 shows significant peak broadening, however, which we assign to both finite size effects and lattice disorder. (b) Scanning electron microscope image of nc-MoS_2 show a network of agglomerated nanocrystals. (c-e) Transmission electron microscope images of dispersed nc-MoS_2 show sub-50 nanometer primary particles. Significant defects are observed and are believed to be at least partly responsible for the facile ion insertion into the bulk of the nanocrystal.

Figure 2.2. Nitrogen isotherm of both b-MoS_2 and nc-MoS_2 (a). The calculated surface area for nc-MoS_2 is 35m^2g^{-1} while the bulk is 2 m^2g^{-1}. This 17.5-fold increase in surface area, in part, leads to the pseudocapacitive charge storage mechanism. BJH pore size distribution calculated from the adsorption isotherm in part (a) for nc-MoS_2 (b). The porosity shown in the BJH distribution arises from adhesion of the nanocrystals to each other, which creates pores.

Figure 2.3. X-ray photoelectron spectroscopy of b-MoS_2 (a, b) and nc-MoS_2 (c, d). The data can be well fit with a single 4+ oxidation state for Mo and a 2- oxidation state for S. The elemental stoichiometry calculated from the data is 1.05:2.00, Mo:S. These data thus show that the surface of the nc-MoS_2 is the same as the commercial bulk powder, and both surfaces are consistent with bulk MoS_2.

Figure 2.4. Derivative of the galvanostatic charge discharge plot dQ/dV of the first 10 cycles of nc-MoS_2 (a), and b-MoS_2 (c) showing the irreversible phase transition and subsequent formation of the highly electronically conducting 1T-MoS_2 phase. dQ/dV of cycles 2 - 9 of nc-MoS_2 (b), and b-MoS_2 (d) which shows that the 2H –to – 1T phase change occurs over 10 cycles, while in b-MoS_2 the phase change has occurred after the second cycle. Charge transfer resistance of b-MoS_2 and nc-MoS_2 based

electrodes during the first 10 formation cycles calculated from the corresponding Nyquist plots. Impedance collected at 3V *vs.* Li/Li^+ (green), and 0.8 V *vs.* Li/Li^+ (black) (e). Atomic representation of the 2H-to-1T phase transformation. This transformation only involves a small shift in the easily polarized sulfur layer, which is non-destructive to the nanoscale structure (f).

Figure 2.5. (a) Galvanostatic kinetic analysis, after 10 formation cycles, comparing nc-MoS_2 electrodes made using carbon fibers and mixed using sonication (green), and electrodes made using only carbon black and mixed using a traditional mortar and pestle (red). (b) Charge transfer resistance of nc-MoS_2 / carbon fiber based electrodes (green), and nc-MoS_2 / carbon black based electrodes (red) during the first 10 formation cycles calculated from Nyquist plots collected at 0.8 V *vs.* Li/Li^+. The charge transfer in the carbon fiber based electrode is both lower in absolute value, and decreases with cycle number because the newly formed 1T MoS_2 is electronically well connected to the electrode architecture. By contrast, the charge transfer resistance in the traditional carbon black based electrodes monotonically increases, likely due to SEI formation. Backscatter electron images of the carbon fiber based electrode (c) and carbon black only electrode (d). The brightness in backscattered images is related to the atomic Z number, so the dark-regions are carbon rich and the light-regions are MoS_2 rich.

Figure 2.6. (a) Galvanostatic kinetic analysis comparing b-MoS_2 to the nc-MoS_2 in optimized carbon fiber based electrodes (a). The nanostructured material stores nearly four-times the charge at 100C compared to b-MoS_2. Galvanostatic lithium insertion and deinsertion profiles at different current densities of b-MoS_2 (b), and nc-MoS_2 (c). The galvanostatic traces for the nc-MoS_2 based electrodes are pseudo-linear and are quite different from the standard plateaus observed for b-MoS_2.

Figure 2.7. Analysis of the charge storage in the current maxima for b-MoS_2 (a) and nc-MoS_2 (b) using b-values calculated from Equation 2. This analysis shows that the Faradaic charge storage associated with the peak maxima in CV has a significant diffusion contribution in b-MoS_2, while this analysis shows that the same Faradaic processes are capacitive-like in nc-MoS_2. Quantification of the capacitive

and diffusion charge storage in b-MoS_2 (c) and nc-MoS_2 (d) as a function of voltage. This analysis indicates that the nc-MoS_2 based electrodes store charge largely through a capacitive mechanism.

Figure 2.8. Cycle lifetime of nc-MoS_2 and b-MoS_2 electrodes cycled at 20C. Cycle 1 reported here was started after the kinetic study (1C-100C) shown in Figure 2.7. The long cycle lifetime and high capacity of the nc-MoS_2 is correlated with the established pseudocapacitive charge storage.

Figure 2.9. Average discharge energy density *vs.* average discharge power density for a full cell utilizing a nc-MoS_2 anode and an activated carbon cathode. The voltage of this device operates between 0.4 – 3.2 V. Average discharge energy density *vs.* cycle number for an asymmetric nc-MoS_2 / activated carbon full cell. (b) The voltage of this device operates between 0 – 3.0 V. The fast kinetics and long lifetime is a result of the highly reversible pseudocapacitive charge storage mechanism. This data was mass normalized using the total active mass of both electrodes (~4 mg).

Figure 3.1. (a) XRD patterns of uncycled bMoS_2 and nMoS_2 electrodes and as-synthesized MoS_2 nanocrystals. Peaks labeled with asterisk corresponds to the aluminum current collector while others correspond to the 2H phase of MoS_2. The peak broadening in the nMoS_2 electrode and pure nanocrystal sample is due to the small crystallite size and the onion-like structure of the 10 nm to 30 nm nanocrystals, as shown in the low (b) and high (c) magnification TEM images.

Figure 3.2. (a) *Operando* X-ray diffraction of nMoS_2 showing 2H to 1T conversion. Starting as the (002) 2H phase at the open circuit voltage, the 2H MoS_2 converts to the 1T phase during lithiation as the (002) 2H peak shifts to lower Q and become the (001) peak of the 1T phase. As lithium is deinserted, the (001) 1T peak shifts slightly back to higher Q, indicating the presence of both 1T and 2H phase since not all nanocrystals are converted in the first cycle. This mixture of two phases is confirmed by the peak fit analysis shown in (b), where the final peak position after delithiation lies in between the (001) 1T and (002) 2H phase. Multiple cycles are required to complete the 2H-1T

conversion. Bulk MoS_2 (c) took 4 cycles while nano MoS_2 (d) took up to 8 cycles. This precycling was done prior to the *operando* experiments presented below.

Figure 3.3. Galvanostatic traces and cyclic voltammograms of $nMoS_2$ (a - b) and $bMoS_2$ (c -d). The sloping galvanostatic profiles in (a) for $nMoS_2$ suggests that first-order phase transitions have been suppressed and that the system is pseudocapacitive. This is in agreement with calculated *b* values close to 1 at all the current maxima obtained from sweep rate dependent CV curves in (b); b=1, indicates capacitor-like behavior. Unlike $nMoS_2$, phase transition between the 1T and triclinic Li_1MoS_2 phases are indicated by voltage plateaus in $bMoS_2$ (c). The system also shows mostly diffusion-limited with *b* values close to 0.5 in (d).

Figure 3.4. (a) *Operando* phase change study of $bMoS_2$ and $nMoS_2$. First-order phase transition can be observed in $bMoS_2$ as 1) peaks shift significantly to lower Q then back to higher Q, 2) the emergence of a new peak at 1.09 $Å^{-1}$ and 3) a shoulder near the 101 peak. (b) Unlike $bMoS_2$, no phase transition was observed in $nMoS_2$ due to the improved kinetics and unfavorable two phase coexistence in nanocrystals.

Figure 3.5. Selected XRD patterns for the pristine, lithiated and delithiated state of $bMoS_2$ and $nMoS_2$ with line patterns of the three known phases of MoS_2. This direct comparison indicates that $bMoS_2$ experiences major phase transitions between the 1T trigonal prismatic phase to triclinic Li_1MoS_2 phase, which has also been observed in the literature. However, this phase transition is not observed in $nMoS_2$. Shoulders and peaks corresponding to the triclinic Li_1MoS_2 phase are clearly absent in the $nMoS_2$ at 0.8V (all voltages reported versus Li/Li^+).

Figure 4.1. (a) 2H-MoS_2 semiconducting hexagonal geometry and the metallic 1T trigonal prismatic. (b) Galvanostatic charge-discharge curve of MoS_2 nanoparticles when converting from the 2H to 1T-phase. Voltage plateau at 1 V vs. Na/Na^+ is indicative of the 2H-to-1T phase transition is replaced by the galvanostatic trace for the insertion of Na^+ into 1T-MoS_2 after 10 cycles.(c) Nyquist plot of the

2H-to-1T phase transition confirms the decrease in charge-transfer resistance due to metallic conductivity. (d) b-value analysis done at 0.1 -10 mV/s indicates capacitive charge-storage mechanism for each pair of redox peaks is closed to 1. (e) k_1/k_2 kinetic analysis shows the current response from capacitive processes. The shaded region shows 94% occupation to the overall current response of MoS_2 nanoparticles cycled at 1 $mV \cdot s^{-1}$. (f) Capacity versus $\upsilon^{-1/2}$ shows the separation in the capacity due to diffusion-controlled and capacitive processes cycled from 0.1 to 100 $mV \cdot s^{-1}$. The dashed diagonal line is extrapolated to identify the infinite sweep rate capacity.

Figure 4.2. X-ray diffraction patterns collected during the intercalation and de-intercalation processes of a pre-cycled Na half-cell containing (a) bulk MoS_2, (b) nano MoS_2 as positive electrode (with charging/discharging rate of C/4.5). The sharp peak at 2.08 $Å^{-1}$ is attributed to Na counter electrode in the cell. Change in d-spacing of (c) bulk MoS2 and (d) nano MoS2 during the sodiation process.

Figure 4.3. (a) Galvanostatic cycling of MoS_2 at various c-rates (1C, 5C, 10C, 20C, 40C, 60C, 100C) (b) Galvanostatic cycling performance of MoS_2 showing attainable capacity as a function of cycle number at various rates. Corresponding coulombic efficiencies are well above 99%. (c) Long-term cycling performance of MoS_2 cycled at 20C showing minimal capacity fade (97% capacity retention) up to 1800 cycles.

Figure 5.1. XRD patterns indicate both 15 nm (a) and 50 nm (b) domain size samples are phase pure $LiMn_2O_4$; average domain sizes were calculated from these patterns using the Scherrer equation. SEM shows images show that both the 15 nm (c) and 50 nm (d) domain size materials are made of interconnected particles in a nanoporous network.

Figure 5.2. (a) Long term galvanostatic cyclability and (b, c) cyclic voltammetry at 0.2 mV/s with inlayed capacitive contribution for 15 nm and 50 nm domain size nanoporous $LiMn_2O_4$ samples cycled in Swagelok cells versus Li metal using 1M $LiPF_6$ in EC:DMC 1:1 as the electrolyte.

Figure 5.3. *Operando* XRD patterns of the 50 nm domain size $LiMn_2O_4$ sample during charge and discharge. The <311> and <511> peaks show substantial shifting as well as the existence of a two-phase coexistence region. Dotted lines have been added to help guide the eye for the two-phase coexistence. The total discharge capacity of this cycle was 66 mAh/g.

Figure 5.4. Peak positions and full width at half max values for all *operando* XRD patterns of the 50 nm domain size $LiMn_2O_4$ sample during charge and discharge. The <311> and <511> peak positions are fit with one peak until two peaks were needed to maintain the peak width. Full width half max values are relatively constant for all patterns, including the two peak coexistence regions, suggesting proper fits. The total change in Q-spacing was found to be 0.0456 Å and 0.0738 Å for the <311> and <511> peaks, respectively.

Figure 5.5. *Operando* XRD patterns for the 15 nm domain size $LiMn_2O_4$ sample during charge and discharge. The <311> and <511> peaks show modest shifting with no visible two-phase coexistence region, suggesting solid solution behavior. Dotted lines have been added to help guide the eye. The total discharge capacity of this cycle was 50 mAh/g.

Figure 5.6. Peak positions and full width at half max values for all o*perando* XRD patterns of the 15 nm domain size $LiMn_2O_4$ sample during charge and discharge. The <311> and <511> peak positions are fit with one peak for all patterns. Full width half max values are relatively constant for all patterns, suggesting proper fits. The total change in Q-spacing was found to be 0.0201 Å and 0.0277 Å for the <311> and <511> peaks, respectively. The total change in Q-spacing for the 15 nm domain size sample is around 40% of that for the 50 nm domain size sample.

Figure 6.1. a) X-ray diffraction pattern of the c-nLVPF. No impurities are observed. b-c) SEM images of the as synthesized nanoporous c-nLVPF powder by sol-gel polymer template synthesis. The uniform porous structure resulted from the polymer template can be seen from both low and high magnifications.

Figure 6.2. a-b) TEM images of the c-nLVPF. The carbon coating wraps around the particle and is approximately 5 nm thick. c) TGA of c-nLVPF from room temperature to 550 °C. The 8 wt.% mass loss from 300-450 °C is attributed to the carbon content. d) Isotherm of c-nLVPF obtained from N_2 porosimetry. The surface area calculated from the BET model is 21 m^2/g.

Figure 6.3. a) CV curves of c-nLVPF collected at 0.1 mV/s. The redox peaks resembles the electrochemical process described in equation 6. b) Galvanostatic charge and discharge profiles of the first three cycles of at 1C. c) Charge and discharge voltage profiles of c-nLVPF at various rates (charging and discharging are done at the same rate for each cycle) d) Rate capability at various rate. e) Capacity retention at 20C charge and discharge for 2000 cycles.

Figure 6.4. a) Cyclic voltammograms of the c-nLVPF at 0.1 mV/s and 0.75 mV/s with calculated *b*-values. The system is mostly diffusion-limited with *b* values close to 0.5. (b) *Operando* phase change study of c-nLVPF. First-order phase transition can be observed as peak shifts to position that corresponds to the VPO_4F phase.

Figure 6.5. Self discharge behavior of c-nLVPF a) voltage curves of each cycle (charge, rest for 12 hr then discharge) b) charge curves c) the following discharge curves after resting.

Figure 6.6. a) CV curves of the full cell device (Nb_2O_5|c-nLVPF) b) charge and discharge profiles of the full cell device at 1C c) charge and discharge voltage profiles of the full cell device at various rates (charging and discharging are done at the same rate for each cycle).

Figure 7.1. Microscopy characterization of NP-Sn. Secondary electron images of NP-Sn showing particles between 1-10 μm that are comprised of an interconnected network of tin nano-ligaments and nano-pores (a,b) Higher resolution images suggest hierarchical porosity extending down to the few nanometer lengthscale. Backscattered image of NP-Sn after ball mill slurry processing showing that these structures are not compromised during the vigorous mixing process (c). Transmission X-ray

microscopy image of NP-Sn demonstrating the nano-scale resolution of this technique that allows visualization of many of the nanoscale pores and ligaments (d).

Figure 7.2. Nitrogen adsorption analysis on MP-Sn. Nitrogen isotherm at 77K of NP-Sn displaying hysteretic behavior above 0.6 P/P_0 indicating the presence of meso and macropores (a). Cumulative pore volume *vs.* pore width trace, which was derived from the adsorption branch of the nitrogen isotherm (b). The total pore volume is 0.045 cm^3/g, which is used to calculate the porosity of NP-Sn as ~25%. In addition, this plot shows that more than 60% of the pore volume is within the resolution limit of the transmission X-ray microscope used to study this material. Barrett-Joyner-Halenda pore-size distribution calculated from the adsorption branch of the nitrogen isotherm (c). The average pore size is ~70 nm, and this value is indicated in the plot.

Figure 7.3. Capacity *vs.* cycle number obtained from NP-Sn and dense tin slurry electrodes made with a 65:20:15 ratio of active material:carbon fiber:CMC with a 1 mg/cm^2 mass loading, cycled at 250 mAh/g (a). Voltage *vs.* capacity plots of dense tin (b) and NP-Sn (c) normalized by only the mass of tin in the electrode collected during the TXM experiment. The current density used for the dense tin electrodes was 356 mA/g, and the current density used for NP-Sn was 724 mA/g. Plots of dQ/dV for dense tin (d) and NP-Sn (e) showing typical profiles for the lithiation/delithiation of tin. The dQ/dV profile for NP-Sn is broadened compared to dense tin, indicative of the nanoscopic nature of the material.

Figure 7.4. Absorption images of dense and nanoporous tin collected using an X-ray transparent pouch cell using a Transmission X-ray microscopeoperating at 8.95 KeV. Decreasing voltage (left-to-right) corresponds to increasing Li-concentrations (a). Dense tin (top) undergoes a burst-expansion mechanism, which occurs predominantly at the end of the insertion process. This process leads to tremendous strain in the material followed by crack formation observed at 0.05V. The NP-Sn (bottom) expands less than dense tin and evolves to the final lithiated state more homogeneously.

Increasing voltage (left-to-right) corresponds to decreasing Li-concentrations (b). Dense tin (top) was found to be irreversibly deformed, and does not return to its original shape or size. Cracks formed during lithiation remain in the material. By contrast, the nanostructured NP-Sn (bottom) contracts back nearly to its original size, leading to the long cycle lifetimes of this material. Quantification of the areal expansion of the TXM in this figure (c). Percent areal expansion is shown for dense tin (black-squares), 5 μm NP-Sn (green circles), and 10 μm NP-Sn (red triangles) at different voltages and thus different lithiation states.

Figure 7.5. Absorption images and pore analysis for a larger NP-Sn collected using TXM; image contrast has been adjusted to increase visibility. Parts (a) shows the full NP-Sn grain used for the pore evolution study. The yellow square indicates the area we focused on in order to track the same pores throughout cycling. Part (b-d) show the magnified TXM images before cycling (b), in the lithiated state (c), and in the delithiated state (d). Panels (e-f) show the average pores size and standard deviation of the pores size at each voltage plateau throughout lithiation and delithiation. Both pore size and pores size distribution increase upon lithiation due to the volume expansion. Pore size and pore size distribution first decrease upon delithiation due to volume contraction. Both metrics then increase at full delithiation as some pores crack and due to the volume change, resulting in a bimodal pores size distribution with a few very large pores. Despite the pore size changes, the interconnections of the nano-tin based ligaments appear to be uninterrupted; interconnected pores and ligaments are fundamental to the favorable performance of this system.

Figure 8.1. a) X-ray diffraction pattern of the parent alloy and the as dealloyed NP-SbSn. b-c) SEM images of the NP-SbSn at low and high magnifications. d) TEM image of the NP-SbSn. e) N_2 porosimetry isotherm of the nanoporous structure.

Figure 8.2. X-ray photoelectron spectroscopy of np-SbSn a) before Ar beam etch and b) after etch. Most of the oxide layer was gone after the Ar etch, suggesting that the surface oxide layer is thin.

Figure 8.3. a) CV curves of the first five cycles of NP-SbSn at 0.1 mV/s. b) charge and discharge profiles the 1st, 2nd, 5th, 10th, and 20th cycle of NP-SbSn. c) Long term cycle lifetime study of NP-SbSn up to 100 cycles at 0.2C.

Figure 8.4. Adsorption images of a) NP-Sn and b) NP-SbSn at OCV, fully lithiated and delithiated state c) The areal expansion of bulk and NP-Sn and NP-SbSn throughout the first cycle.

Figure 8.5. a) Pore size evolution of NP-Sn and NP-SbSn throughout the first cycle. High magnification adsorption images of b) NP-Sn and c) NP-SbSn at OCV, lithiated and delithiated state.

Figure 8.6. a) Low and high magnifications of the adsorption images of NP-SbSn at the 36th cycle at OCV, 0.05 V and 1.5 V. b) The change in areal expansion and c) pore size throughout the cycle.

Figure 9.1. Materials Characterization of b- and np-SbSn. a) XRD patterns of b-SbSn in dark gray and np-SbSn in blue. They both match the stick pattern of JCPD card No.00-033-0118 for rhombohedral Stistaite *β*-SbSn b-c) Low and high magnification SEM images of b-SbSn and d-e) np-SbSn.

Figure 9.2. Electrochemical cycling of b- and np-SbSn. a) CV curves of the first five cycles of np-SbSn cycled at 0.1 mV/s. b) Galvanostatic charge and discharge profiles of 1st, 2nd, 5th, 10th and 20th cycle of NP-SbSn at 0.2C. c) Longterm cycling of np-SbSn (red) in comparison to the bulk (black). The coulombic efficiency of np- and b- SbSn are plotted in blue and green, respectively.

Figure 9.3. Adsorption images of b- and np-SbSn collected during operando TXM study. a) b- and b) np-SbSn collected at OCV, fully sodiated (0.05 V) and desodiated (1.5 V) state. c) Percent areal expansion calculation of b- and np-SbSn throughout the whole cycle.

Figure 9.4. Adsorption images of the pores of np-SbSn at a) OCV, b) 0.05 V (sodiated) and c) 1.5 V (desodiated). d) The change in pore size throughout the first cycle.

Figure 10.1. a) Powder X-ray diffraction pattern of NP-SbSn. b) Isotherm of N_2 porosimetry. The inset shows the pore size distribution calculated from BJH. c-d) TEM images of pristine and e) Al_2O_3-coated NP-SbSn powder.

Figure 10.2. Cyclic Voltammogram of the a) bare electrode and the b) Al_2O_3-coated electrode. c) Stability test of the bare and Al_2O_3-coated SbSn in a three-electrode flooded cell. d) Long term cycling of the Al_2O_3-coated SbSn in a two-electrode Swagelok cell.

Figure 10.3. Adsorption images of the a) bare and b) Al_2O_3-coated SbSn particle. c) Areal expansion of the two electrodes throughout cycling.

Figure 10.4. a) Pore evolution of bare and coated SbSn throughout cycling b) Absorption images of pores of the Al_2O_3-coated NP-SbSn powder at OCV, 0.05 V (sodiated), and 1.5 V (desodiated) *vs.* Na/Na^+. The black regions resulting from image thresholding correspond to domains of the NP-SbSn.

Figure 10.5. a) Adsorption images of the coated NP-SbSn on the 10^{th} cycle. b) High magnification of the adsorption images of the pores. The black regions resulting from image thresholding correspond to domains of the NP-SbSn. c) Areal expansion of the Al_2O_3-coated NP-SbSn powder on the first and the 10^{th} cycle. d) Pore area evolution of the Al_2O_3-coated NP-SbSn powder on the first and 10^{th} cycle.

List of Tables

Table 2.1. Gravimetric capacity of nanostructured MoS_2 based half-cells. *The capacity increased from ~200 – 220 mAh/g over ~500 cycles, so we normalized the capacity retention by the maximum capacity value and not the initial capacity of 200 mAh/g. **The capacitance reported in this study was converted to capacity using the reported voltage window of 0.85 V. The galvanostatic trace used to calculate the capacitance are nearly linear, so the relationship capacity = (capacitance · Voltage)/3.6 is an excellent approximation for this system.

Table 4.1. Gravimetric capacity of nanostructured MoS_2 based on sodium-ion half-cells. *Capacity estimated from plot.

Acknowledgements

Undertaking this PhD has truly been a life changing experience and it would not be possible without a number of people. First and foremost, I would like to thank my advisor Professor Sarah Tolbert for giving me the opportunity to be a part of her group. Without her support and guidance, I would not have become the scientist I am today. During the times when projects are not working, she would always stay patient and be understanding especially during synchrotron runs when things can be really stressful. I also want to express gratitude for the opportunity to have such a wonderful committee: Professor Richard Kaner, Professor Xiangfeng Duan, and Professor Bruce Dunn. Through many insightful conversations with them, I have had the opportunity to learn from the best in the inorganic, materials, and electrochemistry field.

In completing the work in this thesis, I have to start by acknowledging a few people.

1) The MoS_2 work was a collaboration between a big group of people from the Tolbert and the Dunn Lab: Dr. John B. Cook, Dr. Hyung-Seok Kim, Dr. Yan Yan, Dr. Jesse S. Ko, Dr. Shauna Robbennolt, Dr. Chun-Hun Lai, Andrew Siordia and myself.
2) In studying the pseudocapacitive behavior of nanostructured $LiMn_2O_4$, Dr. Benjamin K. Lesel synthesized all the materials and went to SSRL with me to obtain the *operando* X-ray diffraction data. Victoria Basile was a big help in fabricating the electrodes and in data processing.
3) The synthesis of fast charging nanoporous $LiVPO_4F$ would not be possible without the PMMA colloids that Dr. Yan Yan made and the endless discussions I had with a number of people (Dr. Jonathan Lau, Dr. Chun-Hun Lai, Chris Choi, Danielle Butts, Yiyi Yao, Victoria Basile and Sophia King who took the TEM images)
4) The nanoporous metal work was started by Professor Eric Detsi and Dr. John B. Cook. I was fortunate to become a part of the team later on to synthesize the nanoporous tin and to conduct the tomography experiments. This has allowed me expand my research beyond nanoporous tin to

other systems that I had later developed with the help of a few collaborators from UCLA (Andrew Dawson, Dr. Yan Yan and Dr. David Ashby) and the beamline scientist, Dr. Johanna N. Weker, at SSRL.

5) With the ALD coating work, I want to specifically thank Ryan Shiel from Professor Jane P. Chang's group for doing all the depositions. Many electrodes have been coated in order to obtain the results presented in this thesis but there has never been a single complain. I also want to thank Dr. Jonathan Lau for the helpful discussions and in performing the electrochemical cycling.

Once again, I want to thank all my collaborators. It has been a pleasuring working with each and every one of you. I hope that in the future, we can continue working together and help each other for the rest of our careers.

Depicting this graduate school experience as a long roller coaster ride cannot be more accurate. I am very fortunate to have the Tolbies as my companion. Everyone in the group has always been extremely fun and supportive in many ways beyond science. I also want to thank the Dunn lab for treating me as one of their own group member. In order to survive this journey, my family, my fiancé and my friends have been a great help. To those I do not mention, please know that I did not forget about you. I am simply trying to keep this list short. This amazing group of people who have made me laugh, kept me calm, and listened to my endless complaints in the past four year includes my parents, my grandma, my sister, Dr. Jonathan Lau, Ty Karaba, Patrick Yee, Dr. Janice Lin, Dr. Hyeyeon Kang, Dr. Abraham Buditama, Dr. Chiya Yu, Ryan DeBlock, Dr. Dean Chieks, Leibniz Huang, Alvin Li, Kevin Yeh, Stephanie Edwards and many more. I cannot thank all of you enough for going through this incredible journey with me!

Vita

2012	*B. S. in Chemistry*
	Environmental Studies Certificate – The Nelson Institute
	University of Wisconsin - Madison
2012-2013	*M.S. in Chemistry*
	University of Oregon
2014-2018	*Graduate Student Researcher*
	Department of Chemistry and Biochemistry
	University of California, Los Angeles

Publications

Cook, J. B.;‡ **Lin, T. C.**;‡ Kim, H.-S.; Siordia, A.; Dunn, B.; Tolbert, S. H. Suppression of Electrochemically Driven Phase Transition in Nanostructured MoS_2 Pseudocapacitors Probed Using *Operando* X-ray Diffraction. *ACS Nano.* **2019**, *13*, 1223-1231.

Moni, P.; Lau, J.; Mohr, A.; **Lin, T. C.**; Tolbert, S. H.; Dunn, B.; Gleason, K. Growth Temperature and Electrochemical Performance in Vapor-Deposited Poly(3,4-Ethylenedioxythiophene) Thin Films for High-Rate Energy Storage. *ACS Applied Energy Materials.* **2018**, *1*, 7093-7105.

Fischer, S.; Roeser, J.; **Lin, T. C.**; DeBlock, R.; Lau, J.; Dunn, B.; Hoffmann, F.; Fröba, M.; Thomas, A.; Tolbert, S. H. A Metal-Organic Framework with Tetrahedral Aluminate Sites as a Single-Ion Li^+ Solid Electrolyte. *Angew. Chem.* **2018**, *57*, 16683-16687.

Mei, B.-A.; Lau, J.; **Lin, T. C.**; Tolbert, S. H.; Dunn, B.; Pilon, L. Physical Interpretations of Electrochemical Impedance Spectroscopy (EIS) of Redox Active Electrodes. *J. Phys. Chem. C* **2018**, *122*, 24499-24511.

Lai, C.-H.; Ashby, D.; **Lin, T. C.**; Lau, J.; Dawson, A.; Tolbert, S. H.; Dunn, B. The Application of Poly(3-hexylthiophene-2,5-diyl) as a Protective Coating for High Rate Cathode Materials. *Chem. Mater.* **2018**, *30*, 2589-2599.

Lesel, B. K.; Cook, J. B.; Yan, Y.; **Lin, T. C.**; Tolbert, S. H. Using Nanoscale Domain Size To Control Charge Storage Kinetics in Pseudocapacitive Nanoporous $LiMn_2O_4$ Powders. *ACS Energy Lett.* **2017**, *2*, 2293-2298.

Cook, J. B.; Kim, H.-S.; **Lin, T. C.**; Robbennolt, S.; Detsi, E.; Dunn, B.; Tolbert, S. H. Tuning Porosity and Surface Area in Mesoporous Silicon for Application in Li-ion Battery Electrodes. *ACS Appl. Mater. Interfaces* **2017**, *9*, 19063-19073.

Cook, J. B.; **Lin, T. C.**; Detsi, E.; Weker, J. N.; Tolbert, S. H. Using X-ray Microscopy to Understand How Nanoporous Materials Can Be Used To Reduce the Large Volume Change in Alloying Anodes. *Nano Lett.* **2017**, *17*, 870-877.

Cook, J. B.; Kim, H.-S.; **Lin, T. C.**; Lai, C.-H.; Dunn, B.; Tolbert, S. H. Pseudocapacitive Charge Storage in Thick Composite MoS_2 Nanocrystals-Based Electrodes. *Adv. Energy Mater.* **2017**, *7*, 1601283.

Presentations

Lin. T. C.; Cook, J. B.; Detsi, E.; Weker, J. N.; Sheil, R.; Lau, J.; Dawson, A.; Ashby, D.; Dunn, B.; Chang, J. P.; Tolbert, S. H. "Nanoporous Metals, Sn and SbSn, for Energy Storage Applications" The 10th International Mesostructured Materials Symposium; 2018 Sept. 10-13; Los Angeles, CA; Oral Presentation

Lin, T. C.; Cook, J. B.; Detsi, E.; Dawson, A.; Weker, J. N.; Tolbert, S. H. Using *operando* Transmission X-ray Microscopy to Understand the Expansion Mechanism of Nanoporous Metal Upon Lithiation and Sodiation. 2018 MRS Spring Meeting; 2018 April 2-6; Phoenix, AZ; Oral Presentation.

Lin, T. C.; Cook, J. B.; Detsi, E.; Weker, J. N.; Tolbert, S. H. Nanoporous Sn and SbSn Anode for Li and Na ion Batteries through One-step Selective Etching. ACS 253rd National Meeting; 2017 April 2-6; San Francisco, CA; Oral Presentation.

Lin, T. C.; Cook, J. B.; Kim, H.-S.; Ko, J.; Yan, Y.; Dunn, B.; Tolbert, S. H. MoS2 Nanocrystals as Fast Charging Pseudocapacitors for Li and Na Battery. 2016 MRS Fall Meeting; 2016 Nov. 25-Dec. 1; Boston, MA; Oral Presentation.

Lin, T. C.; Cook, J. B.; Detsi, E.; Weker, J. N.; Tolbert, S. H. Reducing the Large Volume Change in Alloy Anodes through Porous Nanoscale Architecture. ACS 251st National Meeting; 2016 March 13-17; San Diego, CA; Oral Presentation.

Patents

Tolbert, S. H.; Dunn, B.; Cook, J.; Kim, H.-S.; **Lin, T. C.** Metal Chalcogenides for Pseudocapacitive Applications. *2017*.

Chapter 1. Introduction

Electrochemical energy storage is a growing need within our current society, with an ever broadening range of applications requiring different functionality. For example, personal electronics require faster charging times and higher capacity per mass. Electric vehicles need high capacity, long life-time, and ideally very fast charging times. Grid level energy storage for use with intermittent renewable energy sources such as wind or solar needs low cost, high capacity and extremely long cycle life.[1] To address these varying needs, a broad range of energy storage technologies are currently being explored, including traditional lithium secondary-ion batteries,[2,3] alternative secondary-ion batteries that utilize lower cost metals such as Na^+ or Mg^{2+},[4-10] high capacity alloy and conversion type batteries,[11-13,14,15,16] low cost flow batteries,[17] high rate double layer capacitors or supercapacitors,[18-20] and pseudocapacitors.[21-23]

At its most basic level, energy storage system can be categorized into three different types, batteries, electric double layer capacitors (EDLC) and pseudocapacitors. Traditional batteries can have high capacities because the charge of a redox reaction is compensated for the addition or subtraction of an ion, resulting in net charge neutrality and the potential for a very high density of redox sites (Figure 1.1, left). Alloy and conversion type reactions increase this density even higher by allowing for multi-electron redox at the same site.[15,16] While the energy densities in these systems are quite high, the power densities are generally low for two reasons. In the first place, solid state diffusion of Li^+ (or Na^+ or Mg^{2+}) is needed for the secondary ion to reach the active redox sites (Figure 1.1, left), and that solid state ion diffusion is generally slow, particularly for larger ions like Na^+ or more highly charged ions like Mg^{2+}.[4,7-10] Moreover, restructuring of the electrode materials to accommodate the addition or loss of a metal ion, or to accommodate entirely new bonding geometries in the case of alloy and conversion reactions, is an intrinsically slow process that further reduces the power density of conventional rechargeable batteries.[15]

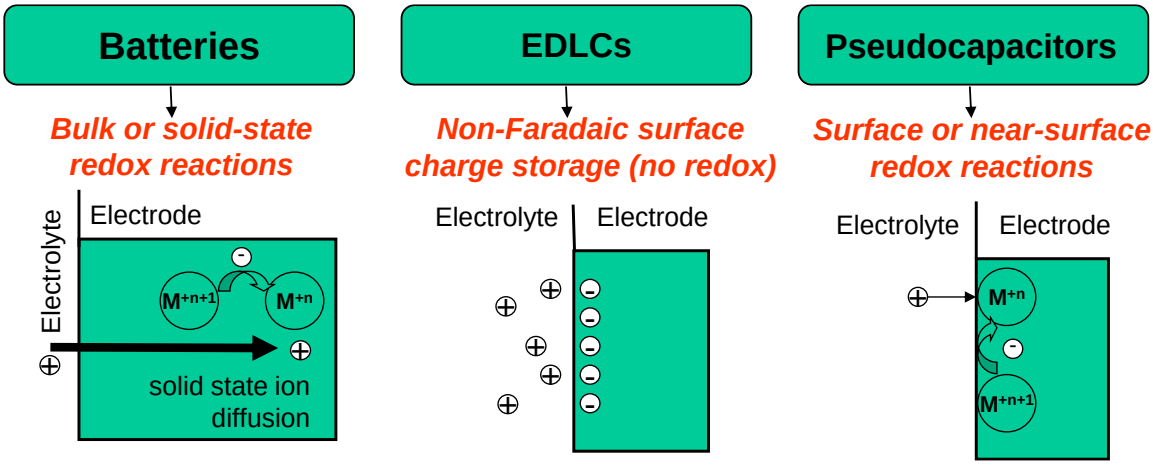

Figure 1.1. Schematic diagram of various electrochemical energy storage systems.

In the opposite extreme, EDLCs are extremely fast, as the only motion that is needed is the motion of electrons within the active material, and free motion of ions within the electrolyte (Figure 1.1, middle). For these systems, however, electrostatic repulsion between ions in solution or charges on the electrode material results in lower charge density and reduced energy density compared to traditional batteries.[24-28] Pseudocapacitors (Figure 1.1, right) offer the potential for both high energy and high power density by combining the storage mechanism of a battery with the kinetics more similar to an EDLC.[29] While each of these technologies offer unique capabilities to address important practical problems in energy storage, this thesis has chosen to focus on pseudocapacitors and high capacity alloy type batteries because of their exceptional rate capabilities and high capacity that are critical to the development personal electronics, and, electric vehicles and grid level energy storage, respectively.

Pseudocapacitors can combine many of the favorable aspects of batteries and supercapacitors by relying on surface or near-surface Faradaic redox reactions, so that high power density can be combined with reasonably high energy density. Historically, these reactions have been divided into two categories: When ions are electrochemically adsorbed onto redox sites at the solid electrolyte

interface of the material, the process is termed redox or surface pseudocapacitor, and this is standardly what is thought of a pseudocapacitive charge storage. Alternatively, when ions intercalate into the channels or layers of the redox-active material in a non-diffusion controlled manner without inducing a phase transition, the process is called intercalation pseudocapacitance.[30-32] Large scale structural changes, like those observed in most batteries, are unfavorable for fast charging systems because the nucleation and growth of these new phases can be slow and can impede rapid battery cycling. However, as the dimensions of a material reduce from the micron-scale to the nanoscale, the fraction of redox sites on the materials surface can significantly increase. Moreover, both the kinetics and thermodynamics of phase transitions can be altered in small size due to changes in interfacial energy and in nucleation kinetics.[33-37] This can cause pseudocapacitance to manifest and even dominate over diffusion controlled intercalation reactions in nanostructured materials.[38] Ultimately, this means pseudocapacitors may be derived from traditional battery intercalation materials by manipulating their size and nanoscale architecture.[39-46]

We thus postulate that intercalation pseudocapacitance can occur in nanostructured versions of traditional battery materials when two structural constraints are satisfied. First, solid-state diffusion path lengths need to be short and matched to the ion diffusion rate of a given materials to significantly decrease the diffusion time (note that diffusion length is proportional to the square root of diffusion time[47]).[48] Second, ion insertion and de-insertion into the material cannot lead to a first-order phase transition because these transitions limit the kinetics of ion transport. To further understand the fundamental aspects of pseudocapacitance, a library of nanostructured metal oxides and sulfides was synthesized. Their charge storage mechanisms, cycling behaviors, and structural changes were studied through a combination of electrochemical cycling, kinetics analysis and synchrotron *operando* X-ray diffraction. This will offer the potential to broaden our knowledge on pseudocapacitive charge storage while simultaneously impacting what could be an important future energy storage technology.

Unlike pseudocapacitors, batteries rely on bulk or solid state redox reactions. Though these reactions are slow, they offer much higher energy densities. This is especially true with alloying type anodes that possess specific capacities 3-10 times greater than typical battery electrodes by allowing for multi-electron redox reactions. Unfortunately, these electrochemical reactions are accompanied by severe volume expansion (~400%) that reduce the lifetime of the active material. Three well-recognized approaches to limit the detrimental effects of this expansion include the use of nanoporous structures,[49-52] using multiphase composites such as intermetallics,[53-54] and using artificial solid electrolyte interphase (SEI) coatings.[55-56] Nanoporous structures accommodate bulk volume expansion using internal void space. A three-dimensional (3D) framework with tunable pore size and highly interconnected and interpenetrating pathways for both electrons and ions, may offer considerable advantages in addressing the fundamental challenge in charge transport and volume change.[50-52] By contrast, intermetallics and artificial SEI coatings improve the mechanical properties of the active material and of the composite electrode. By incorporating a second electrochemically active metal, the process of alloying with Li or Na will occur at a broader range of potentials, leading to a more gradual expansion process that decreases the likelihood of crack formation.[53] Meanwhile, artificial SEI coating, which normally consist of inert amorphous oxides, allows the active material to maintain electrical contact with the current collector by acting as a glue and a ionically conductive protective layer that prevents the formation of new SEI during the volume expansion process.[57-58]

We seek to understand the critical role of each approach mentioned above in accommodating volume change by working with Beamline 6-2 at the Stanford Synchrotron Radiation Lightsource (SSRL) using a series of *operando* imaging with transmission X-ray microscopy (TXM). Key to the success of establishing materials and architectural design rules is the use of X-ray imaging to directly follow changes in nanoscale structure during battery cycling. Transmission X-ray microscopy (TXM) utilizes X-ray's low cross section with most battery materials to image thicker samples. [59-64] Imaging

of this type is representative of the actual electrode environment. The resolution of this method is ~30 nm, which is ideal to the morphology of most nanoporous systems.[64] The goal is to mechanistically understand how each approach accommodates volume expansion and how the approaches can be combined to best advantage for future devices.

The work presented in the following chapters is unified around the common theme of establishing materials design rules for the next generation electrochemical energy storage systems, focusing on intercalation pseudocapacitors and high energy density alloying anodes. Chapter 2 introduces the technical and scientific details of MoS_2 nanocrystals as a novel pseudocapacitive anode. Chapters 3 and 4 present work on the suppression of first order phase transition in MoS_2 nanocrystals during lithium and sodium ion intercalation. Chapter 5 discusses our first pseudocapacitive cathode $LiMn_2O_4$ (LMO) and the observation of a critical size where the cross over behavior of a battery and a pseudocapacitor is found. Chapter 6 features another cathode, $LiVPO_4F$ with higher operating voltage window and higher capacity than LMO. Exceptional rate capabilities were demonstrated when nanosized as the diffusion path length significantly shortens. We then switch gears to high capacity alloying anodes starting from Chapter 7, where the stabilization mechanism of a nanoporous alloying anode is elucidated during the volume expansion process. Nanoporous tin (NP-Sn) was used as the platform for this study. Chapter 8 then follows up on an analogue of NP-Sn, nanoporous antimony tin (NP-SbSn), to reveal the different volume expansion process in intermetallics and pure metals. Chapter 9 discusses the fundamental differences between lithium and sodium induced volume expansion using NP-SbSn as a model system. Chapter 10 investigates the effects of surface coatings on nanoporous alloying anodes in helping them alleviate the volume change. Finally, Chapter 11 concludes and summarizes the key findings of this work.

1.1. Reference

[1] B. Dunn, H. Kamath, J. M. Tarascon, *Science* **2011**, *334*, 928.

[2] M. S. Whittingham, *Chem. Rev.* **2004.** *104*, 4271.

[3] M. Winter, J. O. Besenhard, M. E. Spahr, P. Novák, *Adv. Mater.* **1998**, *10*, 725.

[4] L. P. Wang, L. Yu, X. Wang, M. Srinivasan, Z. J. Xu, *J. Mater. Chem. A* **2015**, *3*, 9353.

[5] Y. Liu, X. Liu, T. Wang, L. Fan, L. Jiao, *Sustainable Energy Fuels* **2017**, *1*, 986.

[6] J. Hwang, S. Myung, Y. Sun, *Chem. Soc. Rev.* **2017**, *46*, 3529.

[7] R. Mohtadi, F. Mizuno, *Belistein J. Nanotechnol.* **2014**, *5*, 1291.

[8] P. Saha, M. K. Datta, O.I. Velikokhatnyi, A. Manivannan, D. Alman, P.N. Kumta, *Progress in Materials Science* **2014**, *66*, 1.

[9] J. Song, E. Sahadeo, M. Noked, S. B. Lee, *J. Phys. Chem. Lett.* **2016**, *7*, 1736.

[10] H. D. Yoo, I. Shterenberg, Y. Gofer, G. Gershinsky, N. Pour, D. Aurbach, *Energy Environ. Sci.* **2013**, *6*, 2265.

[11] W. J. Zhang, *J. Power Sources* **2011**, *196*, 13.

[12] A. Manthiram, Y. Fu, S. H. Chung, C. Zu, Y. S. Su, *Chem. Rev.* **2014**, *114,* 11751.

[13] S. H. Yu, S. H. Lee, D. J. Lee, Y. E. Sung, T. Hyeon, *Small* **2016**, *12*, 2146.

[14] W. J. Zhang, *J. Power Sources* **2011**, *196*, 877.

[15] N. Nitta, G. Yushin, *Part. Part. Syst. Charact.* **2014**, *31*, 317.

[16] R. Chen, R. Luo, Y. Huang, F. Wu, L. Li, *Adv. Sci.* **2016**, *3*, 1600051.

[17] P. Alotto, M. Guarnieri, F. Moro, *Renewable and Sustainable Energy Reviews* **2014**, *29*, 325.

[18] J. R. Miller, P. Simon, *Science* **2008**, *321*, 651.

[19] R. Kötz, M. Carlen, *Electrochim. Acta* **2000**, *45*, 2483.

[20] A. González, E. Goikolea, J. A. Barrena, R. Mysyk, *Renewable and Sustainable Energy Review.* **2016,** *58*, 1189.

[21] B. E. Conway, W. G. Pell, *J. Solid State Electrochem.* **2003**, *7*, 637.

[22] B. E. Conway, V. Birss, J. Wojtowicz, *J. Power Sources* **1997**, *66*, 1.

[23] Y. Zhang, H. Feng, X. Wu, L. Wang, A. Zhang, T. Xia, H. Dong, X. Li, L. Zhang, *Int. J. Hydrog. Energy* **2009**, *34*, 4889.

[24] L. L. Zhang, X. S. Zhao, *Chem. Soc. Rev.* **2009**, *38*, 2520.

[25] P. Simon, A. Burke, *Electrochem. Soc. Interface* **2008**, *17*, 38.

[26] L. Pilon, H. Wang, A. d'Entremont, *J. Electrochem. Soc.* **2015**, *162*, A5158.

[27] E. Raymundo-Piñero, K. Kierzek, J. Machnikowski, F. Béguin, *Carbon* **2006**, *44*, 2498.

[28] D. Lozano-Castelló, D. Cazorla-Amorós, A. Linares-Solano, S. Shiraishi, H. Kurihara, A. Oya, *Carbon* **2003**, *41*, 1765.

[29] Y. Wang, Y. Song, Y. Xia, *Chem. Soc. Rev.* **2016**, *45*, 5925.

[30] Y. Zhu, L. Peng, D. Chen, G. Yu, *Nano Lett.* **2016**, *16*, 742.

[31] V. Augustyn, J. Come, M. A. Lowe, J. W. Kim, P. Taberna, S. H. Tolbert, H. D. Abruña, P. Simon, B. Dunn, *Nat. Mater.* **2013**, *12*, 518.

[32] B. E. Conway, W. G. Pell, *J. Solid State Electrochem.* **2003**, *7*, 637.

[33] S. H. Tolbert, A.P. Alivisatos, *Science* **1994**, *265*, 373.

[34] S. H. Tolbert, A. P. Alivisatos, *J. Chem. Phys.* **2014**, *102*, 4642.

[35] B. M. Wagemaker, F. M. Mulder, A. Van Der Ven, *Adv. Mater.* **2009**, *21*, 2703.

[36] J. Maier, *Solid State Ionics* **2002**, *154-155*, 291.

[37] A. Van Der Ven, J. Bhattacharya, A. A. Belak, *Accounts of Chemical Research* **2013**, *46*, 1216.

[38] J. Wang, J. Polleux, J. Lim, B. Dunn, *J. Phys. Chem. C* **2007**, *2*, 14925.

[39] T. Brezesinski, J. Wang, S. H. Tolbert, B. Dunn, *Nat. Mater.* **2010**, *9*, 146.

[40] H.-S. Kim, J. B. Cook, S. H. Tolbert, B. Dunn, *J. Electrochem. Soc.* **2015**, *162*, A5083.

[41] G. A. Muller, J. B. Cook, H. Kim, S. H. Tolbert, B. Dunn, *Nano Lett.* **2015**, *15*, 1911.

[42] H. S. Kim, J. B. Cook, H. Lin, J. S. Ko, S. H. Tolbert, V. Ozolins, B. Dunn, *Nature Materials* **2017**, *16*, 454.

[43] B. K. Lesel, J. Cook, Y. Yan, T. C. Lin, S. H. Tolbert, *ACS Energy Letters* **2017**, *2*, 2293.

[44] B.K. Lesel, J. S. Ko, B. Dunn, S. H. Tolbert, *ACS Nano* **2016**, *10*, 7572.

[45] J. B. Cook, H.-S. Kim, T. C. Lin, C.-H. Lai, B. Dunn, S. H. Tolbert, *Adv. Energy Mater.* **2017**, *7*, 1601283.

[46] J. B. Cook, H. Kim, Y. Yan, J. S. Ko, S. Robbennolt, B. Dunn, S. H. Tolbert, *Adv. Energy Mater.* **2016**, *6*, 1501937.

[47] N. Balke, S. Jesse, A. N. Morozovska, E. Eliseev, D. W. Chung, Y. Kim, L. Adamczyk, R. E. Garcia, N. Dudney, S. V. Kalinin, *Nat. Nanotechnol.* **2010**, *5*, 749.

[48] I. E. Rauda, V. Augustyn, L. C. Saldarriaga-Lopez, X. Chen, L. T. Schelhas, G. W. Rubloff, V. Dunn, S. H. Tolbert, *Adv. Funct. Mater.* **2014**, *24*, 6717.

[49] C.-M. Park, K. J. Jeon, *Chem. Commun.* **2011**, *47*, 2122.

[50] J. B. Cook, E. Detsi, Y. Liu. Y.-L. Liang, H.-S. Kim, X. Petrissans, B. Dunn, S. H. Tolbert, *ACS*

Appl. Mater. Interfaces **2017**, *9*, 293.

[51] J. B. Cook, H.-S. Kim, T. C. Lin, S. Robbennolt, E. Detsi, B. S. Dunn, S. H. Tolbert, *ACS Appl. Mater. Interfaces* **2017**, *9*, 19063.

[52] J. B. Cook, T. C. Lin, E. Detsi, J. N. Weker, S. H. Tolbert, *Nano Lett.* **2017**, *17*, 870.

[53] X.-L. Wang, W.-Q. Han, J. Chen, J. Graetz, *ACS Appl. Mater. Interfaces* **2010**, *2*, 1548.

[54] M. Winter, J. O. Besenhard, *Electrochim. Acta* **1999**, *45*, 31.

[55] X. Meng, *J. Mater. Chem. A* **2017**, *5*, 10127.

[56] X. Meng, X.-Q. Yang, X. Sun, *Adv. Mater.* **2012**, *24*, 3589.

[57] X. Han, Y. Liu, Z. Jia, Y.-C. Chen, J. Wan, N. Weadock, K. J. Gaskell, T. Li, L. Hu, *Nano Lett.* **2014**, *14*, 139.

[58] D. Wang, J. Yang, J. Liu, X. Li, R. Li, M. Cai, T.-K. Sham, X. Sun, *J. Mater. Chem. A* **2014**, *2*, 2306.

[59] S. C. Chao, Y. F. Song, C. C. Wang, H. S. Sheu, H. C. Wu and N. L. Wu, *J. Phys. Chem. C* **2011**, *115*, 22040.

[60] S. C. Chao, Y. C. Yen, Y. F. Song, Y. M. Chen, H. C. Wu and N. L. Wu, *Electrochem. commun.* **2010**, *12*, 234.

[61] J. Wang, Y.-C. K. Chen-Wiegart and J. Wang, *Angew. Chem. Int. Ed.* **2014**, *53*, 4460.

[62] J. N. Weker, N. Liu, S. Misra, J. C. Andrews, Y. Cui and M. F. Toney, *Energy Environ. Sci.* **2014**, *7*, 2771.

[63] J. Nelson Weker and M. F. Toney, *Adv. Funct. Mater.* **2015**, *25*, 1622.

[64] J. Nelson, S. Misra, Y. Yang, A. Jackson, Y. Liu, H. Wang, H. Dai, J. C. Andrews, Y. Cui, M. F.

Toney and J. C. Andrews, *J. Am. Chem. Soc.* **2012**, *134*, 6337.

Chapter 2. Pseudocapacitive Charge Storage in Thick Composite MoS_2 Nanocrystal-Based Electrode

2.1. Introduction

Fast charging batteries are highly desired for portable electronics, electric vehicles, and regenerative energy storage. Traditional Li-ion batteries offer high energy density storage by utilizing reversible redox reactions, but slow ionic diffusion leads to long charging times (~1-10 hours).[1] Electrochemical capacitors, such as electrochemical double layer capacitors (EDLCs), offer some advantages over batteries, including fast charging times (<1 minute) and long lifetimes (>500,000 cycles).[2] However, EDLCs have low energy densities (5-10 Wh/kg) compared to batteries (100-250 Wh/kg), since they do not involve redox reactions.[3]

Pseudocapacitors are another type of electrochemical capacitor that have the potential to combine the attractive high energy density storage of batteries with the fast rates of EDLCs.[4,5] Pseudocapacitance was originally described by Conway who identified faradaic mechanisms that can result in capacitive electrochemical features. The most useful of these for energy storage are redox pseudocapacitance and intercalation pseudocapacitance.[6,7] Redox pseudocapacitance occurs when a Faradaic charge transfer process take place at or near the surface of a material, accompanied by adsorption of charge balancing ions.[8–14] Conway originally described the pseudocapacitive mechanism to also include lithium intercalation into layered host materials,[6] but the majority of the work published in this field focuses on the surface redox-based electrochemical reactions of ultra-high surface area materials like RuO_2,[8–12] and MnO_2.[14] This bias toward materials showing surface pseudocapacitance has led to intercalation pseudocapacitance (another distinguishable pseudocapacitive mechanism) being dismissed or confused in some cases with traditional battery reactions. However, several papers clearly distinguish key differences between intercalation

pseudocapacitance and battery-like reactions.[15–19] Intercalation pseudocapacitance is similar to familiar battery-type intercalation, but unlike traditional battery materials, the charge storage mechanism and electrochemical response is not dominated by diffusion limitations. Another key feature that distinguishes intercalation pseudocapacitance from traditional battery-type intercalation reactions is that these materials do not undergo phase transitions in association with charge storage.[18,19] As a result, materials that store charge dominantly through intercalation pseudocapacitance display fast kinetics and long cycle lifetimes.[17,18,20,21]

The electrochemistry of ruthenium oxide in acidic solutions exhibits classic surface redox pseudocapacitance, and has been studied for over 30 years because of its relatively high capacitances, high proton conductivity and high electronic conductivity. [8–10,12] However, the high cost of ruthenium has led groups to develop materials based on less expensive transition metals. We have developed a variety of oxide based nanostructures that store charge through intercalation pseudocapacitance, such as MoO_2,[18] MoO_3,[16,22] and Nb_2O_5.[17,22–24] As mentioned above, intercalation pseudocapacitance is distinguishable from diffusion dominated charge storage, and as a result, the characteristic electrochemical signatures are markedly different.[4,7,25] For example, the galvanostatic charge and discharge curves of pseudocapacitors are typically pseudo-linear with respect to intercalant concentration; compared to batteries, which show plateaus.[26,27] Since intercalant diffusion does not dominate the charge storage in pseudocapacitors, the energy hysteresis between guest-ion insertion and deinsertion is typically small, which can be seen as a small peak separation in a cyclic voltammogram.[17,22–24] These properties lead to two key technologically relevant properties of pseudocapacitors: (1) The majority of the theoretical capacity can be accessed within minutes to seconds. (2) The reactions are highly reversible leading to low parasitic heat generation and long cycle lifetimes.

Much of the work on pseudocapacitors has focused on transition metal oxide based materials, but metal sulfides are attractive pseudocapacitive materials, too. The interaction between the guest ion (Li^+, for example), and the sulfide lattice, should be weakened compared to oxides. Furthermore, this weakened interaction should lead to faster ion migration through the lattice. In support of those ideas, we have recently demonstrated high levels of pseudocapacitive charge storage in TiS_2 nanoplatelets,[19] and mesoporous MoS_2 thin films.[21] MoS_2 is a particularly attractive pseudocapacitive electrode material because its large van der Waals gaps of 6.2 Å in micrometer sized samples increase up to 6.9 Å in nanostructured samples. [28,29] The increased van der Waals spacing should further reduce the guest-host interaction making this an ideal pseudocapacitive material.

MoS_2 also has a second advantage, which is that lithium insertion into the semi-conducting 2H phase of MoS_2 induces a phase transition to the metallic 1T phase of MoS_2.[30–33] This metallic phase is more conductive than the semi-conducting phase of MoS_2, which is an advantage for Faradaic based charge storage. The thermodynamically stable 2H phase of MoS_2 consists of sulfur atoms coordinated in a trigonal prismatic arrangement around the metal, while in the 1T phase, the atoms conform to an octahedral arrangement around the metal center.[34] The physical rearrangement of the molybdenum coordination environment induces a change in the electronic structure of the MoS_2, leading to metallic conductivity.[31] In agreement with this idea, our group has recently used conductive atomic force microscopy to demonstrate that ordered mesoporous 1T-MoS_2 thin films are significantly more conductive than the 2H form.[21] It was also recently reported that 10 nm thick exfoliated 1T-MoS_2 has a low sheet resistance (2 kΩ/sq),[35] corresponding to a calculated bulk conductivity of ~500 S/cm. In hydrogen evolution applications the intrinsically high electronic conductivity of 1T-MoS_2 is utilized to decrease the overpotential required for hydrogen evolution.[36] However, the high electronic conductivity of MoS_2 has not been fully leveraged in Li-ion battery applications because many studies have focused on high capacity conversion reaction of MoS_2, which interrupt the metallic 1T form of

MoS_2. [29,37–46] Additionally, the volume change on cycling for the conversion reaction limits lifetimes to ~100-300 cycles. [47]

We note that Li^+ intercalation in MoS_2 is not a new idea. [48–50] MoS_2 was seriously considered as a commercial secondary battery in the 1980's because the reversibility is extremely favorable when the lithium concentration in MoS_2 is limited to 1 mole, [50–53] usually by limiting the lower cut-off voltage window to above 0.8 V *vs.* Li/Li^+.[54] In our previous paper, we demonstrated that mesoporous MoS_2 thin films exhibited high levels of pseudocapacitive charge storage, emphasizing the promise of this material system as a fast charging, high power, long lifetime material.[21] That study motivated us to see if those observations were limited to thin films, or if those exciting properties could be recreated in thick film composite electrodes, as we have done here.

MoS_2 can be synthesized using a variety of different techniques. Monodispersed 5 nm MoS_2 nanocrystals can be synthesized directly by low temperature colloidal synthesis methods.[55] The hydrothermal method is another versatile technique, which has been used to synthesize a variety of nanostructured MoS_2 architectures.[29,56,57] However, both of these methods typically lead to very disordered crystal structures. The energy and power density of pseudocapacitive materials are, to a high degree, dependent on the crystallinity.[58] Therefore, in this work, we use a two-step process, first creating MoO_2 nanocrystals as a precursor using straightforward hydrothermal methods, and then converting those MoO_2 nanocrystals to MoS_2 nanocrystals. This two-step process enables precise control of both the nanoscale architecture and atomic-scale crystallinity. The synthesis method is versatile, and should be applicable to other nanoscale architectures such as wires, belts, and a broad range of porous architectures. Here we specifically use thermal sulfurization in H_2S to convert the MoO_2 to MoS_2, which preserves the carefully constructed nanoscale architecture formed from the solvothermal reaction.[44,56,59–61] This oxide-to-sulfide conversion is typically achieved above 600 °C, which can lead to well crystalized MoS_2 with good preservation of the preformed nanoscale

architecture.[56] It is worth noting that sulfur vapor can also be used instead of H_2S to convert molybdenum oxides to MoS_2.[62] Extensive discussion on the various methods used to synthesize MoS_2 can be found in several recent reviews.[47,63–65]

Commercial electrodes for Li-ion batteries are required to have high active material volumetric loadings to maximize the energy density of the cell. In order for this requirement to be satisfied in pseudocapacitive based composite electrodes, close attention also needs to be paid to the electrode architecture. The three main components that form a composite electrode are the active material, the conductive additive, and the non-conductive polymeric binder. Optimization of these parameters strongly influences the energy density and power density of the final electrode.[66,67] Furthermore, nanoparticle active material tends to agglomerate, making them difficult to disperse homogeneously within the electrode matrix.[68,69] This random agglomeration results in electronically resistive inter-particle contact, ultimately leading to poor power density due to inhomogeneous current gradients. Therefore, even if a material shows basic pseudocapacitive responses, the characteristic charge/discharge rates cannot be realized if the electrode architecture is not optimized for pseudocapacitive charge storage. Porous electrode architectures, which are highly electronically conductive, represents an effective design strategy to maintain the fast rates inherent to pseudocapacitive active materials.

In this study, we combine all of these ideas to synthesize MoS_2 nanocrystals with an expanded layer spacing for use as a high rate and long lifetime pseudocapacitor. The nanocrystals are fabricated into carbon fiber based composite electrode architectures, and the electrodes show extremely fast charging and discharging kinetics along with long cycling lifetimes. We further utilize pre-cycling steps to convert the 2H phase into the highly conductive 1T phase, which then synergistically couples to the highly conductive carbon fiber mesh electrode architecture. Detailed electrochemical kinetic analyses performed on the nanocrystal based electrodes are used to quantify the amount of capacitive

charge storage. These values can then be compared to electrodes containing micrometer size MoS_2 to fully establish advantages of the MoS_2 nanocrystal containing composite electrodes.

2.2. Results and Discussion

2.2.1. Materials and Characterization

The MoS_2 nanocrystals (nc-MoS_2) studied in this report were synthesized by the sulfurization of hydrothermally prepared MoO_2 nanocrystals. The X-ray diffraction (XRD) patterns of bulk MoS_2 (b-MoS_2) and nc-MoS_2 match JCPDS No. 37-1492 (Figure 2.1a). We have refined the b-MoS_2 structure in Celref using the hexagonal P63/mmc hexagonal space group. We have calculated the lattice parameters for b-MoS_2 as $a \,\&\, b = 3.163\ \text{Å} \pm 0.002\ \text{Å}$ and $c = 12.3092\ \text{Å} \pm 0.0002\ \text{Å}$..The lattice parameters for nc-MoS_2 are $a \,\&\, b = 3.14\ \text{Å} \pm 0.01\ \text{Å}$ and $c = 12.544\ \text{Å} \pm 0.003\ \text{Å}$. The c-axis lattice parameter is expanded in the nanoparticles to 6.272Å, compared to 6.15Å for the bulk sample, in agreement with previous reports for nano-size MoS_2 (aluminum foil was used as an internal reference).[28,29] Furthermore, significant XRD peak broadening is observed for the nc-MoS_2 due to both finite size effects and lattice defects. The domain size calculated from the Scherrer equation is 7 nm, which is smaller than the primary particle size observed from the scanning electron microscopy (SEM) and transmission electron microscopy images (TEM) in Figures 2.1b and 2.1c, respectively. This difference in the calculated Scherrer size versus observed size clearly indicates that the XRD peak broadening is due to a combination of finite size effects and lattice disorder. In agreement with this idea, defects and curvature of the MoS_2 layers can be clearly seen in the high resolution TEM images (Figures 2.1d and e).

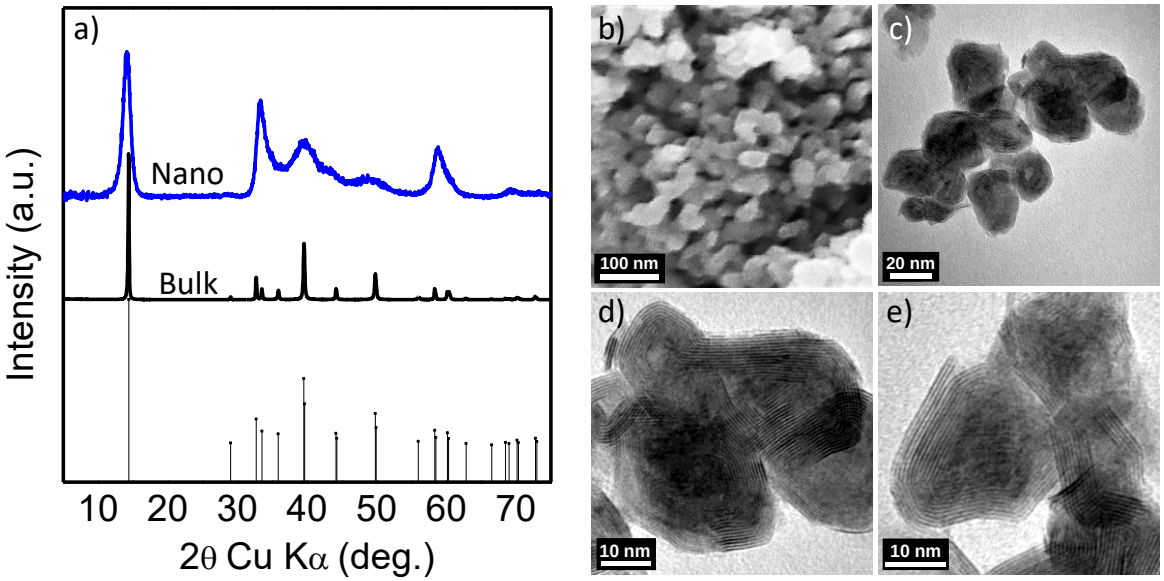

Figure 2.1. (a) X-ray diffraction of b-MoS_2 and nc-MoS_2 shows that both materials crystalize in the 2H hexagonal crystal structure (JCPDS 037-1492). The nc-MoS_2 shows significant peak broadening, however, which we assign to both finite size effects and lattice disorder. (b) Scanning electron microscope image of nc-MoS_2 show a network of agglomerated nanocrystals. (c-e) Transmission electron microscope images of dispersed nc-MoS_2 show sub-50 nanometer primary particles. Significant defects are observed and are believed to be at least partly responsible for the facile ion insertion into the bulk of the nanocrystal.

Beyond the primary particle size and lattice structure, Figure 2.1b further shows that in bulk form, the nanocrystals aggregated into a nearly ideal interconnected porous network. The surface area and pore sizes in that network can be characterized using nitrogen porosimetry. The surface area for both b-MoS_2 (2 m^2/g) and nc-MoS_2 (35 m^2/g) was calculated from the nitrogen adsorption isotherms shown in Figure 2.2a using the Brunauer-Emmett-Teller (BET) method.[70] The surface area of the nc-MoS_2 is almost twenty-times larger than b-MoS_2, and leads to a higher density of redox active surface

sites for pseudocapacitive charge storage. This is coupled to short intra-grain diffusion distance, which favor intercalation-pseudocapacitance. The pore size distribution shown in Figure 2.2b was calculated using the Barrett-Joyner-Halenda (BJH) method,[71] and was used to characterize the pores that are created in the nc-MoS_2 by adhesion of the nanocrystals to each other. The pore size distribution is remarkably narrow for a material formed by random nanocrystal agglomeration, and the 25 nm pore diameter is well suited to allow facile electrolyte diffusion into the nanoparticle aggregates.

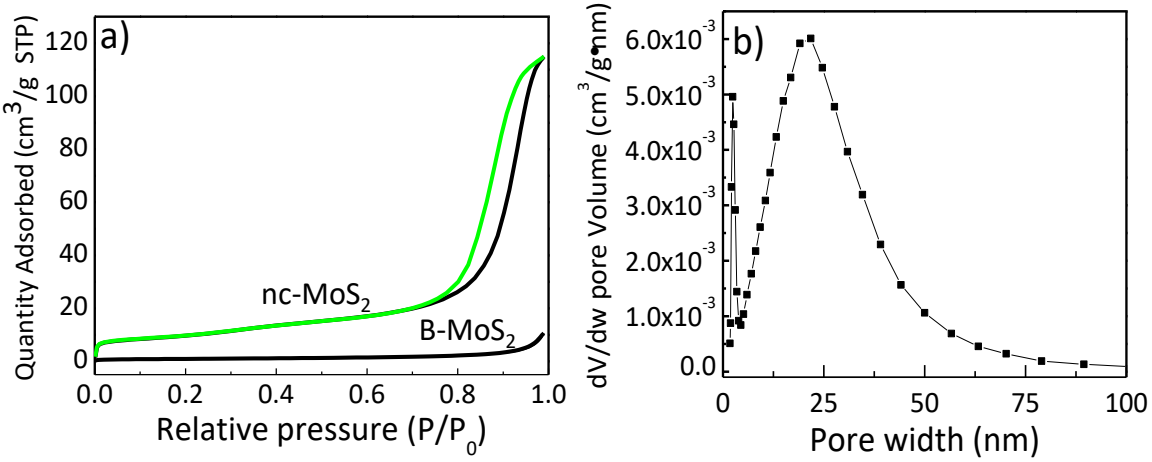

Figure 2.2. Nitrogen isotherm of both b-MoS_2 and nc-MoS_2 (a). The calculated surface area for nc-MoS_2 is 35m^2g^{-1} while the bulk is 2 m^2g^{-1}. This 17.5-fold increase in surface area, in part, leads to the pseudocapacitive charge storage mechanism. BJH pore size distribution calculated from the adsorption isotherm in part (a) for nc-MoS_2 (b). The porosity shown in the BJH distribution arises from adhesion of the nanocrystals to each other, which creates pores.

The chemical surface properties of b-MoS_2 and nc-MoS_2 were examined using X-ray photoelectron spectroscopy (XPS), as shown in Figure 2.3. These high resolution spectra can be fit with a single oxidation state for both Mo and S, corresponding to the Mo^{4+} and S^{2-} valence states. The peak area ratio between these two elements further yield a Mo:S = 1.05:2.00 stoichiometry ratio for both samples. Since the surface chemistry is identical in bulk and nano-sized samples, strong

conclusions can be drawn about the effect of size, surface area, and atomic disorder on the enhanced electrochemical performance in the nano-sized materials.

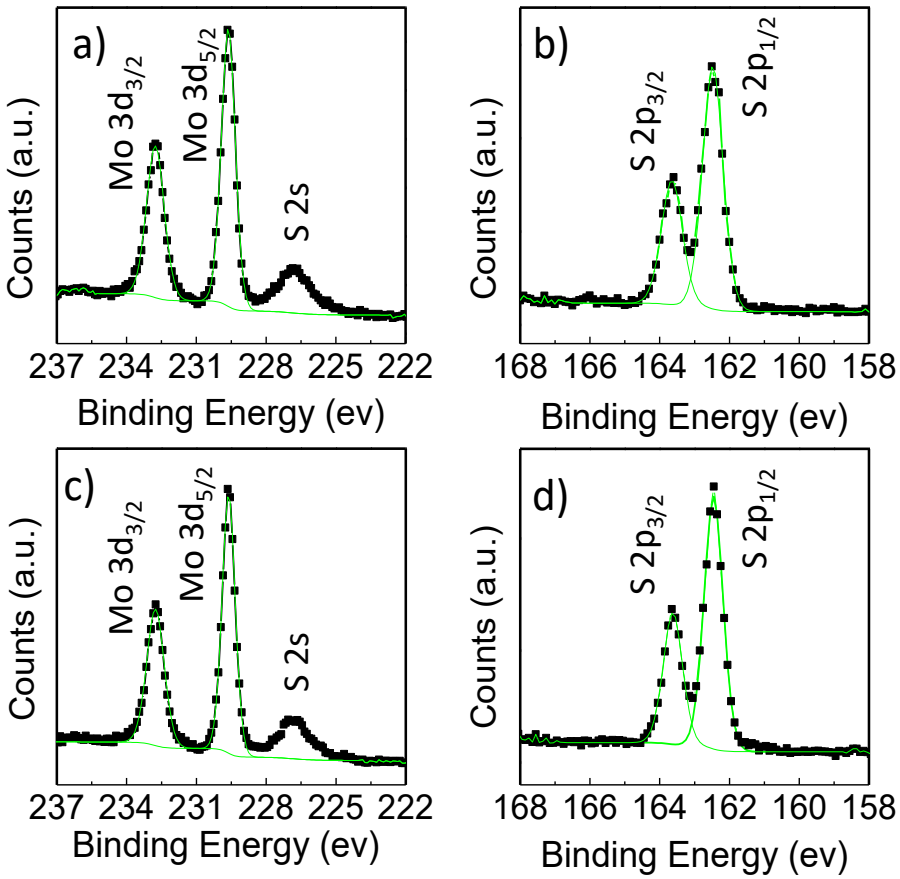

Figure 2.3. X-ray photoelectron spectroscopy of b-MoS_2 (a, b) and nc-MoS_2 (c, d). The data can be well fit with a single 4+ oxidation state for Mo and a 2- oxidation state for S. The elemental stoichiometry calculated from the data is 1.05:2.00, Mo:S. These data thus show that the surface of the nc-MoS_2 is the same as the commercial bulk powder, and both surfaces are consistent with bulk MoS_2.

2.2.2. Electrochemistry

The reversible lithium insertion and deinsertion process for MoS_2 is represented by the following equation:

$$MoS_2 + xLi^+ + xe^- \leftrightarrow Li_xMoS_2 \qquad \textit{Equation 2.1}$$

where: $0 \leq x \leq 1$

Intercalation of Li-ions proceeds through the weakly bonded van der Waals gaps of MoS_2.[47,72] The lithium ion binding energy is higher for adsorption into the octahedral interstitials compared to the tetrahedral interstitials, and hence is preferentially stored in the octahedral sites between sulfur layers.[73] Below $x = 0.1$ in Li_xMoS_2 intercalation into the 2H-MoS_2 occurs without much change to the initial atomic lattice structure.[57] However, increasing the concentration of Li between the range $0.1 < x < 1$ causes an advantageous irreversible phase change from the semiconducting 2H phase to the metallic 1T phase at ca. 1.0 V *vs.* Li/Li^+.[31,74] This phase change does not involve a significant structural rearrangement, but instead is accomplished by a glide process of the highly polarizable sulfur layers with respect to the molybdenum plane.[75]

Figure 2.4 shows dQ/dV plots of the first ten formation cycles at 1C of b-MoS_2 and nc-MoS_2 (carbon fiber based electrodes). The 2H-to-1T phase transition is observed electrochemically as the large differential charge response at ca. 1.2 V *vs.* Li/Li^+ in Figures 2.4a and c. Figures 2.4b and d show the same data with cycle 1 omitted (cycles 2 – 10), so that the evolution of lower intensity peaks can be more easily observed. The data clearly demonstrate the nc-MoS_2 electrodes require multiple cycles to convert to the 1T phase while b-MoS_2 is rapidly converted just after 2 cycles. [21, 36] This type of behavior is often seen in nanocrystal based phase transitions where many isolated nucleation events are needed to fully transform a sample.[76] During the ten formation cycles at 1C, new cathodic and anodic peaks develop, and correspond to the lithiation / delithiation of the electronically conductive MoS_2 1T phase.[77]

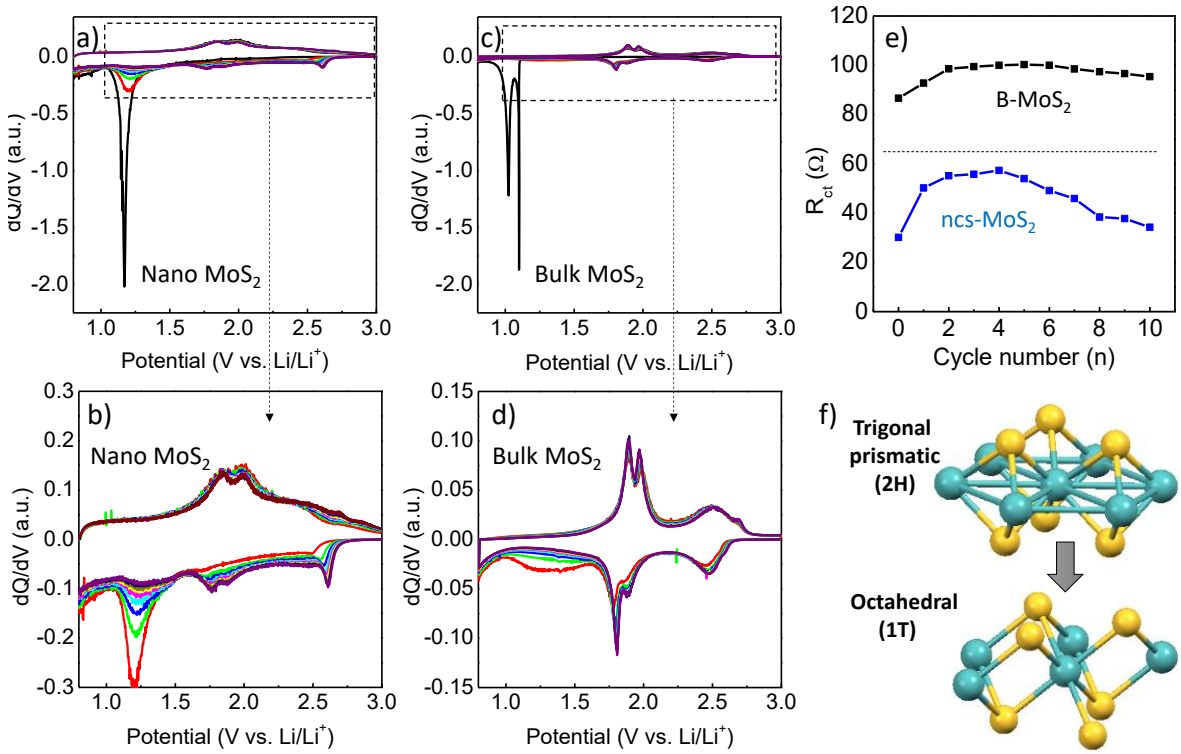

Figure 2.4. Derivative of the galvanostatic charge discharge plot dQ/dV of the first 10 cycles of nc-MoS_2 (a), and b-MoS_2 (c) showing the irreversible phase transition and subsequent formation of the highly electronically conducting 1T-MoS_2 phase. dQ/dV of cycles 2 - 9 of nc-MoS_2 (b), and b-MoS_2 (d) which shows that the 2H –to – 1T phase change occurs over 10 cycles, while in b-MoS_2 the phase change has occurred after the second cycle. Charge transfer resistance of b-MoS_2 and nc-MoS_2 based electrodes during the first 10 formation cycles calculated from the corresponding Nyquist plots. Impedance collected at 3V *vs.* Li/Li$^+$ (green), and 0.8 V *vs.* Li/Li$^+$ (black) (e). Atomic representation of the 2H-to-1T phase transformation. This transformation only involves a small shift in the easily polarized sulfur layer, which is non-destructive to the nanoscale structure (f).

Electrochemical impedance spectroscopy was then used to characterize changes in conductivity as a function of pre-cycling. Figure 2.4e shows the charge transfer resistance of both nc-MoS_2 and b-MoS_2, which was obtained from their respective Nyquist plots.[10] During the formation

cycles (0.8 V – 3.0 V *vs.* Li/Li^+), the charge transfer resistance is reduced by the 2H-to-1T phase change, and increased by the formation of the solid electrolyte interphase (SEI). The net result for both nc-MoS_2 and b-MoS_2 is that the charge transfer resistance increases during the first two cycles, mainly due to SEI formation, followed by a gradual decay during the next eight cycles mainly due to the formation of the electronically conductive 1T phase.

Electrode architectures for high rate pseudocapacitive charge storage were optimized in order to maximize the properties of the electronically conductive MoS_2 1T phase. One effective way to achieve highly conductive and porous composite electrodes, is to utilize carbon fibers. The shape anisotropy of the carbon fibers can lead to a highly porous mesh that extends from the current collector throughout the electrode.[78,79] In this work, the electrode components are sonicated together in ethanol to disperse the nanocrystals homogeneously with the carbon fibers and carbon black, which upon drying lead to a highly conductive and porous electrode. We chose to use a poly(acrylic acid) binder since it has demonstrated high rate performance in other systems.[80,81] SEM image of these electrodes are shown in Figure 2.5c, which demonstrate that the carbon fiber based electrodes consist of a mesh-type network that appears to be macroporous. A traditional electrode formulation of polyvinylidene fluoride binder and carbon black was used as a comparative baseline to understand the synergy between the electrode architecture, composition, and the pseudocapacitive active material (Figure 2.5d).

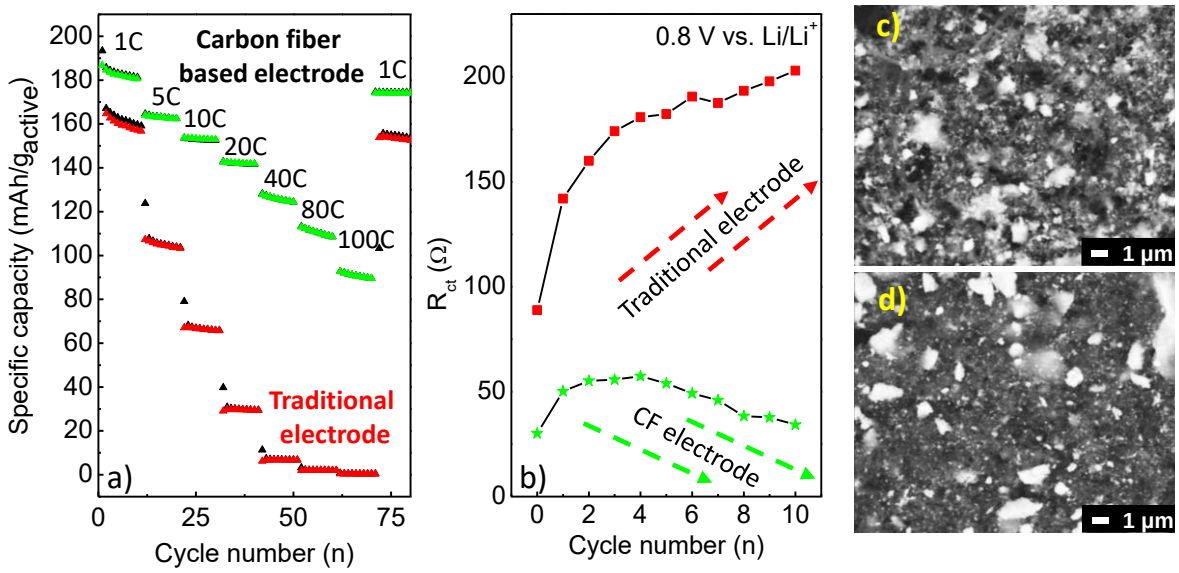

Figure 2.5. (a) Galvanostatic kinetic analysis, after 10 formation cycles, comparing nc-MoS_2 electrodes made using carbon fibers and mixed using sonication (green), and electrodes made using only carbon black and mixed using a traditional mortar and pestle (red). (b) Charge transfer resistance of nc-MoS_2 / carbon fiber based electrodes (green), and nc-MoS_2 / carbon black based electrodes (red) during the first 10 formation cycles calculated from Nyquist plots collected at 0.8 V *vs.* Li/Li^+. The charge transfer in the carbon fiber based electrode is both lower in absolute value, and decreases with cycle number because the newly formed 1T MoS_2 is electronically well connected to the electrode architecture. By contrast, the charge transfer resistance in the traditional carbon black based electrodes monotonically increases, likely due to SEI formation. Backscatter electron images of the carbon fiber based electrode (c) and carbon black only electrode (d). The brightness in backscattered images is related to the atomic Z number, so the dark-regions are carbon rich and the light-regions are MoS_2 rich.

The kinetic performance of nc-MoS_2 is shown for these two different electrode formulations in Figure 2.5a. The nc-MoS_2 active material in the carbon fiber based electrodes show much better kinetic performance compared to the traditional electrodes. We believe that both particle dispersion and

electronic conductivity are dominating factors leading to the superior performance. The traditional electrodes were mixed by hand with mortar and pestle, and the final composite electrode probably suffers from poor nanoparticle dispersion since nanoparticles tend to agglomerate. In contrast, the carbon fiber based electrodes were mixed using sonication and show extremely good kinetic performance. Sonication assisted mixing homogeneously distributes the nanocrystals throughout the electrode, [82] enabling synergistic coupling between the nc-MoS_2 1T-conductive phase and the conductive carbon scaffold. It has previously been shown that improving dispersion in nanocrystal based electrodes can produce markedly better rate performance compared to traditional electrodes.[68] In order to further understand the disparity in kinetics between the two different electrode formulations, we also performed electrochemical impedance spectroscopy on the carbon black based nc-MoS_2 electrodes. We found that the pristine charge transfer resistance is significantly higher in the carbon black based electrode architecture compared to the carbon fiber based electrode architecture. Furthermore, the charge transfer resistance of the carbon black based electrodes increase over the first ten formation cycles in stark contrast to the decrease in charge transfer resistance of the carbon fiber based electrodes over the same interval (Figure 2.5b). These data suggests that the improved rate kinetics in the carbon fiber based electrodes are a combination of the dispersed nanocrystals in the composite electrode, and the good electronic coupling of the nanocrystals to the carbon scaffolding.

Using the optimized carbon fiber based electrode architecture enables the quantification of important metrics related to pseudocapacitors in a standard slurry-type electrode. We can now move on to compare these metrics between b-MoS_2 and nc-MoS_2 fabricated in the same electrode architecture to understand how nanostructuring affects the electrochemical properties. The kinetic analysis of the nc-MoS_2 shown in Figure 2.6 shows markedly better rate performance compared to b-MoS_2. The nc-MoS_2 electrodes retain 50% of the original 1C capacity at 100C while the b-MoS_2 electrodes retain only 17%. Remarkably, these thicker film electrodes based on nc-MoS_2 store more

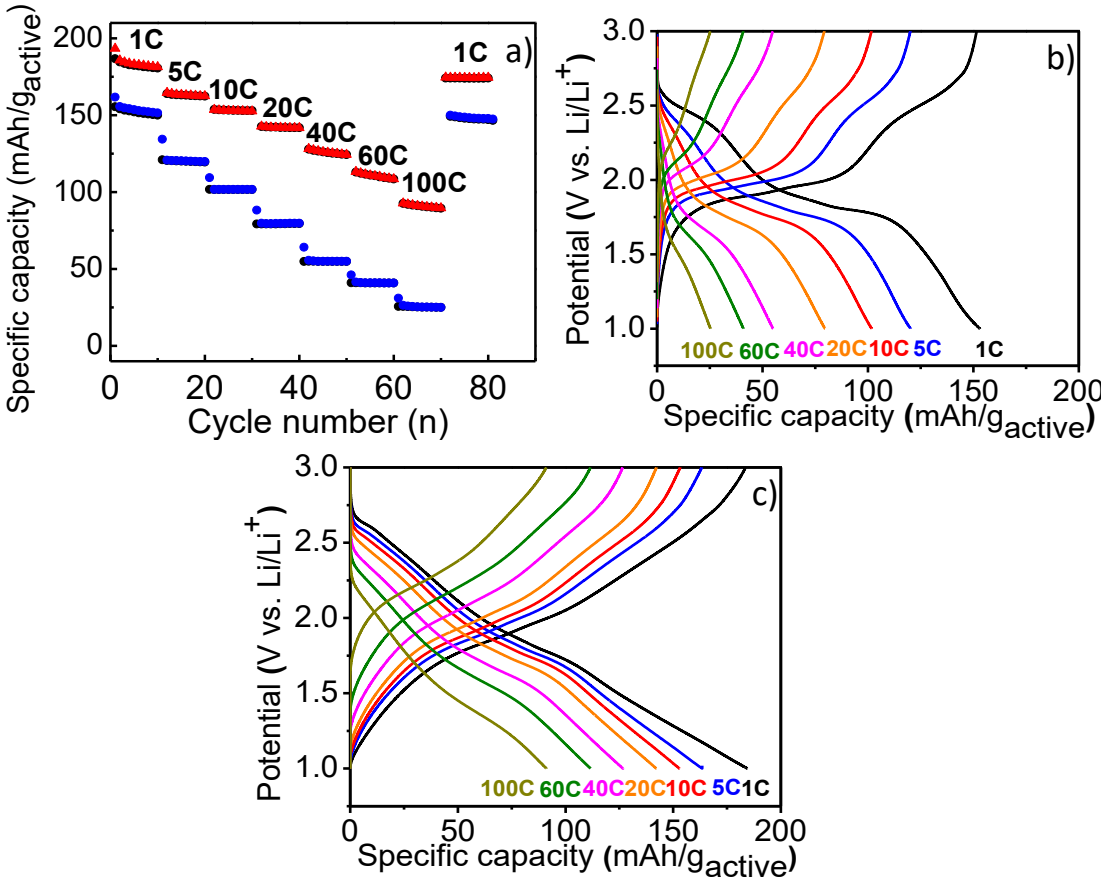

Figure 2.6. (a) Galvanostatic kinetic analysis comparing b-MoS_2 to the nc-MoS_2 in optimized carbon fiber based electrodes (a). The nanostructured material stores nearly four-times the charge at 100C compared to b-MoS_2. Galvanostatic lithium insertion and deinsertion profiles at different current densities of b-MoS_2 (b), and nc-MoS_2 (c). The galvanostatic traces for the nc-MoS_2 based electrodes are pseudo-linear and are quite different from the standard plateaus observed for b-MoS_2.

than 90 mAh/g in less than 20 seconds. Comparing the RC time constant of these two materials leads to an understanding of the fast kinetic response in nanostructured MoS_2. We evaluate the evolution of the RC time constant during the activation process (ten cycles between 0.8 – 3.0 V *vs.* Li/Li^+). After the first cycle the RC time constant stabilizes at 1.25 ms for nc-MoS_2 and 1.86 ms for b-MoS_2. Both

of these values are comparatively high to other psudocapacitive materials.[83] The nc-MoS_2 based electrodes have a 30% shorter RC time constant compared to b-MoS_2 in agreement with the faster observed charge storage for the nanostructured material.

In order to compare these exciting performance results discussed above to other state of the art MoS_2 based pseudocapacitors, we have aggregated important performance characteristics of non-conversion type reactions (including both intercalation and surface reactions) in (Table 2.1). At low current densities, the nc-MoS_2 reported here delivers similar capacity to the best materials reported to date. Most materials reported in the table show current densities between 3-4 A/g as their fastest rates, and the nc-MoS_2 reported here delivers 142 mAh/g at a current density of 3.3 A/g, a value two

Material type	**Guest ion**	**Slow rate A/g, mAh/g**	**Fast rate A/g, mAh/g**	**Capacity retention cycles, % retention**	**Reference**
nc-MoS_2	Li^+	**0.167, 182**	**16.7, 91**	**3000, 81**	**this study**
Hydrothermal MoS_2	Li^+	0.2, 200	3, 50	1400, 83*	[48]
Fullerene type MoS_2	Na^+	0.1, 160	4, 61	30, 47	[50]
Exfoliated MoS_2 (thin film)	H^+	5 mV/s, 57** (potentiostatic)	100 mV/s, 49** (potentiostatic)	5000, 75	[91]

Table 2.1. Gravimetric capacity of nanostructured MoS_2 based half-cells. *The capacity increased from ~200 – 220 mAh/g over ~500 cycles, so we normalized the capacity retention by the maximum capacity value and not the initial capacity of 200 mAh/g. **The capacitance reported in this study was converted to capacity using the reported voltage window of 0.85V. The galvanostatic trace used to calculate the capacitance are nearly linear, so the relationship capacity = (capacitance · Voltage)/3.6 is an excellent approximation for this system.

to three-fold higher than other materials included in the table. Even when nc-MoS_2 is cycled at 16.7 A/g, the delivered capacity is still nearly double the capacities reported for the other materials at a significantly lower current density. In our recent work on nanostructured MoS_2 thin films, we found similarly fast kinetics,[21] but what makes this report significant, is the ability to preserve those rates in thicker composite electrodes. This is enabled through the porous electrode morphology and coupling of the highly conductive 1T-MoS_2 nanocrystals to the composite electrode architecture.

The fast charge transfer kinetics in nc-MoS_2 can also be understood by the physical charge storage mechanism of ions in the material. Figure 2.6b shows the galvanostatic charge and discharge traces for b-MoS_2 between 1C and 100C. These traces display the traditional stepped plateau features that are indicative of charge storage accompanied by a phase transition in a battery material. Structural studies have shown that indeed bulk 1T Li_xMoS_2 undergoes multiple first order phase changes during Li-ion storage.[77] Phase transformations are in part responsible for the sluggish kinetics in battery-type materials because the nucleation and propagation of new phases are typically slow. In contrast to b-MoS_2, Figure 2.6c shows galvanostatic traces for nc-MoS_2 that display a pseudo-linear voltage response with respect to Li-ion concentration. This sloping response is a hallmark of pseudocapacitance, and is also indicative of a solid-solution storage mechanism where no phase change occurs to accommodate the lithiation.[18,19] As described in the introduction, pseudocapacitance occurs whenever the charge (Q) depends on the change in potential (dE), yielding a capacitance (dQ=dE).[3] Although these charge storage redox processes are Faradaic in nature, their phenomenological behavior, and response to experimental variables such as sweep rate, are those typical of capacitors. Generally, the dependency of the current response on the sweep rate in a cyclic voltammetry experiment can be utilized to distinguish the charge storage process according to Equation 2.2. [84,85]

$$i = av^b \qquad \textit{Equation 2.2}$$

In the framework of this analysis, the measured current i is fit to a power law with scan rate v, and the exponential term b can be determined from the slope of the $log\ (i)$ *vs.* $log\ (v)$ plot. Values of $b = 0.5$ indicate that the current is proportional to the square root of the scan rate, which is consistent with traditional diffusion dominated charge storage.[84] On the other hand, when $b = 1$ the current is linearly proportional to the scan rate, which is characteristic of a capacitor-like charge storage mechanism.[84] Figure 2.7 shows several of the cyclic voltammograms used to calculate the b-values at the current maxima in the anodic and cathodic regimes. The b-values that are calculated for b-MoS_2 are labeled on the CV plots next to the corresponding peaks used in their calculation. The various peaks display values between 0.65 - 0.83. These values are indicative of a diffusion dominated charge storage mechanism, as expected for micrometer size MoS_2. The b-values for nc-MoS_2 samples are generally much higher, and are found to be between 0.93 - 1.00, indicating that the dominant charge storage mechanism in the nanocrystal based electrodes is capacitor-like. The fast rate performance in nc-MoS_2 is enabled by this capacitive-type charge storage mechanism, quantified using Equation 2.

Another related analysis using cyclic voltammetry enables the measured current (i) at a fixed potential (V) to be quantitatively separated into a diffusion contribution and a capacitive contribution.[86]

$$i(\mathrm{V}) = k_1 v + k_2 v^{0.5} \qquad \textbf{\textit{Equation 2.3}}$$

In Equation 2.3, $k_1 v$, and $k_2 v^{0.5}$ correspond to capacitive and diffusion contributions to the measured current, respectively, where v is the scan rate in mV/s. Equation 3 enables the capacitive charge storage at specific potentials to be quantified along with total capacitive contribution over the entire voltage range. Figure 2.7 shows the results of this analysis for b-MoS_2, and indicates that charge storage is largely diffusion controlled at current maxima in the cyclic voltammograms, which is supported by the calculated peak current b-values calculated from Equation 2. The total integrated capacitive charge

storage is about 60%, which indicates that the parent atomic structure of MoS_2 is an extremely good candidate for pseudocapacitive charge storage.

When we perform the same analysis on nc-MoS_2, we find that over 80% of the charge storage is capacitive in nature. Furthermore, the capacitive current is significantly enhanced at the peak maxima voltages compared to b-MoS_2, again in good agreement with the calculated b-values from Equation 2, which are close to 1 in all cases. The broad non-capacitive cathodic peak in Figure 7d ca. 1.6 – 1.1 V *vs.* Li/Li^+ is attributed to the 2H-to-1T phase transformation. Even though this phase transition was largely completed before running these CV scans, some slow CV scan rates were used for this analysis to compare the slower diffusion processes in b-MoS_2 to the fast storage processes in nc-MoS_2. However, it has been reported that the 1T MoS_2 phase can convert back to the 2H phase at higher voltages,[77] and this is apparently occurs in the nc-MoS_2 samples cycled at the slowest rates. As indicated in Figure 2.7d, the 2H-to-1T phase transition in the nc-MoS_2 is largely diffusion limited. We expect that even higher total capacitive contributions are possible by elimination of this phase transition by limiting the time that the nc-MoS_2 electrode spends in the fully delithiated state (3.0 V).

The origin of this fast capacitive charge storage mechanism in nc-MoS_2 can be described through structural considerations. Much of the structural information available on the electrochemical phase stability of MoS_2 has focused on the so called 2H (semiconductor with hexagonal symmetry) to 1T (metal with trigonal symmetry) transformation.[31,32,36,74,87] Once this conversion is complete, the 1T-metallic MoS_2 phase has been reported to undergo several first-order phase transformations[77] between 1 – 2.8 V *vs.* Li/Li^+; therefore, the fast kinetics observed here raises a fundamental question about the underlying charge storage processes occurring with nc-MoS_2 because these phase transitions should be slow. We have shown in both an oxide and sulfide based material system that phase transformation suppression is a hallmark of pseudocapacitive charge storage.[18,19] We thus postulate that similar effects are also occurring here. If charge storage kinetics are not limited by the nucleation

and propagation of new phases, charge storage can proceeded directly through fast migration of ions through the weakly interacting sulfide lattice. The sloping voltage profiles observed in the galvanostatic measurements in Figure 2.7 for nc-MoS_2 electrodes strongly suggests that phase transitions are being suppressed here.

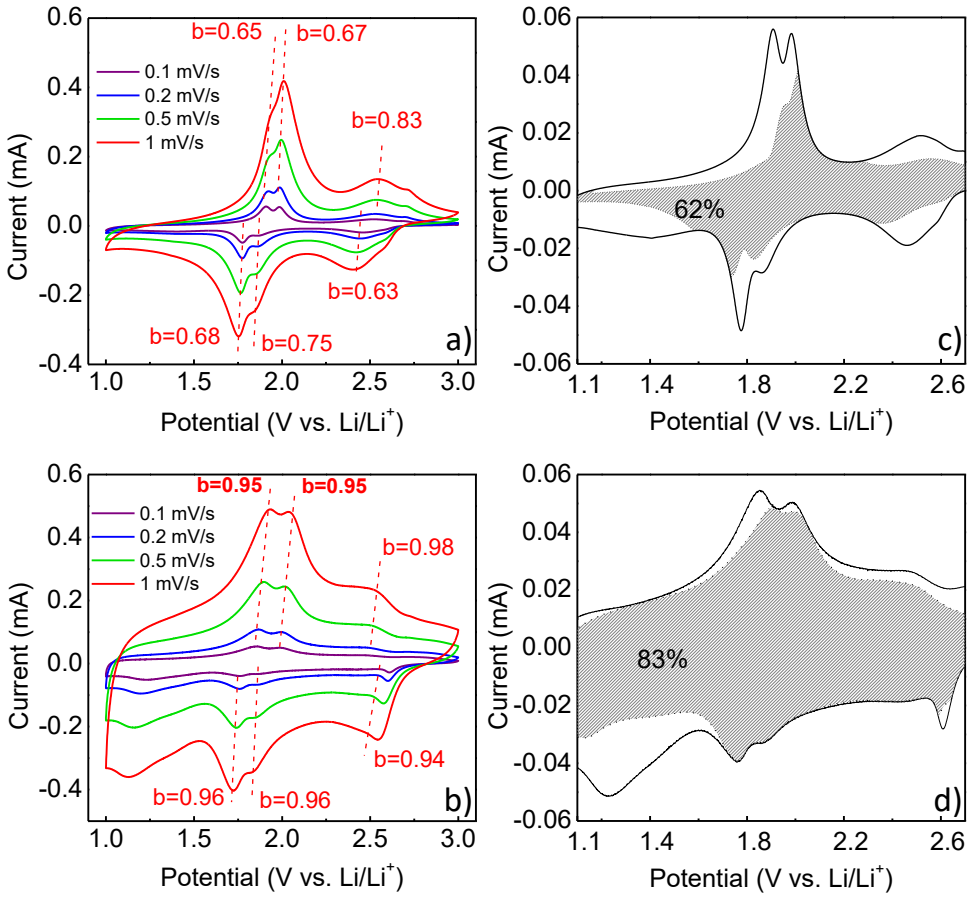

Figure 2.7. Analysis of the charge storage in the current maxima for b-MoS_2 (a) and nc-MoS_2 (b) using b-values calculated from Equation 2. This analysis shows that the Faradaic charge storage associated with the peak maxima in CV has a significant diffusion contribution in b-MoS_2, while this analysis shows that the same Faradaic processes are capacitive-like in nc-MoS_2. Quantification of the capacitive and diffusion charge storage in b-MoS_2 (c) and nc-MoS_2 (d) as a function of voltage. This analysis indicates that the nc-MoS_2 based electrodes store charge largely through a capacitive mechanism.

High levels of capacitive charge storage are often associated with long cycle life, and this system is no exception. The cycling stability measured for b-MoS_2 and nc-MoS_2 is shown in Figure 2.8, and indicates capacity retention for both samples is above 80% after 3000 cycles at 20C. The excellent cycling performance of the b-MoS_2 and nc-MoS_2 is mainly attributed to small structural changes (after the initial formation of the 1T phase) with a reported expansion in the c-axis direction of only ~ 4-6%.[57] The charge storage capacity in nc-MoS_2 at 20C is nearly 70% greater after 3000 cycles compared to b-MoS_2 as a result of its superior charge transfer properties. Referring back to Table 2.1, the nc-MoS_2 composite electrodes also cycle more reversibly than all of the intercalation based entries in the table as a result of the pseudocapacitive charge storage mechanism.

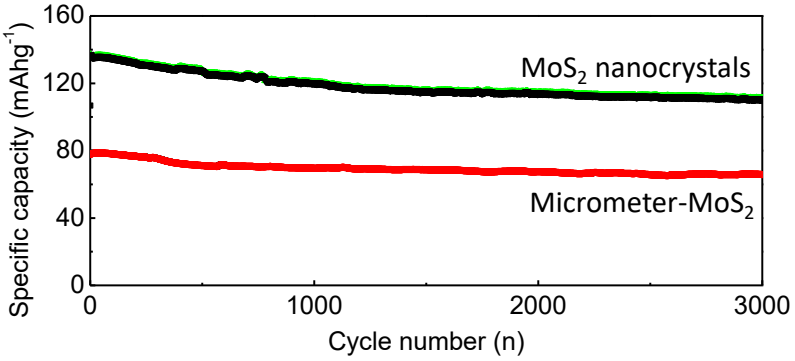

Figure 2.8. Cycle lifetime of nc-MoS_2 and b-MoS_2 electrodes cycled at 20C. Cycle 1 reported here was started after the kinetic study (1C-100C) shown in Figure 7. The long cycle lifetime and high capacity of the nc-MoS_2 is correlated with the established pseudocapacitive charge storage mechanism.

While the half-cell experiments described above provide a clear picture of fundamental redox processes occurring in these MoS_2 based electrodes, they do not fully demonstrate the potential of these materials in practical devices. To this end, a final set of experiments were performed to assess the technological relevance of this new pseudocapacitive electrode. Hybrid lithium capacitor devices

were fabricated using an activated carbon cathode and a nc-MoS_2 anode. Activated carbon (AC) is a typical electrochemical capacitor material used in EDLCs for high rate applications, but the energy density is low compared to Faradaic storage processes because charge is stored only in the double layer of the electrode-electrolyte interface.[2,3] Figure 2.9a shows the hybrid lithium capacitor device made from a nc-MoS_2 and AC electrode delivers 37 Wh/kg at slow rates. In comparison, symmetric AC devices cycled in a similar electrolyte, and between a similar voltage window, delivers a maximum energy of ~20 Wh/kg.[88] The redox based charge storage mechanism found in the nc-MoS_2 is responsible for producing a higher energy density than the double layer charge storage of AC based devices. If an appropriate pseudocapacitive cathode was used instead of the AC, even higher energy density would be expected. The maximum power density of the nc-MoS_2 hybrid devices is 5.3 kW/kg (6 Wh/kg), while symmetric AC devices in similar conditions are reported to only deliver 3.5 kW/kg (2 Wh/kg).[88] Furthermore, the energy densities and power densities of this sulfide based material are comparable with the other state of the art oxide hybrid lithium-ion capacitors, such as Nb_2O_5-AC,[88] TiO_2-AC,[89] and $Li_4Ti_5O_{12}$-AC[90] chemistry. Figure 2.9b further shows the excellent reversibility of the nc-MoS_2 full cell, which can be cycled 8,000 times with little decay in the delivered energy. This data thus indicates that nc-MoS_2 full cells overlap with the power density typically thought to be limited to double-layer type EC devices, while also overlapping with the energy density of some Li-battery materials.

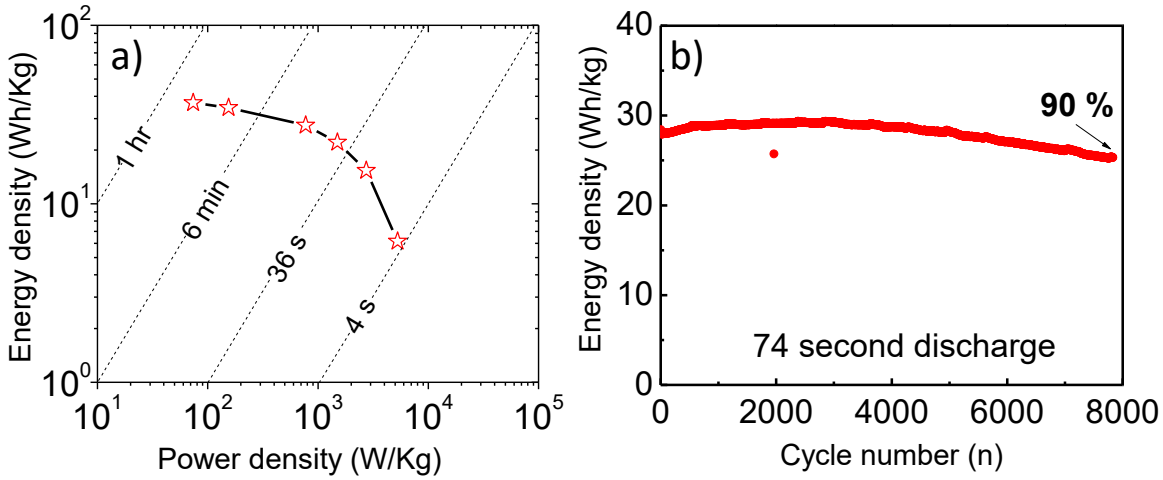

Figure 2.9. Average discharge energy density *vs.* average discharge power density for a full cell utilizing a nc-MoS_2 anode and an activated carbon cathode. The voltage of this device operates between 0.4 – 3.2 V. Average discharge energy density *vs.* cycle number for an asymmetric nc-MoS_2 / activated carbon full cell. (b) The voltage of this device operates between 0 – 3.0 V. The fast kinetics and long lifetime is a result of the highly reversible pseudocapacitive charge storage mechanism. This data was mass normalized using the total active mass of both electrodes (~4 mg).

2.3. Conclusion

We have successfully synthesized high surface area MoS_2 nanocrystals with expanded van der Waals gaps, which show high levels of pseudocapacitive charge storage when built into a composite electrode. We have also demonstrated that the electrode architecture can be a dominating factor in the development of composite electrodes in pseudocapacitors. The high capacitive contribution measured for the nc-MoS_2 based electrodes is due to the interplay between the nanoscale architecture of the active material and the composite electrode. The high surface area and expanded layer structure of nc-MoS_2 enable fast Faradaic reactions, which leads to charge storage that appears capacitive even though ion migration occurs over distances that normally would be limited by semi-infinite diffusion.

We have shown that over 80% of the charge storage is capacitive in nanocrystal based electrodes, which enables over 90 mAh/g to be accessed in only 20 seconds. Furthermore, the cycling stability of nc-MoS_2 shows over 80% retention after 3000 cycles as a result of the pseudocapacitive charge storage mechanism. Full cell devices utilizing an activated carbon cathode and an nc-MoS_2 anode show extremely attractive charge storage behavior and little capacity fade after 8000 cycles. Moreover, the energy density of devices based on nc-MoS_2 could be almost doubled if a cathode with similar kinetic performance is developed.

The results of this study highlight the importance of sulfide based pseudocapacitive active charge storage materials. The large 2-D galleries of MoS_2 and other metal chalcogenides make them of particular interest to the pseudocapacitive charge storage field. The next frontier will be developing new sulfide materials that enable intercalation pseudocapacitance over large length scales. This work also highlights the dire need for composite electrode architectures that are optimized for nanostructured pseudocapacitive active materials. The electrodes discussed in this work represent a significant accomplishment, but if practical devices are to be made from pseudocapacitive materials like these, attention needs to be paid to the synergistic coupling of the active material and the composite electrode in order to move to even thicker composite electrodes. We hope this demonstration of attractive electrochemical properties in sulfide based pseudocapacitors will stimulate the exploration of other chalcogenide based materials.

2.4. Experimental

2.4.1. Synthesis

All starting materials were obtained from commercial suppliers and used without further purification. The synthesis of nanosized-MoO_2 has been reported elsewhere,[18] and is briefly described here. MoO_2 nanocrystals were prepared solvothermally by dissolving anhydrous $MoCl_5$ (Strem Chemicals) in a

mixture of ethanol and deionized water at a reaction temperature of 180°C for 6 hrs. The MoO_2 nanocrystals were converted to MoS_2 with H_2S gas. The reaction was carried out in a tube furnace at 600°C under flowing H_2S/H_2 (H_2S 5 mol % : H_2 95 mol %, Air Gas) for 10 hours. A graphite boat was used to convert ~ 100 - 200 mg of MoO_2 to MoS_2.

2.4.2. Characterization

Powder X-ray diffraction (XRD) was performed in a PANalytical X'Pert Pro operating with Cu Kα (λ = 1.5418 Å) using a 0.03° step size, a voltage of 45kV, and a current of 40mA. XRD patterns were recorded in the range of $10° < 2\theta < 80°$. Transmission electron microscopy (TEM) was performed using an FEI Technai T12 operating at 120 kV. Nitrogen porosimetry was carried out using a Micromeritics TriStar II 3020. The surface area was calculated from the adsorption branch of the isotherm between (0.04 – 0.30 P/P_0) using the Brunauer-Emmett-Teller (BET) model. The pore diameter and pore volume was also calculated from the adsorption branch of the isotherm using the Barret-Joyner-Halenda (BJH) model. X-ray photoelectron spectroscopy (XPS) analysis was performed using a Kratos Axis Ultra DLD with a monochromatic Al (Kα) radiation source. The charge neutralizer filament was used to control charging of the sample, 20 eV pass energy was used with a 0.1 eV step size, and scans were calibrated using the C 1s peak shifted to 284.8 eV. The integrated area of the peaks was found using the CasaXPS software, and atomic ratios were also found using this software. The atomic sensitivity factors used were from the Kratos library within the Casa software.

2.4.3. Electrochemistry

The carbon fiber based electrodes were made from a slurry consisting of 70 wt.% nc-MoS_2 or b-MoS_2 (Alfa Asear) powder used as the active component for Li storage, 10 wt.% vapor grown carbon fibers (Sigma Aldrich), 10 wt.% carbon black (Alfa Asear) used as conductive additive, and 10 wt.%

polyacrylic acid solution (M_w=250K, Sigma Aldrich) used as binder. The polyacrylic acid was used as a predissolved 5 wt.% solution in 200 proof ethanol. A typical slurry was prepared with 40 mg nc-MoS_2, 5.7 mg carbon black, 5.7 mg carbon fiber, 114 mg 5 wt.% polyacrylic acid solution, and 1 ml 200 proof ethanol. These four components were sonicated for 30 minutes to obtain a homogeneous dispersion. Ethanol evaporation over one hour resulted in a homogeneous thick paste that was cast onto 25 μm carbon coated Al foil (gift from Coveris) using doctor blading. The slurry was dried at ambient temperature for 1 h, and further dried at 25°C under vacuum overnight to evaporate the excess solvent. The traditional electrode was made from a slurry consisting of 70 wt.% nc-MoS_2, 20 wt.% carbon black (Alfa Asear), and 10 wt.% polyvinyl difluoride (gift from Kynar) dissolved in n-methyl-2-pyrrolidone (Alfa Asear). Components were mixed using a mortar and pestle, and again cast onto 25 μm carbon coated Al foil using doctor blading. The electrodes were dried in a vacuum oven at 110°C overnight. The mass loading of all the electrodes in this study were ~1 mg/cm^2 of active material. These electrodes were assembled into in-house built SwageLoc cells using lithium metal as counter electrode, glass fiber (Watman) as separator, and 1 M $LiPF_6$ in a 1:1 ethylene carbonate/dimethylcarbonate solvent (Sigma Aldrich) with 5% (v/v) fluorinated ethylene carbonate (TCI America) as electrolyte. Half-cell cycling was carried out on a VSP potentiostat/galvanostat (Bio-Logic) using a 1C rate that corresponds to 167 mAh/g. The half cells were precycled ten times between 0.8 - 3.0 V *vs.* Li/Li$^+$ to drive the 2H-1T phase transition before the kinetic analysis and cycling stability measurements.

2.4.4. Full cells

SwageLok cells were used to cycle the full cells. Those devices were made with a nc-MoS_2 anode and an activated carbon cathode in a 1:5 active material ratio, respectively. The activated carbon electrodes were fabricated from YP50F activated carbon (85 wt%), carbon nanotubes (CNTs) (5

wt%), and polyvinylidene fluoride (PVDF) (10 wt%). These components were mixed in n-methyl-2-pyrrolidone (Alfa Asear) to form a homogeneous slurry, and cast onto a stainless steel sheet by doctor blading. The cast electrode sheet was dried in vacuum at 110°C for 12 hours. The electrodes were removed from the substrate to form free-standing electrodes with mass loadings of 4 - 6 mg/cm^2. As with the half cells described above, the nc-MoS_2 electrodes in all full cells were precycled ten times between 0.8 - 3.0 V *vs.* Li/Li$^+$ to drive the 2H-1T phase transition before the full cell device testing. The same electrolyte used in the half-cell testing was used for the full cell testing. The active mass of both electrodes was used to calculate the energy density and power density.

2.4.5. Electrochemical impedance spectroscopy

Electrochemical impedance spectroscopy was carried out on a VSP potentiostat/galvanostat (Bio-Logic). The impedance measurements were performed on two-electrode SwageLoc cells between 900 kHz and 100 mHz using a 10 mV input under no bias. Impedance data was collected at 0.8V *vs.* Li/Li$^+$ after each insertion cycle. A 5 minute potentiostatic hold was applied before each impedance measurement during which time the current dropped from ~200 mA/g to ~20 mA/g. The impedance spectra was fit using the Z fit plug-in available in EC-Lab V10.40 (Bio-Logic).

2.5 Reference

[1] B. Scrosati, *J. Echem. Soc.* **1992**, *139*, 2776.

[2] M. Winter, R. J. Brodd, *Chem. Rev.* **2004**, *104*, 4245.

[3] P. Simon, Y. Gogotsi, *Nat. Mater.* **2008**, *7*, 845.

[4] P. Simon, Y. Gogotsi, B. Dunn, *Science* **2014**, *343*, 1210.

[5] V. Augustyn, P. Simon, B. Dunn, *Energy Environ. Sci.* **2014**, *7*, 1597.

[6] B. E. Conway, V. Birss, J. Wojtowicz, *J. Power Sources* **1997**, *66*, 1.

[7] B. E. Conway, *J. Electrochem. Soc.* **1991**, *138*, 1539.

[8] N. Yoshida, Y. Yamada, S. I. Nishimura, Y. Oba, M. Ohnuma, A. Yamada, *J. Phys. Chem. C* **2013**, *117*, 12003.

[9] J. P. Zheng, *J. Electrochem. Soc.* **1995**, *142*, L6.

[10] W. Wang, S. Guo, I. Lee, K. Ahmed, J. Zhong, Z. Favors, F. Zaera, M. Ozkan, C. S. Ozkan, *Sci. Rep.* **2014**, *4*, 4452.

[11] D. Michell, D. A. J. Rand, R. Woods, *J. Electroanal. Chem.* **1978**, *89*, 11.

[12] J. P. Zheng, P. J. Cygan, T. R. Jow, *J. Echem. Soc.* **1995**, *142*, 2699.

[13] Z. Tong, Y. Yang, J. Wang, J. Zhao, B.-L. Su, Y. Li, *J. Mater. Chem. A* **2014**, *2*, 4642.

[14] L. Deng, G. Zhu, J. Wang, L. Kang, Z. H. Liu, Z. Yang, Z. Wang, *J. Power Sources* **2011**, *196*, 10782.

[15] A. A. Lubimtsev, P. R. C. Kent, B. G. Sumpter, P. Ganesh, *J. Mater. Chem. A* **2013**, *1*, 14951.

[16] T. Brezesinski, J. Wang, S. H. Tolbert, B. Dunn, *Nat. Mater.* **2010**, *9*, 146.

[17] V. Augustyn, J. Come, M. A. Lowe, J. W. Kim, P. Taberna, S. H. Tolbert, H. D. Abruña, P. Simon, B. Dunn, *Nat. Mater.* **2013**, *12*, 518.

[18] H.-S. Kim, J. B. Cook, S. H. Tolbert, B. Dunn, *J. Electrochem. Soc.* **2015**, *162*, A5083.

[19] G. A. Muller, J. B. Cook, H.-S. Kim, S. H. Tolbert, B. Dunn, *Nano Lett.* **2015**, *15*, 1911.

[20] Z. Chen, V. Augustyn, J. Wen, Y. Zhang, M. Shen, B. Dunn, Y. Lu, *Adv. Mater.* **2011**, *23*, 791.

[21] J. B. Cook, H.-S. Kim, Y. Yan, J. S. Ko, S. Robbennolt, B. Dunn, S. H. Tolbert, *Adv. Energy Mater.* **2016**, *6*, 1501937.

[22] K. Brezesinski, J. Wang, J. Haetge, C. Reitz, S. O. Steinmueller, S. H. Tolbert, B. M. Smarsly, B. Dunn, T. Brezesinski, *J. Am. Chem. Soc.* **2010**, *132*, 6982.

[23] V. Augustyn, J. Come, M. A. Lowe, J. W. Kim, P. Taberna, S. H. Tolbert, H. D. Abruña, P. Simon, B. Dunn, *Nat. Mater.* **2013**, *12*, 1.

[24] K. Brezesinski, J. Wang, J. Haetge, C. Reitz, S. O. Steinmueller, S. H. Tolbert, B. M. Smarsly, B. Dunn, T. Brezesinski, *J. Am. Chem. Soc.* **2010**, *132*, 6982.

[25] A. G. Dylla, G. Henkelman, K. J. Stevenson, *Acc. Chem. Res.* **2013**, *46*, 1104.

[26] E. Lim, H. Kim, C. Jo, J. Chun, K. Ku, S. Kim, H. Lee, I.-S. Nam, S. Yoon, K. Kang, J. Lee, *ACS Nano* **2014**, *8*, 8968.

[27] M. Okubo, E. Hosono, J. Kim, M. Enomoto, N. Kojima, T. Kudo, H. Zhou, I. Honma, *J. Am. Chem. Soc.* **2007**, *129*, 7444.

[28] Y. Liang, R. Feng, S. Yang, H. Ma, J. Liang, J. Chen, *Adv. Mater.* **2011**, *23*, 640.

[29] H. Hwang, H. Kim, J. Cho, *Nano Lett.* **2011**, *11*, 4826.

[30] F. Wypych, R. Schollhorn, *J. Chem. Soc., Chem. Commun.* **1992**, *0*, 1386.

[31] M. A. Py, R. R. Haering, *Can. J. Phys.* **1983**, *61*, 76.

[32] Y.-C. Lin, D. O. Dumcenco, Y.-S. Huang, K. Suenaga, *Nat. Nanotechnol.* **2014**, *9*, 391.

[33] L. F. Mattheiss, *Phys. Rev. B* **1973**, *8*, 3719.

[34] E. Benavente, M. A. S. Ana, F. Mendiza, G. Gonza, *Coord. Chem. Rev.* **2002**, *224*, 87.

[35] F. Xiong, H. Wang, X. Liu, J. Sun, M. Brongersma, E. Pop, Y. Cui, *Nano Lett.* **2015**, *15*, 6777.

[36] H. Wang, Z. Lu, S. Xu, D. Kong, J. J. Cha, G. Zheng, P.-C. Hsu, K. Yan, D. Bradshaw, F. B. Prinz, Y. Cui, *Proc. Natl. Acad. Sci. U. S. A.* **2013**, *110*, 19701.

[37] H. Li, K. Yu, H. Fu, B. Guo, X. Lei, Z. Zhu, *J. Phys. Chem. C* **2015**, *119*, 7959.

[38] L. David, R. Bhandavat, U. Barrera, G. Singh, *Sci. Rep.* **2015**, *5*, 9792.

[39] A. P. Tiwari, H. Yoo, J. Lee, D. Kim, J. H. Park, H. Lee, *Nanoscale* **2015**, *7*, 11928.

[40] F. Sun, Y. Wei, J. Chen, D. Long, L. Ling, Y. Li, J. Shi, *Nanoscale* **2015**, *7*, 13043.

[41] J.-Z. Wang, L. Lu, M. Lotya, J. N. Coleman, S.-L. Chou, H.-K. Liu, A. I. Minett, J. Chen, *Adv. Energy Mater.* **2013**, *3*, 798.

[42] S. H. Choi, Y. N. Ko, J.-K. Lee, Y. C. Kang, *Adv. Funct. Mater.* **2015**, *25*, 1780.

[43] G. Du, Z. Guo, S. Wang, R. Zeng, Z. Chen, H. Liu, *Chem. Commun.* **2010**, *46*, 1106.

[44] H. Liu, D. Su, R. Zhou, B. Sun, G. Wang, S. Z. Qiao, *Adv. Energy Mater.* **2012**, *2*, 970.

[45] H. Jiang, D. Ren, H. Wang, Y. Hu, S. Guo, H. Yuan, P. Hu, L. Zhang, C. Li, *Adv. Mater.* **2015**, *27*, 3687.

[46] F. Xiong, Z. Cai, L. Qu, P. Zhang, Z. Yuan, O. K. Asare, W. Xu, C. Lin, L. Mai, *ACS Appl. Mater. Interfaces* **2015**, *7*, 12625.

[47] T. Stephenson, Z. Li, B. Olsen, D. Mitlin, *Energy Environ. Sci.* **2014**, *7*, 209.

[48] Z. Hu, Q. Liu, W. Sun, W. Li, Z. Tao, S. Chou, J. Chen, S. X. Dou, *Inorg. Chem. Front.* **2016**, *3*, 532.

[49] C. Julien, S. I. Saikh, G. A. Nazri, *Mater. Sci. Eng. B* **1992**, *15*, 73.

[50] S. H. Woo, L. Yadgarov, R. Rosentsveig, Y. Park, D. Song, R. Tenne, S. Y. Hong, *Isr. J. Chem.* **2015**, *55*, 599.

[51] D. Ilic, K. Wiesener, W. Schneider, G. Krabbes, H. Oppermann, *J. Power Sources* **1985**, *14*, 223.

[52] A. J. Jacobson, R. R. Chianelli, M. S. Whittingham, *J. Electrochem. Soc.* **1979**, *126*, 2277.

[53] J. J. Auborn, *J. Electrochem. Soc.* **1987**, *134*, 580.

[54] R. R. Haering, J. A. Stiles, K. Brandt, *(Moli Energy Ltd) US Patent*, **1980**.

[55] H. Yu, Y. Liu, S. L. Brock, *Inorg. Chem.* **2008**, *47*, 1428.

[56] X. Fang, X. Yu, S. Liao, Y. Shi, Y.-S. Hu, Z. Wang, G. D. Stucky, L. Chen, *Microporous Mesoporous Mater.* **2012**, *151*, 418.

[57] T. Stephenson, Z. Li, B. Olsen, D. Mitlin, *Energy Environ. Sci.* **2014**, *7*, 209.

[58] T. Brezesinski, J. Wang, S. H. Tolbert, B. Dunn, *Nat. Mater.* **2010**, *9*, 146.

[59] X. W. Lou, H. C. Zeng, *Chem. Mater.* **2002**, *14*, 4781.

[60] H. C. Zeng, F. Xie, K. C. Wong, K. a. R. Mitchell, *Chem. Mater.* **2002**, *14*, 1788.

[61] J. A. Arnoldy, P;van den heijkant, J. A. M.; de Bok, G. D; Moulijn, *J. Catal.* **1985**, *55*, 35.

[62] M. V Reddy, R. Jose, A. Le Viet, K. I. Ozoemena, B. V. R. Chowdari, S. Ramakrishna, *Electrochim. Acta* **2014**, *128*, 198.

[63] X. Hu, W. Zhang, X. Liu, Y. Mei, Y. Huang, *Chem. Soc. Rev.* **2015**, *44*, 2376.

[64] Q. Lu, J. G. Chen, J. Q. Xiao, *Angew. Chem. Int. Ed. Engl.* **2013**, *52*, 1882.

[65] Y. Zhao, Y. Zhang, Z. Yang, Y. Yan, K. Sun, *Sci. Technol. Adv. Mater.* **2013**, *14*, 043501.

[66] G. Liu, H. Zheng, A. S. Simens, A. M. Minor, X. Song, V. S. Battaglia, *J. Electrochem. Soc.* **2007**, *154*, A1129.

[67] A. Ponrouch, M. R. Palacín, *J. Power Sources* **2012**, *212*, 233.

[68] T. J. Patey, A. Hintennach, F. La Mantia, P. Novák, *J. Power Sources* **2009**, *189*, 590.

[69] C. Jiang, M. Ichihara, I. Honma, H. Zhou, *Electrochim. Acta* **2007**, *52*, 6470.

[70] S. Brunauer, L. S. Deming, W. E. Deming, E. Teller, *J. Am. Chem. Soc.* **1940**, *1139*, 1723.

[71] E. P. Barrett, L. G. Joyner, P. P. Halenda, *J. Am. Chem. Soc.* **1951**, *73*, 373.

[72] Y. Jung, Y. Zhou, J. Cha, *Inorg. Chem. Front.* **2016**, *3*, 452.

[73] Y. Li, D. Wu, Z. Zhou, C. R. Cabrera, Z. Chen, *J. Phys. Chem. Lett.* **2012**, *3*, 2221.

[74] X. Fang, C. Hua, X. Guo, Y. Hu, Z. Wang, X. Gao, F. Wu, J. Wang, L. Chen, *Electrochim. Acta* **2012**, *81*, 155.

[75] M. A. Py, R. R. Haering, *Can. J. Phys.* **1983**, *61*, 76.

[76] S. H. Tolbert, A. P. Alivisatos, *Science* **1994**, *265*, 373.

[77] P. J. Mulhern, *Can. J. Phys.* **1989**, *67*, 1049.

[78] V. Sivasankaran, C. Marino, M. Chamas, P. Soudan, D. Guyomard, J. C. Jumas, P. E. Lippens, L. Monconduit, B. Lestriez, *J. Mater. Chem.* **2011**, *21*, 5076.

[79] B. Lestriez, S. Desaever, J. Danet, P. Moreau, D. Plée, D. Guyomard, *Electrochem. Solid-State Lett.* **2009**, *12*, A76.

[80] C. Erk, T. Brezesinski, H. Sommer, R. Schneider, J. Janek, *ACS Appl. Mater. Interfaces* **2013**, *5*, 7299.

[81] N. P. W. Pieczonka, V. Borgel, B. Ziv, N. Leifer, V. Dargel, D. Aurbach, J. H. Kim, Z. Liu, X. Huang, S. A. Krachkovskiy, G. R. Goward, I. Halalay, B. R. Powell, A. Manthiram, *Adv. Energy Mater.* **2015**, *5*, 1501008.

[82] A. Ponrouch, M. R. Palacín, *J. Power Sources* **2011**, *196*, 9682.

[83] K. Makgopa, P. M. Ejikeme, C. J. Jafta, K. Raju, M. Zeiger, V. Presser, K. I. Ozoemena, *J. Mater. Chem. A* **2015**, *3*, 3480.

[84] J. Wang, J. Polleux, J. Lim, B. Dunn, *J. Phys. Chem. C* **2007**, *111*, 14925.

[85] H. Lindström, S. Södergren, A. Solbrand, H. Rensmo, J. Hjelm, A. Hagfeldt, S.-E. Lindquist, *J. Phys. Chem. B* **1997**, *101*, 7717.

[86] T.-C. Liu, *J. Electrochem. Soc.* **1998**, *145*, 1882.

[87] N. Imanishi, M. Toyoda, Y. Takeda, O. Yamamoto, *Solid State Ionics* **1992**, *58*, 333.

[88] V. Augustyn, W. Kim, P. Rozier, P. Taberna, P. Gogotsi, J. W. Long, B. Dunn, P. Simon, *J. Echem. Soc.* **2014**, *161*, 718.

[89] H. Kim, M. Y. Cho, M. H. Kim, K. Y. Park, H. Gwon, Y. Lee, K. C. Roh, K. Kang, *Adv. Energy Mater.* **2013**, *3*, 1500.

[90] H. G. Jung, N. Venugopal, B. Scrosati, Y. K. Sun, *J. Power Sources* **2013**, *221*, 266.

[91] Q. Mahmood, S. K. Park, K. D. Kwon, S. J. Chang, J. Y. Hong, G. Shen, Y. M. Jung, T. J. Park, S. W. Khang, W. S. Kim, J. Kong, H. S. Park, *Adv. Energy Mater.* **2016**, *6*, 1.

Chapter 3. Direct Observation of Suppression of Electronically Drive Phase Transition in Nanosized MoS_2 Using *Operando* X-ray Diffraction

3.1. Introduction

Pseudocapacitance offers the potential for high power density (fast charging and discharging) without significant reduction in energy density. These values are typically highly anti-correlated in traditional Li-ion battery materials, and this decoupling of energy and power occurs by combining the storage mechanism of a battery and the kinetics more similar to an electric double layer capacitor (EDLC). Most battery materials have high energy density because the energy is stored through redox reactions in the bulk of the material. However, slow solid-state diffusion of the intercalating ions limits the kinetics of these reactions. EDLCs, on the other hand, store energy through the adsorption of ions onto high surface area electrodes, which produces fast kinetics, but sacrifices energy density. [1 – 5] Pseudocapacitive behavior commonly occurs when near-surface Faradaic charge transfer reactions take place, [2] accompanied by ion adsorption electrochemically onto the host lattice in a process termed redox or surface pseudocapacitor. It can also occur, however, when ions intercalate into the channels or layers of a redox-active material, often near the surface of a material, without inducing a phase transition. This later process is called intercalation pseudocapacitance.[3,4,5]

Typically, first-order phase transitions arise when there is a large variation in Li concentration during intercalation. This leads to the coexistence of Li-rich and Li-poor phase and results in a migration barrier that leads to slow kinetics observed in most intercalation materials.[6-8] The difference in volume of the two phases can also induce strain in the electrode, causing material failure and potentially reducing battery life.[7] Such phase transitions thus make traditional battery materials less attractive for fast charging applications.[34]

In keeping with the pseudocapacitor definition above, a number of materials that do not required a discontinuous phase transition for ion intercalation have been shown to exhibit pseudocapacitive behavior when diffusion oath lengths are sufficiently reduced through nanostructuring to allow for fast ion diffusion into the bulk of the material. Such materials, which are known as intrinsic pseudocapacitors, include materials such as RuO_2,[9] MnO_2,[10,11] andNb_2O_5.[4] Intrinsic pseudocapacitors have crystalline networks with ion transport pathways that allow for capacitive behavior and fast ion diffusion over a broad range of crystallite sizes.

Recently, it has been shown that pseudocapacitive behavior can also be achieved through suppression of first-order ion intercalation and deintercalation induced phase transitions.[1-4] Through nanostructuring, certain materials that do not display fast kinetics in the bulk can be engineered to become pseudocapacitive. These materials, termed extrinsic pseudocapacitors, are size dependent and do not show pseudocapacitive behavior above a critical size.[1,12] This phenomenon has been previously observed and shown in MoO_2,[12] TiO_2,[13–15] TiS_2,[16] and $LiMn_2O_4$. [17,18] When the diffusion path length shortens, rapid rates can be achieved because diffusion time is proportional to the square of diffusion length and inversely proportional to diffusivity.[19] In addition, as crystallite size decreases, two-phase coexistence (Li-rich and Li-poor) likely becomes undesirable, due to the increased activation energy for nucleation of the new phase or other thermodynamic or kinetic factors. This has the potential to again give rise to solid solution behavior, in which there is no miscibility gap and ions are interstitially dissolved into the lattice, causing only slight changes in the lattice parameter without major reconstruction of the crystal structure.[13,20,21]

Materials experiencing first-order phase transition *vs.* solid solution behavior show different features in their electrochemistry profiles, particularly in their galvanostatic (GV) traces. A voltage *vs.* composition curve provides information on an electrode's thermodynamic properties such as the chemical potential, Gibbs free energy and entropy.[6,8] For systems with a miscibility gap in which Li-

rich and -poor phases coexist, the chemical potential is derived using the common tangent construction of the Gibbs free energy minima of the two phases.[8] This results in distinctive plateaus in the voltage curve because the slope of the chemical potential is constant. As lithium intercalates and deintercalates into the host lattice of a pseudocapacitor without a phase transition, by contrast, the chemical potential of the active material is equal to the derivative of the Gibbs free energy and change smoothly over the course of the electrochemical reaction. This leads to a linearly sloping voltage curve in the galvanostatic trace.[6,8] Thus, pseudocapacitive materials with solid solution-type behavior due to phase transition suppression do not show plateaus and can be easily differentiated from battery-like material with inherent first-order phase transitions.

Though pseudocapacitance has been demonstrated in several metal oxides, it has not been explored in many metal sulfides. Metal dichalcogenides are particularly interesting for their layered structure comprised of highly polarizable sulfur ions that allow reversible intercalation.[2,22,23] In the past, Muller et al. have demonstrated pseudocapacitive charge storage in few-layered 2D TiS_2 nanocrystals. In the past, Muller et al. have demonstrated pseudocapacitive charge storage in few-layered 2D TiS_2 nanocrystals. In that study, 85% of the total current obtained from potentiostatic cycling was capacitive, leading to a high specific capacitance of 320 F/g with a 30 s charge/discharge time.[16] Recently, we have explored the pseudocapacitive properties of MoS_2 nanocrystals. MoS_2 is an attractive material for pseudocapacitive charge storage because of its relatively large van der Waals gap, and electrochemically active metallic 1T phase. The 1T phase can be generated from the standard 2H phase by alkali metal intercalation.[22-26] Metallic materials are desirable in energy storage application due to their enhanced electronic conductivity. Details regarding the MoS_2 1T phase will be elaborated in the results and discussion section. In our previous study, we showed that thick electrodes made from MoS_2 nanocrystal arrays were pseudocapacitive. The electrodes could be cycled 3000 times with

80% capacity retention while accessing over 90 mA h g^{-1} in only 30 seconds (theoretical capacity 167 mAh g^{-1}).[27]

Despite MoS_2 being reported to undergo multiple phase changes to accommodate one mole of Li, these transitions appear to be suppressed in our MoS_2 nanocrystals arrays as evidenced by the high reversibility and fast kinetics.[27] In this work, we thus use *operando* X-ray diffraction during electrochemical cycling at Stanford Synchrotron Radiation Lightsource (SSRL) to further understand the structural origin of the fast pseudocapacitive mechanism in MoS_2 nanocrystals. *Operando* X-ray diffraction has been shown to be an effective method for monitoring phase change and lattice expansion in energy storage materials in real time. It has been used to study materials such as $LiCoO_2$,[28] $LiMn_2O_4$,[29] $LiNiO_2$,[30] TiO_2,[14] and TiS_2. [20] This study provides a direct crystallographic comparison of micron-sized bulk MoS_2 ($bMoS_2$) and MoS_2 nanocrystal assemblies ($nMoS_2$) upon cycling with Li^+ with a goal of better understanding the drastic difference in performance between these two materials.

3.2. Results and Discussion

3.2.1. Materials and Characterization

Bulk MoS_2 particles (~45 μm) used in this study are commercially available powders while MoS_2 nanocrystals were synthesized according to methods in our previous work.[27] The powders were cast into composite slurry electrodes containing the active materials, carbon and polymeric binder. The synchrotron based X-ray diffraction patterns (XRD) of pristine $bMoS_2$ and $nMoS_2$ electrodes used in this *operando* study show characteristic reflections for the hexagonal MoS_2 phase matching JCPDS No.37-1492 (Figure 3.1a). Since the XRD signal is attenuated by at least 50% due to absorption from various cell components and electrolyte, electrodes with relatively high mass loadings were made for this study. These electrodes were optimized in this study to produce a large XRD signal, but could

not be cycled at very high rate due to conductivity limitations. Any kinetic suppression of phase transitions that occurs at slow rate, however, should increase at faster rates, so the need to cycle slowly for these operando studies means only that these experiment represent a lower limit on the extent of phase transition suppression that could be observed at faster rates. Below we will show basically complete suppression, confirming that these scan rate differences do not modify our fundamental conclusions. In addition, the use of thick electrodes ensures that not all the $bMoS_2$ platelets settles parallel to the current collector, which would result in diminished peak intensities for the (00*l*) planes in the transmission geometry used in this work. The $nMoS_2$ nanocrystals (Figure 3.1b-c), are roughly spherical, leading to random orientation in the electrode. Indeed, the XRD patterns are consistent with a randomly dispersed polycrystalline MoS_2 powder.

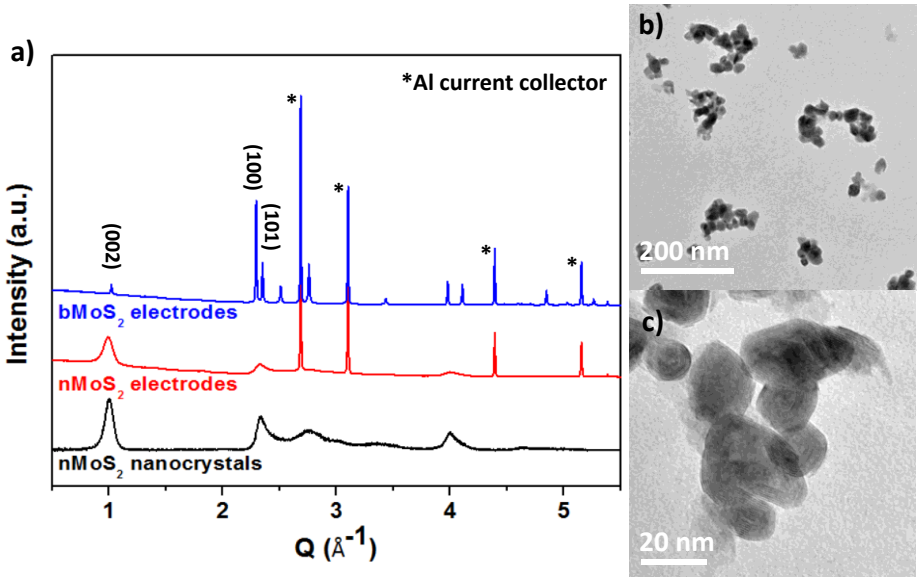

Figure 3.1. (a) XRD patterns of uncycled $bMoS_2$ and $nMoS_2$ electrodes and as-synthesized MoS_2 nanocrystals. Peaks labeled with asterisk corresponds to the aluminum current collector while others correspond to the 2H phase of MoS_2. The peak broadening in the $nMoS_2$ electrode and pure nanocrystal sample is due to the small crystallite size and the onion-like structure of the 10nm to 30nm nanocrystals, as shown in the low (b) and high (c) magnification TEM images.

3.2.2. Electrochemistry

MoS_2 has been studied as an energy storage material for decades. However, most current research focuses on the high capacity (670 mA h g^{-1}) conversion reaction which occurs between 1.1 V and 0 V,[31-36] rather than the one electron intercalation reaction between 2.7 V and 1.0 V. The cycle lifetimes for MoS_2 are typically poor for the conversion reaction even with engineered nanoparticle-based electrodes.[37] For the above reasons, we chose to focus on the intercalation reaction of MoS_2 between 2.7 V and 1.0 V and have demonstrated high reversibility with our previous study.[23,2738] The intercalation reaction can be described by Equation 3.1:

$$MoS_2 + x\text{Li}+ + x\text{e}- \rightarrow \text{Li}x\text{MoS}_2 \qquad \textit{Equation 3.1}$$

The 1T phase MoS_2 has been widely studied as a hydrogen storage material but has only recently been explored as an energy storage material for pseudocapacitors.[39] The metallic 1T phase and the semiconducting 2H pristine phase are similar in structure, except 2H MoS_2 has a close-packed, layered hexagonal structure of S-Mo-S' in an ABA configuration while 1T MoS_2 has an ABC configuration.[40-42] It is well known that MoS_2 undergoes a phase conversion from 2H to 1T when alkali metals are inserted into the van der Waals gap, causing the highly polarizable sulfur layer to glide along the plane normal to the c-axis of the unit cell.[42-45] Lithium, in particular, causes an irreversible phase conversion from 2H to 1T (hexagonal to trigonal prismatic) at 1.1 V *vs.* Li/Li^+ when the lithium concentration increases between the range of $0.1 < x < 1$.[43,46] Though the 2H to 1T phase conversion of $bMoS_2$ is well known, it has not been directly observed in nanosized MoS_2. In addition to the *operando* phase change study of lithium intercalation within the 1T phase, we also performed *operando* X-ray diffraction to study the 2H to 1T phase conversion of $nMoS_2$ to help us better understand the conversion process and the 1T phase itself in $nMoS_2$.

The diffraction patterns of $nMoS_2$ during the first cycle are shown in Figure 3.2a in the pristine, lithiated (Li_1MoS_2) and delithiated states. The (002) peak shifts to a lower Q value ($Q = \frac{2\pi}{d}$) corresponding to the (001) peak of the 1T trigonal phase.[43,44, 47] This same phenomenon has been observed in the bulk as 2H MoS_2 converts to 1T MoS_2 during alkali metal insertion. This peak shift is not simply a result of intercalation induced lattice expansion because the galvanostatic trace in Figure 3.2d show a distinct plateau for this process that signifies a first-order phase transition. The peak broadening in this nanosized sample prohibited us from matching all high-order XRD reflections to the 1T phase, but a general matching is observed in Figure 3.1a. After delithiation, the (001) 1T peak shifted back to higher Q, to a value between the (001) 1T and (002) 2H peak position, indicating that not all $nMoS_2$ in the electrode completed the 2H-1T conversion after the first cycle. Figure 3.2b shows the peak fit analysis of the delithiated $nMoS_2$ diffraction pattern, indicating the presence of both phases in the electrode.

Due to our interests in fast intercalation reaction of MoS_2 in the 1T phase, all samples were precycled prior to *operando* diffraction studies to convert 2H $bMoS_2$ and $nMoS_2$ to the 1T phase via alkali metal intercalation. To ensure that most of the 2H phase is converted, $bMoS_2$ and $nMoS_2$ were precycled multiple times until the plateau corresponding the 2H-1T conversion (1.1 V) completely disappeared. Moreover, it is known that 1T MoS_2 is not the thermodynamically stable at high potential and can back convert to the 2H phase when cycled above 2.8 V *vs.* Li/Li^+.[43,48] Therefore, all electrochemical cycling carried out in this study is limited to a voltage window of 1 V to 2.7 V. We found that, $bMoS_2$ took fewer cycles than $nMoS_2$ to complete the conversion as shown in the precycling GV traces in Figures 3.2c-d. Figures 3.2c and d shows the GV curves of $bMoS_2$ and $nMoS_2$, respectively at 0.2 C during the 2H to 1T conversion and precycling process. The 2H $bMoS_2$ is completely converted to the 1T phase after four cycles, while $nMoS_2$ requires eight cycles. The longer

conversion process for $nMoS_2$ foreshadows the results below, and can be justified by considering nucleation kinetics. The conversion of 2H MoS_2 to the 1T phase requires the formation of 1T nuclei in the MoS_2 grain. Once the nuclei are formed, the new phase can propagate throughout the domain.

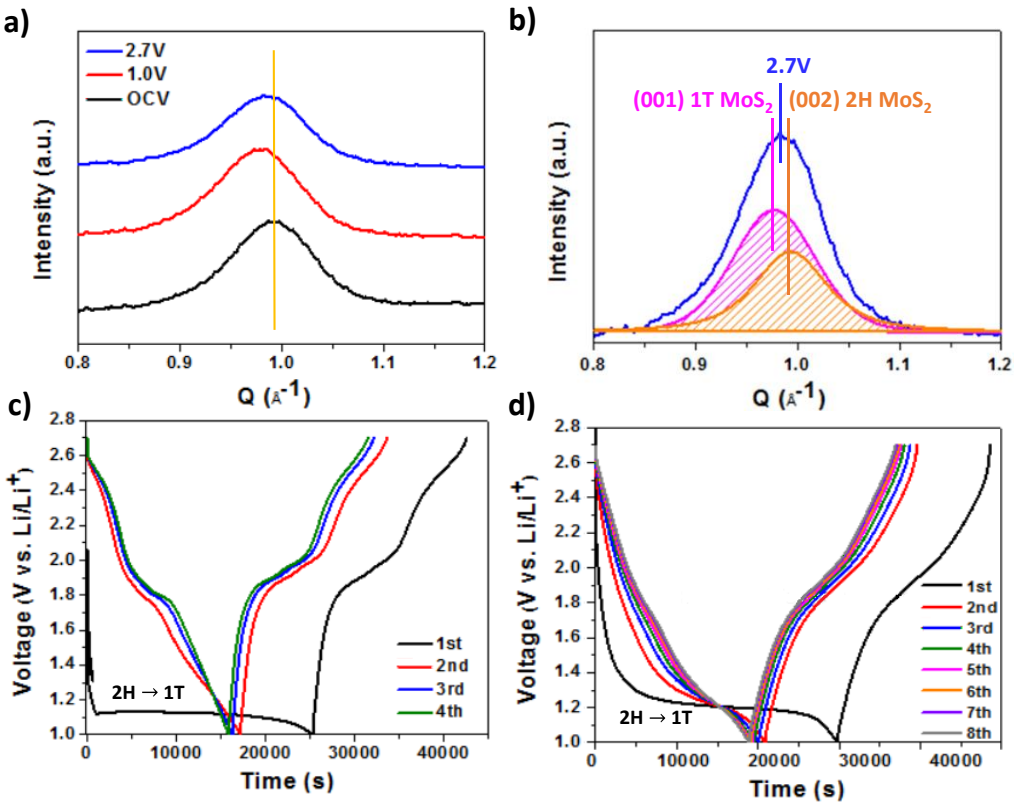

Figure 3.2. (a) *Operando* X-ray diffraction of $nMoS_2$ showing 2H to 1T conversion. Starting as the (002) 2H phase at the open circuit voltage, the 2H MoS_2 converts to the 1T phase during lithiation as the (002) 2H peak shifts to lower Q and become the (001) peak of the 1T phase. As lithium is deinserted, the (001) 1T peak shifts slightly back to higher Q, indicating the presence of both 1T and 2H phase since not all nanocrystals are converted in the first cycle. This mixture of two phases is confirmed by the peak fit analysis shown in (b), where the final peak position after delithiation lies in between the (001) 1T and (002) 2H phase. Multiple cycles are required to complete the 2H-1T conversion. Bulk MoS_2 (c) took 4 cycles while nano MoS_2 (d) took up to 8 cycles. This precycling was done prior to the *operando* experiments presented below.

The probability of phase transition should be higher in the $bMoS_2$ for two reasons. First, nucleation may be suppressed in nanosized domains because of the limited number of atoms; many more nucleation events are also needed because of the limited domain volume transformed by each nucleation event.[49-52] In order for all nanocrystals to be converted, every nanocrystal requires its own nucleation event. As a result, more cycles are required to propagate and complete the 2H-1T phase conversion in $nMoS_2$ electrode.

3.2.3. Kinetic Analysis

Pseudocapacitive energy storage is a distinct electrochemical mechanism that gives rise to fast charge storage. As mentioned earlier in the introduction, typical battery materials undergo distinct phase changes during lithium intercalation and deintercalation, and this type of charge storage is slow. In contrast, charge stored through intercalation pseudocapacitance does not result in phase transitions, but instead is thought to occur through fast intercalation. Suppressing phase transitions permits fast intercalation reactions throughout the nanoparticle, enabling a pseudocapacitive charge storage mechanism that is not limited to the surface.

Pseudocapacitive storage gives rise to distinct electrochemical features in cyclic voltammogram (CV) and GV profiles. Specifically the sloping GV profiles discussed above should be accompanied by CV curves that show little polarization induced splitting between the anodic and cathodic peaks due to the fast kinetics and reduced crystallite size.[4] Figure 3.3a shows the GV curves at 1C and 60C for $nMoS_2$ while panel b shows the CV curves collected at 0.2 mV/s and 1 mV/s for the same material. Though there are no plateaus observed in the $nMoS_2$ GV curves, redox peaks are present in the CV data, even at high rates. This suggests that the redox reactions are happening under suppression of phase transition, which is a characteristic of pseudocapacitive energy storage mechanism. Minimal peaks splitting is observed between anodic and cathodic peaks in Figure 3.3b. In

comparison to $nMoS_2$, electrochemical traces of $bMoS_2$ show none of these features. Figures 3.3c and d show the GV and CV curves (same rates as the nanocrystals) for the bulk electrode. The distinctive plateaus in $bMoS_2$'s GV curve correspond to the phase transitions between the trigonal prismatic 1T phase and triclinic (Li_xMoS_2) phase during lithium intercalation.[48] Moreover, highly polarized redox peaks are observed in the CV as a result of the slower kinetics, indicating battery-like behavior in $bMoS_2$.

Kinetic analysis was performed to further understand the difference in behavior of $bMoS_2$ and $nMoS_2$ and to validate the pseudocapacitive behavior of $nMoS_2$ since sloping GV traces can also be triggered by the nanosize effect.[53] It has been observed that nanosize crystallites can lead to a sloping voltage curve due to a shorter voltage plateau width (i.e. a narrower two phase coexistence region) and can create solid solution-like electrochemical features, even when the first-order phase transition is not suppressed.[53] To distinguish the type of charge storage process, 'b-value' analysis was performed. This kinetic analysis has also been performed on many other newly found pseudocapacitive material such as Nb_2O_5,[4,54] V_2O[5,55] MoO_3.[21,56] Generally, the current response as a function of scan rate in a cyclic voltammetry measurement can be used to distinguish between a capacitor-like or diffusion controlled charge storage mechanism according to the following equation:

$$i = av^b \qquad \textit{Equation 3.2}$$

where, i is the measured current, v is the scan rate, and a and b are both constants but the value of the exponential term distinguishes the charge storage mechanism: when b is equal to 0.5 (the current i is proportional to scan rate $v^{1/2}$), the current is dominantly governed by diffusion.[2,4] When b equals 1 (i directly proportional to v), it indicates a capacitor-like behavior, where the current is not diffusion controlled, a situation that arises for surface pseudocapacitive reactions or when intercalation reaction kinetics are capacitive in nature due to the suppression in phase transitions.[2,4] According to our analysis shown in Figures 3.3b and d, $bMoS_2$ is found to be mostly diffusion-limited with b values at

current maxima (0.65, 0.67, 0.68, 0.75) closer to 0.5. On the other hand, $nMoS_2$ is highly capacitive, with *b* values (0.95, 0.95, 0.96, 0.96) close to 1. The *b*-values with their corresponding peaks of $bMoS_2$ and $nMoS_2$ can be found in the CV in Figures 3.3b and d. This result suggests that $nMoS_2$'s sloping GV profile is due to phase transition suppression and not nanosize effect. Details regarding our

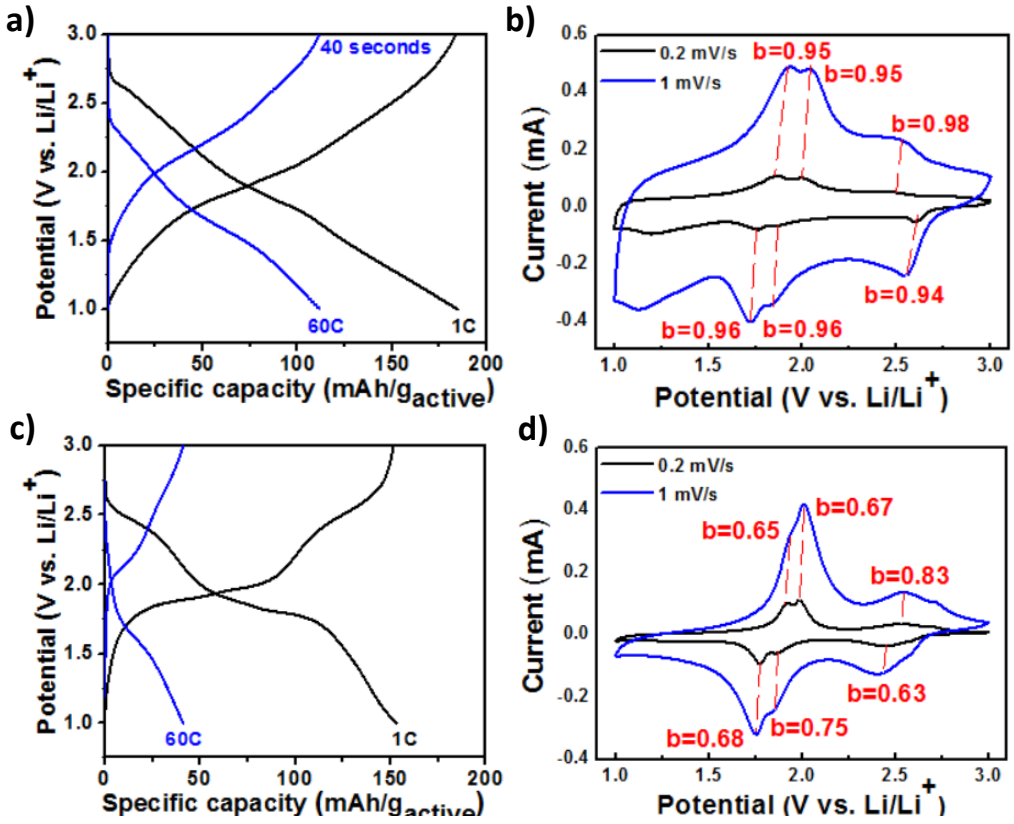

Figure 3.3. Galvanostatic traces and cyclic voltammograms of $nMoS_2$ (a - b) and $bMoS_2$ (c -d). The sloping galvanostatic profiles in (a) for $nMoS_2$ suggests that first-order phase transitions have been suppressed and that the system is pseudocapacitive. This is in agreement with calculated *b* values close to 1 at all the current maxima obtained from sweep rate dependent CV curves in (b); b=1, indicates capacitor-like behavior. Unlike $nMoS_2$, phase transition between the 1T and triclinic Li_1MoS_2 phases are indicated by voltage plateaus in $bMoS_2$ (c). The system also shows mostly diffusion-limited with *b* values close to 0.5 in (d).

analysis can be found in our previous studies on nanoscale MoS_2 and other nanoscale pseudocapacitors.[2,4]

3.2.4 *Operando* X-ray Diffraction Study

The structural changes occurring during Li^+ intercalation into 1T MoS_2 materials were observed using *operando* synchrotron X-ray diffraction. The diffraction patterns in Figures 3.4 and 3.5 were collected from $bMoS_2$ and $nMoS_2$ electrodes, respectively, that were precycled several times to drive the 2H-1T conversion. To reiterate, we are not studying the semiconductor to metal phase transformation. We are studying the phase stability of the metallic 1T phase during charge storage to understand the origins of fast charge storage in $nMoS_2$. Any resulting changes in the atomic structure of the host lattice will be reflected in changes to the peak positions in the X-ray diffraction patterns, since Li-ions are preferentially inserted and stored in the van der Walls gap of the material.

As mentioned earlier, first-order phase transitions are not suppressed in $bMoS_2$ during lithiation. Figure 3.4a shows the diffraction pattern of $bMoS_2$ upon cycling at 0.22C. During lithiation of $bMoS_2$, the (001) peak first shifts toward lower Q values. This is then followed by a shift to higher Q at a voltage of ~ 1.76 V and is accompanied by the appearance of a new peak at 1.09 $Å^{-1}$ that grows continuously in intensity as the Li-ion concentration increases. During delithiation, the structural processes that occurred during lithiation are reversible. The peak at 1.09 $Å^{-1}$ disappears while the (001) peak gradually returns to its original position. In addition to this change, significant structural changes corresponding to rearrangement of the covalent network in the MoS_2 layers can also be found in the region between 2.1 $Å^{-1}$ and 2.5 $Å^{-1}$. Similar to the (001) peak, the (100) and (101) peaks shift significantly towards lower Q and the (101) peak merges with its shoulder peak during lithiation, and then moves back to higher Q during delithiation. These diffraction signatures are consistent with a

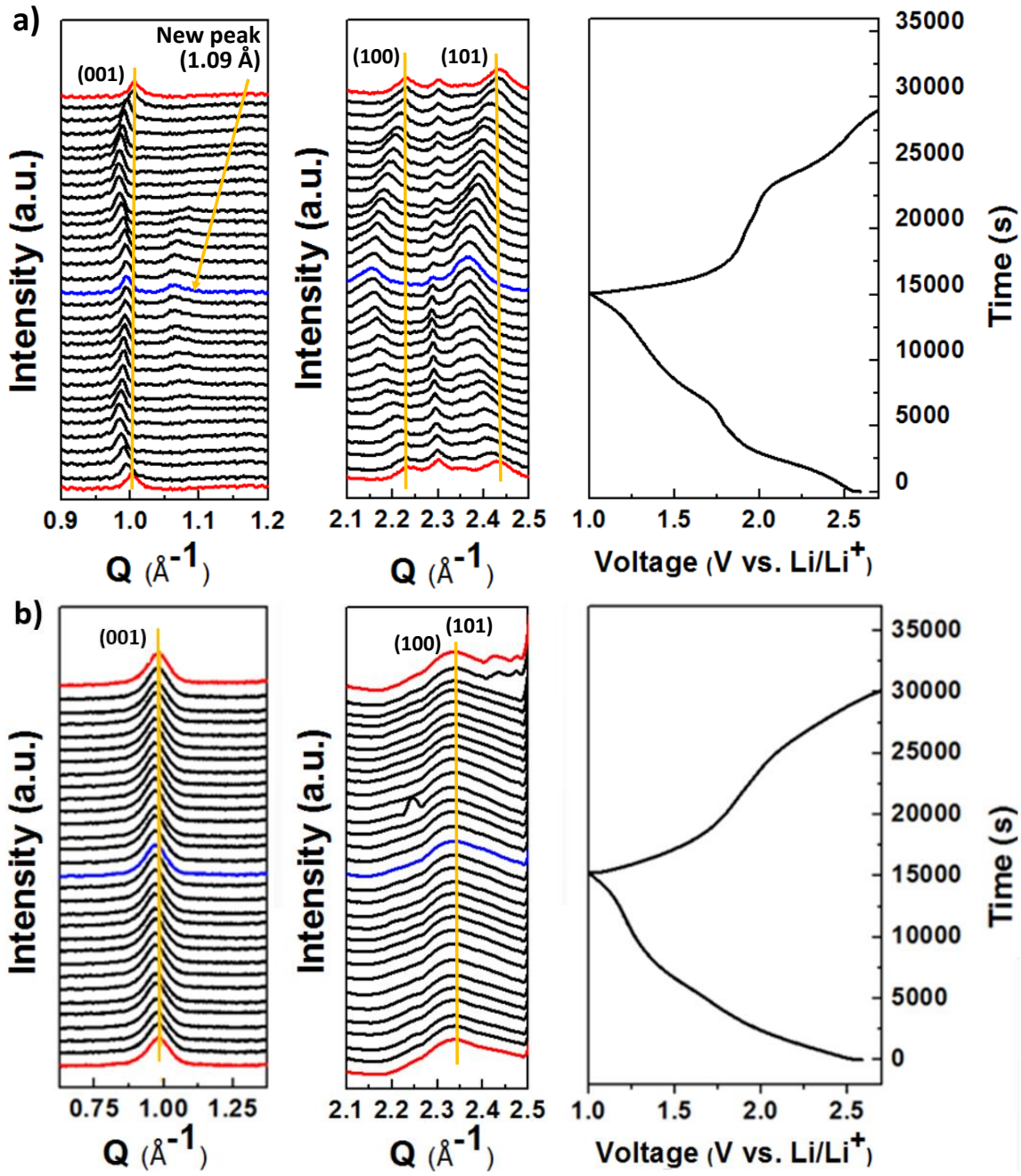

Figure 3.4. (a) ***Operando*** **phase change study of $bMoS_2$ and $nMoS_2$. First-order phase transition can be observed in $bMoS_2$ as 1) peaks shift significantly to lower** ***Q*** **then back to higher** ***Q*****, 2) the emergence of a new peak at 1.09 $Å^{-1}$ and 3) a shoulder near the 101 peak. (b) Unlike $bMoS_2$, no phase transition was observed in $nMoS_2$ due to the improved kinetics and unfavorable two phase coexistence in nanocrystals.**

reversible first order phase change, which typically occurs when Li-ions have a low solubility in the parent phase (the 1T-metallic phase in this case).

Very different structural changes are found in $nMoS_2$ compared to $bMoS_2$ during Li-ion charge storage. Figure 3.4b shows the XRD patterns of $nMoS_2$ collected during the *operando* phase change study at 0.22C. As seen in Figure 3.4b, all (001), (100) and (101) peaks shift to lower Q (0.013 $Å^{-1}$) without the emergence of any new peaks (the distinct shoulder at 1.09 $Å^{-1}$ is not present) during lithium intercalation and deintercalation of $nMoS_2$, indicating the suppression of phase transition. It is also worth noting that unlike $bMoS_2$, the expansion of $nMoS_2$ lattice tracks the Li-ion concentration linearly, like a solid solution. This lattice expansion indicates that the fast charge storage in this system is not limited to the surface of the nanocrystal, and is indeed related to the fact that a large portion (80%) of the theoretical capacity being stored through capacitive mechanisms in a process that can best be described as intercalation pseudocapacitance.[57]

To further emphasize this point, three known MoS_2 phases, 2H, 1T and triclinic Li_1MoS_2, were compared to the diffraction patterns for $bMoS_2$ and $nMoS_2$ in different states of charge. Figure 3.5 shows the diffraction line pattern of the hexagonal (2H), trigonal prismatic (1T) and triclinic phases and the synchrotron based XRD pattern of the pristine, lithiated and delithiated states of $bMoS_2$ and $nMoS_2$. Prior to the *operando* study cycling (after 2H-1T conversion precycling), $bMoS_2$ consists mainly of the expected trigonal prismatic 1T phase with some residual hexagonal 2H phase. The back conversion of the 1T-2H phase is known to occur slowly at room temperature in the fully delithiated state, and probably happened during the 24-hour transit period before the samples were analyzed.[43] The Li_1MoS_2, which is a distinctly different phase than the 1T phase, matches the triclinic MoS_2 powder pattern indicating that $bMoS_2$ undergoes a first-order phase change upon Li-ion intercalation.[58] The full reversibility of this phase transformation can be seen from the diffraction patterns as the delithiated MoS_2 returns to the trigonal phase, this time with reduced hexagonal phase

content. By contrast, distinct changes in the XRD patterns are not observed in $nMoS_2$. If phase changes were to occur in $nMoS_2$, even with peak broadening due to finite size effects, a shoulder should have appeared on the (001) peak and a new peak should appear at 2.1 $Å^{-1}$ in the covalent region, indicating the presence of triclinic Li_1MoS_2 phase. The absence of those peaks confirms phase

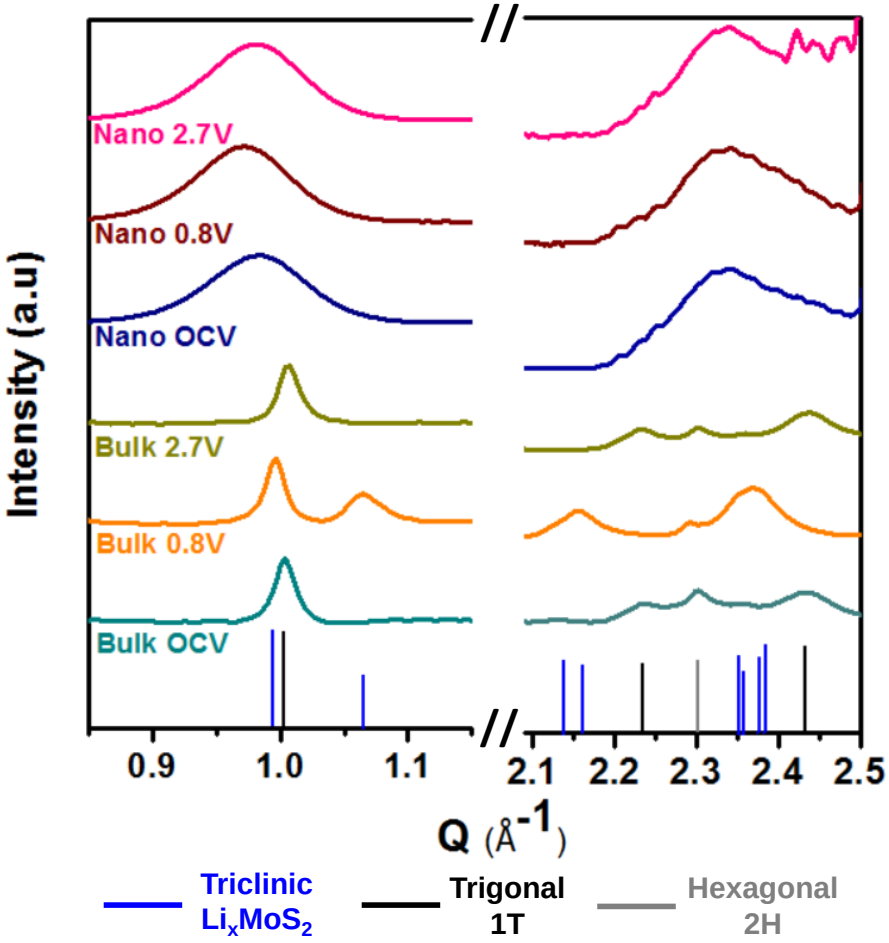

Figure 3.5. Selected XRD patterns for the pristine, lithiated and delithiated state of $bMoS_2$ and $nMoS_2$ with line patterns of the three known phases of MoS_2. This direct comparison indicates that $bMoS_2$ experiences major phase transitions between the 1T trigonal prismatic phase to triclinic Li_1MoS_2 phase, which has also been observed in the literature. However, this phase transition is not observed in $nMoS_2$. Shoulders and peaks corresponding to the triclinic Li_1MoS_2 phase are clearly absent in the $nMoS_2$ at 0.8V (all voltages reported versus Li/Li^+).

transition suppression in $nMoS_2$ and confirms that intercalation in $nMoS_2$ nanocrystals is pseudocapacitive. As mentioned earlier, only a peak shift to lower Q is observed during lithiation as a result of lattice expansion. We note that the $nMoS_2$ peaks are already shifted to lower Q to begin with due to a larger than standard van der walls gap (6.27 Å versus 6.15 Å in bulk). Interesting, this expansion does not affect the changes in peak position observed during charge and discharge.

We speculate that the difference in structural changes between the bulk and the nano could be related to kinetic barrier.[59] The phase transition found in $bMoS_2$ could be suppressed in the nanoscale material if the formation of stable nuclei in a confined space was energetically unfavorable. Even if such nuclei were formed, the formation of a phase boundary interface would incur a significant free energy penalty.[51,52,60] Thus, two-phase coexistence could be inhibited in nanocrystals due to the limited crystallite size. The fact that each nucleation event can only transform one crystallite could also result in phase transition suppression and the accompanying fast insertion kinetics. We also postulate that the miscibility gap could be reduced in $nMoS_2$, either because of the increased Van der Waal's gap ore because of increased surface energy contribution to the overall system energy.

3.3. Conclusion

In order to better understand differences in charge storage mechanisms for $bMoS_2$ and $nMoS_2$, we have investigated the structural changes and phase stability that occur during the lithiation and delithiation of both bulk and nano MoS_2. We have correlated the disparate electrochemistry of these two samples with structural information obtained from synchrotron based *operando* X-ray diffraction upon electrochemical cycling. The galvanostatic voltage profiles of $bMoS_2$ and $nMoS_2$ electrodes show discrete plateaus and linear voltage responses, respectively. This behavior, along with the fast kinetics and low polarization observed in $nMoS_2$ suggests battery-like behavior in the bulk material, and pseudocapacitive behavior in the nanoscale system. In agreement with this observation $bMoS_2$, shows

a first order phase change between the trigonal to triclinic phase as Li ions insert into the host lattice. By contrast, $nMoS_2$ shows no change other than a small shift in lattice constant. This indicates that the pseudocapacitive behavior of $nMoS_2$ is mostly due to a suppressed first-order phase transition that occurs in the 1T phase, in a process that can best be described as intercalation pseudocapacitance. These results help explain the very fast cycling kinetics that have been demonstrated for nanostructured MoS_2.

Perhaps more importantly, this work adds another concrete realization to the hypothesis that intercalation pseudocapacitance can occur when ion-intercalation is not accompanied by a phase transition. Some past studies have demonstrated this correlation in materials that are intrinsically able to intercalate Li^+ with minimal structural change.[4] Such material have been termed intrinsic pseudocapacitors.[61] In this case, however, a materials that shows standard battery behavior in the bulk is converted to a pseudocapacitor in finite size, and that conversion is accompanied by suppression of the standard intercalation induced phase transition. Such materials have been termed extrinsic pseudocapacitors,[61] and this family of materials is potentially very large and thus very interesting for future energy storage applications. By directly correlating the altered electrochemical kinetics with suppression of phase transitions in finite sized materials, we strengthen this correlation and hopefully add insight that will lead to the future development of pseudocapacitive nanostructured materials.

3.4. Experimental

3.4.1. Synthesis

All starting materials were obtained from commercial suppliers and used without further purification. Bulk MoS_2 was purchased from Alfa Aesar. The MoS_2 nanocrystals were synthesized through sulfurization of nanosized MoO_2. The synthesis of MoO_2 nanocrystals has been reported elsewhere, and is briefly described here. MoO_2 nanocrystals were prepared by solvothermal method

by dissolving anhydrous $MoCl_5$ (Strem Chemicals) in a mixture of ethanol and deionized water at a reaction temperature of 180°C for 6 hrs. The MoS_2 nanocrystals were obtained by converting the MoO_2 nanocrystals with H_2S gas in a tube furnace at 600 °C under flowing H_2S/H_2 (H_2S 5 mol% : H_2 95 mol%, Air Gas) for 10 hrs.[27]

3.4.2. Characterization

Powder X-ray diffraction (XRD) was performed on a PANalytical X'Pert Pro operating with Cu Kα (λ = 1.5418 Å) using a 0.03° step size, a voltage of 45 kV, and a current of 40 mA to characterize the pristine nMoS2 diffraction. XRD patterns were recorded in the range of $10° < 2\theta < 80°$. Transmission electron microscopy (TEM) was performed using a FEI Technai T12 operating at 120 kV. *Operando* XRD was performed at SSRL at beamline 11-3 at an X-ray energy of 12300 eV. *Operando* data was collected using a MAR 345 Image Plate with 130 mm work distance. Data was collected from Q = 0 to 5.5 $Å^{-1}$.

3.4.3. Electrochemistry

Carbon-based slurry electrodes were made and used for all electrochemical cycling. Electrodes has an overall composition of 70 wt.% active material ($nMoS_2$ or $bMoS_2$): 10 wt.% vapor grown carbon fibers (Sigma Aldrich): 10 wt.% carbon black (Alfa Aesar): 10 wt.% polyvinylidene fluoride (Kynar) binder, all dispersed in n-methyl-2-pyrrolidone (Alpha Aesar). All components were mixed in a mortar and pestle to obtain a homogeneous paste and cast onto a 25 μm carbon-coated aluminum current collector. The slurry was dried in ambient temperature for 5 hrs prior drying in a vacuum oven for 15 hrs at 125 ºC. The mass loading of the electrodes was 3.42 mg cm^{-2} and 5.82 mg cm^{-2} for $bMoS_2$ and $nMoS_2$ respectively. These electrodes were cycled from 1.0 V to 2.7 V in Swagelok cells using lithium metal counter electrodes, glass fiber separator (Watman), and 1M $LiPF_6$ electrolyte in 1 ethylene

carbonate: 1 diethylene carbonate by volume (Sigma). $nMoS_2$ samples were cycled using VSP potentiostat/galvanostat (Bio-Logic) at a 0.2C rate (138.6 mA h g^{-1}) while the $bMoS_2$ electrodes were cycled on Arbin using at a 0.2C rate (50 mA h g^{-1}).

After precycling, the electrodes were taken out of the Swagelok cells in an Ar-filled glovebox and reassembled into in a coin cell with 3 mm holes and Kapton tape windows for the *operando* studies. The Kapton tape window was chosen for X-ray transparency. The coin cells were stored in an Ar atmosphere until cycling was performed to prevent exposure. Due to time constraints, all cycling was performed at 0.22C for the *operando* studies at SSRL.

3.4.4. Data Processing

All diffraction intensity data is plotted as a function of the scattering vector length $Q = \frac{4\pi}{\lambda}\sin(\theta)$, where θ is half of the scattering angle and $\lambda =$ is the wavelength of the incident radiation; the *d*-spacing thus is simply $\frac{2\pi}{Q}$. All diffraction peaks were normalized to the Al peak using Area Diffraction Machine. Backgrounds subtraction of all spectra were later performed in Origin. Diffraction of a blank cell (a regular coin cell with Kapton window containing all components except the active material) was used as the background diffraction pattern.

3.5 Reference

[1] V. Augustyn, P. Simon, B. Dunn, *Energy Environ. Sci.* **2014**, *7*, 1597.

[2] J. B. Cook, H.-S. Kim, Y. Yan, J. S. Ko, S. Robbennolt, B. Dunn, S. H. Tolbert, *Adv. Energy Mater.* **2016**, *6*, 1501937.

[3] Y. Zhu, L. Peng, D. Chen, G. Yu, *Nano Lett.* **2016**, *16*, 742.

[4] V. Augustyn, J. Come, M. A. Lowe, J. W. Kim, P. Taberna, S. H. Tolbert, H. D. Abruña, P. Simon, B. Dunn, *Nat. Mater.* **2013**, *12*, 518.

[5] B. E. Conway. W. G. Pell, *J. Solid State Electrochem.* **2003**, *7*, 637.

[6] D. Li, H. Zhou, *Materials Today* **2014**, *17*, 451.

[7] A. Van Der Ven, K. Garikipati, S. Kim, M. Wagemaker, *J. Electrochem. Soc.* **2009**, *156*, A949.

[8] A. Van Der Ven, J. Bhattacharya, A. A. Belak, *Accounts of Chemical Research* **2013**, *46*, 1216.

[9] J. P. Zheng, P. J. Cygan, T. R. Jow, *J. Electrochem. Soc.* **1995**, *142*, 2699.

[10] H. Y. Lee, J. B. Goodenough, *Journal of Solid State Chemistry* **1999**, *144*, 220.

[11] T. Brousse, M. Toupin, R. Dugas, L. Athouël, O. Crosnier, D. Bélanger, *J. Electrochem. Soc.* **2006,** *153*, A2171.

[12] H. Kim, J. B. Cook, S. H. Tolbert, B. Dunn, *J. Electrochem. Soc.* **2015**, *162*. A5083.

[13] R. V. D. Krol, A. Goossens, E. A. Meulenkamp, *J. Electrochem. Soc.* **1999**, *146*, 3150.

[14] T. Brezesinski, J. Wang, J. Polleux, B. Dunn, S. H. Tolbert, *J. Am. Chem. Soc.* 2009, *131*, 1802.

[15] J. Wang, J. Polleux, J. Lim, B. Dunn, *J. Phys. Chem. C* **2007**, *2*, 14925.

[16] G. A. Muller, J. B. Cook, H.-S. Kim, S. H. Tolbert, B. Dunn, *Nano Lett.* **2015**, *15*, 1911.

[17] B. K. Lesel, J. S. Ko, B. Dunn, S. H. Tolbert, *ACS Nano* **2016**, *10*, 7572.

[18] B. K. Lesel, J. B. Cook, Y. Yan, T. C. Lin, S. H. Tolbert, *ACS Energy Lett.* **2017**, *2*, 2293.

[19] N. Balke, S. Jesse, A. N. Morozovska, E. Eliseev, D. W. Chung, Y. Kim, L. Adamczyk, R. E. Garcia, N. Dudney, S. V. Kalinin, *Nat. Nanotechnol.* **2010**, *5*, 749.

[20] X. Zhang, M. V. Hulzen, D. P. Singh, A. Brownrigg, J. P. Wright, N. H. V. Dijk, M. Wagemaker, *Nano Lett.* **2014**, *14*, 2279.

[21] T. Brezesinski, J. Wang, S. H. Tolbert, B. Dunn, *Nat. Mater.* **2010**, *9*, 146.

[22] M. Acerce, D. Voiry, M. Chhowalla, *Nat. Nanotechnol.* **2015**, 10, 313.

[23] T. Stephenson, Z. Li, B. Olsen, D. Mitlin, *Energy Environ. Sci.* **2014**, *7*, 209.

[24] M. Pandey, P. Bothra, S. K. Pati, *J. Phys. Chem. C* **2016**, *120*, 3776.

[25] R. Zhang, I. Tsai, J. Chapman, E. Khestanova, J. Waters, I. V. Grigorieva, *Nano Lett.* **2016**, *16*, 629.

[26] Q. Huang, X. Li, M. Sun, L. Zhang, C. Song, L. Zhu, P. Chen, Z. Xu, W. Wang, X. Bai, *Adv. Mater. Interfaces* **2017**, *4*, 1700171.

[27] J. B. Cook, H.-S. Kim, T. C. Lin, C.-H. Lai, B. Dunn, S. H. Tolbert, *Adv. Energy Mater.* **2016**, *1601283*.

[28] J. N. Reimers, J. R. Dahn, *J. Electrochem. Soc.* **1992**, *139*, 2091.

[29] S. Mukerjee, R. Thurston, N. M. Jisrawi, X. Yang, J. Mcbreen, *J. Electrochem. Soc.* **1998**, *145*, 466.

[30] W. Li, J. N. Reimers, J. R. Dahn, *Solid State Ionics* **1993**, *67*, 123.

[31] H. Yoo, A. P. Tiwari, J. Lee, D. Kim, J. H. Park, H. Lee, *Nanoscale* **2015**, *7*, 3404.

[32] Y. Teng, H. Zhao, Z. Zhang, Z. Li, Q. Xia, Y. Zhang, L. Zhao, X. Du, Z. Du, P. Lv, K. Swierczek, *ACS Nano* **2016,** *10*, 8526.

[33] H. Hwang, H. Kim, J. Cho, *Nano Lett.* **2011**, *11*, 4826.

[34] Z. Deng, H. Jiang, Y. Hu, Y. Liu, L. Zhang, H. Liu, C. Li, *Adv. Mater.* **2017**, *29*, 1603020.

[35] Y. Jiao, A. Mukhopadhyay, Y. Ma, L. Yang, A. M. Hafez, H. Zhu, *Adv. Energy Mater.* **2018**, 1702779.

[36] Q. Wei, M.-R. Gao, Y. Li, D. Zhang, S. Wu, Z. Chen, Y. Sun, *Mater. Chem. Front.* **2018**, Advance Article.

[37] F. C. Laman, K. Brandt, *J. Power Sources* **1998**, *24*, 195.

[38] X. Fang, C. Hua, X. Guo, Y. Hu, Z. Wang, X. Gao, F. Wu, J. Wang, L. Chen, *Electrochim. Acta* **2012**, *81*, 155.

[39] H. Wang, Z. Lu, S. Xu, D. Kong, J. J. Cha, G. Zheng, P. Hsu, K. Yan, *Proc. Natl. Acad. Sci. U.S.A* **2013**, *110*, 19701.

[40] X. Wang, X. Shen, Z. Wang, R. Yu, L. Chen, *ACS Nano* **2014**, 8, 11394.

[41] L. Wang, Z. Xu, W. Wang, X. Bai, *J. Am. Chem. Soc.* **2014**, *136*, 6693.

[42] Y. Lin, D. O. Dumcenco, Y. Huang, K. Suenaga, *Nat. Nanotechnol.* **2014**, *9*, 391.

[43] A. Py, R. R. Haering, *Can. J. Phys.* **1982**, *61*, 76-84.

[44] N. Imanishi, M. Toyoda, Y. Takeda, O. Yamamoto, *Solid State Ionics.* **1992**, *58*, 333.

[45] D. Voiry, A. Mohite, M. Chhowalla, *Chem. Soc. Rev.* **2015**, *44*, 2702.

[46] F. Xiong, H. Wang, X. Liu, J. Sun, M. Brongersma, E. Pop, Y. Cui, *Nano Lett.* **2015**, *15*, 6777.

[47] F. Wypych, R. Schollhorn, *J. Chem. Soc., Chem. Commun.* **1992**, *0*, 1386.

[48] P. J. Mulhern, *Can. J. Phys.* **1989**, *67*, 1049.

[49] P. Gao, L. Wang, Y. Zhang, Y. Huang, K. Liu, *ACS Nano* **2015**, *9*, 11296.

[50] Y. Guo, D. Sun, B. Ouyang, A. Raja, J. Song, T. F. Heinz, L. E. Brus, *Nano Lett.* **2015***, 15*, 5081.

[51] S. H. Tolbert, A. P. Alivisatos, *J. Chem. Phys.* **2014**, *102*, 4642.

[52] S. H. Tolbert, A. P. Alivisatos, *Science* **1994**, *265*, 373.

[53] A. Van Der Ven, M. Wagemaker, *Electrochem. Commun.* **2009**, *11*, 881.

[54] H. Li, Y. Zhu, S. Dong, L. Shen, Z. Chen, X. Zhang, G. Yu, *Chem. Mater.* **2016**, *28*, 5753.

[55] I. E. Rauda, V. Augustyn, L. C. Saldarriaga-lopez, X. Chen, L. T. Schelhas, G. W. Rubloff, B. Dunn, S. H. Tolbert, *Funct. Mater.* **2014**, *24*, 6717.

[56] X. Xiao, Z. Peng, C. Chen, C. Zhang, M. Beidaghi, Z. Yang, N. Wu, Y. Huang, L. Miao, Y. Gogotsi, J. Zhou, *Nano Energy* **2014**, *9*, 355.

[57] R. A. Huggins, *Solid State Ionics* **2000**, *134*, 179.

[58] A. H. Reshak, S. Auluck, *Phys. Rev. B* **2003**, *68*, 125101.

[59] L. E. Brus, J. A. W. Harkless, F. H. Stillinger, *J. Am. Chem. Soc.* **1996**, *118*, 4834.

[60] B. M. Wagemaker, F. M. Mulder, A. Van Der. Ven, *Adv. Mater.* **2009**, *21*, 2703.

[61] P. Simon, Y. Gogotsi, B. Dunn, *Science* **2014**, *343*, 1210.

Chapter 4. Crossover from Slow Sodium-Ion Storage in MoS_2 to Ultrafast Intercalation Pseudocapacitance in MoS_2 Nanoparticles by Phase Transition Suppression

4.1. Introduction

Pseudocapacitance is a form of electrochemical energy storage that combines the high energy density characteristics of batteries and the high rates associated with capacitors. Similar to capacitance, pseudocapacitance (C) can be understood according to Equation 1, in which a potential change (ΔE) scales linearly with the charge (q) withdrawn or added to the electrochemical system. The charge-discharge processes in a pseudocapacitor are Faradaic, hence high energy densities, while the kinetic response resembles the high power densities of a capacitor.[1,2]

qCE ***Equation 4.1***

Three Faradaic processes that result in pseudocapacitive electrochemical features are: (1) adsorption pseudocapacitance, e.g. faradaic deposition and desorption of H^+ on metal surfaces, (2) redox pseudocapacitance, e.g. near surface reactions in hydrous RuO_2,[3] and (3) intercalation pseudocapacitance.[4–9] The kinetics of adsorption and redox pseudocapacitance are intrinsically fast because the charge storage takes place on the surface and is not impeded by solid state diffusion. Intercalation pseudocapacitance maintains the high rates associated with those surface processes even though the charge storage occurs in the bulk of a nanostructured material.

Typically, intercalation of ions in most solid-state energy storage materials are accompanied by distinct phase transitions that occur between the intercalated and non-intercalated states. [10–18] Phase transitions can dominate the kinetics of the intercalation reactions even in systems with short solid-state diffusion lengths. Materials that store charge primarily through intercalation pseudocapacitance, however, do not undergo a first order phase transition. One method to suppress these first-order

phase transitions is to reduce the size of the primary particles, as has been shown in TiS_2,[4] MoS_2,[9,19] MoO_2,[6] and $LiFePO_4$.[20]

Although Li^+ systems (namely Nb_2O_5 and MoO_3) have demonstrated high levels of intercalation pseudocapacitance,[21–24] pseudocapacitive materials with such rate have yet to be explored for Na^+. The difference in performance between Li^+ and Na^+ systems are due to the different properties of the two ions. The size and molar mass of Na^+ are larger than Li^+, which leads to slower diffusion kinetics and shorter cycle lifetimes in most lattice hosts.[25,26]

MoS_2 is especially amenable to fast Na^+ intercalation reactions because it can accommodate bigger ions with its larger interatomic spacing. These large van der Waals (vdW) gaps are 6.2 Å in large crystals, and are expanded up to 6.9 Å in small nanocrystals.[27,28] Another advantage of MoS_2 is that certain allotropes are highly conductive. As shown in Figure 4.1(a), MoS_2 exists as two predominate polytypes, the semiconducting 2H-phase, and the metastable metallic 1T-phase.[2] The 2H- and 1T-phase are both layered structures that consist of S – Mo – S 'sandwich' building blocks. The 2H-MoS_2 phase can be converted to the metastable 1T-phase when alkali-ions, such as Li^+ and Na^+, intercalate between the layers due to the limited miscibility. [31–33] This phase conversion from 2H to 1T consists of a glide-plane mechanism of the sulfur layers, which changes the molybdenum coordination from hexagonal to trigonal prismatic while preserving the layered vdW gaps for fast Na^+ migration. [31] This phase change is also accompanied by a modification of the electronic structure, which leads to high electronic conductivity.[7] With these properties, MoS_2 is an ideal material for fast charge storage. We have previously shown that Na^+ undergo extremely fast intercalation in MoS_2 thin film. [7,9]

Most of the work on the charge storage properties of MoS_2 is focused on the four-electron conversion reaction for its high capacity (637 mAh/g). The conversion occurs when >1.5 moles of Na^+ are inserted in the MoS_2 structure, leading to an irreversible decomposition of the MoS_2 structure to Mo and Na_2S.[34] While this reaction offers higher energy storage, the cycle lifetimes are short, and

the kinetics are slow.[35,36] In contrary, when the Na^+ concentration in MoS_2 is limited to ~ 1 mole, the MoS_2 structure does not decompose.[34] The reversibility of this intercalation reaction is better, and the kinetics are faster.[19] In this paper, we investigate the pseudocapacitive Na^+ storage in MoS_2 nanoparticles that were prepared by a two-step synthesis in 10-15 μm thick electrodes (≈1 $mg.cm^{-2}$). A series of kinetic analyses have been carried out to quantify the dominant charge storage processes in order to elucidate the charge storage mechanism. The electrochemical determination of the charge storage mechanism is further supported by *operando* structural characterization using synchrotron based X-ray diffraction. Based on the idea that suppression of phase transition is required for intercalation pseudocapacitance, we have investigated markedly different storage properties of bulk and nanostructured MoS_2 with Na^+.

4.2. Result and Discussion

4.2.1. Electrochemistry

The synthesis and characterization of these MoS_2 nanoparticles can be found in our previous study on the Li^+ intercalation pseudocapacitance of MoS_2 nanoparticles.[9] These 10 – 40 nm MoS_2 nanoparticles have a surface area of 35 $m^2.g^{-1}$ and their X-ray diffraction pattern well matches the hexagonal 2H-MoS_2 phase. Furthermore, the vdW gaps are expanded to 0.63 nm from the bulk value of 0.62 nm. An extremely important material property of MoS_2 that we leverage in this study is the high conductivity in the 1T-MoS_2 phase.[30,32,37–39] We converted the MoS_2 nanoparticles from the 2H- to the 1T-phase via alkaline-ion intercalation. The electrodes were cycled at 1C ten times between 0.55 V – 2.50 V *vs.* Na/Na^+. The voltage was limited to above 0.55 V in order to prevent the conversion reaction, which would disrupt the metallic conductivity and layered crystal structure of the 1T-phase. Figure. 4.1(b) shows the galvanostatic trace of the 1st and 10th formation cycle. The plateau ca. 1 V *vs.* Na/Na^+ is indicative of the 2H- to 1T-phase conversion, which is later replaced by the galvanostatic

signatures of Na^+ insertion into 1T-MoS_2 after 10 cycles.[7] In order to confirm the increased conductivity after the 2H to 1T conversion, impedance spectroscopy was carried out on these half

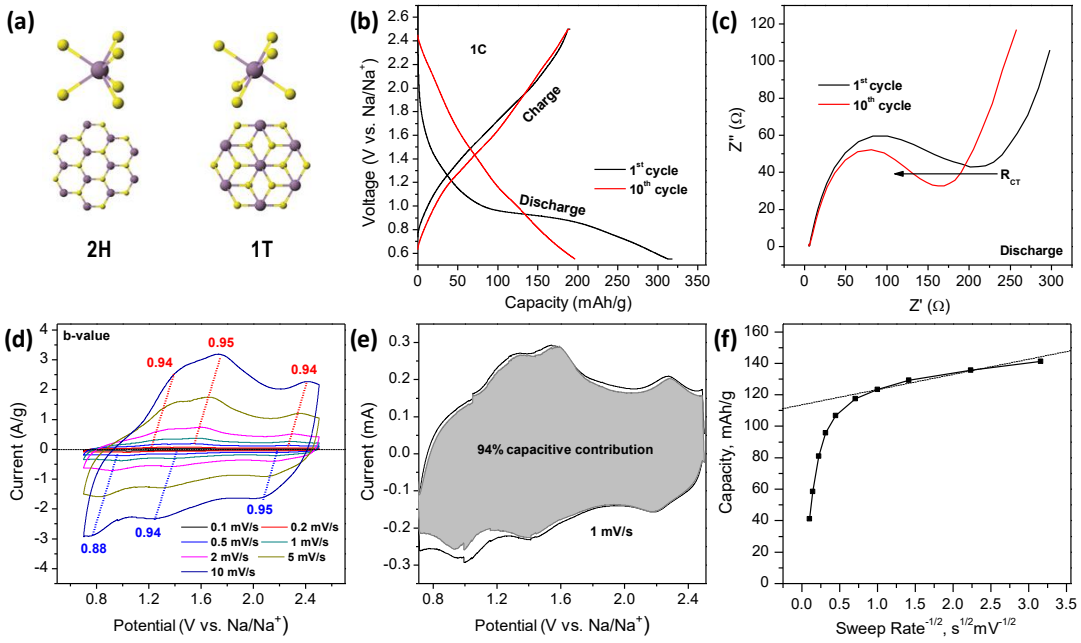

Figure 4.1. (a) 2H-MoS_2 semiconducting hexagonal geometry and the metallic 1T trigonal prismatic. (b) Galvanostatic charge-discharge curve of MoS_2 nanoparticles when converting from the 2H to 1T-phase. Voltage plateau at 1 V vs. Na/Na^+ is indicative of the 2H-to-1T phase transition is replaced by the galvanostatic trace for the insertion of Na^+ into 1T-MoS_2 after 10 cycles.(c) Nyquist plot of the 2H-to-1T phase transition confirms the decrease in charge-transfer resistance due to metallic conductivity. (d) b-value analysis done at 0.1 -10 mV/s indicates capacitive charge-storage mechanism for each pair of redox peaks is closed to 1. (e) k_1k_2 kinetic analysis shows the current response from capacitive processes. The shaded region shows 94% occupation to the overall current response of MoS_2 nanoparticles cycled at 1 $mV{\cdot}s^{-1}$. (f) Capacity versus $\upsilon^{-1/2}$ shows the separation in the capacity due to diffusion-controlled and capacitive processes cycled from 0.1 to 100 $mV{\cdot}s^{-1}$. The dashed diagonal line is extrapolated to identify the infinite sweep rate capacity.

cells. A 23% decrease in charge transfer resistance from (211 to 177 Ω) is indeed observed between the 1st and 10th formation cycles (Figure. 4.1(b)).

After the formation of the 1T-phase through electrochemical precycling, cyclic voltammetry (CV) was performed to study the electrochemical kinetics of MoS_2 nanoparticles. Since the charge storage response times are different for a battery, electrical double layer capacitor (EDLC), and pseudocapacitor, the storage mechanism can be distinguished and quantified using electrochemical kinetic analyses. These analyses utilize the dependency of the current response on the potential sweep rate in a cyclic voltammetric experiment. [1,2] Batteries predominately exhibit slow kinetics due to slow ion-diffusion and phase transition, resulting in a voltage separation between cathodic (Vp,c) and anodic (Vp,a) peaks ($\Delta V = Vp,a - Vp,c > 60$ mV). [1,40] An EDLC, on the other hand, exhibits a box-shaped CV curve.[1] This electrochemical signature indicates a fast capacitive electrochemical process where the charge exchanged between the material and the electrolyte is independent of the voltage. For capacitive processes, the current (i) depends linearly on the scan rate (v) in a cyclic voltammetry experiment

$$i = Cv \qquad \textbf{Equation 4.2}$$

where C is the capacitance and is independent of υ. Pseudocapacitance is a mixture between a battery and an EDLC, which exhibits a capacitive box-shaped CV curve with superimposed broad redox peaks.[2,5] A characteristic signature of a pseudocapacitor is the small peak voltage separation of approximately 60 mV.[40] A classic material that exhibits this type of behavior is hydrous RuO_2, which displays fast Faradaic charge storage.[41]

Charge storage from the Na^+ intercalation between the vdW gaps of MoS_2 nanoparticle is expressed by the following electrochemical reaction:

$$MoS_2 + xNa^+ + xe^- \leftrightarrow Na_xMoS_2 \qquad \textbf{Equation 4.3}$$

where the theoretical capacity is 167 $mAh.g^{-1}$ ($x = 1$). The cyclic voltammograms (Figure. 4.1(d)) from 0.1 to 10 $mV.s^{-1}$ show a capacitive box-like curve with broad redox peaks. This electrochemical signature is similar to hydrous RuO_2,[41] which is typical of a charge-storage mechanism not limited by solid-state diffusion.

The fundamental charge-storage mechanism of MoS_2 nanoparticles can be determined by studying the dependency of the current response on the sweep rate using *b*-value analysis. Assuming that the current and the sweep rate in a CV experiment obeys the power-law relationship:

$$i = av^b \qquad \textbf{Equation 4.4}$$

where *a* and *b* are adjustable parameters.[42] For processes limited by semi-infinite linear diffusion, the *b*-value is 0.5. On the other hand, for a capacitive process the *b*-value is 1. The *b*-value can be obtained by calculating the slope of the line in a plot of log(*i*) *vs.* log(*v*). These *b*-values are specified on the CV plots over their corresponding peaks, and are all between 0.88 – 0.95 (Figure. 4.1(d)), indicating that the charge storage of Na^+ in MoS_2 nanoparticles are predominantly capacitive.

Another related analysis used to quantify the capacitive contribution over the entire voltage range of MoS_2 nanoparticles is the k_1k_2 analysis:[43]

$$i(V) = k_2v + k_1v^{1/2} \qquad \textbf{Equation 4.5}$$

At a given voltage (V), electrochemical redox reactions limited by semi-infinite linear diffusion have a corresponding current response varying with $v^{1/2}$ and for capacitive processes, the current varies linearly with v. Solving for the values of k_1 and k_2 at a given potential provides a quantitative distinction between diffusion and capacitive currents. Furthermore, the total capacitive contribution to the charge storage can be calculated by summing the fractional contributions over the entire voltage window. The CV in Figure. 4.1(e) shows that over 90% of the stored energy in MoS_2 nanoparticles is capacitive. This is a clear demonstration of the none diffusion limited nature of Na^+ intercalation into the vdW gap even though they are reminiscent of a battery-type intercalation reaction.

To further support the capacitive storage mechanism of the MoS_2 nanoparticles, the Trasatti analysis was used to quantify the kinetic properties by studying the relationship between capacity and sweep rate.[44,45] In Figure. 4.1(f), a plot of q (capacity in mAh.g^{-1}) versus $v^{-1/2}$ shows that the capacity contribution is nearly independent of the sweep rate when cycled from 0.1 to 10 mV.s^{-1}. However, the linear regions at faster rates, represent diffusion-controlled limitations. At sweep rates below 10 mV.s^{-1}, the infinite sweep rate capacity was determined by extrapolating the y-intercept. Within the range of sweep rates between 1 and 10 mV.s^{-1}, the infinite sweep rate capacitance is measured to be 115 mAh.g^{-1} and this capacity represents the available capacity attainable without solid-state diffusion limitations. At a sweep rate of 1 mV.s^{-1}, MoS_2 nanoparticles stores 124 mAh.g^{-1} (90% capacitive contribution), which is in excellent agreement with the k_1k_2 analysis. The question we will address next is the origins of the storage process that enables this cross-over from diffusion limited intercalation reactions, to the capacitive controlled intercalation reactions we have just described.

4.2.2. *Operando* X-ray Diffraction

In order to understand the pseudocapacitive electrochemical response in MoS_2 nanoparticles from a structural perspective, we utilized synchrotron based X-ray diffraction to follow the changes in the crystal structure during cycling. Since structural work on the 2H to 1T-phase transition through Li^+ and Na^+ insertion is vast,[30,32,37–39] we will only focus on the structural characterization after the 2H to 1T-phase transition has occurred completely. The first XRD pattern of bulk MoS_2 (micronsize slabs) shown in the stack plots (Figure 4.2(a)) correspond to a cell at OCV after being cycled four times between 0.55 V – 2.50 V *vs.* Na/Na^+. Three phases can be clearly identified in this first pattern: predominately 1T-Na_xMoS_2 ($0 \leq x \leq 1.0$),[34] a small amount of 2H-MoS_2, and a trace of triclinic Na_xMoS_2 ($0 \leq x \leq 1.0$). The presence of triclinic $NaMoS_2$ in our diffraction patterns indicates that some Na^+ are remained in the structure from previous cycling. In support of this observation, the

(001) lattice spacing observed in our first pattern (d = 7.09 Å) is larger than what has been observed, representing the residual Na^+ content.[34,46] The presence of the 2H-phase is related to the back conversion of the metastable 1T-phase to the thermodynamically stable 2H-phase,[47] which most likely occurred during the transportation of these samples.

As Na^+ is inserted into the structure of bulk MoS_2, a first-order phase change from the 1T phase to the triclinic phase of $NaMoS_2$ is observed. The (001) peak is indistinguishable in the 1T and the triclinic phase, so they cannot be used to differentiate each other. However, the increasing intensity of the triclinic peak at 1.1 $Å^{-1}$ seen in Fig. 4.2(a) during Na^+ insertion is a clear indication of the 1T to triclinic phase transition. Notably, this peak at 1.1 $Å^{-1}$ is not present in the 2H or 1T-phase, but only in the triclinic phase. Peak splitting is also observed (ca. 1 V) between 2-2.5 $Å^{-1}$, which is another clear signature of a first order-phase transition. This type of behavior is consistent with reports on the phase behavior of the closely related Li^+ system, showing that the insertion of lithium-ions (x) between $0 \leq x \leq 1.0$ in bulk MoS_2 induces several first-order phase transition47. After 0.4 mol of Na+ is intercalated into bulk MoS_2, the (001) lattice spacing increases from 0.89 $Å^{-1}$ (d = 7.07 Å) to 0.88 $Å^{-1}$ (d = 7.12 Å) (Figure 4.2(c)). Further insertion then drives a contraction of the lattice to 0.94 $Å^{-1}$ (d = 6.95 Å) due to cationic interactions.[46] During the deinsertion process, the (001) lattice increases to a maximum followed by a contraction of the lattice nearly to the original position. The hysteretic behavior of the lattice expansion suggests that bulk MoS_2 experiences a significant kinetic limitation, such as a phase transition, during the deinsertion of Na^+ (Figure 4.2(c)).

In stark contrast to the phase transitions observed during charge and discharge of the bulk MoS_2, MoS_2 nanoparticles do not undergo a phase change. Similar to the bulk stack XRD patterns described above, the first XRD pattern of nano MoS_2 in the stack plots shown in Figure 4.2(b) corresponds to the cell at OCV after being cycled five times between 0.55 V – 2.50 V *vs.* Na/Na^+. Only the 1T-phase can be identified in the first XRD pattern. Insertion of Na^+ does not drive a phase

transition as was seen in bulk MoS_2, instead the near linear expansion and contraction of the (001) MoS_2 lattice planes suggests that a solid-solution of Na^+ in MoS_2 is formed instead. The absence of the characteristic triclinic peak at 1.1 $Å^{-1}$ provides convincing evidence that the 1T to triclinic phase transition is suppressed in the nanostructured form. Furthermore, no peak splitting is observed in the 2-2.5 $Å^{-1}$ region of the stack plot (Figure 4.2(b)), providing more evidence that the phase transformation is suppressed.

The modification of phase transition onsets has been clearly established by Tolbert and Alivisatos in their work on the influence of nanocrystal size on the high pressure phase transition in CdSe.[48] In our work, we speculate that the interfacial energy penalty for two phase coexistence (triclinic phase and the 1T-phase) is too high in the confined space of the nanocrystal. However, it is interesting to note that even though the 1st order phase transition described above is suppressed, the 2H to 1T phase transition was not suppressed in this system, nor in our previous work on thin films with even smaller structure sizes.[19] While it is clear that more work is needed to understand the underlying mechanism for this suppression, the rich governing physics makes this an interesting fundamental question with real world applicability.

In contrast to bulk MoS2, the vdW gaps of MoS_2 nanoparticles increase linearly during insertion up to about 0.4 moles, followed by a lattice contraction as a result of cationic interaction (Fig. 4.2(d)). The near linear change in the (001) lattice spacing during the insertion process clearly distinguishes the charge storage mechanism in MoS_2 nanoparticles to be the solid solution type. The hysteresis in lattice expansion is also not observed in the MoS_2 nanocrystals, indicating that the phase transformation has been suppressed. Finally, the XRD peaks return to their original position after deinsertion, which shows that the insertion and deinsertion process is structurally reversible.

Our *operando* study demonstrates that the trigonal to triclinic phase transition is suppressed in nanostructured MoS_2, and that Na^+ is incorporated as a solid solution. Even if the solid-state diffusion

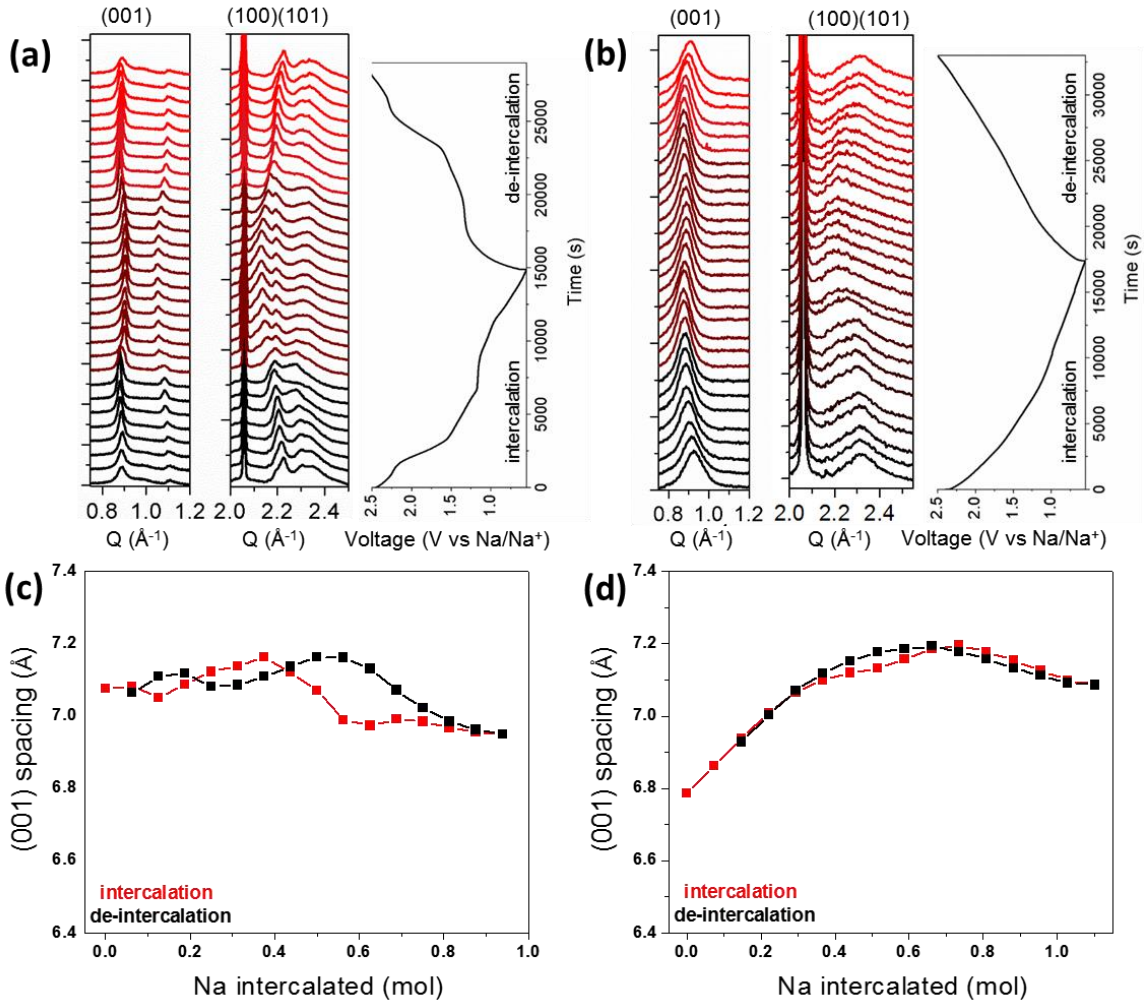

Figure 4.2. X-ray diffraction patterns collected during the intercalation and de-intercalation processes of a pre-cycled Na half-cell containing (a) bulk MoS_2, (b) nano MoS_2 as positive electrode (with charging/discharging rate of C/4.5). The sharp peak at 2.08 $Å^{-1}$ is attributed to Na counter electrode in the cell. Change in d-spacing of (c) bulk MoS_2 and (d) nano MoS_2 during the sodiation process.

lengths are short enough to afford fast kinetics in a nanostructured material, if it undergoes a phase transition, the rate limiting step may become the phase conversion – regardless of the size. We believe that the fast kinetics is resulted from the phase transition suppression, and not simply the reduced ion

migration path lengths. In Figure 4.2(b), the lattice of nanostructured MoS_2 clearly expands and contracts during charge and discharge. This further demonstrates that the majority of the stored charge originates from intercalation of Na^+ into the bulk of the MoS_2 nanocrystals and not just the surface of the nanocrystal. Another benefit of this modified charge storage mechanism is the structural reversibility, which leads to increased cycle lifetimes as will be described in the next section. By combining the detailed electrochemical kinetic analyses and this structural understanding of the charge storage process, we can provide compelling data of Na^+ intercalation pseudocapacitance in MoS_2 nanoparticles. This characterization distinguishes this system as a clearly identifiable capacitive system, and not simply a nanostructured battery material. While this latter statement may seem to be parsing nomenclature, it is important to distinguish the two different charge storage mechanisms as unique as they both undergo Faradaic processes that are typically confused with each other.

4.2.3. Superior Electrochemical Properties

MoS2 nanoparticle based electrodes were cycled galvanostatically between 1C to 100C to demonstrate their practicality as Na^+ pseudocapacitors. The sloping voltage profiles of MoS_2 nanoparticles shown in Figure 4.3(a), at all measured C-rates,[49] has an electrochemical signature of solid-solution behavior. Charge storage without phase transitions are linear galvanostatic traces, which are observed for the nanostructured MoS_2; in stark contrast to the stepped-plateau galvanostatic traces observed for the micron-sized samples. With their pseudocapacitive bahavior, the MoS_2 nanoparticles exhibit fast rate performance, delivering about 150 $mAh.g^{-1}$ at a rate of 5C. Our nanostructured MoS_2 preforms similarly or slightly better than other nanostructured MoS_2 materials (Table 4.1).[46,50] For example, Wu *et al.* showed that closed shell, fullerene-type MoS_2 nanocrystals deliver 115 $mAh.g^{-1}$ at 5C, and 60 $mAh.g^{-1}$ at 20C.[46] In another study, Bang *et al.* reported on exfoliated MoS_2 nanosheets that delivered 120 $mAh.g^{-1}$ at 800 $mA.g^{-1}$ (≈5C).[50] While these rates are still more typical of battery-

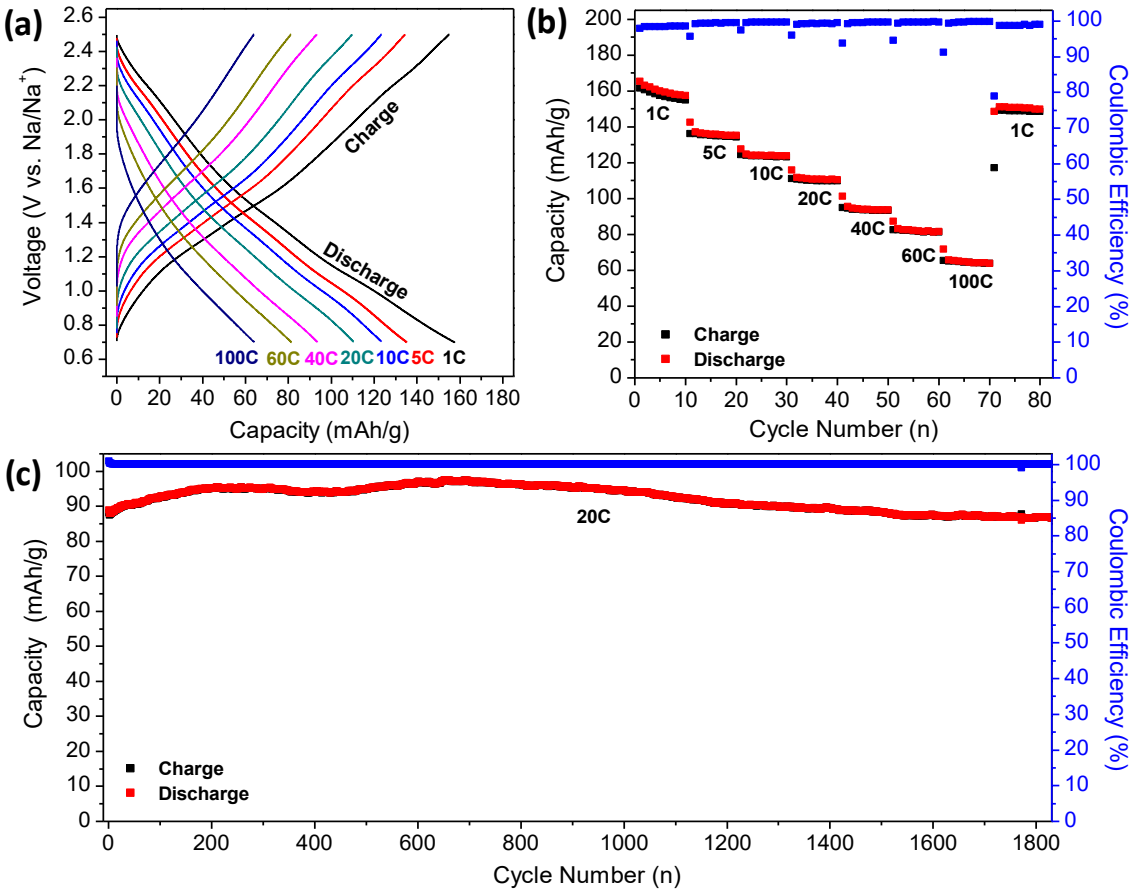

Figure 4.3. (a) Galvanostatic cycling of MoS_2 at various c-rates (1C, 5C, 10C, 20C, 40C, 60C, 100C) (b) Galvanostatic cycling performance of MoS_2 showing attainable capacity as a function of cycle number at various rates. Corresponding coulombic efficiencies are well above 99%. (c) Long-term cycling performance of MoS_2 cycled at 20C showing minimal capacity fade (97% capacity retention) up to 1800 cycles.

type reactions, these studies reported here demonstrate that MoS_2 is an example of a material that stores charge by intercalation pseudocapacitance. At rates > 20C, our material outperforms the fullerene-type MoS_2 by nearly two-fold. At a much faster rate of 100C (charging time of only 36 seconds), a capacity of 65 $mAh.g^{-1}$ is still achieved, making MoS_2 nanoparticles the first Na^+ conducting material to exhibit intercalation pseudocapacitance. Materials that do not undergo a phase transition

upon intercalation also tend to exhibit long lifetimes, and MoS_2 nanocrystals are no exception. Very little degradation to the delivered capacity (retention of 97%) is observed even after 1800 cycles at 20C (Figure 4.3(c)). In comparison to other reports, this nanostructured MoS_2 demonstrates up to sixty-fold greater cycle lifetimes (Table 4.1). It is clear that suppressing intercalation-induced phase transitions leads to new and useful properties in MoS_2, which are not observed in the corresponding bulk material.

Material type	Slow rate C-rate, mAh/g	Fast rate C-rate, mAh/g	Ultra fast rate C-rate, mAh/g	Capacity retention cycles, % retention	Ref.
MoS_2 nanoparticles	5, 135	20, 111	100, 65	1800, 97	this work
Fullerene type MoS_2	5, 115*	20, 60*	n/a	30, 47	[46]
Exfoliated MoS_2	5, 120*	Not reported	n/a	100, ~95*	[50]

Table 4.1. Gravimetric capacity of nanostructured MoS_2 based on sodium-ion half-cells. *Capacity estimated from plot.

4.3. Conclusion

We have demonstrated that the energy storage mechanism associated with Na^+ intercalation in MoS_2 is from intercalation pseudocapacitance. While most reports on MoS_2 largely focus on the high capacity conversion reaction at low potentials, this study demonstrates several attractive properties of the intercalation reaction. The quantitative electrochemical kinetic analysis shows that over 90% of the storage in this system is capacitor-like. As a result, this material system can be charged

to nearly 50% of its 1C capacity in just under 40 seconds. These fast rates overlap with the performance characteristics of EDLC, while delivering much higher capacities as a result of the Faradaic based charge storage. We have performed synchrotron based *operando* XRD on this system to elucidate the structural origins of the fast pseudocapacitive charge storage. We confirmed that micron-sized MoS_2 undergoes a trigonal to triclinic first-order phase transition during the charge storage process. This phase transition is suppressed in nanostructured MoS_2 and enables charge storage to occur with capacitor-like kinetics. We believe that the Na^+ can migrate very rapidly through the vdW gap when they are not impeded by a slow phase transition. In addition, the nanostructured MoS_2 shows almost no capacity decay even after being cycled 1800 times. These results demonstrate the prospect of using chalcogenide based materials as high performance Na^+ hosts. More importantly, these results provide a clear basis for establishing the intercalation pseudocapacitance charge storage mechanism and distinguishing it from materials which possess battery-like kinetics.

4.4. Experimental

4.4.1. Synthesis

All starting materials were obtained from commercial suppliers and used without further purification. The synthesis of MoO_2 nanocrystals has been reported elsewhere,[51] and is briefly described here. MoO_2 nanocrystals were prepared solvothermally by dissolving anhydrous $MoCl_5$ (Strem Chemicals) in a mixture of ethanol and deionized water at a reaction temperature of 180°C for 6 hrs. The MoO_2 nanocrystals were converted to MoS_2 with H_2S gas. The reaction was carried out in a tube furnace at 600°C under flowing H_2S/H_2 (H_2S 5 mol % : H_2 95 mol %, Air Gas) for 10 hours. A graphite boat was used to typically convert ~ 100 - 200 mg of MoO_2 to MoS_2.

4.4.2. Characterization

Powder X-ray diffraction (XRD) was performed in a PANalytical X'Pert Pro operating with Cu Kα (λ = 1.5418 Å) using a 0.03° step size, a voltage of 45kV, and a current of 40mA. XRD patterns were recorded in the range of $10° < 2\theta < 80°$. Transmission electron microscopy (TEM) was performed using a FEI Technai T12 operating at 120 kV. Nitrogen porosimetry was carried out using a Micromeritics TriStar II 3020. The surface area was calculated from the adsorption branch of the isotherm between (0.04 – 0.30 P/Po) using the Brunauer-Emmett-Teller (BET) model. The pore diameter and pore volume was also calculated from the adsorption branch of the isotherm using the Barret-Joyner-Halenda (BJH) model.

4.4.3. Electrode Formulation

The carbon fiber based electrodes were made from a slurry consisting of 70 wt.% nc-MoS_2 or b-MoS_2 (Alfa Asear) powder used as active component for Li storage, 10 wt.% vapor grown carbon fibers (Sigma Aldrich), and 10 wt.% carbon black (Alfa Asear) used as conductive additive, and 10 wt.% polyacrylic acid solution in ethanol (Mw=250K, Sigma Aldrich) used as binder. The four components were sonicated for 30 minutes to obtain a homogeneous dispersion. Ethanol evaporation over one hour resulted in a homogeneous thick paste that was cast onto 25 μm carbon coated Al foil (gift from Coveris). The slurry was dried at ambient temperature for 1 h, and further dried at 25°C under vacuum overnight to evaporate the excess solvent. The mass loading of the electrode was ~1 mg cm^{-2} of active material.

4.4.4. Electrochemical Measurements

Electrochemical measurements of the MoS2 electrodes were carried out in a 2-electrode SwageLok configuration using a Bio-Logic VMP3 potentiostat. Electrochemical SwageLok cells were all assembled in an argon-filled glovebox with oxygen and moisture levels of <1 ppm. Sodium metal

foils served as the auxiliary electrode and the electrolyte used was 1M $NaClO_4$ in propylene carbonate:fluoroethylene carbonate (PC:FEC; 95:5 v/v). Cut-off voltages for both chronopoteniometric and cyclic voltammetric experiments were between 0.7 and 2.5 V *vs.* Na/Na^+. Current rates were normalized by the theoretical capacity of MoS_2 (167 $mAh.g^{-1}$). Pre-cycling to convert MoS_2 from the 2H to 1T phase was carried out using both chronopotentiometric and cyclic voltammetric experiments cycled between 0.55 and 2.5 V *vs.* Na/Na^+. AC Impedance was taken after every pre-cycle with an AC amplitude of 10 mV scanned within a frequency range of 100 mHz to 900 kHz.

4.4.5. *Operando* Synchrotron based X-ray diffraction

Carbon based slurry electrodes were made for this *Operando* study. The slurry consists of 70 wt.% active material (bulk or nano MoS_2), 10 wt.% vapor grown carbon fibers (Sigma Aldrich), and 10 wt.% carbon black (Alfa Asaer) used as conductive, and 10 wt.% polyvinylidene fluoride in n-methyl-2-pyrrolidone used as binder. All four components were blended to obtain a homogeneous paste with honey like consistency. The paste was then cast onto 25 μm carbon coated Al foil. The slurry was dried in ambient temperature for a several hours and further dried at 125 °C under vacuum overnight to evaporate the excess NMP. The mass loading of the electrodes is approximately 3-5 mg/cm^2. These electrodes were cycled from 0.5 V-2.5 V as half cells in swagelok cells using sodium metal as counter electrode, glass fiber (Whatman) as separator, and 1M $NaClO_4$ in a 1:1 ethylene carbonate/ diethylene carbonate solvent (Sigma) as electrolyte. Nano MoS_2 was precycled on a VSP potentiostat/galvanostat (Bio-Logic) using 0.2C rate that corresponds to 138.6 mAh/g while bulk MoS_2 were cycled on Arbin using 0.2C rate that corresponds to 50 mAh/g. After precycling, these electrodes were taken out of the Swagelok cells in an Ar filled glovebox and were further reassembled into in-house built coin cell with 3mm holes and kapton tape window to allow transmission of the X-ray during the in situ study.

The coin cells were stored in an Ar atmosphere until cycling was performed to prevent exposure. Due to time constraint, in situ studies up at SSRL were done at 0.22C. *Operando* XRD was performed at beamline 11-3 at the Stanford Synchrotron Radiation Laboratory (SSRL) at 12735 eV. Patterns were collected with exposure times between 1-30 seconds. The diffraction intensity data is plotted as a function of the scattering vector length $Q = \frac{4\pi}{\lambda}\sin(\theta)$, where θ is half of the scattering angle, λ = is the wavelength of the incident radiation; the d-spacing thus is simply $\frac{2\pi}{Q}$. Standard 2032 coin cells were modified with a 3 mm diameter central hole, and used for the operando measurements. The MoS_2 electrodes were assembled into these coin cells using lithium metal as counter electrode, glass fiber (Whatman) as separator, 1M $NaClO_4$ in 1:1 ethylene carbonate/diethyl carbonate (Sigma Aldrich) with 5% (v/v) fluoroethylene carbonate (TCI America) as the electrolyte. To maintain pressure, the pouch cells were encased within an aluminum frame with a small 4 mm diameter hole to allow for transmission of the X-ray beam through the electrode. The cell was charged and then discharged 4-5 times to drive the 2H-1T phase transition at a current density of 0.2C. -The operando measurement was carried out at 0.2C using a VSP potentiostat/galvanostat (Bio-Logic USA). In order to aid in phase identification, XRD patterns of 2H-MoS_2, 1T-Na_xMoS_2, and triclinic Na_xMoS_2 were simulated using Mercury 3.5.

4.5. Reference

[1] B. E. Conway, *J. Electrochem. Soc.* **1991**, *138*, 1539.

[2] B. E. Conway, Kluwer Academic / Plenum Publishers, **1999**.

[3] D. Michell, D. A. J. Rand, R. A. Woods, *J. Electroanal. Chem.* **1978**, *89*, 11.

[4] G. A. Muller, J. B. Cook, H.-S. Kim, S. H. Tolbert, B. Dunn, *Nano Lett.* **2015**, *15*, 1911.

[5] B. E. Conway, V. Birss, J. Wojtowicz, *J. Power Sources* **1997**, *66*, 1.

[6] H.-S. Kim, J. B. Cook, S. H. Tolbert, B. Dunn, *J. Electrochem. Soc.* **2015**, *162*, A5083.

[7] J. B. Cook, H.-S. Kim, Y. Yan, J. S. Ko, S. Robbennolt, B. Dunn, S. H. Tolbert, *Adv. Energy Mater.* **2016**, *6*, 1501937.

[8] H.-S. Kim, J. B. Cook, H. Lin, J. S. Ko, S. H. Tolbert, V. Ozolins, B. Dunn, Nat. Mater. **2017**, *16*, 454.

[9] J. B. Cook, H.-S. Kim, T. C. Lin, C.-H. Lai, B. Dunn, S. H. Tolbert, *Adv. Energy Mater.* **2016,** 1601283.

[10] J. N. Reimers, J. R. Dahn, *J. Echem. Soc.* **1992**, *139*, 2.

[11] J. R. Dahn, W. R. Mckinnon, S. T. Coleman, *Phys. Rev. B* Condens Matter. **1985**, *31*, 484.

[12] J. R. Dahn, W. R. McKinnon, *J. Electrochem. Soc.* **1984**, *131***,** 1823.

[13] M. Fehse, L. Monconduit, F. Fischer, C. Tessier, L. Stievano, *Solid State Ionics* **2014**, *268*, 252.

[14] J. Wang, Y. K. Chen-Wiegart, J. Wang, *Nat. Commun.* **2014**, *5*, 1.

[15] H. He, C. Huang, C. W. Luo, J. J. Liu, Z. S. Chao, *Electrochim. Acta* **2013**, *92*, 148.

[16] J. R. Dahn, *Phys. Rev. B* **1991**, *44*, 9170.

[17] J. B. Leriche, S. Hamelet, J. Shu, M. Morcrette, C. Masquelier, G. Ouvrard, M. Zerrouki, P. Soudan, S. Belin, E. Elkaim, F. Baudelet, *J. Electrochem. Soc.* **2010**, *157*, A606.

[18] D. Li, H. Zhou, *Mater. Today* **2014**, *17*, 451.

[19] J. B. Cook, H.-S. Kim, T. C. Lin, C.-H. Lai, B. Dunn, S. H. Tolbert, *Adv. Energy Mater.* **2016,** 1601283.

[20] P. Gibot, M. Casas-Cabanas, L. Laffont, S. Levasseur, P. Carlach, S. Hamalet, J. M. Tarascon, C. Masquelier, *Nat. Mater.* **2008**, *7*, 741.

[21] V. Augustyn, J. Come, M. A. Lowe, J. W. Kim, P. Taberna, S. H. Tolbert, H. D. Abruña, P. Simon, B. Dunn, *Nat. Mater.* **2013**, *12*, 1.

[22] K. Brezesinski, J. Wang, J. Haetge, C. Reitz, S. O. Steinmueller, S. H. Tolbert, B. M. Smarsly, B. Dunn, T. Brezesinski, *J. Am. Chem. Soc.* **2010**, *132*, 6982.

[23] H.-S. Kim, J. B. Cook, S. H. Tolbert, B. Dunn, *J. Electrochem. Soc.* **2015**, *162*, A5083.

[24] Z. Chen, V. Augustyn, X. Jia, Q. Xiao, B. Dunn, Y. Lu, *ACS Nano* **2012**, *6*, 4319.

[25] S. P. Ong, V. L. Chevrier, G. Hautier, A. Jain, C. Moore, S. Kim, X. Ma, G. Ceder, *Energy Environ. Sci.* **2011**, *4*, 3680.

[26] P. Gao, L. Wang, Y. Zhang, Y. Huang, K. Liu, *ACS Nano* **2015**, *9*, 11296.

[27] Y. Liang, R. Feng, S. Yang, H. Ma, J. Liang, J. Chen, *Adv. Mater.* **2011**, *23*, 640.

[28] H. Hwang, H. Kim, J. Cho, *Nano Lett.* **2011**, *11*, 4826.

[29] E. Benavente, M. A. S. Ana, F. Mendizabal, G. Gonzalez, *Coord. Chem. Rev.* **2002**, *224*, 87.

[30] F. Wypych, R. Schollhorn, *J. Chem. Soc., Chem. Commun.* **1992**, *0*, 1386.

[31] M. A. Py, R. R. Haering, *Can. J. Phys.* **1983**, *61*, 76.

[32] X. Wang, X. Shen, Z. Wang, R. Yu, L. Chen, *ACS Nano* **2014**, *8*, 11394.

[33] M. S. Whittingham, Progress in Solid State Chemistry **1978**, *12*, 41.

[34] X. Wang, X. Shen, Z. Wang, R. Yu, L. Chen, *ACS Nano* **2014**, *8*, 11394.

[35] D. Su, S. Dou, G. Wang, *Adv. Energy Mater.* **2014**, *5*, 1.

[36] D. Lamuel, R. Bhandavat, G. Singh, *ACS Nano* **2014**, *8*, 1759.

[37] M. A. Py, R. R. Haering, *Can. J. Phys.* **1983**, *61*, 76.

[38] H. Wang, Z. Lu, D. Kong, J. J. Cha, G. Zheng, P. C. Hsu, K. Yan, D. Bradshaw, F. B. Prinz, Y. Cui, *Proc. Natl. Acad. Sci.* **2013**, *110*, 19701.

[39] F. Xiong, H. Wang, X. Liu, J. Sun, M. Brongerma, E. Pop, Y. Cui, *Nano Lett.* **2015**, *15*, 6777.

[40] P. T. Kissinger, W. R. Heineman, *J. Chem. Educ.* **1983**, *60*, 702.

[41] J. P. Zheng, *J. Electrochem. Soc.* **1995**, *142*, 2699.

[42] H. Lindström, S. Södergren, A. Solbrand, H. Rensmo, J. Hjelm, A. Hagfeldt, S.-E. Lindquist, *J. Phys. Chem. B* **1997**, *101*, 7717.

[43] T.-C. Liu, W. G. Pell, B. E. Conway, S. L. Roberson, *J. Electrochem. Soc.* **1998**, *145*, 1882.

[44] D. Baronetto, N. Krstajic, S. Trasatti Electrochimica Acta **1994**, *39*, 2359.

[45] S. Ardizzone, G. Fregonara, S. Trasatti, *Electrochim. Acta* **1990**, *35*, 263.

[46] S. H. Woo, L. Yadgarov, R. Rosentsveig, Y. Park, D. Song, R. Tenne, S. Y. Hong, *Isr. J.*

Chem. **2015**, *55*, 599.

[47] P. J. Mulhern, *Can. J. Phys.* **1989**, *67*, 1049.

[48] S. H. Tolbert, A. P. Alivisatos, *Science.* **1994**, *265*, 373.

[49] V. Augustyn, P. Simon, B. Dunn, *Energy Environ. Sci.* **2014**, *7*, 1597.

[50] G. S. Bang, K. W. Nam, J. Y. Kim, J. Shin, J. W. Choi, S.-Y. Choi, *ACS Appl. Mater. Interfaces* **2014**, *6*, 7084.

[51] H.-S. Kim, J. B. Cook, S. H. Tolbert, B. Dunn, *J. Electrochem. Soc.* **2015**, *162*, A5083.

Chapter 5. Suppression of Phase Transition in Nanostructured $LiMn_2O_4$ with Small Crystallite Sizes during Charge and Discharge

5.1. Introduction

Improvements in battery technology are essential to meet the demand for today's wide range of mobile electronics and electric vehicles. Improvements, particularly in charging speed and cyclability of Li-ion batteries, are paramount for broadened and sustained use. Many of the kinetic limitations in today's commercial batteries are due to long solid state Li-ion diffusion distances in micron sized electrode powders. Reducing these solid state Li-ion diffusion distances by fabricating smaller sized electrode powders can lead to improved kinetics.[1] When fast kinetics are observed in electrode materials, the term pseudocapacitance is used to describe the fast near surface redox reaction. When these near surface redox reaction extend into the bulk of a nanoscale material and can occur without a structural phase transition, the fast insertion (intercalation) and removal (deintercalation) of Li-ions within the material has been termed intercalation pseudocapacitance.[1-4] These fast kinetics arise when solid state diffusion lengths within the materials are sufficiently small, usually due to nanostructuring, compared to the Li^+ diffusion coefficient in the material. In addition to short solid state diffusion distances, the fast kinetics of intercalation pseudocapacitance are characterized by electrical interconnections between the active material grains and effective electrolyte penetration between the particles to reach an effective surface area. For materials that normally undergo phase transitions upon Li^+ cycling, suppression of those phase transitions in finite size is also needed.[5,6] Optimization of the first two parameters leads to porous nanostructures which have been studied and optimized for many materials. [4-17] When the crystallite size is sufficiently small, suppression of phase transition can also occur and has been demonstrated using *operando* X-ray diffraction for a number pseudocapacitive anode materials such as MoO_2, MoS_2 and TiS_2. [5-7] This phase suppression is

important since phase transitions play a major role in the sluggish kinetics of bulk Li-ion intercalation and deintercalation. These sluggish kinetics arise when new phases undergo nucleation and growth, a process that can becomes the rate limiting step in solid state lithium ion diffusion. Additionally, phase transitions cause slight structural deterioration with each cycle, which can contribute to capacity fade over many cycles.[18-20] The mechanism of capacity reduction from phase transitions has been largely contributed to the fracturing of particles, which lose contact to the electrode matrix.[18-20]

To date, many pseudocapacitive materials have been identified through electrochemical kinetic techniques, which reveals their redox processes to be largely capacitive (non-diffusion controlled) by separating the current response at any given voltage into a diffusion controlled and non-diffusion controlled component. [5-12, 21-24] Among these identified pseudocapacitive materials, nanostructured $LiMn_2O_4$ stands out as a material with a high enough voltage (> 3.2 V *vs.* Li/Li^+) to be ideal for the positive electrode in Li-ion batteries. Because pseudocapacitive cathode materials are needed to complete a pseudocapacitive full cell, understanding the nature of charge storage in nanostructured $LiMn_2O_4$ and other pseudocapacitive cathodes is of significant importance. Many other cathode materials, however, are not as easy to nanostructure as $LiMn_2O_4$, since $LiMn_2O_4$ has a relatively low crystallization temperature (550 °C *vs.* 700-900 °C for many other materials), which allows for fabrication of fine nanostructures without fear of coarsening. Additionally, $LiMn_2O_4$ is less toxic and cheaper than many other commercial cathode materials and exhibits relatively fast kinetics even in the bulk.[25]

Our previous work on pseudocapacitive $LiMn_2O_4$ includes a kinetic study where nanoporous materials with various crystalline domain sizes from 10 to 70 nm were compared. [17] From this work we recognized that the electrochemical properties of nanostructured $LiMn_2O_4$ below a crystallite size of 40 nm exhibited a relatively sharp change compared to bigger sizes. Nanoporous materials with crystallite sizes below 40 nm seemed to show significantly more capacitive current than the larger 70

nm domain sample. The smaller domain sizes nanoporous materials also showed greatly improved cyclability when compared to materials with the larger crystallite size of 70 nm. From these data, it was hypothesized that a critical grain size exists, below which the material behaved as a pseudocapacitor, possibly due to suppression of Li^+ induce phase transitions. It is well known that structural changes occur in bulk $LiMn_2O_4$ during cycling, including a two-phase coexistence and modest lattice expansions/contractions upon lithium deintercalation/intercalation, respectively.[26] Indeed, it has been hypothesized that the disturbance in the structure due to this phase change and two-phase co-existence is responsible for the poor cyclability observed in bulk $LiMn_2O_4$ systems.[26] Additionally, previous reports have used indirect methods to show that phase changes in nanoparticles of $LiMn_2O_4$ below 40 nm in size are suppressed upon Li^+ addition to the structure (< 3 V *vs.* Li/Li^+).[27] This suppression, however, has never been demonstrated for the primary voltage region in $LiMn_2O_4$ above 3 V *vs.* Li/Li^+ where Li^+ is removed during cycling.

In this paper, we aimed to study the changes in the crystal structure of nanostructured $LiMn_2O_4$ while cycling above 3 V *vs.* Li/Li^+ for small and large crystallite sizes of 15 nm and 50 nm, respectively. Synchrotron in-situ XRD was employed during charging and discharging in order to structurally understand the improved kinetics and cyclability observed in the 15 nm nanostructured $LiMn_2O_4$ system compared to the 50 nm system. The structures of both the 15 and 50 nm $LiMn_2O_4$ are made in similar ways with porous structures and as close to single domain wall thicknesses as possible.

5.2. Results and Discussion

5.2.1. Synthesis and Characterization of 15 and 50 nm $LiMn_2O_4$ Nanostructured Powders

Two nanoporous powders of $LiMn_2O_4$ with interconnected grains were synthesized via a templated sol-gel method with crystallite sizes of 15 and 50 nm. The sol-gel method used involved

combining lithium and manganese salts in a ratio of 1.1:2 to reach the stoichiometric ratios needed for slightly over lithiated $Li_{1.1}Mn_2O_4$. The salts were dissolved in a 50 mg/mL aqueous colloidal suspension of 50 nm diameter poly(methylmethacrylate) (PMMA) nanospheres. Solution were mixed and heated in air at 95 °C until the volume of the mixture was reduced to 2/3 of the initial solution volume by evaporation and the solution became viscous. The resulting gels were poured into borosilicate petri dishes and heated at 550 °C for 10 hours and 750 °C for 10 hours, for the 15 and 50 nm samples, respectively. Crystallite sizes were calculated from diffraction peak widths using the Scherrer equation, as shown in Figures 5.1a and b. From the SEM in Figures 5.1c and d the nanoscale structure of the powders can be observed, which appear to be made of interconnected particles in a porous structure

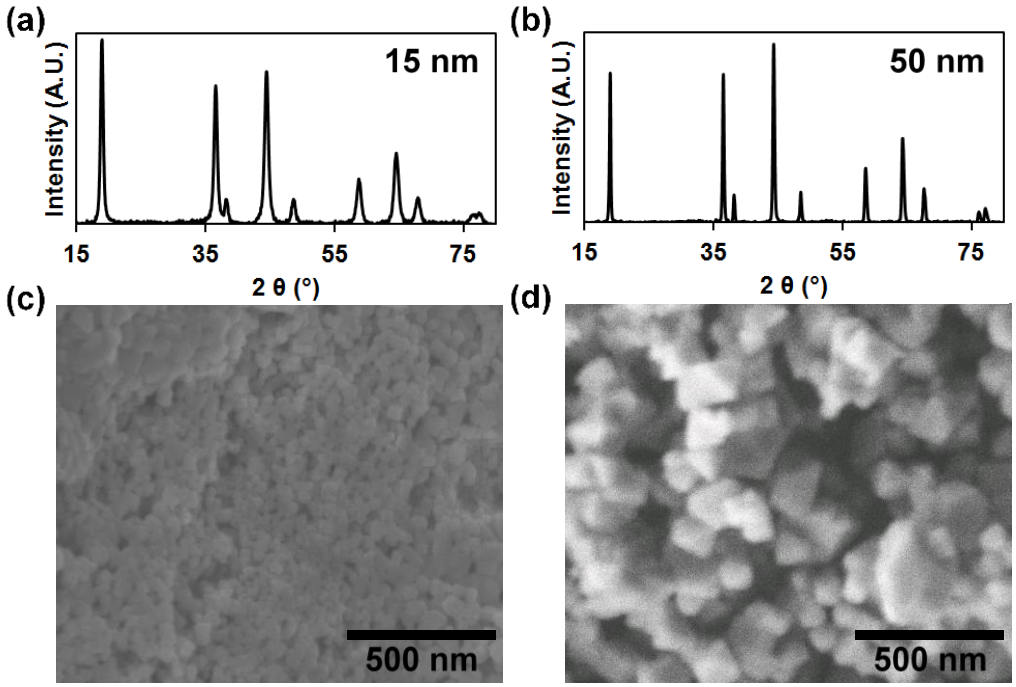

Figure 5.1. XRD patterns indicate both 15 nm (a) and 50 nm (b) domain size samples are phase pure $LiMn_2O_4$; average domain sizes were calculated from these patterns using the Scherrer equation. SEM shows images show that both the 15 nm (c) and 50 nm (d) domain size materials are made of interconnected particles in a nanoporous network.

with wall thicknesses similar to the XRD domain size. This architecture allows for optimal electrical connectivity between the particles as well as ample pathways for electrolyte to permeate during cycling.

5.2.2. Electrochemical Properties of 15 and 50 nm $LiMn_2O_4$ Nanostructured Powders

Slurry electrodes were prepared from both 15 and 50 nm $LiMn_2O_4$ nanostructured powders. Slurries were made using a mixture of 75 wt.% active powder, 10 wt.% carbon black, 5 wt.% carbon nanofibers and 10% polyvinylidene fluoride (PVDF) in an N-methyl-2-pyrrolidone (NMP) solvent. Polished stainless steel foil was used as the current collector for the slurries; this material was chosen to minimize peak interference with $LiMn_2O_4$ in XRD, compared with aluminum foil. Resulting slurries with mass loadings around 2 mg/cm2 were punched into electrodes with surface area 0.71 cm^2 and loaded into Swagelok cells in a glovebox (under argon atmosphere) with lithium metal as the counter electrode, 1M $LiPF_6$ in ethylene carbonate (EC) and dimethyl carbonate (DMC) as the electrolyte, and a glass fiber separator. Four such cells were prepared, two with 15 nm nanostructured $LiMn_2O_4$ and two with 50 nm nanostructured $LiMn_2O_4$. One cell of each sample was used for galvanostatic long term cycling and cyclic voltammetry (CV) while the other was precycled for use in the in-situ experiment. Figure 5.2 shows the results of long term cyclability for the 15 and 50 nm samples as well as the results of kinetic studies based on CV curves measured at different scan rates. The 15 nm nanostructured $LiMn_2O_4$ shows superior capacity retention over 3,000 cycles, compared to the 50 nm sample. This disparity suggests that the 15 and 50 nm samples have divergent structural evolutions during cycling, which could potentially be explained by the lack and presence of a phase transition, respectively. Additionally, a clear disparity in the percent capacitive contribution between the two nano samples can be observed by using the k_1/k_2 kinetic analysis discussed earlier, [4-12] where the 15 nm sample is upwards of 90% capacitive, while the 50 nm sample is only 74% capacitive. The high capacitive fraction in the 15 nm domain size material suggests that this sample displays intercalation

pseudocapacitance, a process where non-diffusion controlled kinetics are accompanied by Li^+ intercalation without a phase transition.[2-4] All diffusion controlled processes observed in the CVs for both samples are concentrated near the redox peaks, which further reinforce the possibility of structural evolution playing a key role in the performance differences between the two samples.

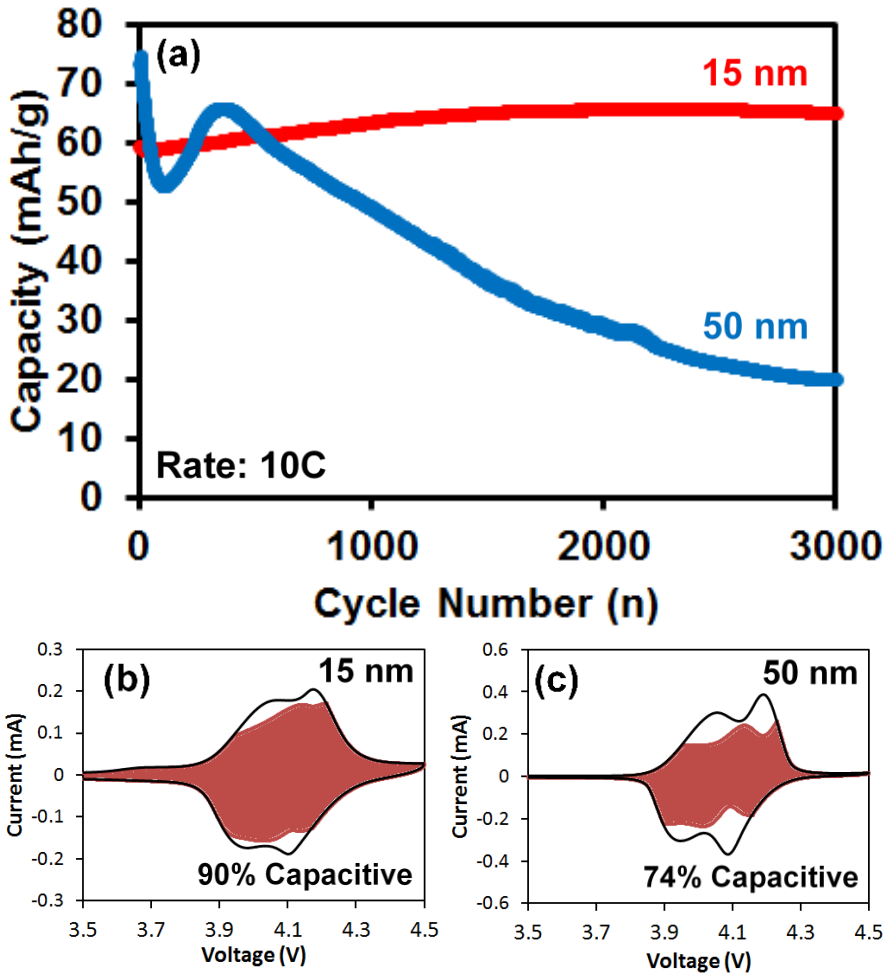

Figure 5.2. (a) Long term galvanostatic cyclability and (b, c) cyclic voltammetry at 0.2 mV/s with inlayed capacitive contribution for 15 nm and 50 nm domain size nanoporous $LiMn_2O_4$ samples cycled in Swagelok cells versus Li metal using 1M $LiPF_6$ in EC:DMC 1:1 as the electrolyte.

Galvanostatically precycled cells were cycled at a rate of C/5 in a Swagelok cell to assess stability of the electrodes before transfer to coin cells for the in-situ study. The Swagelok cells with the precycled samples were then opened in a glovebox and the $LiMn_2O_4$ electrodes were transferred into coin cells with a lithium metal anode, 1M $LiPF_6$ in EC:DMC as the electrolyte, and a glass fiber separator. The coin cells each had ~3 mm diameter round holes cut into the top and bottom caps and were sealed with kapton tape to allow the X-rays to pass through the cell during the in-situ experiments.

5.2.3. *Operando* X-ray Diffraction of 15 and 50 nm $LiMn_2O_4$ Nanostructured Powders

Operando synchrotron X-ray diffraction was performed on coin cells containing 15 and 50 nm domain size nanoporous $LiMn_2O_4$ powders during galvanostatic cycling at C/5. Resulting diffraction for the 50 nm sample over one charge and discharge cycle at C/5 can be seen in Figure 5.3. Fully discharged patterns (blue) with peak positions of ~2.6 $Å^{-1}$ and ~4.0 $Å^{-1}$ correspond to the <311> and <511> Bragg reflections of $LiMn_2O_4$, respectively. Both peaks shift towards higher Q-value and therefore lower d-spacing upon lithium deintercalation (charge) and return to their initial values upon intercalation (discharge). Upon close inspection, however, one can see that the shift in both the <311> and <511> peaks is monotonic only up to ~4.1 V *vs.* Li/Li^+ upon charging, at which point a second peak, shifted to higher Q, appears, giving the impression of significant peak broadening. As the original peak loses intensity, this new peak again shifts linearly to highest voltages reached in this study. Upon discharge, this same broadening/two peak effect appears to take place between 4.0 V and 3.95 V. Guiding lines have been added to the stacked diffraction patterns in Figure 5.3, showing the trajectory of the peak shifts from the fully discharged state to the full charged state and back to the discharged state for both the <311> and <511> reflections. The lines help emphasize the fact that

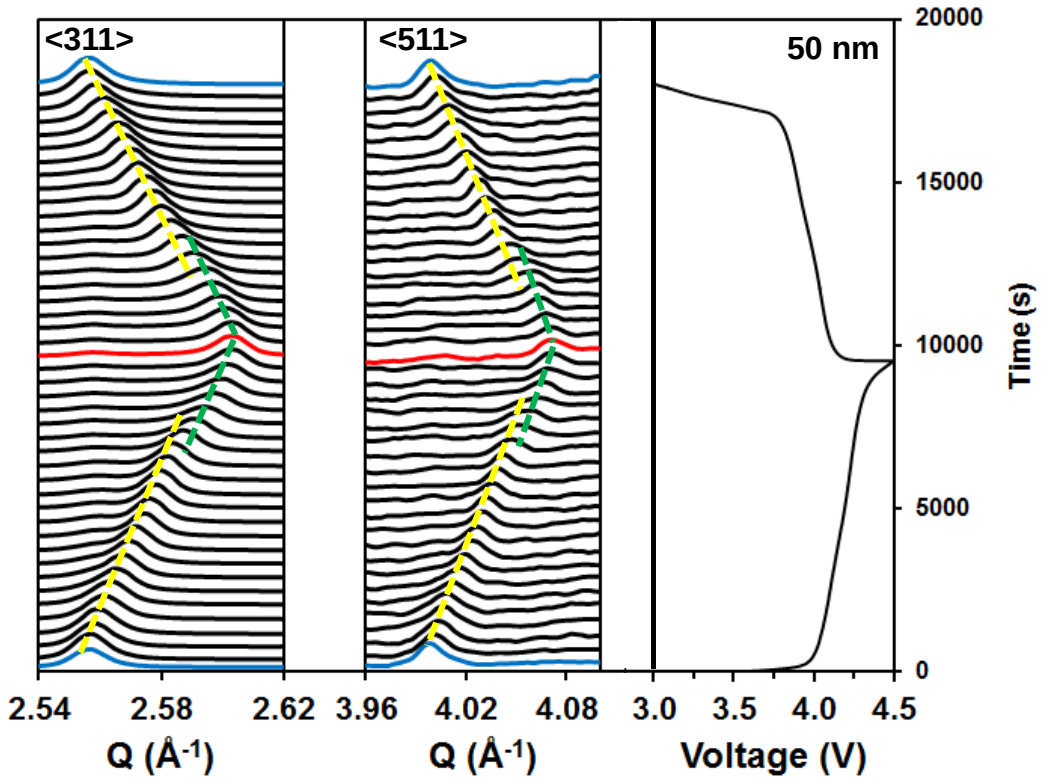

Figure 5.3. ***Operando*** **XRD patterns of the 50 nm domain size $LiMn_2O_4$ sample during charge and discharge. The <311> and <511> peaks show substantial shifting as well as the existence of a two-phase coexistence region. Dotted lines have been added to help guide the eye for the two-phase coexistence. The total discharge capacity of this cycle was 66 mAh/g.**

the broadening is actually a transition region involving two-phase coexistence between the fully charged and fully discharged states.

To reinforce this observation, <311> and <511> Bragg reflections were fit to Gaussians using peak fitting software (PeakFit) and the resulting peak positions and peak widths are shown in Figure 5.4. The total peak shifts for the 50 nm <311> and <511> patterns were calculated to be 0.0456 $Å^{-1}$ and 0.0738 $Å^{-1}$, respectively. Peaks which appeared broaden compared to the pristine peak widths were fit with two Gaussians to represent regions of twophase coexistence. The peak widths accompanying each fit are also included in Figure 5.4 and are given as the full width at half max height

(FWHM). A relatively low spread is observed for the FWHM, particularly given the inclusion of multiple Gaussians in the two-phase coexistence region, which indicates that our model is correct. If instead, the reflections for the 50 nm sample are fit to only one Gaussian across the entire voltage range, we find that the FWHM shows marked broadening only in the region around the phase transition, as expected.

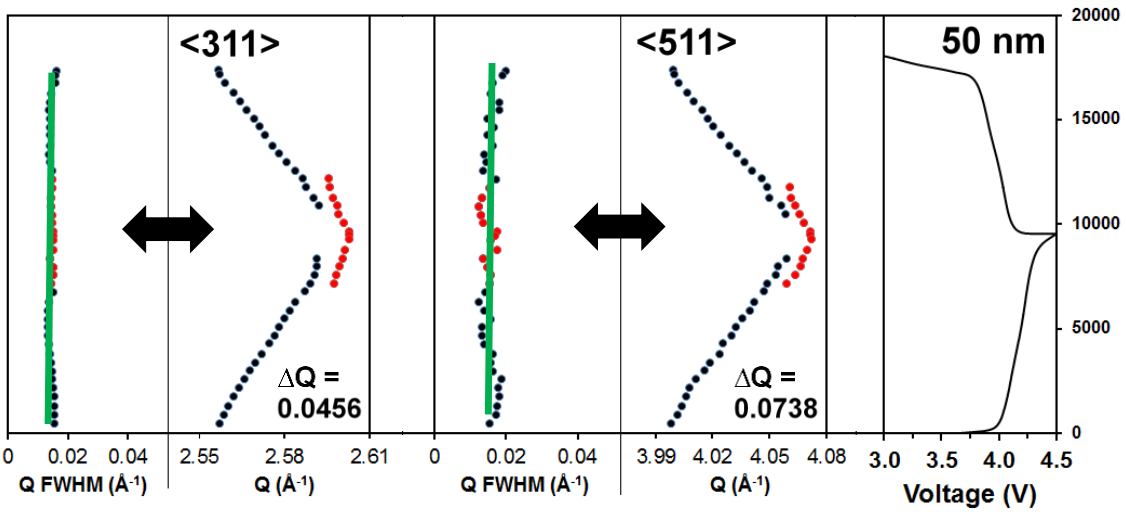

Figure 5.4. Peak positions and full width at half max values for all *in-situ* XRD patterns of the 50 nm domain size $LiMn_2O_4$ sample during charge and discharge. The <311> and <511> peak positions are fit with one peak until two peaks were needed to maintain the peak width. Full width half max values are relatively constant for all patterns, including the two peak coexistence regions, suggesting proper fits. The total change in Q-spacing was found to be 0.0456 Å and 0.0738 Å for the <311> and <511> peaks, respectively.

The existence of two-phase coexistence in the 50 nm domain size nanoporous $LiMn_2O_4$ sample during both charge and discharge indicates that for this crystalline domain size of 50 nm, a first order phase transition occurs upon cycling with Li^+, similar to that seen in bulk systems.[26] A first order phase transitions here is classified as having a discontinuity in the first derivative of free energy

and a discontinuous change in unit cell volume, both with respect to Li-ion displacement. That discontinuous change in unit cell volume appears as the two phase coexistence seen in both Figures 5.3 and 5.4. This suggests that much like in the bulk, de-intercalation/intercalation of Li-ions in 50 nm domain size nanoporous $LiMn_2O_4$ requires kinetically limited nucleation of a new phase, likely followed by propagation of the phase front across each grain. This high energy process should directly affect the kinetics of these systems, leading to a relatively smaller fraction of capacitive charge storage and more diffusion controlled processes. Since the phase transitions occur at the galvanostatic plateau or the peak in the CVs, we expect to see most diffusion controlled current around the peaks in CV, which we do in fact observe in the 50 nm system (Figure 5.2). Additionally, because the nucleation and growth requires the formation of a two phase boundary, we would expect wear and tear on the system to be significant during charge and discharge. That wear and tear experienced during cycling should lead to reduced capacity retention over many cycles as the active material cracks and loses electrical connectivity, which indeed we do observe for the 50 nm sample (Figure 5.2). From this we can deduce that the relatively slow charge/discharge kinetics and poor cyclability seen in the $LiMn_2O_4$ with a crystallite size greater than 50 nm is due to a rate limiting and structurally disruptive first order phase transition that occurs upon Li^+ extraction and reintercalation.

In contrast to the nanoporous $LiMn_2O_4$ powders with domains sizes on the order of 50 nm that show two phase coexistence, diffraction from the 15 nm domain size sample shows very different structural evolution upon charge and discharge. Figure 5.5 shows the resulting synchrotron X-ray diffraction patterns for the 15 nm $LiMn_2O_4$ sample as it is charged and discharged at C/5. A smooth transition in peak position can be observed for both the <311> and <511> Bragg reflections of $LiMn_2O_4$ during cycling. The patterns for the fully discharged 15 nm sample (blue) show peak positions similar to that of the 50 nm sample but with far less shifting and no apparent two-phase coexistence.

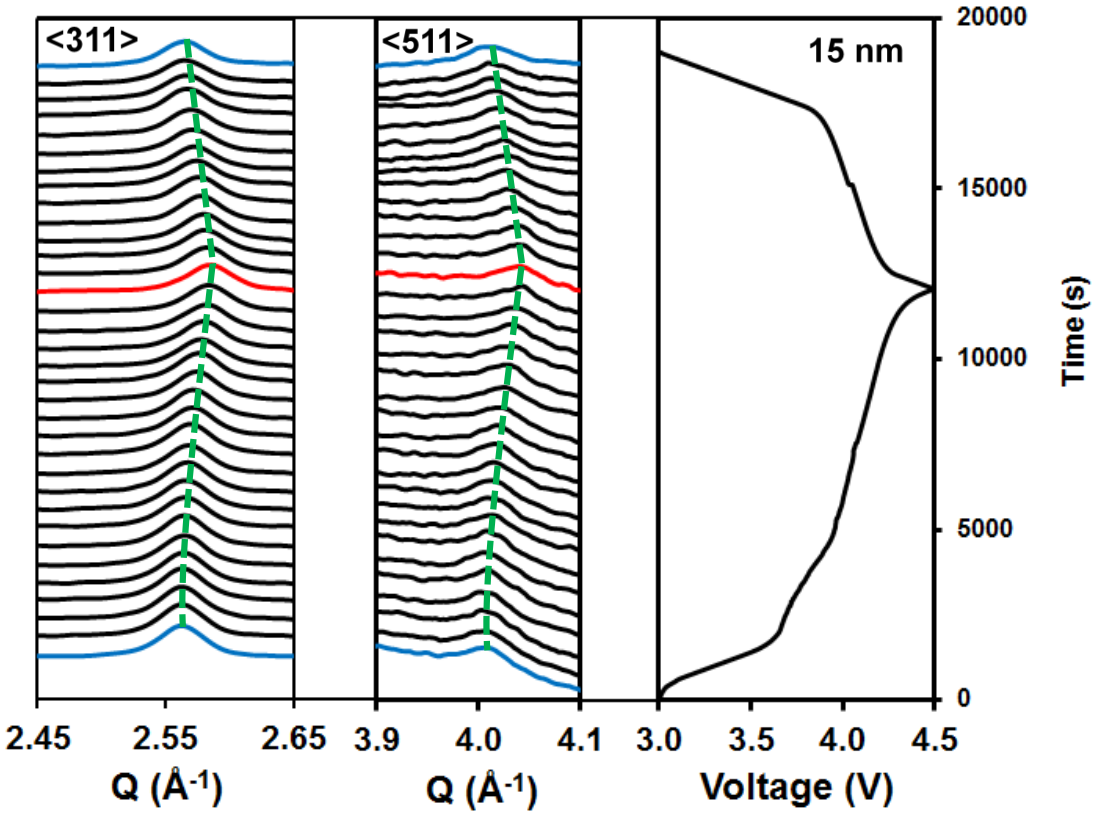

Figure 5.5. ***Operando*** **XRD patterns for the 15 nm domain size $LiMn_2O_4$ sample during charge and discharge. The <311> and <511> peaks show modest shifting with no visible two-phase coexistence region, suggesting solid solution behavior. Dotted lines have been added to help guide the eye. The total discharge capacity of this cycle was 50 mAh/g.**

Figure 5.6 shows peak positions and widths obtained by fitting all data with a single Gaussian. Resulting FWHM values show little deviation throughout the charge and discharge cycle, indicating that the data is well fit with a single Gaussian. Moreover, the total shifting of the <311> and <511> peaks is calculated to be 0.020 $Å^{-1}$ and 0.028 $Å^{-1}$, respectively, which is only about 40% of the total shifting observed in the 50 nm sample.

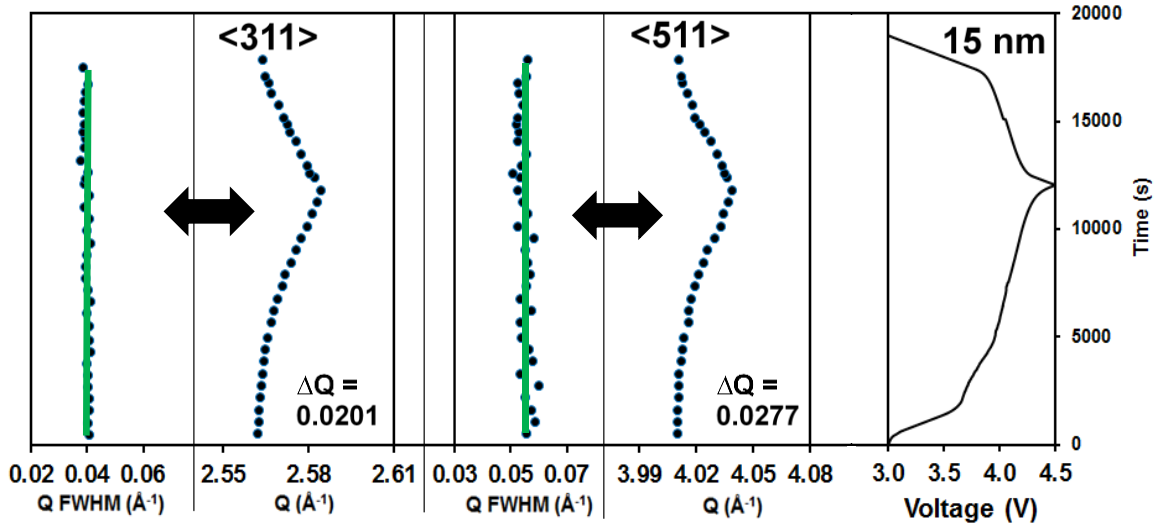

Figure 5.6. Peak positions and full width at half max values for all *in-situ* XRD patterns of the 15 nm domain size $LiMn_2O_4$ sample during charge and discharge. The <311> and <511> peak positions are fit with one peak for all patterns. Full width half max values are relatively constant for all patterns, suggesting proper fits. The total change in Q-spacing was found to be 0.0201 Å and 0.0277 Å for the <311> and <511> peaks, respectively. The total change in Q-spacing for the 15 nm domain size sample is around 40% of that for the 50 nm domain size sample.

The absence of two separate peaks in 15 nm $LiMn_2O_4$, the smooth shift in peak position, and the relatively small magnitude of the peak shift all indicates a continuous free energy function and no discontinuous volume change upon lithium deintercalation/intercalation. This, in turn, indicates that any phase transitions occurring in the 15 nm domain size material are second order, unlike that of the 50 nm sample which we concluded was first order. Mechanistically, a second order phase transition for solid state de-intercalation/intercalation of Li-ions can be represented by a solid-solution mechanism. Within a solid-solution reaction, the entirety of the material de-intercalates/intercalates lithium simultaneously, without the need for nucleation and growth of a new phase. This effect allows for lithium to pass in and out the structure without formation of grain boundaries and thus eliminates

much of the wear and tear on the material. This, in turn, reduces the probability of parts of the material losing electrical connections with the slurry matrix, thus increasing capacity retention over many cycles, which we indeed see with the 15 nm sample in Figure 5.2. Additionally, the lack of a two-phase intermediate means less of a kinetic barrier for deintercalation/intercalation on charge/discharge, leading to faster and more capacitive cycling kinetics in the 15 nm sample. Finally, the reduced shifting in Q-spacing up Li^+ deintercalation/intercalation means less flexing of the overall crystal structure during charge and discharge, which in turn means a more reversible process.

We thus conclude that the improved kinetics and cyclability observed in the 15 nm domain size sample compared to the 50 nm domain sample is a result of phase suppression in the 15 nm crystallite size nanoporous $LiMn_2O_4$. The observation of a bulk-like phase transition in 50 nm domain size materials, but its suppression in materials with 15 nm domains, supports the existence of a critical crystallite size for the onset of pseudocapacitive behavior in $LiMn_2O_4$, above which phase transitions occurs and below which, phase transitions are suppressed. In general, the improved kinetics observed when phase transitions are suppressed in redox active materials are associated with intercalation pseudocapacitance.[5-7] We thus conclude that the 15 nm sample exhibits intercalation pseudocapacitance, whereas the 50 nm sample shows only standard surface or redox pseudocapacitance, combined with battery-like intercalation at the interior of each domain. The largest domain size where these nanoporous powders can be fully cycled without a phase transition would thus correspond to the critical size for the onset of intercalation pseudocapacitance. Taking into consideration our previous work on kinetics of $LiMn_2O_4$ nanoporous powders, large kinetic and cyclability differences were observed between 40 and 70 nm crystallite sized $LiMn_2O_4$ samples.[17] We can combine the results of that work with this work, to narrow our determination of the critical crystallite size for nanoporous $LiMn_2O_4$ to be between 40 and 50 nm. These results agree with the previously referenced work on the cubic to tetragonal transition that occurs below 3 V *vs.* Li/Li^+ in

$LiMn_2O_4$ and corresponds to the addition of Li^+ to the $LiMn_2O_4$ structure. That work placed the critical size for the onset of solid solution behavior to be around 43 nm.[27] We note that it is not obvious that the critical size for both phase transitions should be the same, given that different combinations of interfacial energies are involved. Knowing the critical crystallite size for pseudocapacitance in $LiMn_2O_4$ is very useful for optimizing capacity, cyclability, and kinetics with a goal of producing fast charging cathode material for Li-ion pseudocapacitors.

5.3. Conclusion

Two nanoporous $LiMn_2O_4$ powders were synthesized via a sol-gel templating method yielding average crystallite sizes of 15 and 50 nm. Electrochemical testing of these powders revealed that the 15 nm domain size sample had significantly improved kinetics and cyclability compared to the 50 nm sample. To understand if the disparity in electrochemical performance was due to a difference in structural evolution during charge and discharge, in-situ synchrotron X-ray diffraction was utilized during cycling to study the phase transitions taking place within the materials. Resulting XRD patterns from the 50 nm domain size material showed two-phase coexistence using both the <311> and <511> Bragg reflections upon Li^+ extraction and reintercalation. By contrast, XRD patterns from the 15 nm cycling showed no evidence of two-phase coexistence, suggesting that Li^+ induced phase changes were suppressed in the smaller domain size sample. We hypothesize that this phase transition suppression leads to both improved cyclability and improved charge storage kinetics in the small domain size material. Combining this data with other electrochemical studies allows us to identify the critical point at which phase change suppression and thus intercalation pseudocapacitance emerges for $LiMn_2O_4$; this size was estimated to be between 40 and 50 nm.

5.4 Experimental

5.4.1. Synthesis

Synthesis of 50 nm poly(methylmethacrylate) (PMMA) template: The PMMA spheres were prepared by emulsion polymerization of methyl methacrylate (Aldrich) monomer (MMA) using ammonium persulfate (APS, Alfa Aesar) as the initiator in deionized water; the method is a modified version of an established method from the literature.[28] First, 165 mL DI water were bubbled with nitrogen for 20 min under stirring to remove any oxygen. Then, 0.3 mL ammonium lauryl sulfate (Aldrich), which serves as a surfactant, and 12.55mL of MMA were added. The APS initiator solution was prepared separately by dissolving 0.075 g APS in 10 mL water. The initiator solution was then added to the surfactant and monomer solution at 65 °C under stirring. The solution was heated to 73 °C and reacted for 3 h. As-prepared colloidal PMMA solution has a concentration of about 50 mg/mL, and were used without further purification. The average size of the PMMA colloids was determined to be 50 nm based by Dynamic Light Scattering and Scanning Electron Microscopy (SEM).

Synthesis of 15 nm $LiMn_2O_4$: In this method, 2.2 mmol of lithium acetate dihydrate (Sigma) and 4.0 mmol of manganese (II) acetate (Sigma) were mixed with 7.5 mL of the 50 mg/mL aqueous solution of 50 nm PMMA colloids. The solution was then heated and stirred in a round bottom flask for 20 minutes at 90 °C in an oil bath to evaporate part of the water. The resulting viscous solution was poured into a glass petri dish and left to dry for several hours in a fume hood. The resulting solid was heated in a muffle furnace with a ramp of 50 °C/hour from room temperature to 550 °C and soaked for 1 hour. The nano-sized $LiMn_2O_4$ powder was obtained by scrapping the solid from the petri dish surface.

Synthesis of 50 nm $LiMn_2O_4$: This synthetic method was almost the same as the 15 nm $LiMn_2O_4$ synthesis described above, except as noted here. The inorganic salts used were 2.2 mmol of lithium acetate (Sigma) and 4.0 mmol of manganese (II) nitrate tetrahydrate (Sigma). Also, the final

solid formed in the petri dish was heated at 50 °C/hour from room temperature to 750 °C and soaked for 10 hours.

5.4.2. Characterization

Powder X-ray diffraction (XRD) was performed on a Panalytical X'Pert Pro X-ray Powder Diffractometer using a Bragg-Brentano setup. Scherrer widths were calculated and corrected using peak broadening parameters specific for a Bragg-Brentano geometry. SEM images were obtained using a model JEOL JSM-6700F field emission electron microscope with 3 kV accelerating voltage and secondary electron detector configuration**.**

5.4.3. Electrode Fabrication and Electrochemical Analysis

Typically, 36.5 mg of nano $LiMn_2O_4$ powder was ground in a mortar and pestle with 5.0 mg of carbon black (Super P) and 2.5 mg vapor grown carbon fiber for 5 minutes. Approximately 100 mg of a 5% polyvinylidene fluoride (PVDF) solution in N-Methyl-2-pyrrolidone (NMP) was added to the homogenized powder along with 10 additional drops of NMP. The resulting slurry was doctor bladed onto a stainless steel substrate with a height of ~0.3 mm. The slurry was then place under a heat lamp for 1 hour to dry, and then transferred to a vacuum oven heated to ~130 °C while pulling vacuum overnight. The dried slurry electrode sheet was then punched out using a 0.71 cm^2 puncher and the electrodes transferred to Swagelock cells which were assembled with Li metal in a glove box with 1M $LiPF_6$ in EC:DMC as the electrolyte, and a glass fiber separator.

Two Swagelok cells were prepared for each sample (15 and 50 nm) and one of each was precycled at C/5 on a Bio-Logic 4 channel potentiostat for use in the in-situ experiment. The other two cells were cycled using cyclic voltammetry for kinetic studies at 1, 0.5 and 0.2 mV/s and then galvanostatically for 4000 cycles at a 10C rate.

5.4.3. *Operando* X-ray Diffraction

After precycling, the electrodes were taken out of the Swagelok cells in an Ar-filled glovebox and reassembled into coin cells with 3 mm Kapton tape windows for the operando studies. Kapton was chosen for its combination of X-ray transparency and low gas permeability. The coin cells were stored in an Ar atmosphere until cycling was performed to further prevent oxygen and water exposure. All *operando* cycling was performed at 0.22 C.

Operando studies on 15 and 50 nm domain size nanoporous $LiMn_2O_4$: *Operando* powder X-ray diffraction (XRD) was performed in a transmission geometry at the Stanford Synchrotron Radiation Lightsource (SSRL) on beamline 11-3 using an X-ray energy of 12300 eV. *Operando* data was collected using a MAR 345 Image Plate with 130 mm work distance, which corresponded to a Q range from Q = 0 to 5.0 $Å^{-1}$. All diffraction data was plotted as a function of the scattering vector, $Q = \frac{4\pi}{\lambda}\sin(\theta) = \frac{2\pi}{Q}$ prior to fitting; here θ is half of the scattering angle and λ is the wavelength of the incident radiation. All diffraction peaks were normalized to the intensity of the Li peak using Wxdiff and Area Diffraction Machine. Backgrounds subtraction of all spectra were later performed in Origin; diffraction from a blank cell (a regular coin cell with Kapton window, Li metal, separator and electrolyte but no active material) and a linear subtraction was used as the background. Peaks were then fit using PeakFit version 4.11 using Gaussian functions with an additional linear background subtraction.

5.5. Reference

[1] P. Simon, Y. Gogotsi, B. Dunn, *Science* **2014**, *343*, 1210.

[2] B. E. Conway, W. G. Pell, *J. Solid State Electrochem.* **2003**, *7*, 637.

[3] V. Augustyn, P. Simon, B. Dunn, *Energy Environ. Sci.* **2014**, *7*, 1597.

[4] V. Augustyn, J. Come, M. A. Lowe, J. W. Kim, P. Taberna, S. H. Tolbert, H. D. Abruña, P. Simon, B. Dunn, *Nat. Mater.* **2013**, *12*, 1.

[5] J. B. Cook, H.-S. Kim, Y. Yan, J. S. Ko, S. Robbennolt, B. Dunn, S. H. Tolbert, *Adv. Energy Mater.* **2016**, *6*, 1501937.

[6] H.-S. Kim, J. B. Cook, S. H. Tolbert, B. Dunn, *J. Electrochem. Soc.* **2015**, *162*, A5083.

[7] G. A. Muller, J. B. Cook, H.-S. Kim, S. H. Tolbert, B. Dunn, *Nano Lett.* **2015**, *15*, 1911.

[8] T. Brezesinski, J. Wang, S. H. Tolbert, B. Dunn, *Nat. Mater.* **2010**, *9*, 146.

[9] T. Brezesinski, J. Wang, J. Polleux, B. Dunn, S. H. Tolbert, *J. Am. Chem. Soc.* **2009**, *131*, 18021809.

[10] K. Brezesinski, J. Wang, J. Haetge, C. Reitz, S. O. Steinmueller, S. H. Tolbert, B. M. Smarsly, B. Dunn, T. Brezesinski, *J. Am. Chem. Soc.* **2010**, *132*, 6982.

[11] I. E. Rauda, V. Augustyn, L. C. Saldarriaga-Lopez, X. Chen, L. T. Schelhas, G. W. Rubloff, B. Dunn, S. H. Tolbert, *Adv. Funct. Mater.* **2014**, *24*, 6717.

[12] B. K. Lesel, J. Ko, B. Dunn, S. H. Tolbert, *ACS Nano* **2016**, *10*, 7572.

[13] J. Luo, Y. Wang, H. Xiong, Y. Xia, *Chem. Mater.* **2007**, *19*, 4791.

[14] B. Hwang, S. Kim, Y. Lee, B. Han, S. Kim, W. Kim, K. Park, *J. Electrochem. Sci.* **2013**, *8*, 9449.

[15] S. Jayaraman, V. Aravindan, P. S. Kumar, W. C. Ling, S. Ramakrishna, S. Madhavi, *Chem.*

Commun. **2013**, *49*, 6677.

[16] F. Jiao, J. Bao, A. H. Hill, P. G. Bruce, *Angew. Chem. Int. Ed.* **2008**, *47*, 9711.

[17] B. K. Lesel, J. B. Cook, Y. Yan, T. Lin, S. H. Tolbert, *ACS Energy Lett.* **2017**, *2*, 2293.

[18] P. Arora, R. E. White, *J. Electrochem. Soc.* **1998**, *10*, 3647.

[19] M. Wohlfahrt-Mehrens, C. Vogler, J. Garche, *J. Power Source* **2014**, *127*, 58.

[20] M. Broussely, Ph. Biensan, F. Bonhomme, Ph. Blanchard, S. Herreyre, K. Nechev, R. J. Staniewicz, *J. Power Source* **2005**, *146*, 90.

[21] N. Wu, H. Wu, W. Yuan, S. Liu, J. Liao, Y. Zhang, *J. Mater. Chem. A* **2015**, *3*, 13648

[22] T.-J. Park, J.-B. Lim, J. T. Son, *Bull. Korean Chem. Soc.* **2014**, *35*, 357.

[23] M. Okubo, E. Hosono, J. Kim, M. Enomoto, N. Kojima, T. Kudo, H. Zhou, I. Honma, *J. Am. Chem. Soc.* **2007**, *129*, 7444.

[24] Y. Zhu, L. Peng, D. Chen, G. Yu, *Nano Lett.* **2016**, *16*, 742.

[25] C. M. Julien, A. Mauger, K. Zaghib, H. Groult, *Inorganics* **2014**, *2*, 132.

[26] Y. J. Lee, F. Wang, S. Mukerjee, J. McBreen, C. P. Grey, *J. Electrochem. Soc.* **2000**, *157*, 803.

[27] M. Okubo, Y. Mizuno, H. Yamada, J. Kim, E. Hosono, H. Zhou, T. Kudo, I. Honma, *ACS Nano* **2010**, 4, 741.

[28] T. Wang, O. Sel, I. Djerdj, B. Smarsly, *Colloid Polym. Sci.* **2006**, *285*, 1.

Chapter 6. Polymer-templated Nanoporous $LiVPO_4F$ as a Fast Charging Cathode for Lithium-ion Batteries

6.1. Introduction

As technology continues to evolve, the need for energy storage devices with both high energy and power densities also grows. Nanostructured high-voltage cathodes are of increasing interest to accomplish the first of those goals.[1-3] To push the operating voltage window above the 3.6 V typical of lithium cobalt oxide (LCO)|graphite cells, spinel oxides, Li(M, M', M'')O_4, and layer oxides, Li(M, M', M'')O_2 with M= Co, Ni, Mn, Al, have been the systems of choice due to their high operating potential (> 4.3V), high theoretical capacity, good electronic conductivity and decent rate capabilities.[4,5] Unfortunately, these layered and spinel oxides suffer from low thermal stability due to the formation of metastable phases in the charge state that can readily decompose and release O_2. [6-9] In addition, their sensitivity to moisture makes them hard to process and can significantly shorten the lifetime as impurities such as LiOH and Li_2CO_3 can form on the surface.[10-13] Phosphate based polyanionic cathodes on the other hand, have demonstrated much better thermal stability due to the more thermodynamically stable P-O bonds. [14] These P-O bonds are largely covalent in nature and are stronger than polar oxygen-metal bonds in transition metal oxides. [15,16] Though many polyanion cathodes have been explored, such as $LiFePO_4$, most of them have low redox potentials because they rely on polyanionic groups with low electronegativity such as $(PO_4)^{3-}$ and $(SiO_4)^{4-}$. [17,18]

To overcome these issues, alternative polyanionic cathodes with higher potentials and higher capacity such as tavorite-structured fluorophosphates, $LiMPO_4F$ and Li_2MPO_4F (M = Fe, Mn, Co, Ti, and V), have been explored. [19-21] By taking advantage of inductive effects, the introduction of fluorine into these structures induces a more ionic metal-ligand bond and therefore increases the redox potential as the energy of the antibonding orbital level decreases. [22,23] Among the fluorine containing

polyanions, $LiVPO_4F$ (LVPF) is the most attractive cathode because it has a reasonable theoretical capacity of 156 mAh/g and a high redox potential of 4.28 V vs Li/ Li^+, a value which is the highest redox potential among V^{3+}/V^{4+} redox couples in polyanion compounds. [17,24] In addition, LVPF shows a relatively high bulk ionic conductivity of $\sim 8 \cdot 10^{-7}$ S cm^{-1} due to quasi 1D diffusion paths along the (111) direction and has excellent thermal and structural stability. [20,25]

Although LVPF has been known for some time, little effort has been put towards improving its rate capabilities, because most studies have focused on developing simpler synthetic routes for pure phase LVPF.[26-29] Synthesis of LVPF can be challenging because LVPF can easily turn into $LiVPO_4O$ and $Li_3V_2(PO_4)_3$ if oxygen is present and if a fluorine rich environment is not created during the synthesis. [30] Until recently, most LVPF was obtained from a two-step synthesis based on carbo-thermal reduction (CTR). [31-33] This method relies on using large amount of carbon to reduce V^{5+} precursors to V^{3+} to produce an intermediate phase – VPO_4/C. LiF is then added to the intermediate, followed by a second heat treatment, to make the final LVPF product. Though this two-step synthesis has been adapted by many groups, it is difficult to optimize because the amount of carbon in VPO_4/C needs to be precisely controlled as any deviation can lead to impurities.[30] In addition, the transfer process from the first annealing step to the second can introduce oxygen into the system.

Among all LVPF syntheses, only a few publications have been reported on nanoscale LVPF. [34-38] Nanostructures are favorable because the rate capabilities of most battery materials can be significantly improved when the ion diffusion path length is shortened, and in some cases when the first order phase transitions are suppressed. Under these conditions, traditional battery materials can be converted to nanoporous pseudocapacitors with impressive rate capabilities. [39-47] Unfortunately, the performance of most reported nanoscale LVPF materials is not impressive, possibly due to agglomeration of the LVPF nanoparticles, compounding the established problem of poor conductivity in nanoparticle based materials. To realize fast kinetics in high voltage LVPF, on solution is to move

from nanoparticles to nanoporous networks that are fully electrically interconnected. To accomplish this goal, we take advantage of a recent one-step solid state synthesis of submicron LVPF particles that starts with simple precursors ($NH_4H_2PO_4$, LiF, V_2O_5, and Teflon (Polytetrafluoroethylene, PTFE).[17] The PTFE creates both a fluorine rich and anoxic environment, since the carbon in PTFE can scavenge oxygen to make either CO or CO_2.[17] By adapting similar precursors using an aqueous sol-gel polymer template method, nanoporous structures can be created.

In this manuscript, we thus report a carbon coated nanoporous LVPF (c-nLVPF) with exceptional rate capabilities up to 30 C and an extended operating voltage window up to 4.6 V. With a two minutes charge and discharge, 110 mAh/g were obtained. These c-nLVPF materials were made from a simple water based synthesis using both PTFE and PMMA colloids, which constitute the fluorine source, the oxygen scavenger, and the polymer template. Interestingly, electrochemical kinetics and *operando* X-ray diffraction reveal that charge storage in c-nLVPF remains dominantly diffusion controlled and that there is a phase transition during charge and discharge, confirming that energy storage in these materials remains battery-like and not pseudocapacitive, despite their impressive rate capabilities. When paired with pseudocapacitive anodes, however, fast charging full cells can be realized.

6.2. Results and Discussion

6.2.1. Materials and Characterization

Polymer templating of sol-gel derived materials provides a facile synthetic route to many nanoporous materials.[46, 48-50] A typical synthesis consists two major components: inorganic precursors and structural directing agents such as preformed colloids or surfactants or block copolymers that will readily form micelles in solution. When well-suspended in solution, structural directing agents co-assemble with the metal salts as the inorganic precursor undergo hydrolysis and condensation reaction

to form a gel network around the colloids or micelles. The gel can then be dried and thermally annealed to crystallize the inorganic framework and decompose the polymer template, leaving the nanoporous network behind.[51]

To make c-nLVPF powder, inorganic precursors (V_2O_5, NH_4VO_3, and LiF) and a reducing/chelating agent (oxalic acid, $H_2C_2O_4$) were dissolved in water to form a sapphire blue sol. With its bidendate nature, oxalic acid is responsible for reducing V^{5+} to V^{2+} to make vanadium oxalate, which further reacts with other metal salts.[52] Furthermore, oxalic acid is the precursor for the carbon coating as it decomposes.[29] This whole process is described below in Equation 6.1-6.3.

$$V_2O_5 + 3H_2C_2O_4 \rightarrow 2VOC_2O_4 + H_2O + 2CO_2 \qquad \textit{Equation 6.1}$$

$$2VOC_2O_4 + 2LiF + 2NH_4H_2PO_4 \rightarrow 2LiVPO_4F + CO + 3CO_2 + 2NH_3 + 3H_2O \qquad \textit{Equation 6.2}$$

$$CO \rightarrow C(s) + CO_2(g) \qquad \textit{Equation 6.3}$$

A mixture of colloids, PTFE (avg. 180 nm) and PMMA (avg. 30-50 nm), were used as the polymer template and later mixed with the sol to create high surface area c-nLVPF. In order to keep the PMMA colloids suspended throughout the gelation process to form a uniform porous network, small amount of the surfactant Pluronic F127 ($(EO)_{98}(PO)_{67}(EO)_{98}$) was added to the solution to improve their stability. As a nonionic surfactant, Pluronic F127 can interact with the ammonium lauryl sulfate (ALS) stabilizing the PMMA colloids to increase the solubility of PMMA colloids as the concentration of the sol increases during the gelling process. Very small PMMA colloids can be readily synthesized, and these colloids are thus key to the high surface area and short diffusion path lengths needed for fast charging and discharging. Unlike the PMMA, which can crash out of solution without stabilization at high concentration, the PTFE colloids can readily be dispersed in solution and stay stably suspended in the acidic sol even at high concentrations. PTFE colloids are critical to the synthesis as they serve as both the polymer template and the fluorine source for creating a fluorine-rich environment. Very

small LVPF colloids are not readily available, however, and so the combination of colloidal PTFE and colloidal PMMA is required to produce appropriately small nanostructures.

We note that while the fluorine rich environment created by the decomposition of PTFE is required to produce the fluorphosphate, rather than the related oxo-phosphate, it can also have detrimental effects. During calcination, fluorine can react with the H_2O generated from combustion of the polymer template to form HF. VF_3 gas can also be generated if LVPF is calcine for an extended period of time. Both of these reaction routes are described in Equation 6.4 and 6.5 and result in impurity phases such as $Li_3V_2(PO_4)_3$ and V_2O_3.[26]

$$6LiVPO_4F + 3H_2O \rightarrow 2Li_3V_2(PO_4)_3(s) + HF(g) + V_2O_3(s) \qquad \textit{Equation 6.4}$$

$$3LiVPO_4F(s) \rightarrow VF_3(g) + Li_3V_2(PO_4)_3(s) \qquad \textit{Equation 6.5}$$

The crystal structure of c-nLVPF was verified by X-ray diffraction. The diffraction pattern of c-nLVPF (Figure 6.1a) agrees well with the typical tavorite structure with a triclinic unit cell (space group *P-1,* JCPDS No. 42-1412). No impurity phases, $Li_3V_2(PO_4)_3$ or V_2O_3, were detected. The crystal structure of LVPF can be described as a 3-D framework consists of corner sharing polyhedrals of VO_4F_2 octahedra and PO_4 tetrahedra with open tunnels along the 100, 010, and 101 plane, making it a 1-D ionic conductor.[30,53]

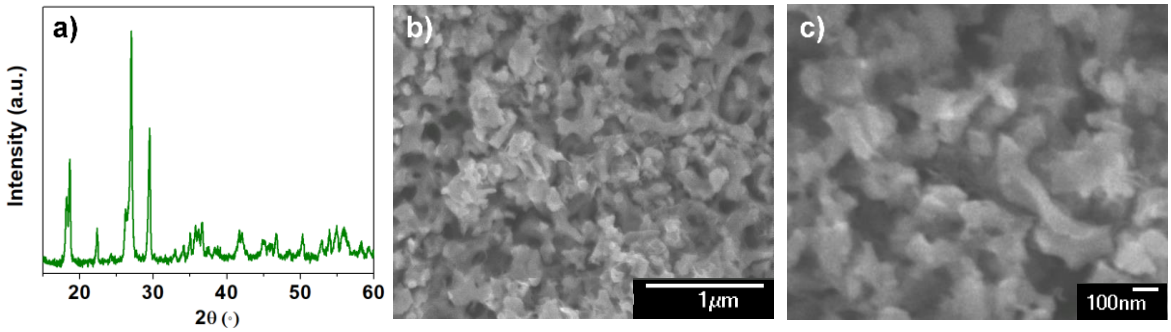

Figure 6.1. a) X-ray diffraction pattern of the c-nLVPF. No impurities are observed. b-c) SEM images of the as synthesized nanoporous c-nLVPF powder made by sol-gel polymer templating methods. The uniform porous structure results from the polymer template and can be seen at both low and high magnifications.

The evenly distributed pores in c-nLVPF are shown in both low and high magnification scanning electron microscopy (SEM) images (Figures 6.1b and 6.1c). These porous structures are made of interconnected pore walls 100-250 nm thick and pores roughly 20-100 nm big in diameter. With its unique mesoporous morphology, both ion and electrolyte diffusion can be significantly improved across the active material, giving rise to the exceptional rate capabilities. The carbon coating of c-nLVPF can be seen in the transmission electron microscopy (TEM) images in Figures 6.2a and 6.2b. The layer of amorphous carbon is approximately 5 nm thick, which agrees with other works using similar V_2O_5 to oxalic acid ratio.[28] Thermal gravimetric analysis (Figure 6.2c) indicates that the c-nLVPF materials contains ~8 % carbon, including both the oxalic acid derived carbon coating and any residual carbon from the polymer template. The carbon content is calculated using the mass loss from 375°C to 450°C, which corresponds to the elimination of carbon to form CO_2.[54] The subsequent transition up to 550 °C corresponds to the substitution of oxygen for fluorine in the c-nLVPF structure.[54]

Nitrogen porosimetry was performed to calculate the total surface area and to measure the pore size distribution in c-nLVPF. The calculated surface area using the Brunauer-Emmett-Teller (BET) model is 21 m^2/g. The type II adsorption isotherm (Figure 6.2d) signifies the presence of both macro and mesopores from the large PTFE and small PMMA templates. The pore size distribution calculated from the Barrett-Joyner-Halenda region (< 100 nm) is 10-80 nm, with mostly 10-30 nm pores. This pore size distribution measured from N_2 porosimetry agrees well with the wide range of

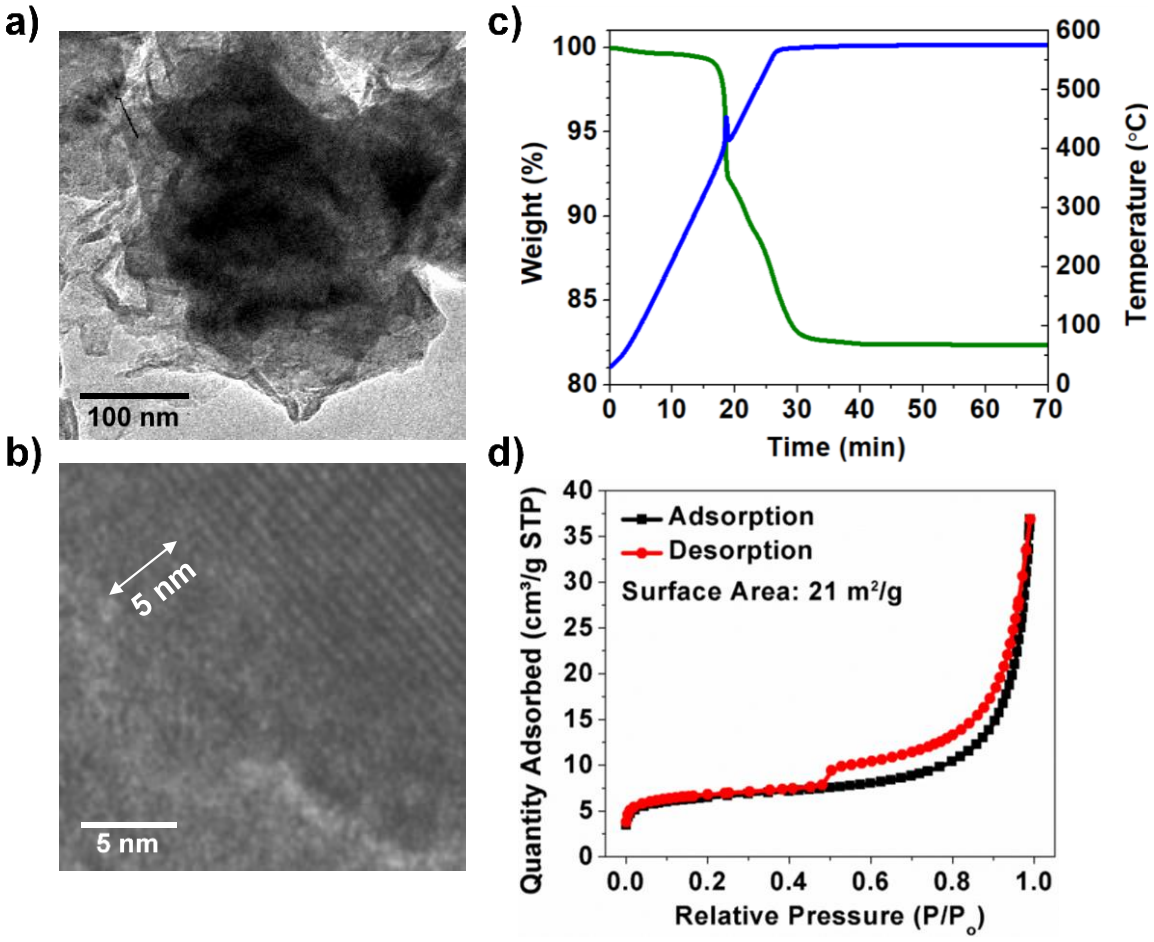

Figure 6.2. a-b) TEM images of the c-nLVPF. The carbon coating wraps around the particle and is approximately 5 nm thick. c) TGA of c-nLVPF from room temperature to 550 °C. The 8 wt.% mass loss from 375-450 °C is attributed to the carbon content. d) Isotherm of c-nLVPF obtained from N_2 porosimetry. The surface area calculated from the BET model is 21 m^2/g.

pore sizes observed in the SEM images. In addition, the fraction porosity of c-nLVPF, 15%, is also calculated from the bulk density and the single point pore volume.

6.2.2. Electrochemical Cycling

To investigate the redox processes and electrochemical performances of c-nLVPF, c-nLVPF electrodes were cycled in 2032 coin cells with glass fiber separators against lithium metal. The cyclic voltammogram (CV) and galvanostatic cycling (GV) curves were measured in 1M $LiClO_4$ in PC and 1.2M $LiPF_6$ in 2FEC:8DMC vol.% , receptively. The one electron process of c-nLVPF during charge and discharge relies on the V^{3+}/V^{4+} redox couple. The electrochemical reaction is described below in Equation 6.6.

$$LiV_{III}PO_4F \rightarrow V_{IV}PO_4F + Li^+ + e^- \qquad \textit{Equation 6.6}$$

A slow rate cyclic voltammagram measured at 0.1 mV/s from 3 to 4.5V vs. Li/Li^+ is shown in Figure 6.3a. The oxidation peaks at 4.27 V and 4.33 V correspond to the intermediate phase, $Li_{0.65}VPO_4F$, and the fully delithiated phase, VPO_4F, respectively. [55] The broader peak at 4.33V in the first cycle can be attributed to solid-electrolyte interphase (SEI) layer formation. During discharge, only one reduction peak is observed at 4.18 V as Li intercalates into VPO_4F to reversibly form LVPF. This asymmetric redox pair suggests that different reaction pathways are taken upon lithiation and delithiation. Even though this phenomenon has been found in many other LVPF studies, it is not yet fully understood.[30,33,55,56]

Regardless of these questions, the oxidation and reduction peaks obtained from the CV curves are well match to the plateaus in the charge and discharge profiles at 1C (calculated from theoretical capacity) from 3V-4.6V (Figure 6.3b). A step function corresponding to the two oxidation peaks is observed during charge while a smooth plateau is found during discharge. The discharge capacity on the first cycle is 152 mAh/g, which is almost the total theoretical capacity (158 mAh/g) with 96%

coulombic efficiency. The rate capabilities of these c-nLVPF are tested at C, 5C, 10C, 15C, 20C, and 30C as shown in Figure 6.3c. Exceptional rate capabilities were demonstrated even up to 30C with a discharge capacity of 110 mAh/g and almost 100% coulombic efficiency.

We note that these favorable results are made possible in part by a recent push to developing stable electrolytes for higher voltage lithium-ion cells in order to increase energy density. It has been demonstrated that by increasing the potential cutoff of the cathode from the typical 4.2 V to 4.5 V and even to 4.8V vs. Li/Li^+, 18% and 36% increase in energy density can be achieved.[57] Unfortunately, most conventional carbonate solvents are only stable up to 4.2 V. However, with additives such as vinylene carbonate (VC) and fluoroethylene carbonate (FEC), the operating voltage window can be extended. [58,59] In particular, FEC has been cycled up to 5 V with very stable cycling behaviors In particular, FEC has been cycled up to 5V with very stable behaviors.[60-62] To realize c-nLVPF's full capacity at its high redox potentials and faster rates, electrolyte consists of fluoroethylene carbonate (FEC) and dimethyl carbonate (DMC) were used in this study. The c-nLVPF cycled in 1M $LiClO_4$ in PC does not show such fast rate capability. This drastic difference in performance can be attributed to the different types of SEI formed on the surfaces of c-nLVPF in PC, compared to FEC/DMC. It is known that the process of FEC decomposition results in highly-effective, compact surface thin films consist of mainly PEO-like polymer and MCO_3 species.[60] Meanwhile, thick and irregular SEI layers are typically formed from conventional carbonate electrolytes with mostly organic carbonates/polycarbonate moieties. [60,61] With FEC forming a compact thin passivating layer to prevent further electron transfer, the electrical resistance is significantly reduced and the stability and reversibility are also improved. Even after cycling at 20C for 2000 cycles, 115 mAh/g is still retained with only 9% capacity fade (Figure 6.3d).

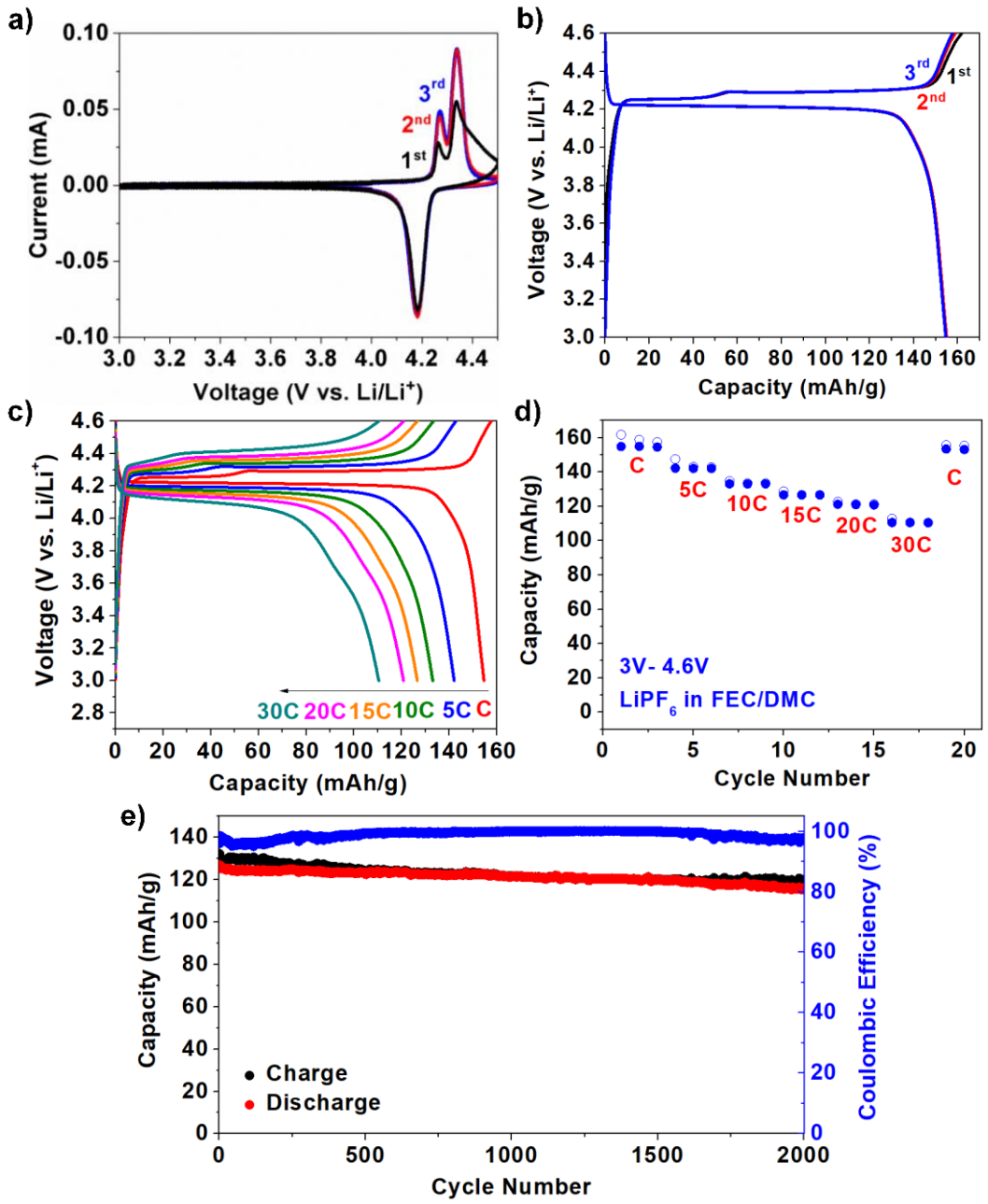

Figure 6.3. a) CV curves for c-nLVPF collected at 0.1 mV/s. The redox peaks indicate the electrochemical process described in equation 6. b) Galvanostatic charge and discharge profiles for the first three cycles of at 1C. c) Charge and discharge voltage profiles of c-nLVPF at various rates (charging and discharging are done at the same rate for every cycle) d) Capability and Coulomb efficiency at various rate. e) Capacity retention at 20C charge and discharge showing good stability over 2000 cycles.

6.2.3. Charge Storage Mechanism and *Operando* X-ray Diffraction Study

Nanostructured materials are attractive compared to bulk materials because interesting phenomenon can occur at the nanoscale. It has been previously shown that when battery materials such as TiS_2,[47] TiO_2,[40,41] MoO_2,[42] MoS_2,[43,44] $LiMn_2O_4$[45,46] are nanostructured, the phase transition (Li-rich and Li-poor phase) can be suppressed and the charge storage mechanism can change from a diffusion controlled mechanism to capacitive behavior. Such materials are classified as intercalation pseudocapacitors rather than batteries. This phenomenon, however, does not always occur. As we show below, certain materials, including LVPF, do not exhibit this crossover from a battery-like behavior to pseudocapacitance, even when nanostructured. To understand the charge storage mechanism of our c-nLVPF, the current response as a function of scan rate in a cyclic voltammetry measurement can be used to distinguish between a capacitor-like or diffusion controlled charge storage mechanism according to the following equation:

$$i = av^b \qquad \textbf{Equation 6.7}$$

where, i is the measured current, v is the scan rate, and a and b are both constants. Here the exponential term, b, distinguishes the charge storage mechanism: when b is equal to 0.5 (i.e. when the current i is proportional to scan rate $v^{1/2}$), the current is dominantly governed by diffusion. When b equals 1 (i directly proportional to v), it indicates a capacitor-like behavior, where the current is not diffusion controlled, a situation that arises for surface pseudocapacitive reactions or when intercalation reaction kinetics are capacitive in nature due to the suppression in phase transitions. According to our analysis (Figure 6.4a), the b values of c-nLVPF at all peak currents are close to 0.5 (0.55 and 0.54 for the cathodic peaks and 0.55 for the anodic peak), indicating a diffusion controlled charge storage mechanism that resembles a typical battery material.

To confirm this, any phase transitions in c-nLVPF that occur during charge and discharge were investigated using *operando* X-ray diffraction at Stanford Synchrotron Radiation Lightsource

(SSRL) using beam line 11-3. Previously in the literature, Ateba Mba *et al.* had shown that micron-sized LVPF undergoes a first-order phase transition as Li deintercalates from LVPF to form VPO_4F.[30] The same phase change is observed in our c-nLVPF. Diffraction peaks in two different Q regions, 1.26-1.38 $Å^{-1}$ and 1.8-2.15 $Å^{-1}$, are shown in Figure 6.4b. To guide the readers through all the peak shifts, diffraction profiles at OCV and the fully discharged states are colored in blue, patterns with two phase coexistence are highlighted in orange, and finally the red lines represent the fully charged state. As delithiation begins, the (010) and (100) doublet at 1.28 $Å^{-1}$ and 1.31 $Å^{-1}$ shifts to higher Q. This results in a new set of doublet, representing the VPO_4F phase at 1.32 and 1.34 $Å^{-1}$ at the end of charge. During discharge (lithiation), the doublet shifts back to its original position at OCV (1.28 and 1.31 $Å^{-1}$), indicating the reversibility of this phase transition. The same trend is observed at higher Q. The (-111) and (0-11) peaks at 1.8 $Å^{-1}$ and 1.9 $Å^{-1}$ shifts to slightly higher Q and merges into a new peak at 1.91 $Å^{-1}$ during discharge while (1-10) shifts to lower Q and splits into a doublet at 2.02 and 2.04 $Å^{-1}$. Again, all of these new peaks match the diffraction pattern of VPO_4F and transform back to the original LVPF peak positions during discharge.

We speculate that the fast charging capabilities of c-nLVPF can be enabled even when there is a phase transition due to the unique structures of these polyanionic cathodes with corner sharing polyhedral subunits comprised of covalent X-O bonds (X = S, P, Mo, etc).[63,64] LVPF is composed of corner sharing VO_4F_2 octahedra and PO_4 tetrahedra. The delithiated phase, monoclinic VPO_4F, is made of the same building blocks as the triclinic LVPF with the removal of Li ion in the 1-D conduction pathways.[53] As the conduction pathways remain open throughout charge and discharge, the Li-ions can intercalate and deintercalate rapidly even in the presence of a phase transition. In addition, the activation energy for lithium diffusion in VPO_4F is low (328 meV), which also contributes to the excellent rate capabilities.[65] These corner sharing polydedral subunits not only build the 3-D network of the polyanionic cathodes, but also help preserve their structural integrity during repetitive

phase changes. The corner sharing polyhedrals allow a concerted rotation of the subunits during the phase transition and allows much greater lattice flexibility than in layered or spinel oxides where severe structural reconstructions are found.[66,67] With its shortened diffusion path length, open 1-D tunnels (even at the delithiated state) and 3-D framework that rotate during phase transition (triclinic to monoclinic), c-nLVPF exhibits performances similar to a psueodocapacitor even though it is a battery.

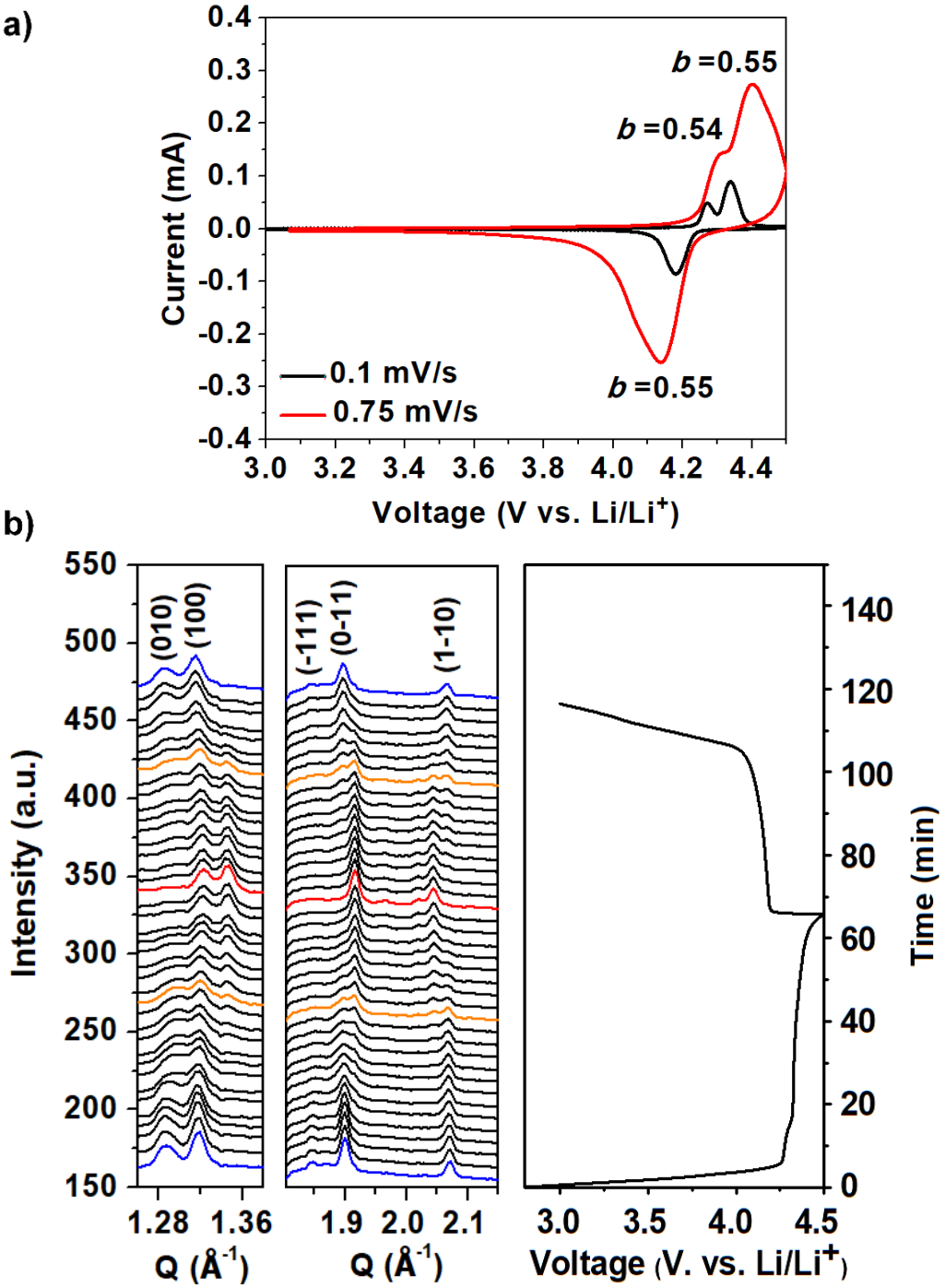

Figure 6.4. a) Cyclic voltammograms of the c-nLVPF at 0.1 mV/s and 0.75 mV/s with calculated *b*-values. The system is mostly diffusion-limited with *b* values close to 0.5. (b) *Operando* X-ray diffraction for c-nLVPF. First-order phase transitions can be observed as peak shifts to position that corresponds to the VPO_4F phase.

6.2.4. Self-Discharge Study

To evaluate the surface stability of c-nLVPF, self-discharge studies were performed. The c-nLVPF half-cell in 1.2 M $LiPF_6$ 2FEC:8DMC vol.% was charged to 4.6V at 1C, rested for 12 hr and discharged to 3V again at 1C (Figures 6.5a to 6.5c). During the 12hr rest, the open circuit voltage (OCV) drops from 4.6V to 4.25V, which is above the discharge plateau at 4.1V, allowing the c-nLVPF to retain a high discharge capacity. Almost 140 mAh/g was obtained on the first discharge with 92% coulombic efficiency. In the subsequence self-discharge cycles, the coulombic efficiencies improve while maintaining similar discharge capacity. This suggests c-nLVPF has a stable solid-liquid interface and no capacity fade is observed due to metal dissolution or other catalytic reaction. This can be attributed to the carbon coating and the stable SEI resulted from the FEC/DMC decomposition.

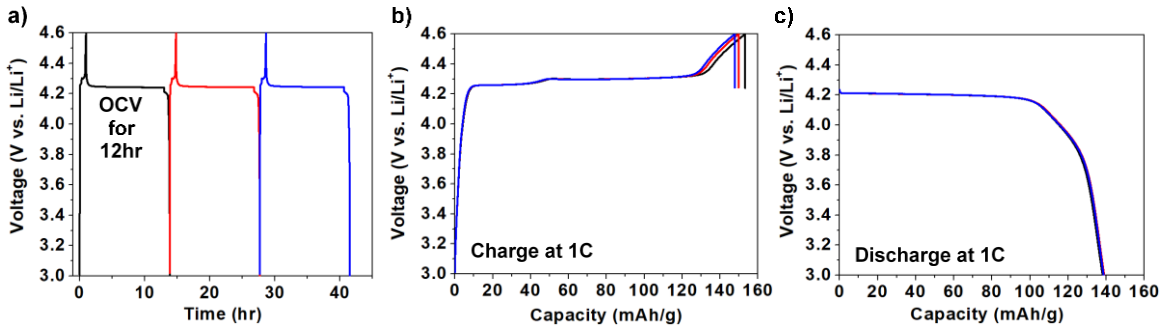

Figure 6.5. Self discharge behavior of c-nLVPF a) Voltage curves of each cycle (charge, rest for 12 hr then discharge) b) The three charge curves plotted together. c) The three discharge curves obtained after resting.

6.2.5. Full Cell Device

As a proof of concept for a fast charging device, c-nLVPF was paired with pseudocapacitive nanostructured Nb_2O_5 in a full cell. The CV of overload Nb_2O_5 and c-nLVPF cycled at 0.1 mV/s

between 1.5V to 2.8V is shown in Figure 6.6a. The irreversible oxidation peaks on the first cycle can be attributed to SEI formation. In later cycles, oxidation peaks of c-nLVPF can be identified at 2.1V and 2.3V while the corresponding reduction peak is present at 2.05V. The broadening of the redox peaks and the sloping profiles observed in the galvaonostatic cycling curves can be attributed to the Nb_2O_5 anode, as the cell voltage is no longer referenced to Li metal. Figure 6.6b shows the first three galvanostatic cycling charge and discharge curves at 1C. Since c-nLVPF is the limiting electrode, all capacity are normalized to the mass loading of the cathode. At 1C, 200 mAh/$g_{c\text{-}nLVPF}$ were obtained and at 30C, 100 mAh/$g_{c\text{-}nLVPF}$ were still achieved. This fast charging capability of the full cell is demonstrated in Figure 6.6c.

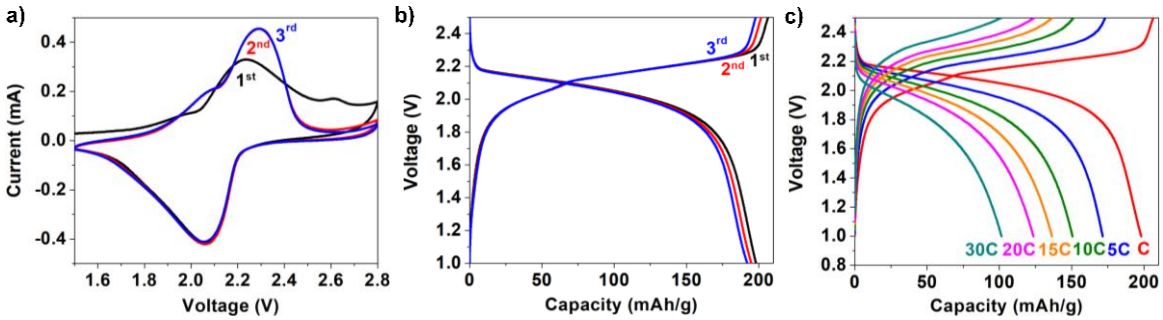

Figure 6.6. a) CV curves of the full cell device (Nb_2O_5|c-nLVPF). b) Charge and discharge profiles of the full cell device at 1C. c) Charge and discharge voltage profiles of the full cell device at various rates (charging and discharging are done at the same rate for each cycle).

6.3. Conclusion

This work presents a facile synthesis for c-nLVPF using colloidal PTFE and PMMA as polymer templates. By deviating from the traditional electrolytes that begin to decompose at 4.2V, the operating voltage window can be extended to 4.6V, enabling fast charging with excellent stability. This fast charging behavior can be attributed to three key factors: 1) the short diffusion distances in c-nLVPF attained through nanostructuring, 2) the open tunnels on both LVPF and VPO_4F that allows

fast ion diffusion, and 3) the thin and compact SEI resulted from FEC/DMC decomposition. Together, these factors allow for high capacities even at 30 C. Interestingly, despite this excellent rate capability, c-nLVPF remains fundamentally a battery and does not show pseudocapacitive behavior. The c-nLVPF can be effectively paired with pseudocapacitive anodes to produce a high rate energy-storage system. Overall, we have demonstrated c-nLVPF's potential as a promising cathode for high-energy, fast-charging application.

6.4. Experimental

6.4.1. Synthesis

c-nLVPF can be made through a water based sol-gel polymer templating synthesis. 1:4 stoichiometric amount of V_2O_5 (Sigma Aldrich) and oxalic acid (Sigma Adrich) was first dissolved in 10 mL of water at 70 °C and stirred for an hour to obtain a blue solution. After the solution had cooled down to room temperature, the other precursors, 1:2 stoichiometric amounts of $NH_4H_2PO_4$ (Alfa Aesar) and LiF (Alfa Aesar), were added and stirred for another few hours. Excess LiF was added to compensate for lithium and fluorine lost during calcination. The 10 mL solution was then heated at 100 °C and reduced to 2 mL, followed by the addition of 0.3 mL PTFE colloids (Chemours, DISP 30) to the sol. Meanwhile, a separate solution of 1 mL colloidal PMMA colloidal (150mg/mL) with 12.5 mg of Pluronic F127 was made. The synthesis of the PMMA colloidal suspension is included in a later paragraph. Last but not least, the PTFE solution with all the precursors was added dropwise to the PMMA/ Pluronic F127 solution. The final mixture was then dried overnight in a petri-dish to obtain a gel. To crystallize the c-nLVPF, the gel was dried in the vacuum oven at 100 °C prior calcination to get rid of the water in the gel. The dried gel was then transferred to an alumina boat and heated at 700 °C for 2 hr under Ar. After heat treatment, the final product, c-nLVPF (dark gray powder) was obtained.

The synthesis of PMMA colloidal solution is adapted from previous literature.[68] Ammonium persulfate (APS) was used as the initiator and ammonium lauryl sulfate (ALS) as the surfactant. 0.08 g APS, 2.29 mL ALS and 84 mL deionized water were put in a three-neck round-bottom flask (250 mL) equipped with magnetic stirrer, reflux condenser, and thermometer. The temperature was raised to 75 °C, and 14 mL of monomer, methyl methacrylate, was added in a differential manner (continuously addition in very small drops) using a syringe pump for about 1 hr. After addition, the reaction temperature was held at 80–85 °C for an additional hour before a cooling to room temperature.

6.4.2. Characterization

Powder X-ray diffraction (XRD) was performed on a D8 diffractometer (Bruker) operating with Cu Kα radiation (λ = 1.5418 Å) with a voltage of 45 kV, and a current of 40 mA. XRD patterns were recorded in the range of $10° < 2\theta < 80°$ using a 0.03° step size. Scanning electron microscopy (SEM) images were obtained using a model JEOL JSM-6700F field emission electron microscope with 3 kV accelerating voltage and secondary electron detector configuration. Transmission electron microscopy (TEM) was performed using a FEI Technai TF20 operating at 200 kV. Nitrogen porosimetry was carried out using a Micromeritics TriStar II 3020. The surface area was calculated from the adsorption branch of the isotherm (between 0.04 – 0.30 P/Po) using the Brunauer-Emmett-Teller (BET) model. The pore diameter and pore volume were also calculated from the adsorption branch of the isotherm using the Barret-Joyner-Halenda (BJH) model. Thermal gravimetric analysis (TGA) was performed on a Perkin Elmer Pyris Diamond TGA/DTA. The sample was heated to 50 °C and held for 1 min then ramped up to 550 °C with a 20°C/min ramp rate and held for 1 hr.

6.4.3. Electrochemistry

Carbon based electrodes with 70 wt.% c-nLVPF, 5 wt.% vapor grown carbon fibers (Sigma Aldrich), 5 wt.% multi-wall cabon nanotube (Sigma Alrich), and 10 wt.% Poly(vinylidene fluoride) (Mw=250K, Sigma Aldrich) were used for all electrochemical testing. Active material, carbon and binder were mixed in a mortar for 10 min until a consistent honey-like slurry was obtained. The slurry was then casted onto an Al current collector and dried at 120 °C in a vacuum oven overnight. A disk 3/8 inch in diameter was then punched out from the electrode for electrochemical testing. All cyclings were performed in 2032 coin cells with glass fiber (Advantec) separators using VSP-100 Biologic. During half-cell testing, c-nLVPF electrodes with (1mg/cm^2) were cycled in 1.2M $LiPF_6$ (Oakwood Inc.) in 2FEC (Alfa Aesar):8DMC (Sigma Aldrich) vol.% against lithium metal except for the CV measurement that was cycled in 1M $LiClO_4$ (Sigma Aldrich) in PC (Sigma Aldrich). In the full cell device, 1mg/cm^2 c-nLVPF electrode was paired with 10 mg/cm^2 Nb_2O_5 electrodes (gifted by Battery Streak Inc.) and cycled in 1M $LiClO_4$ in PC. The operating voltage window was determined both by both CV and half-cell testing.

6.4.4. *Operando* X-ray Diffraction Study

Coin cells with 3mm holes and Kapton tape window was used for the operando study. The Kapton tape window was chosen for X-ray transparency. The coin cells were stored in an Ar atmosphere until cycling was performed to prevent exposure. Due to time constraints, all cycling was performed at 1C for the operando studies at SSRL beamline 11-3 at an X-ray energy of 12300 eV. Operando data was collected using a MAR 345 Image Plate with 130 mm work distance. Data was collected from Q = 0 to 4.5 Å^{-1}. The electrode formulation used here is the same above. All diffraction intensity data is plotted as a function of the scattering vector length $Q = \frac{4\pi}{\lambda}\sin(\theta)$, where θ is half of the scattering angle and λ = is the wavelength of the incident radiation; the d-spacing thus is simply

$\frac{2\pi}{Q}$. All diffraction peaks were normalized to the Al peak using Area Diffraction Machine. Backgrounds subtraction of all spectra were later performed in Origin. Diffraction of a blank cell (a regular coin cell with Kapton window containing all components except the active material) was used as the background diffraction pattern.

6.5. Reference

[1] X. Xu, S. Lee, S. Jeong, Y. Kim, J. Cho, *Mater. Today* **2013**, 16, 487.

[2] Y.-K. Sun, Z. Chen, H.-J. Noh, D.-J. Lee, H.-G. Jung, Y. Ren, S. Wang, C. S. Yoon, S.-T. Myung, K. Amine, *Nat. Mater.* **2012**, *11*, 942.

[3] M. Kunduraci, J. F. Al-Sharab, G. G. Amatucci, *Chem. Mater.* **2006**, *18*, 3585.

[4] Y. Nishi, *J. Power Source* **2001**, *100*, 101.

[5] A. Mathiram, *ACS Cent. Sci.* **2017**, *3*, 1063.

[6] Y. Huang, Y.-C. Lin, D. M. Jenkins, N. A. Chernova, Y. Chung, B. Radhakrishnan, I.-H. Chu, J. Fang, Q. Wang, F. Omenya, S. P. Ong, M. S. Whittingham, *ACS Appl. Mater. Interfaces* **2016**, *8*, 7013.

[7] H.-J. Noh, S. Youn, C. S. Yoon, Y.-K. Sun, *J. Power Sources* **2013**, *233*, 121.

[8] F. Zhou, X. Zhao, A. van Bommel, X. Xia, J. R. Dahn, *J. Electrochem. Soc.* **2011**, *158*, A187.

[9] S. K. Martha, O. Haik, E. Zinigrad, I. Exnar, T. Drezen, J. H. Miners, D. Aurbach, *J. Electrochem. Soc.* **2011**, *158*, A1115.

[10] N. V. Faenza, L. Bruce, Z. W. Lebens-Higgins, I. Plitz, N. Pereira, L. F. J. Piper, G. G. Amatucci, *J. Electrochem. Soc.* **2017**, *164*, A3727.

[11] K. Matsumoto, R. Kuzuo, K. Takeya, A. Yamanaka, *J. Power Sources* **1999**, *558*, 81.

[12] H. S. Liu, Z. R. Zhang, Z. L. Gong, Y. Yang, *Electrochem. Solid-State Lett.* **2004**, *7*, A190.

[13] X. Zhang, W. J. Jiang, X. P. Zhu, A. Mauger, C. M. , Julien, R. Qilu, *J. Power Sources* **2011**, *196*, 5102.

[14] Y. Piao, C.-K. Lin, Y. Qin, D. Zhou, Y. Ren, I. Bloom, Y. Wei, G. Chen, Z. Chen, *J. Power*

Sources **2015**, *273*, 1250.

[15] K. Maher, K. Edström, I. Saadoune, T. Gustafsson, M. Mansori, Electrochim. Acta **2009**, *54*, 5531.

[16] H. Aziam, G. Garhi, Y. Tamraoui, L. Ma, T. Wu, G. L. Xu, B. Manoun, J. Alami, K. Amine, I. Saadoune, *Electrochim. Acta* **2018**, *283*, 1238-1244.

[17] M. Kim, S. Lee, B. Kang, *Adv. Sci.* **2016**, *3*, 1500366.

[18] C. Liu, Z. G. Neale, G. Cao, *Materials Today* **2016**, *19*, 109.

[19] M. S. Whittingham, *Chem. Rev.* **2014,** *114*, 11414.

[20] P. F. Xiao, M. O. Lai, L. Lu, *Solid State Ionics* **2013**, *242*, 10.

[21] L. Croguennec, C. Masquelier, *Chem. Rev.* **2013**, *113*, 6552.

[22] J. M. Tarascon, M. Armand, *Nature* **2001**, *414*, 359.

[23] J. M. Tarascon, B. C. Melot, *Acc. Chem. Res.* **2013**, *46*, 1226-1238.

[24] R. K. B. Gover, P. Burns, A. Bryan, M. Saidi, J. Swoyer, J. Barker, *Solid State Ionics* **2006**, *177*, 2635.

[25] N. V. Kosova, E. T. Devyatkina, A. B. Slobodyuk, A. K. Gutakovskii, *Solid State Electrochem.* **2014**, *18*, 1389.

[26] J. Wang, X. Li, Z. Wang, H. Guo, Y. Zhang, X. Xiong, Z. He, *Electrochim. Acta* **2013**, *91*, 75.

[27] X. Qiao, J. Yang, Y. Wang, Q. Chen, T. Zhang, L. Liu, X. Wang, *J. Solid State Electrochem.* **2012***, 16*, 1211.

[28] J.-C. Zheng, B. Zhang, Z. H. Yang, *J. Power Sources* **2012**, *202*, 380.

[29] J.-X. Wang, Z.-X. Wang, L. Shen, X.-H. Li, H.-J. Guo, W.-J. Tang, Z.-G. Zhu, *Trans.*

Nonferrous Met. Soc. China **2013**, *23*, 1718.

[30] J.-M. Ateba Mba, C. Masquelier, E. Suard, L. Croguennec, Chem. Mater. **2012**, *24*, 1223.

[31] J. Barker, M. Y. Saidi, J. L. Swoyer, *J. Electrochem. Soc.* **2003**, *150*, A1394.

[32] J. Barker, M. Y. Saidi, J. L. Swoyer, *J. Electrochem. Soc.* **2004**, *151*, A1670.

[33] S. Zhong, Z.-L. Yin, Z.-X. Wang, Q.-Y. Chen, *J. Cent. South Univ. Technol.* **2007**, *14*, 340.

[34] Q. Li, Z. Wen, C. Fan, T. Zeng, S. Han, ***RSC Adv.*** **2018**, ***8***, 7044.

[35] Z. Liu, W. Peng, Y. Fan, X. Li, Z. Wang, H. Guo, J. Wang, *J. Alloys Compd.* **2015**, *639*, 496.

[36] H. Yan, X. Wu, Y. Li, *Electrochim. Acta* **2015**, *182*, 437.

[37] Y. Wang, H. Zhao, Y. Ji, L. Wang, Z. Wei, *Solid State Ionics* **2014**, *258*, 169.

[38] Y. Li, Z. Zhou, X. P. Gao, J. Yan, *J. Power Source* **2006**, *160*, 633.

[39] V. Augustyn, P. Simon, B. Dunn, *Energy Environ. Sci.* **2014**, *7*, 1597.

[40] J. Wang, J. Polleux, J. Lim, B. Dunn, *J. Phys. Chem. C* **2007**, *2*, 14925.

[41] T. Brezesinski, J. Wang, J. Polleux, B. Dunn, S. H. Tolbert, *J. Am. Chem. Soc.* **2009***, 131*, 1802.

[42] H.-S. Kim, J. B. Cook, S. H. Tolbert, B. Dunn, *J. Electrochem. Soc.* **2005***, 162*, A5083.

[43] J. B. Cook, H.-S. Kim, Y. Yan, J. S. Ko, S. Robbennolt, B. Dunn, S. H. Tolbert, *Adv. Energy Mater.* **2016***, 6*, 1501937.

[44] J. B. Cook, H.-S. Kim, T. C. Lin, C.-H. Lai, B. Dunn, S. H. Tolbert, *Adv. Energy Mater.* **2016**, *1601283*.

[45] B. K. Lesel, J. S. Ko, B. Dunn, S. H. Tolbert, *ACS Nano* **2016***, 10*, 7572.

[46] B. K. Lesel, J. B. Cook, Y. Yan, T. C. Lin, S. H. Tolbert, *ACS Energy Lett.* **2017**, *2*, 2293.

[47] G. A. Muller, J. B. Cook, H.-S. Kim, S. H. Tolbert, B. Dunn, *Nano Lett.* **2015**, *15*, 1911.

[48] M. G. Fischer, X. Hua, B. D. Wilts, E. Castillo-Martinez, U. Steiner. *ACS Appl. Mater. Interfaces* **2018**, *10*, 1646.

[49] N. K. Sinha, N. Munichandraiah. *J. Electrochem. Soc.* **2010**, *157*, A647.

[50] J. Yue, C. Suchomski, T. Brezesinski, Smarsly, B. M. *ChemNanoMat.* **2015**, *1*, 415.

[51] I. E. Rauda, V. Augustyn, B. Dunn, S. H. Tolbert, *Acc. Chem. Res.* **2012**, *46*, 1113.

[52] K. L. Harrison, C. A. Bridges, C. U. Segre, C. D. Varnado Jr., D. Applestone, C. W. Bielawski, M. P. Paranthaman, A. Manthiram, *Chem. Mater.* **2014**, *26*, 3849.

[53] B. L. Ellis, T.N. Ramesh, L. J. M. Davis, G. R. Goward, L. F. Nazar, *Chem Mater.* **2011**, *23*, 5138.

[54] E. Boivin, J. N. Chotard, M. Menetrier, L. Bourgeois, T. Bamine, D. Carlier, F. Fauth, C. Masquelier, L. Croguennec, *J. Phys. Chem. C* **2016**, *120*, 26187.

[55] J.-M. Ateba Mba, L. Croguennec, N. I. Basir, J. Barker, C. Masquelier, *J. Electrochem. Soc.* **2012**, *159*, A1171.

[56] J. Barker, R. K. B. Gover, P. Burns, A. Bryan, M. Y. Saidi, J. L. Swoyer, *J. Power Sources* **2005**, *146*, 516.

[57] R. Petibon, J. Xia, L. Ma, M. K. G. Bauer, K. J. Nelson, J. R. Dahn, *J. Electrochem. Soc.* **2016**, *163*, A2571.

[58] L. Ma, S. L. Glazier, R. Petibon, J. Xia, J. M. Peters, Q. Liu, J. Allen, R. N. C. Doig, J. R. Dahn, *J. Electrochem. Soc.* **2017**, *164*, A5008.

[59] E. R. Logan, E. M. Tonita, K. L. Gering, L. Ma, M. K. G. Bauer, J. Li, L. Y. Beaulieu, J. R.

Dahn, *J. Electrochem. Soc.* **2018**, *165*, A705.

[60] E. Markevich, G. Salitra, D. F. Aurbach, *ACS Energy Lett.* **2017**, *2*, 1337.

[61] K. Fridman, R. Sharabi, R. Elazari, G. Gershinsky, E. Markevich, G. Salitra, D. Aurbach, A. Garsuch, J. Lampert, *Electrochemistry Communications* **2013**, *33*, 31.

[62] E. Markevich, G. Salitra, K. Fridman, R. Sharabi, G. Gershinsky, A. Garsuch, G. Semrau, M. A. Schmidt, D. Aurbach, Langmuir **2014**, *30*, 7414.

[63] G. Barim, P. Cottingham, S. Zhou, B. C. Melot, R. L. Brutchey, *ACS Appl. Mater. Interfaces* **2017**, *9*, 10813.

[64] P. Barpanda, M. Ati, B. C. Melot, G. Rousse, J. N. Chotard, M. L. Doublet, M. T. Sougrati, S. A. Corr, J. C. Jumas, J. M. Tarascon, *Nat. Mater.* **2011**, *10*, 772.

[65] T. Mueller, G. Hautier, A. Jain, G. Ceder, *Chem. Mater.* **2011**, *23*, 3854.

[66] S. Zhou, G. Barim, B. J. Morgan, B. C. Melot, R. L. Brutchey, *Chem. Mater.* **2016**, *28*, 4492.

[67] N. H. Bashian, S. Zhou, M. Zuba, A. M. Ganose, J. W. Stiles, A. Ee, D. S. Ashby, D. O. Scanlon, L. F. Piper, B. Dunn, B. C. Melot, *ACS Energy Lett.* **2018**, *3*, 2513.

[68] G. He, Q. Pan, G. L. Rempel, *Macromol. Rapid Commun.* **2003**, *24*, 585.

Chapter 7. Using X-ray Microscopy to Understand How Nanoporous Materials can be Used to Reduce the Large Volume Change in Alloy Anodes

7.1. Introduction

Graphite has been used as the anode in most Li-ion batteries for over 20 years because of its ability to reversibly intercalate Li-ions, its high electronic conductivity, its low volume change during cycling, and its long cycle lifetime.[1–4] Even though graphite is a widely used negative electrode in commercial applications, its low capacity for Li-ions (1 Li-ion per 6 carbon atoms) and low density lead to a mediocre gravimetric storage capacity of 372 mAh/g and volumetric storage capacity of 756 mAh/cm^3.[5–7] In response to a desire for higher energy density Li-ion batteries, research on materials that electrochemically alloy with lithium ions has become extremely active because these materials can store significantly more energy through multi-electron processes.[5,8–12] Tin is an attractive candidate for high energy density applications because of its high gravimetric storage capacity of 960 mAh/g and volumetric storage capacity of 1990 mAh/cm^3 combined with high electrical conductivity.[5,13,14] One significant issue that has limited the use of tin in commercial applications (along with most other alloy-type materials) is that tin expands ~300% upon alloying with Li, resulting in the rapid decay of capacity with cycling.[11,13,15–19] These volume changes lead to deformations like cracking and repeated irreversible electrolyte decomposition on these freshly formed cracked surfaces.[16,17,20,21] These degradation processes ultimately lead to electrical isolation of large portions of the active material, which then no longer contribute to the capacity of the battery.

Nanostructuring tin, and other alloy-type materials, is a proven technique to mitigate the abovementioned cycling induced degradation. A common failure mechanism in alloy-type materials arises from inhomogeneous volume changes within a particle due to limited Li-ion diffusion kinetics.[9]

The lithiation tin occurs at the outer surface because this surface is in contact with the electrolyte. The mismatch of lithiation rates within a single particle causes the surface to expand more rapidly than the inner core. This volume mismatch of the lithium rich and lithium deficient phases then lead to interfacial strain build-up. Typically, the strain is relieved by crack propagation, which degrades the active material. Reducing the dimension of the particles decreases the diffusion pathlengths and promotes homogeneous lithiation / delithiation within a single particle. In practice, small tin nanocrystals have been shown to improve cycle lifetimes compared to their bulk counterparts.[22–24] However, the main disadvantage of using small nanocrystals is the large inter-particle contact resistance as a result of these material's intrinsically high surface area.

Nanoporous structures are ideal architectures to resolve the aforementioned issues. The Tolbert group has recently developed methods to create nanoporous tin by selective dealloying of a co-melted Sn/Mg that can be cycled 350 times while retaining over 72% of the initial capacity.[25] This material will be used in the studies presented here. Additionally, various porous silicon[26–32] and porous tin oxide[33–35] architectures have also been shown to significantly increase the cycle lifetimes of these high capacity alloy-type materials compared to the dense non-porous form. While these studies offer practical solutions for increasing the lifetimes of alloy-type materials, it is not well understood how the volume change is actually accommodated in these porous structures.

Various techniques have been used to understand the structural and chemical changes of electrode materials during cycling.[19,36–48] In particular, microscopy techniques such as transmission electron microscopy (TEM), and transmission X-ray microscopy (TXM), especially when performed during the operation of an electrochemical system (*in operando*), are powerful tools to understand the connection between nanoscale architecture and cycling performance. For example, TEM has been used to follow the alloying reaction of a single SnO_2 nanowire, which provided a visual understanding of the lithiation mechanism and the huge anisotropic volume change in those 1-D materials.[19] While

TEM has several advantages, it is generally limited to imaging thin specimens in a small field of view. These constraints preclude the study of thick samples in their native electrode environment so that the TEM results never represent actual operating conditions. TXM addresses these limitations, but had traditionally been limited to micrometer scale resolution.[36] Recent advances in this technology, however, have enabled nanometer scale resolution on Beamline 6-2 at the Stanford Synchrotron Lightsource Laboratory (SSRL).[37–39] The large field of view, high flux, and hard X-ray radiation make this technique well suited for studying battery materials in their native slurry electrode environment with nanoscale resolution. Indeed, TXM has been used for a variety of *in operando* studies, including studies of bulk tin, Li-sulfur, and bulk germanium.[37–43] In all cases, the direct imaging of these active materials during the operation of the battery has led to a fundamental understanding of the mechanisms responsible for structural changes that occur during charge storage.

In this study, we utilize synchrotron based TXM to study the effects of porosity on the volume change occurring in tin during the electrochemical alloying reaction with lithium. We compare micrometer size dense tin to nanoporous tin created by selective dealloying. Our results indicate that the porous nanostructured tin expands significantly less than bulk tin due to the internal void space of the pores. We find that TXM is an excellent method to examine both the nanoscopic changes of the porous material along with the micrometer level changes that are occurring in individual tin particles.

7.2. Results and Discussion

7.2.1. Structural Characterization

We recently reported a novel method for preparing porous tin with a hierarchical granular morphology by selectively dealloying magnesium from a $Sn_{15}Mg_{85}$ alloy.[25] The synthesis method produces 1-10 μm diameter grains that are comprised of an interconnected 3-D nanoporous structure

with ~25% internal porosity. This nanoporous tin (NP-Sn) material showed excellent capacity retention with 72% retention after 350 cycles when cycled in a traditional slurry electrode *vs.* lithium metal. The high reversibility of this material makes this system an ideal platform to study how nanoscale porosity influences electrochemical stability in alloy-type materials.

For this work, we synthesized NP-Sn according to the methods already established in our previous report.[25] The XRD pattern of this dealloyed NP-Sn powder is consistent with tetragonal tin (JPCS no. 00-004-0673). The SEM images shown in Figures 7.1 a and b clearly show the intrinsic porous nanoscale architecture. The backscattered SEM image in Figure 7.1 c shows a NP-Sn particle (bright) in a carbon fiber-based electrode; here the dark striations are carbon fibers. This SEM image demonstrates that the ball milling process used to incorporate the hydrophobic carbon fibers and the NP-Sn into the aqueous binder does not modify the morphology of the NP-Sn. Finally, the TXM image presented in Figure 7.1d, shows the edge of a pristine NP-Sn particle before cycling. The image shows similar spherical pores to those observed in the backscattered SEM image in Figure 7.1b. The TXM image demonstrates the excellent contrast and resolution afforded by this X-ray microscope.

NP-Sn was further analyzed using nitrogen porosimetry (Figure 7.2). The nitrogen isotherm of NP-Sn shown in Figure 7.2 a displays hysteresis above 0.5 P/P_0 indicating the presence of mesoporosity.[49,50] The Barrett-Joyner-Halenda (BJH)[49] cumulative pore volume *vs.* pore width plot in Figure 7.2 b shows that ~60% of the pore volume derives from pores that are within the resolution limit of the microscope on beamline 6-2 at the Stanford Synchrotron Radiation Lightsource (>30 nm). The total pore volume between 20 – 200 nm is 0.045cm^3/g. Using that pore volume, the percent porosity of NP-Sn is calculated to be 25%. The average pore size of NP-Sn was also calculated from the adsorption branch of the nitrogen isotherm using the BJH model (Figure 7.2 c). The peak value on the plot corresponds to the average pore width, which is calculated to be ~70 nm. As we mentioned previously, it is generally accepted that porous structures with smaller pores,

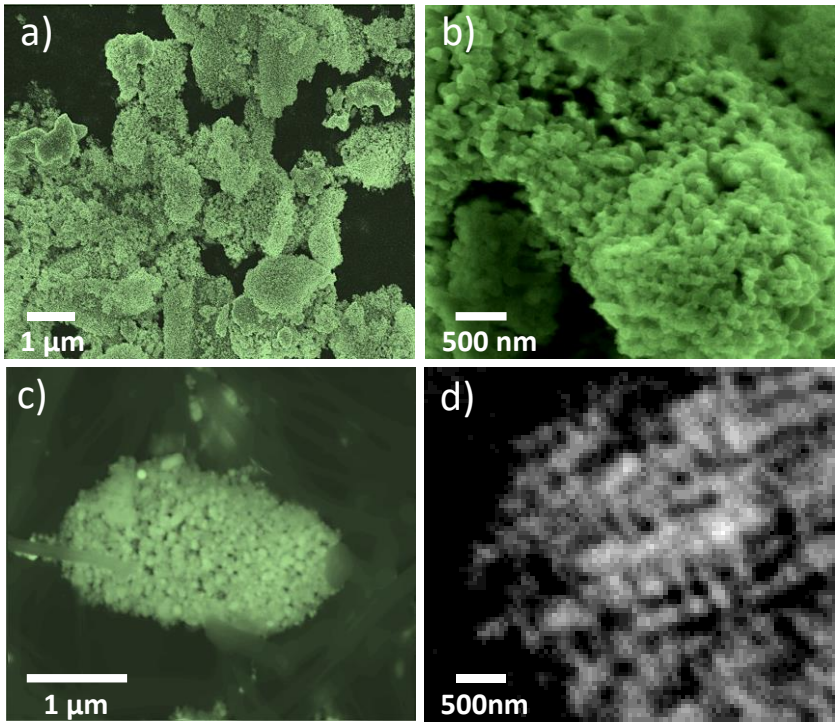

Figure 7.1. Microscopy characterization of NP-Sn. Secondary electron images of NP-Sn showing particles between 1-10 µm that are comprised of an interconnected network of tin nano-ligaments and nano-pores (a,b) Higher resolution images suggest hierarchical porosity extending down to the few nanometer lengthscale. Backscattered image of NP-Sn after ball mill slurry processing showing that these structures are not compromised during the vigorous mixing process (c). Transmission X-ray microscopy image of NP-Sn demonstrating the nano-scale resolution of this technique that allows visualization of many of the nanoscale pores and ligaments (d).

such as the one described here, are better able to accommodate volume expansion and increase cycle lifetimes.[25–29,31,33–35,51] Through *in operando* TXM, we directly observe the mechanisms for this lifetime increase. We expect the results can be applied to various other alloy-type materials like silicon and germanium.

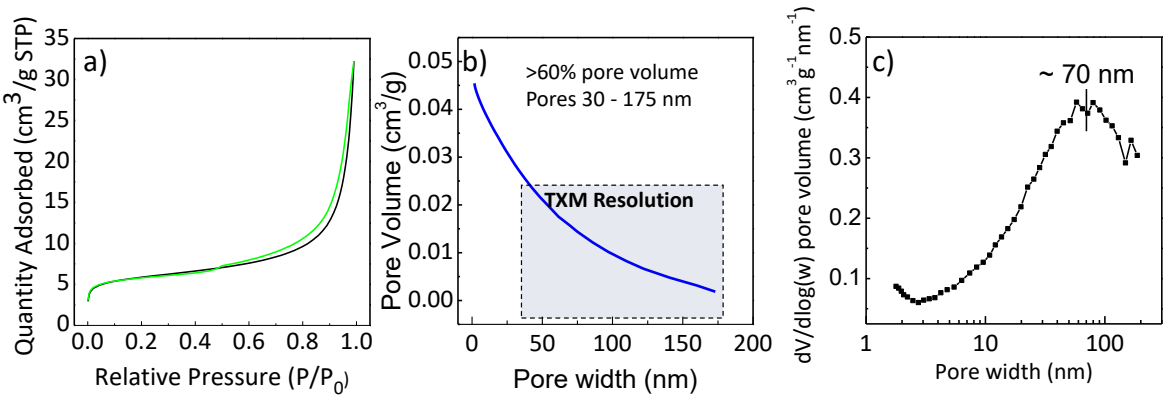

Figure 7.2. Nitrogen adsorption analysis on MP-Sn. Nitrogen isotherm at 77K of NP-Sn displaying hysteretic behavior above 0.6 P/P_0 indicating the presence of meso and macropores (a). Cumulative pore volume *vs.* pore width trace, which was derived from the adsorption branch of the nitrogen isotherm (b). The total pore volume is 0.045 cm^3/g, which is used to calculate the porosity of NP-Sn as ~25%. In addition, this plot shows that more than 60% of the pore volume is within the resolution limit of the transmission X-ray microscope used to study this material. Barrett-Joyner-Halenda pore-size distribution calculated from the adsorption branch of the nitrogen isotherm (c). The average pore size is ~70 nm, and this value is indicated in the plot.

7.2.2. Electrochemistry

The electrochemical lithiation and delithiation of tin proceeds through a number of distinct crystalline Li-tin phases.[52,53] The first crystalline lithiation product of Sn is a Li_2Sn_5 phase, which forms at about 0.760 V *vs.* Li/Li^+ at 25°C.[53] The maximum theoretical capacity of tin is 990 mAh/g, corresponding to the $Li_{22}Sn_5$ phase, which begins to forms around 380 mV *vs.* Li/Li^+ at 25°C.[14,53,54] Volume expansion occurs during lithiation as a result of the added Li volume and the formation of lower density Li-Sn phases. As mentioned above, the porous tin we developed cycles reversibly as a result of its unique nanoscale architecture, despite the large intrinsic volume changes that occur during

alloying of Sn with Li. The cycling lifetime characteristics of micrometer spherical tin powder, and NP-Sn powder in a slurry electrode is shown in Figure 7.3 a, which demonstrates the lifetime enhancement porosity affords this material system. The non-porous tin performs as expected, and quickly fails after ~5 cycles, while NP-Sn delivers its capacity stably over a much longer interval. By comparing the structural evolution of both dense tin and the robust NP-Sn, we aim to develop a structural understanding of just how porous structures accommodate volume expansion during cycling.

For these experiments, X-ray transparent electrochemical pouch cells[8] were galvanostatically cycled to drive the Li insertion and deinsertion process. The galvanostatic traces of dense tin and NP-Sn collected during the *in operando* measurement are shown in Figures 7.3 b and c, respectively. As a result of the nanoporous architecture, the deinsertion process of NP-Sn delivers a deinsertion capacity of 728 mAh/g compared to 588 mAh/g for dense tin, demonstrating better utilization of the active material. The dQ/dV traces of dense tin (Figure 7.3 d) and NP-Sn (Figure 7.3 e) show the typical voltage signatures for the lithiation/delithiation of tin. The dQ/dV profiles for NP-Sn are broader than dense tin due to the high surface area of the material, which has been reported previously.[24] We note that in order to image single NP-Sn particles with TXM, a large percentage of carbon fibers (~55%) was used in these electrodes to decrease the particle loading density, which isolates just a few particles within the microscope's field of view (38 μm). However, this leads to a poor first cycle efficiency (~47%). The carbon fibers used in this study are a graphitic form of carbon with significant crystalline defect density, which tends to trap lithium ions leading to poor reversibility in the carbon fibers component of the electrode.[55] The irreversibility in the first insertion process is thus comprised of irreversibility from solid electrolyte interphase (SEI) formation, along with irreversibility from lithium ion trapping in the carbon fibers. We should note that these processes do not affect the TXM imaging because the X-ray absorption cross-section of these decomposition products are negligible

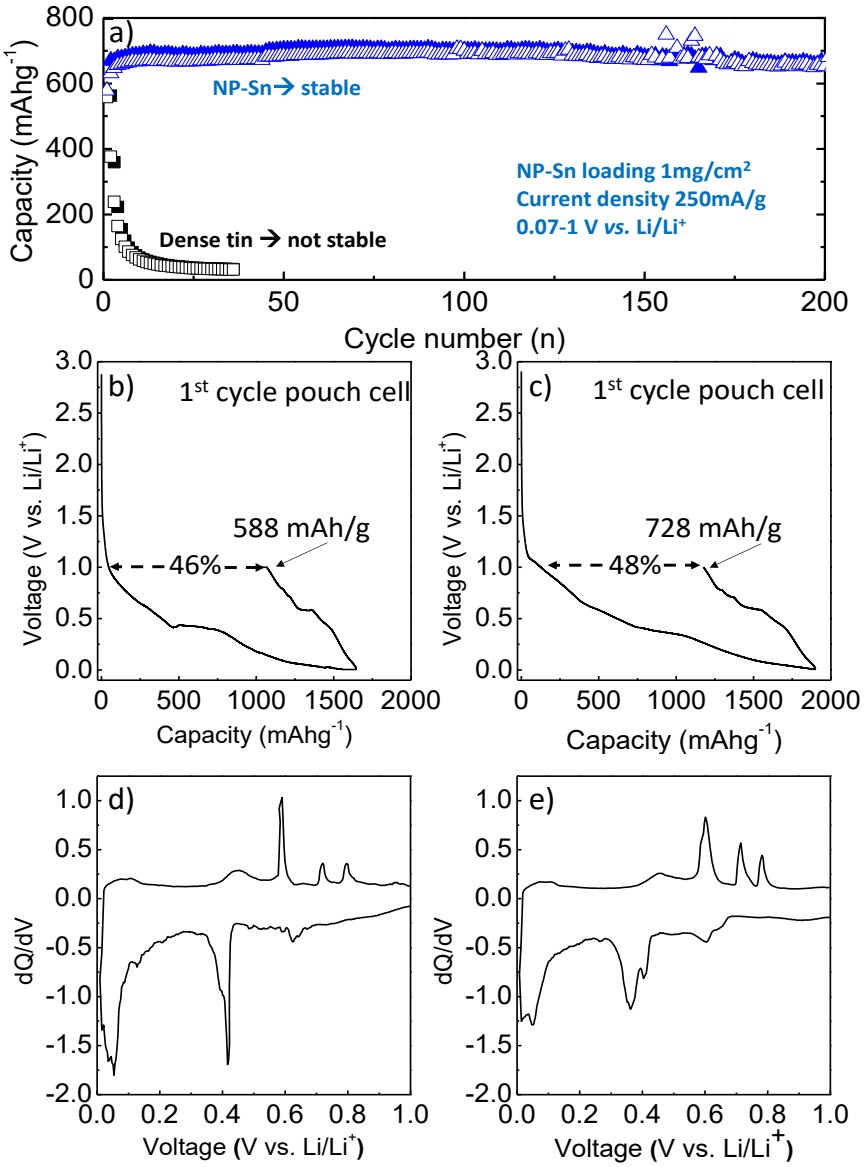

Figure 7.3. Capacity *vs.* cycle number obtained from NP-Sn and dense tin slurry electrodes made with a 65:20:15 ratio of active material:carbon fiber:CMC with a 1 mg/cm² mass loading, cycled at 250 mAh/g (a). Voltage *vs.* capacity plots of dense tin (b) and NP-Sn (c) normalized by only the mass of tin in the electrode collected during the TXM experiment. The current density used for the dense tin electrodes was 356 mA/g, and the current density used for NP-Sn was 724 mA/g. Plots of dQ/dV for dense tin (d) and NP-Sn (e) showing typical profiles for the lithiation/delithiation of tin. The dQ/dV profile for NP-Sn is broadened compared to dense tin, indicative of the nanoscopic nature of the material.

compared to Sn at this X-ray energy and so neither the carbon fibers nor the SEI can be seen. In the following section we display TXM images that correspond to the galvanostatic traces in Figure 7.3, and make correlations between structure and electrochemistry.

7.2.3. Transmission X-ray Microscopy

The images shown in Figure 7.4 were collected from samples in X-ray transparent pouch cells using TXM during continious galvanostatic cycling. Two different 38μm x 38μm regions were imaged (~ 10 - 20 second delay between regions) with a six minute delay between images in the same region. Working directly below the Cu K-shell absorption edge (8.98 keV) afforded excellent X-ray transmission through the 9 μm thick copper current collector and provided excellent contrast between tin and other battery components. The dense tin particle in Figure 7.4 a (top) clearly shows expansion and crack propagation as the Li-concentration increases, which has been reported previously using TXM.[40,42,43] We have defined the percent areal expansion in Equation 7.1.

$$\%\, Areal_{expansion}(E) = \left(\frac{area_E}{area_{OCV}} - 1\right) \cdot 100 \qquad \textit{Equation 7.1}$$

where the areal expansion is a function of the voltage E, and $\mathrm{area_E}$ is the area of the tin particle at voltage E, and $\mathrm{area_{OCV}}$ is the area of the pristine particle at the open circuit voltage (before lithiation).

The areal expansion of this dense tin grain was quantified from these images, using Image J, and is plotted as a function of voltage (Figure 7.4 c, black squares). The areal expansion of this particle increases to 9% at 0.28 V followed by a large expansion to 134% of its original size by 0.05 V. Assuming spherical symmetry and homogenous expansion, geometrically the volume expansion can be estimated from the areal expansion through the geometric relationship in Equation 7.2:

$$\%\, Volume_{expansion} = \left(\sqrt[\frac{3}{2}]{\frac{area_E}{area_{OCV}}} - 1\right) \cdot 100 \qquad \textit{Equation 7.2}$$

Using Equation 2, the calculated volume expansion is 260% of its original size, in agreement with previous reports on tin based materials.[41] Another consideration that effects the reversibility in dense tin is that the volume change mostly occurs at the end of the insertion process, which is also consistent with previous reports.[31] This accelerated expansion is one factor responsible for crack formation, seen in our TXM images, which expose new surfaces to the electrolyte that can undergo reaction with the electrolyte.[31] Figure 7.4 c shows that the particle does not contract back to its original size, most likely because there are non-accessible Li-rich domains within the particle that are either electrically insulated or physically separated from the slurry matrix.[37]

The dramatic expansion observed for dense tin is significantly reduced in NP-Sn (Figure 7.4 a, bottom). The areal expansion of this ~ 5 μm NP-Sn grain was quantified from these images, and plotted as a function of voltage (Figure 7.4 c, green circles). The areal expansion, defined similarly as above, is only 21% compared to the 134% expansion for dense tin – a six-fold decrease. We have estimated this areal expansion to correspond to a volume expansion increase of only 33% of the original size using Equation 2. While this geometric relationship is strictly only valid for spherical symmetry, this analysis does at least provide a reasonable estimation of the volume expansion. As a result of the decreased expansion, no cracks formed during the lithiation or delithiation process. We have also plotted the areal expansion of another larger particle (Figure 7.4 c, red triangles) with a diameter of ~10 μm (particle is shown in Figure 7.5), at the lithiated and delithiated state only. This larger particle appears to expand somewhat more than the smaller particle (50 % areal expansion and 84% volume expansion in the lithiated state), but still contracts back nearly to its original size in the delithiated state (remains just 17% expanded). A full expansion set was not collected on this particle because the edges were in poor focus, making it hard to determine the area. While the expansion apparently depends somewhat on the size of the NP-Sn particles, the areal expansion in this larger tin particle is still nearly three-fold less than the dense tin and much more reversible. The dominating

mechanism for both the reduced expansion and the increase reversibility in these porous particles probably derives from the open porous network that is both flexible, and accommodates the expanding ligaments.

As we mentioned previously, the internal porosity of NP-Sn is ~25%. As a result of this porosity, electrolyte penetrates into the particle and deinsertion is also much more reversible in NP-Sn compared to dense tin. NP-Sn recovers 728 mAh/g capacity while dense tin only recovers 588 mAh/g. This disparity in utilization can be directly seen in the series of TXM images corresponding to the deinsertion process (Figure 7.4 b, top). In contrast to dense tin, which only contracts slightly, the NP-Sn grain contracts back nearly to the same total area as the pristine NP-Sn grain (Figure 7.4 b, bottom). These direct structural observations lead to the understanding that the nanoscale porosity and mechanical flexibility is responsible for the overall reduced expansion and better reversibility, which in turn leads to better utilization of the active material. The long-lifetime observed for NP-Sn is most likely strongly influenced by both of these factors observed here.

Another structural feature of the NP-Sn particle shown in Figure 7.4 b and quantified in Figure 7.4 c, is that it begins to expand sooner (at higher voltage) compared to dense tin, which indicates that the nanoscale architecture influences the lithiation kinetics. The time-scale of the lithiation process in a diffusion controlled system, such as the lithiation of tin, is proportional to the diffusion length squared.[56] Therefore, decreasing the diffusion length by one order of magnitude (e.g. 1 μm to 100 nm), should have an amplified effect of reducing the lithiation time-scales in the nanoporous material by two-orders of magnitude. As a result, the faster kinetics in NP-Sn most likely leads to a more homogeneous lithiation process compared to dense tin, which may lead to the enhanced cycle lifetimes.

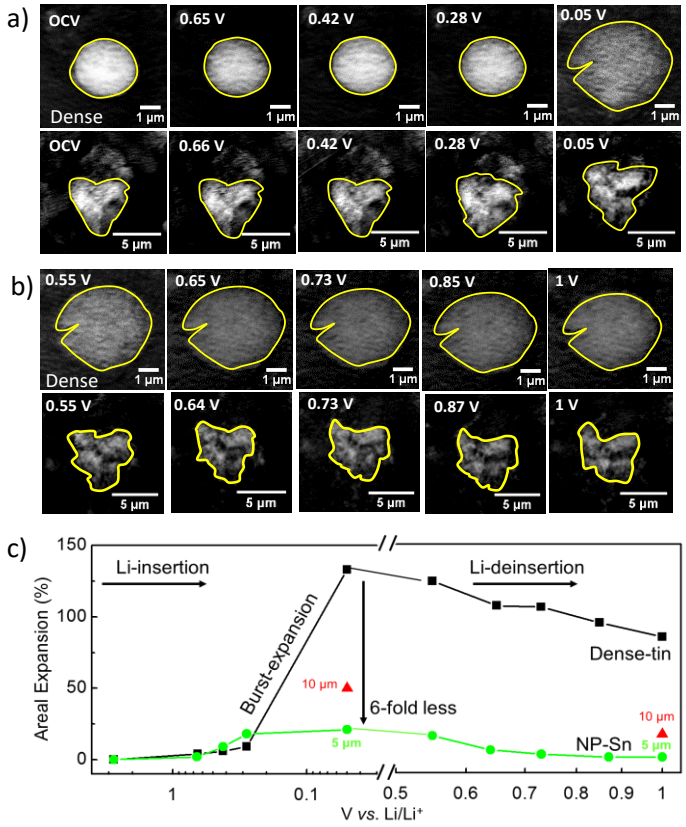

Figure 7.4. Absorption images of dense and nanoporous tin collected using an X-ray transparent pouch cell using a Transmission X-ray microscopeoperating at 8.95 KeV. Decreasing voltage (left-to-right) corresponds to increasing Li-concentrations (a). Dense tin (top) undergoes a burst-expansion mechanism, which occurs predominantly at the end of the insertion process. This process leads to tremendous strain in the material followed by crack formation observed at 0.05V. The NP-Sn (bottom) expands less than dense tin and evolves to the final lithiated state more homogeneously. Increasing voltage (left-to-right) corresponds to decreasing Li-concentrations (b). Dense tin (top) was found to be irreversibly deformed, and does not return to its original shape or size. Cracks formed during lithiation remain in the material. By contrast, the nanostructured NP-Sn (bottom) contracts back nearly to its original size, leading to the long cycle lifetimes of this material. Quantification of the areal expansion of the TXM in this figure (c). Percent areal expansion is shown for dense tin (black-squares), 5 µm NP-Sn (green circles), and 10 µm NP-Sn (red triangles) at different voltages and thus different lithiation states.

In order to further understand the role of porosity in enabling long-term cycle life, a population of individual pores were monitored in a single NP-Sn grain during cycling. While pores are observed in the particle shown in Figure 7.4, those pores are hard to discern and quantify due to the small particle size. To monitor changes in the pores better, we chose to analyze the larger 10 μm NP-Sn grain also shown in Figure 7.4. The center of this NP-Sn grain was in excellent focus throughout cycling and underwent an expansion similar to the smaller ~5 μm NP-Sn particle (Figure 7.5 a).

The evolution of pore size and pore size distribution, in a NP-Sn grain, during cycling is shown in Figure 7.5. Since the same particle is imaged during lithium insertion and deinsertion, the same pores within the NP-Sn particle can be tracked during cycling. As mentioned earlier, the 2D images used in these analyses are projections of the NP-Sn 3D morphology, so we again represent the change in pore sizes in terms of pore area. Because the 2D TXM images are projections of a 3D morphology, the exact pore size and shape cannot be determined exactly from these images. However, they do give a representative size, and can be used to clearly discern changes to the pore system during lithiation and delithiation. We point out that the pores in these absorption based images are distinguished as the dark spots while the lighter portions are the solid ligaments. The clear contrast between the pores and the solid regions enables the pore system to be statistically quantified using image analysis software.

The images shown in Figures 7.5 a-d were used to calculate the statistical information presented in Figures 7.5 e and f. Figure 7.5 a shows an image of our pristine 10 μm grain. Parts b–d show expanded images of a smaller region of the same grain in the pristine, lithiated, and delithiated states. The expanded images were used for statistical analysis. To analyze the images, a series of histograms (number of pores versus individual pore area) were calculated. These histograms were then used to calculate the average pore area and the standard deviation of pore area at each voltage plateau, as shown in Figures 7.5 e and f. The average pore area shows the evolution of the average pore size with lithium insertion and deinsertion. The NP-Sn grain before cycling contains mostly

pores that are < 50 nm. As lithiation proceeds, the number of small pores decreases as some pores grow into the 100-200 nm size range. This produces an increase in average pore size, and a broader pore size distribution. Both the average pore size (Figure 7.5 e) and pore size distribution (Figure 7.5 f), increases during the first charge and discharge, though the change is not fully monotonic.

To more fully understand the changes in porosity, the pores in the NP-Sn grain in the lithiated state can be sorted into two groups: a population of pores that are similar in size to the original porosity before cycling, and a population of larger pores that form as a result of the expansion process. This observation of an increase in pores size is in good agreement with previous work,[57] but it is interesting to find that only part of the pores increase in size upon lithiation. During delithiation, both the average pore size and the distribution remain relative unchanged up to 0.58 V, and then drops significantly at 0.65 V as significant amounts of lithium start to leave the structure. Presumably, the drop in pore size and size distribution at 0.65 V is due to the contraction of NP-Sn grain as higher density tin phases replace lithiated tin. As even more lithium is removed, the bimodal pore size distribution becomes more prominent and both the average pores size and the standard deviation again increase due to a population of very large pores. We hypothesize that the large pores are caused by pore fusion and cracking due to the strain association with pore expansion and contraction. Less strained pores survive the expansion on contraction without fusion, resulting in the overserved bimodal pore size distribution. Potentially, the mechanical flexibility afforded by the smaller pores prevents even more pore evolution, like what is observed in bulk systems. Indeed, like the smaller particle shown in Figure 7.4, no cracks were observed throughout the cycle. These results thus suggest that pore size, pores size distribution, and total grain size all need to be optimized to produce the most stable cycling.

A final feature of the images shown in Figure 7.5 is that the pores appear to remain interconnected throughout the Li alloying and dealloying process. Having an interconnected pore and ligament architecture during charge and discharge is required for good performance. While 3D

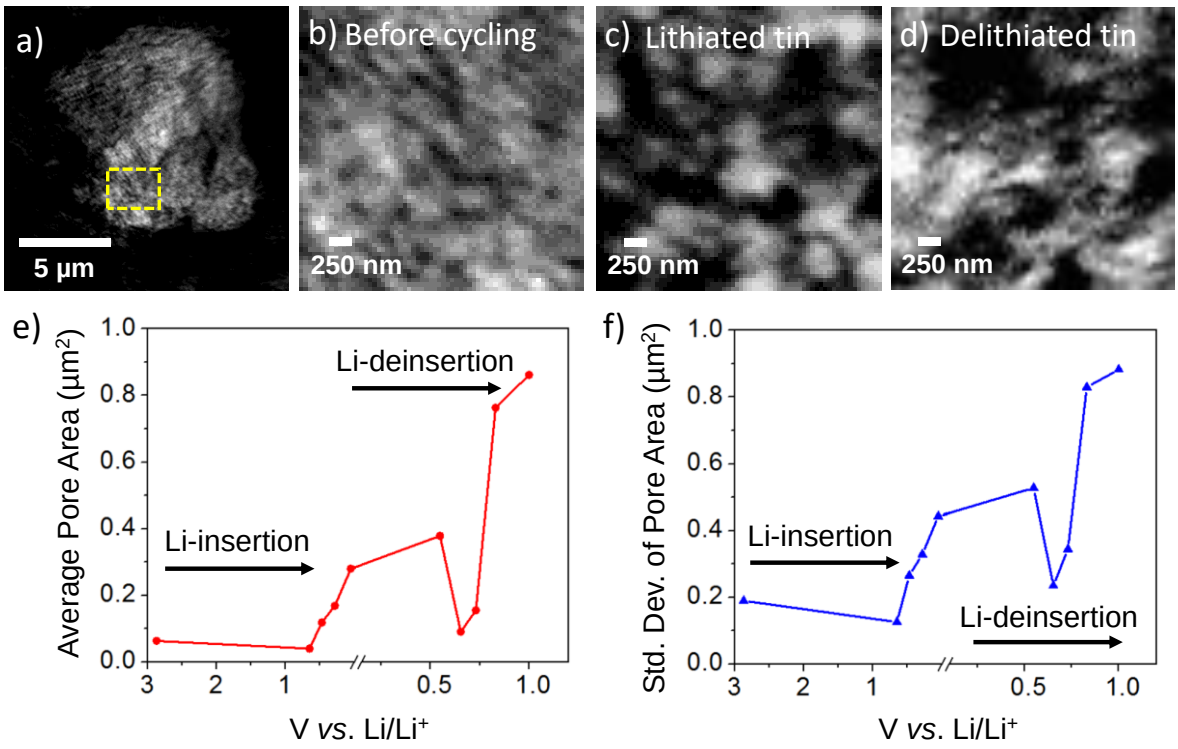

Figure 7.5. Absorption images and pore analysis for a larger NP-Sn collected using TXM; image contrast has been adjusted to increase visibility. Parts (a) shows the full NP-Sn grain used for the pore evolution study. The yellow square indicates the area we focused on in order to track the same pores throughout cycling. Part (b-d) show the magnified TXM images before cycling (b), in the lithiated state (c), and in the delithiated state (d). Panels (e-f) show the average pores size and standard deviation of the pores size at each voltage plateau throughout lithiation and delithiation. Both pore size and pores size distribution increase upon lithiation due to the volume expansion. Pore size and pore size distribution first decrease upon delithiation due to volume contraction. Both metrics then increase at full delithiation as some pores crack and due to the volume change, resulting in a bimodal pores size distribution with a few very large pores. Despite the pore size changes, the interconnections of the nano-tin based ligaments appear to be uninterrupted; interconnected pores and ligaments are fundamental to the favorable performance of this system.

reconstructions, rather than the 2D images shown here would provide more conclusive evidence of connectivity, we found that the samples could not handle the X-ray dose required for tomographic imaging. The 2D TXM images of the NP-Sn, however, do clearly show that the pores do not fully close in the fully lithiated state. Closed pores would prevent effective electrolyte access to the interior of the material, resulting in inhomogeneous Li-ion concentrations, and therefore volume expansion mismatches, which contributes the mechanical failure of bulk materials. In total, several different structural properties all synergistically couple to enable the volume change accommodation and long cycle lifetime in NP-Sn.

7.3. Conclusion

Overall, we found that TXM is a power method for evaluating the structural evolution that occurs with both dense micrometer size grains of tin and nanoporous tin were alloyed with Li. The majority of the degradation in dense tin occurs in the first insertion process. The degradation is exacerbated by the fact that dense tin undergoes a burst expansion upon lithiation, which is mainly attributed to large diffusion lengths and slow diffusion kinetics inherent to dense materials. This process leads to crack formation and presumably thick SEI growth after multiple expansion and cracking cycles. We speculate that the mechanical stability of the carboxymethyl cellulose binder/ carbon fiber matrix is irreversibly deformed during the expansion process and cannot fully contract during the deinsertion process. Ultimately this process may lead to the active material loosing electrical contact with the slurry, resulting in a swift capacity decay.[37]

In stark contrast, we observed that NP-Sn undergoes significantly smaller expansion compared to dense tin. The nanoscale ligaments effectively provide short diffusion pathlengths, which enable homogeneous lithiation. There were no manifestations of cracks during the lithiation and delithiation process of NP-Sn. The pore volume accommodates the lower density Li-rich phases effectively

enabling a six-fold reduction in the areal expansion. We have also demonstrated that NP-Sn particles remain porous in the fully lithiated state. This is an important finding of this study because a closed pore system is not effective at accommodating volume expansion and does not allow the electrolyte to access the active materials between the pores. The synergy between the small interconnected ligaments and the optimal pore space in NP-Sn, combined with the intrinsic flexibility of porous materials, lessen the aggressive failure mechanisms observed in dense tin.[58,59]

Importantly, the conclusions reported here are likely to be generally applicable to other alloy-type anode materials, even if those materials are too low Z to be directly imaged using TXM. We envision that other materials like silicon, antimony, and germanium would benefit from the nanoscale architecture found to be optimal in tin based electrodes. Importantly, our results show that simply adding porosity alone is not sufficient. There appears to be a complex interplay between the pore size, the pore size distribution, and the total particle size, with 5 μm particles showing better reversibility that 10 μm grains. While this complexity may seem daunting, it highlights the potential to use direct imaging to guide the creation of porous anode materials with truly optimized architectures and cycling behavior using highly scalable methods like the dealloying employed here.

7.4. Experimental

7.4.1. Synthesis

The synthesis of nanoporous Sn powder is published elsewhere, but is briefly described here. A $Sn_{15}Mg_{85}$ at.% master alloy was made by melting pure Sn (99.9% Alfa Aesar) and Mg 99.9%, Alfa Aesar) at 700° C in a graphite crucible, using a quartz tube under flowing argon. Mg was selectively removed from the above $Sn_{15}Mg_{85}$ at.% parent alloy by free-corrosion dealloying in 1 M ammonium sulfate. During dealloying, the initially colorless ammonium sulfate solution turns dark grey or black within a few minutes as the parent alloy begins to break apart and the

powder disperses in the solution. After a few minutes, the dark grey solution containing dispersed NP-Sn powder was decanted to separate it from the unreacted Sn/Mg parent alloy, and diluted 2x (or more) with DI water to limit the coarsening of the freshly dealloyed NP-Sn powder. Another 300 mL of 1M ammonium sulfate was then added to the original piece of parent alloy, and the process was repeated multiple times until the Sn/Mg parent alloy was fully dealloyed. The powder was collected by gravity sedimentation, decanted from the mother liquor, and dried at 70°C overnight.

7.4.2. Characterization

Powder X-ray diffraction (XRD) was performed on a PANalytical X'Pert Pro operating with Cu Kα radiation (λ = 1.5418 Å) using a 0.03° step size, a voltage of 45 kV, and a current of 40 mA. XRD patterns were recorded in the range of $10° < 2\theta < 80°$. Nitrogen porosimetry was carried out using a Micromeritics TriStar II 3020. The surface area was calculated from the adsorption branch of the isotherm between (0.04 – 0.30 P/Po) using the Brunauer-Emmett-Teller (BET) model. The pore diameter and pore volume were also calculated from the adsorption branch of the isotherm using the Barret-Joyner-Halenda (BJH) model.

7.4.3. Electrode Preparation

Tin electrodes for standard cycling studies were made from a slurry consisting of 66 wt.% NP-Sn powder, used as the active component for Li storage, 16 wt.% vapor grown carbon fibers (Sigma Aldrich), used as conductive additive, and 18 wt.% carboxymethyl cellulose (M_w=250K, Sigma Aldrich), used as binder. Tin electrodes for TXM imaging were made from a slurry consisting of 25 wt.% NP-Sn powder used as active component for Li

storage, 56 wt.% vapor grown carbon fibers used as conductive additive, and 19 wt.% carboxymethyl cellulose used as binder. In both cases, the three components were mixed together with water by ball-milling in order to obtain a homogeneous thick paste. The slurry was then casted onto 9 μm copper foil (MTI Corp), dried at ambient temperature for 1 h, and further dried at 70° C under vacuum overnight to evaporate the excess solvent. The mass loading of the electrode was ~0.1 – 0.2 mg/cm^2 of active material for the electrodes used for TXM and ~1 mg/cm^2 for the electrodes used for conventional cycling.

7.4.4. *Operando* Transmission X-ray Microscopy

Pouch cells were used for the TXM measurements, and were sandwiched between two aluminium plates with imaging holes.[39] The pouch cells were comprised of 0.5 mm lithium foil as the counter electrode, Celgard (gift from Celgard) soaked in 1 M $LiPF_6$ in a 1:1 ethylene carbonate/dimethylcarbonate solvent (Sigma Aldrich) with 5% (v/v) fluorinated ethylene carbonate (TCI America) as electrolyte, and a porous tin working electrode (described above). Transmission X-ray Microscopy was performed on beamline 6-2C at the Stanford Synchrotron Radiation Lightsource (SSRL), which is part of the SLAC National Accelerator Laboratory. 8.95 KeV X-rays were used to perform investigations of electrode morphology at the nano/meso scale. The X-ray energy was chosen directly below the copper K edge to minimize absorption from the Cu current collector. The spatial resolution of this microscope is ~30 nm, and the field of view at 8.95 KeV is 38.3 μm.

During in operando imaging, the cell was galvanostatically charged and discharged between 1.0 – 0.005V *vs.* Li/Li$^+$ using a current density of 356 mA/g (dense) and 724 mA/g (NP-Sn) using a VSP potentiostat/galvanostat (Bio-Logic). TXM images of two 38.3 μm x 38.3 μm regions in the cell were collected every six minutes during continuous cycling. At each region, ten one-second images

were collected and averaged to improve the signal to noise ratio. A camera binning of two (four pixels are averaged into one) was used to further improve the image quality. These parameters result in a pixel size of 37 nm.

7.4.5. Data Analysis

X-ray micrographs were processed using an in-house developed software package known as TXM-Wizard.[60] The reference correction was done in TXM-Wizard and the images were further processed using ImageJ. The reference corrected images were first converted to 8 bit images in ImageJ in order to linearly scale all pixels within the image to 255 different grey-levels (0 being white and 255 being black). A threshold was then applied to the image to differentiate the grey-level of the particle and the background. Since TXM is an absorption measurement, all features of interest are light while the background is black. The area was then calculated by totalling the number of pixels within the particle after the threshold was applied.

Images used to determine pore size distributions were further processed in ImageJ. A threshold was applied again to the grey scale image described above to convert the 255 grey-levels to black and white. Black and white representations of the porous network provides sharp edges and makes the pore more distinguishable. Black regions (i.e. pores) connected by less than 4 pixels were considered individual domains, and the area of each pore was quantified using ImageJ. For this analysis, we magnified the NP-Sn grain to find a region where pores could be easily distinguished, then counted the number of pores present and the area of each individual pore at each voltage plateau during lithiation and delithiation. Average pore area and the standard deviation of the pores area were also calculated for each voltage plateau. In addition, a series of histograms

with 0.5 μm^2 binning were constructed in an effort to study the change in pore size distribution within NP-Sn upon cycling.

7.5. Reference

[1] S. R. Sivakkumar, A. S. Milev, A. G. Pandolfo, *Electrochim. Acta* **2011**, *56*, 9700.

[2] M. Endo, C. Kim, K. Nishimura, T. Fujino, K. Miyashita, *Carbon* **2000**, *38*, 183.

[3] B. *J.* Scrosati, *Echem. Soc.* **1992**, *139*, 2776.

[4] K. Ozawa, *Solid State Ionics* **1994**, *69*, 212.

[5] N. Nitta, G. Yushin, *Part. Part. Syst. Charact.* **2014**, *31*, 317.

[6] S. R. Sivakkumar, J. Y. Nerkar, A. G. Pandolfo, *Electrochim. Acta* **2010**, *55*, 3330.

[7] H. Buqa, D. Goers, M. Holzapfel, M. E. Spahr, Novák, P. *J. Electrochem. Soc.* **2005**, *152*, A474.

[8] H. Jia, P. Gao, J. Yang, J. Wang, Y. Nuli, Z. Yang, *Adv. Energy Mater.* **2011**, *1*, 1036.

[9] M. T. McDowell, S. W. Lee, W. D. Nix, Y. Cui, *Adv. Mater.* **2013**, *25*, 4966.

[10] C. K. Chan, H. Peng, G. Liu, K. McIlwrath, X. F. Zhang, R. A. Huggins, Y. Cui, *Nat. Nanotechnol.* **2008**, *3*, 31.

[11] D. Larcher, S. Beattie, M. Morcrette, K. Edström, J.-C. Jumas, J.-M. Tarascon, *J. Mater. Chem.* **2007**, *17*, 3759.

[12] W. J. Zhang, *J. Power Sources* **2011**, *196*, 13.

[13] C.-M. Park, J.-H. Kim, H. Kim, H.-J. Sohn, *Chem. Soc. Rev.* **2010**, *39*, 3115.

[14] C. J. Wen, R. A. Hugglns, *J. Echem. Soc.* **1976**, *128*, 1181.

[15] I. A. Courtney, J. R. Dahn, *J. Electrochem. Soc.* **1997**, *144*, 2045

[16] R. A. Huggins, W. D. Nix, *Ionics* **2000**, *6*, 57.

[17] L. Y. Beaulieu, K. W. Eberman, R. L. Turner, L. J. Krause, J. R. Dahn, *Electrochem. Solid-State*

Lett. **2001**, *4*, A137.

[18] J. O. Besenhard, J. Yang, M. Winter, *J. Power Sources* **1997**, *68*, 87.

[19] J. Y. Huang, L. Zhong, C. M. Wang, J. P. Sullivan, W. Xu, L. Q. Zhang, S. X. Mao, N. S. Hudak, X. H. Liu, A. Subramanian, H. Fan, L. Qi, A. Kushima, J. Li, *Science* **2010**, 1515.

[20] X. H. Liu, H. Zheng, L. Zhong, S. Huang, K. Karki, L. Q. Zhang, Y. Liu, A. Kushima, W. T. Liang, J. W. Wang, J.-H. Cho, E. Epstein, S. A. Dayeh, S. T. Picraux, T. Zhu, J. Li, J. P. Sullivan, J. Cumings, C. Wang, S. X. Mao, Z. Z. Ye, S. Zhang, J. Y. Huang, *Nano Lett.* **2011**, *11*, 3312.

[21] V. A. Sethuraman, M. J. Chon, M. Shimshak, V. Srinivasan, P. R. Guduru, *J. Power Sources* **2010**, *195*, 5062.

[22] L. Ding, S. He, S. Miao, M. R. Jorgensen, S. Leubner, C. Yan, S. G. Hickey, A. Eychmüller, J. Xu, O. G. Schmidt, *Sci. Rep.* **2014**, *4*, 1.

[23] H. S. Im, Y. J. Cho, Y. R. Lim, C. S. Jung, D. M. Jang, J. Park, F. Shojaei, H. S. Kang, *ACS Nano* **2013**, *7*, 11103.

[24] Xu, L.; Kim, C.; Shukla, A. K.; Dong, A.; Mattox, T. M.; Milliron, D. J.; Cabana, J. *Nano Lett.* **2013**, *13*, 1800–1805.

[25] E. Detsi, S. H. Tolbert, S. Punzhin, J. T. M. De Hosson, *J. Mater. Sci.* **2015**, *51*, 615.

[26] K. Nishio, S. Tagawa, T. Fukushima, H. Masuda, *Electrochem. Solid-State Lett.* **2012**, *15*, A41.

[27] M. Ge, X. Fang, J. Rong, C. Zhou, *Nanotechnology* **2013**, *24*, 1.

[28] H. Kim, B. Han, J. Choo, J. Cho, *Angew. Chem. Int. Ed.* **2008**, *47*, 10151.

[29] Y. Yu, L. Gu, C. Zhu, S. Tsukimoto, P. A. van Aken, J. Maier, *Adv. Mater.* **2010**, *22*, 2247.

[30] H. Jia, P. Gao, J. Yang, J. Wang, Y. Nuli, Z. Yang, *Adv. Energy Mater.* **2011**, *1*, 1036.

[31] W. Chen, Z. Fan, A. Dhanabalan, C. Chen, C. Wang, *J. Electrochem. Soc.* **2011**, *158*, A1055.

[32] N. Liu, K. Huo, M. T. McDowell, J. Zhao, Y. Cui, *Sci. Rep.* **2013**, *3*, 1.

[33] J. Ba, J. Polleux, M. Antonietti, M. Niederberger, *Adv. Mater.* **2005**, *17*, 2509.

[34] Y. Jiao, D. Han, Y. Ding, X. Zhang, G. Guo, J. Hu, D. Yang, A. Dong, *Nat. Commun.* **2015**, *6*, 1.

[35] V. Etacheri, G. A. Seisenbaeva, J. Caruthers, G. Daniel, J.-M. Nedelec, V. G. Kessler, V. G. Pol, *Adv. Energy Mater.* **2015**, *5*, 1401289.

[36] P. R. Shearing, L. E. Howard, P. S. Jørgensen, N. P. Brandon, S. J. Harris, *Electrochem. Commun.* **2010**, *12*, 374.

[37] J. N. Weker, N. Liu, S. Misra, J. C. Andrews, Y. Cui, M. F. Toney, *Energy Environ. Sci.* **2014**, *7*, 2771.

[38] J. N. Weker, M. F. Toney, *Adv. Funct. Mater.* **2015**, *25*, 1622.

[39] J. Nelson, S. Misra, Y. Yang, A. Jackson, Y. Liu, H. Wang, H. Dai, J. C. Andrews, Y. Cui, M. F. Toney, J. C. Andrews, *J. Am. Chem. Soc.* **2012**, *134*, 6337.

[40] J. Wang, Y.-C. K. Chen-Wiegart, J. Wang, *Angew. Chem. Int. Ed.* **2014**, *53*, 4460.

[41] M. Ebner, F. Marone, M. Stampanoni, V. Wood, *Science* **2013**, *342*, 716.

[42] S. C. Chao, Y. F. Song, C. C. Wang, H. S. Sheu, H. C. Wu, N. L. Wu, *J. Phys. Chem. C* **2011**, *115*, 22040.

[43] S. C. Chao, Y. C. Yen, Y. F. Song, Y. M. Chen, H. C. Wu, N. L. Wu, *Electrochem. Commun.* **2010**, *12*, 234.

[44] R. E. Ruther, H. Dixit, A. M. Pezeshki, R. L. Sacci, V. R. Cooper, J. Nanda, G. M. Veith, *J. Phys. Chem. C* **2015**, *119*, 18022.

[45] J. B. Cook, H.-S. Kim, Y. Yan, J. S. Ko, S. Robbennolt, B. Dunn, S. H. Tolbert, *Adv. Energy Mater.* **2016**, *6*, 1501937.

[46] H.-S. Kim, J. B. Cook, S. H. Tolbert, B. Dunn, *J. Electrochem. Soc.* **2015**, *162*, A5083.

[47] C. R. Becker, K. E. Strawhecker, Q. P. McAllister, C. A. Lundgren, *ACS Nano* **2013**, *7*, 9173.

[48] Q. Shi, L. J. Rendek, W.-B. Cai, D. A. Scherson, *Electrochem. Solid-State Lett.* **2001**, *4*, A101.

[49] E. P. Barrett, L. G. Joyner, P. P. Halenda, *J. Am. Chem. Soc.* **1951**, *73*, 373.

[50] S. Brunauer, L. S. Deming, W. E. Deming, E. Teller, *J. Am. Chem. Soc.* **1940**, *1139*, 1723.

[51] H. Jia, P. Gao, J. Yang, J. Wang, Y. Nuli, Z. Yang, *Adv. Energy Mater.* **2011**, *1*, 1036.

[52] K. J. Rhodes, R. Meisner, M. Kirkham, N. Dudney, C. Daniel, *J. Echem. Soc.* **2012**, *159*, A294.

[53] M. Winter, J. O. Besenhard, *Electrochim. Acta* **1999**, *45*, 31.

[54] J. Wang, R. A. Huggins, *Electrochem. Sci. Technol.* **1986**, *133*, 457.

[55] M. Endo, Y. A. Kim, T. Hayashi, K. Nishimura, T. Matusita, K. Miyashita, *Carbon* **2001**, *39*, 1287.

[56] H. Zhang, X. Yu, P. V. Braun, *Nat. Nanotechnol.* **2011**, *6*, 277.

[57] Q. Chen, K. Sieradzki, *Nat. Mater.* **2013**, *12*, 1102.

[58] E. Detsi, S. Punzhin, J. Rao, P. R. Onck, J. T. M. De Hosson, *ACS Nano* **2012**, *6*, 3734.

[59] J. Biener, A. Hodge, J. Hayes, *Nano Lett.* **2006**, *6*, 2379.

[60] Y. Liu, F. Meirer, P. A. Williams, J. Wang, J. C. Andrews and P. Pianetta, *J. Synchrotron Radiat.*, 2012, **19**, 281.

Chapter 8. Understanding the Stabilization Mechanism in Nanoporous Intermetallic Alloy Anodes through *Operando* Transmission X-ray Microscopy

8.1. Introduction

In recent years, alloying anodes have received tremendous attention due to their high energy density. Though current Li-ion battery (LIB) technology satisfies the need for consumer electronics, it is not ideal for larger applications such as electrical vehicles (EVs) and grid scale storage. Today, approximately 7000 LIBs are installed in a Tesla roadster in order to achieve its quick acceleration and mileage comparable to tradition vehicles that relies combustion engines.[1] With the high capacity of alloying anodes (at least 2 times more than graphite), the gravimetric and volumetric energy density of LIBs can be significantly increased, leading to lighter weight and lower cost battery packs.[2-4]

Among all alloying anodes, Si, Sn and Sb are the most attractive due to their high capacities (4200 mAh/g or 9786 mAh/cm^3, 994 mAh/g or 7246 mAh/cm^3, and 660 mAh/g or 4422 mAh/cm^3, respectively), low market price and safety.[3,5] Though Si's gravimetric energy density is much higher than Sn and Sb, they all have comparable volumetric densities.[6] The main advantages of Sn and Sb are their metallic properties and high electrical conductivities that are 3 folds higher than metalloid Si.[6,7] Alloying anodes have high energy densities because they go through a multiple electron process as they alloy with Li^+ to form Li-rich phases during charge. Unfortunately, this results in large volume change and significant structural reconstruction as alloying anodes accommodate multiple Li^+ in their lattices.[8-11] In addition, the slow Li^+ diffusion in these materials typically gives rise to a Li-poor and Li-rich core-shell structure during lithiation.[12,13] This volume mismatch can lead to substantial interfacial strain within a particle and lead to crack propagation and capacity fade over time. This downfall has limited the potential of alloying anodes in commercial batteries. Recently, small amount of Si (only ~15%) has been incorporated into graphite anodes for EVs to improve the energy densities

of the LIBs without sacrificing the lifetime.[14, 15] However, commercial devices with high content alloying elements have yet to be realized.

To overcome these challenges, many different nanostructures of alloying anodes such as nanocrystals, [16-19] nanorod, [20-22] and nanoporous networks [23-25] have been made. Nanostructuring is known to 1) improve Li^+ diffusion as the diffusion path length shortens, therefore facilitating a homogeneous lithiation/delithiation process [13,26] and 2) reduce the strain in the active material during volume expansion through the stress relaxation effect.[27-29] Stress relaxation is observed when the stress response decreases in a material under the same amount of strain applied to another specimen.[30,31] In bulk materials, structures typically stay in the strained condition for a finite interval of time, which can cause certain amount of plastic strain, leading to dislocation and crack formation. On the other hand, strain can be readily dissipated in nanomaterials, reducing the overall stress response. Among all nanostructures, a nanoporous network composed of a conductive skeleton made of interconnected metallic linkages with high porosity has many advantages because it mitigates agglomeration and the large contact resistance that result nanocrystal based materials. Furthermore, nanoporous networks are mechanically flexible to accommodate the volume expansion.[27,32,33]

From our previous studies, we have demonstrated the improvement in cycling capabilities and lifetimes using nanoporous materials in comparison to micron-sized particles and nanocrystals.[25,34] Nanoporous tin (NP-Sn) showed cycling stability over 200 cycles with 93% capacity retention (650 mAh/g) while bulk tin (micron-sized powder) lost capacity in less than 10 cycles. This NP-Sn also outperformed tin nanocrystals that showed 80% capacity retention after only 70 cycles.[35] *Operando* TXM revealed that NP-Sn showed much less volume expansion during cycling than bulk Sn, which also cracked upon lithiation. More interestingly, the pores in NP-Sn remained open throughout the entire cycle, allowing for good ion and electrolyte diffusion across the active material. Unfortunately,

even though the overall structural stability was improved in comparison to the bulk, some degree of pore wall degradation was observed.

To enhance the mechanical stability of NP-Sn, a secondary metal can be incorporated.[36,37] Intermetallics are attractive because the additional metal can act as a conductive buffer while the other metal alloys with Li^+. Common intermetallics for tin includes SnNi,[38-40] SnCu,[41,42] SnCo [43,44] and SbSn [20,45-52] with only SbSn consisting of two Li^+ active metals. An inactive component (no capacity contribution) is not ideal because it can significantly reduce both the gravimetric and volumetric energy densities, which are important performance metrics. During lithiation, Sb first alloys with Li^+ at ~ 0.8 V followed by the alloying reaction of Li^+ with Sn (~ 0.7 V).[37] This spreads-out the lithiation process and allows the active material to have a non-reactive component at all times to stabilize the overall structural change and maintain good electrical contact. Here, we report a nanoporous antimony tin (NP-SbSn) powder with good cycling stabilities (595 mAh/g after 100 cycles with 93% capacity retention) and improved structural integrity, as demonstrated from a series of *operando* transmission X-ray microscopy (TXM) studies aimed at understanding the stabilization mechanism of Sb in the nanoporous structure.

8.2. Results and Discussion

8.2.1. Material and Characterization

Selective etching, also known as dealloying is a simple and facile method commonly used to synthesize nanoporous metals. It is a top-down technique where a more chemically active element is selectively removed from a dense parent alloy using acidic or basic electrolytes, sometimes in combination with a bias voltage. It is an easily scalable synthesis that has been incorporated into the experimental designs to meet the important requirements for commercial battery electrodes processing. Nanoporous metal powders produced in this manner can then be directly integrated into

composite electrodes using commercial battery electrode processing lines and are viable for large-scale fabrication of nanostructured materials.

To make NP-SbSn, excess Sn is etched away from the parent alloy $Sb_{20}Sn_{80}$ at.% with 4M HBr. X-ray diffraction in Figure 8.1a shows that the parent alloy consists of two phases: Rhombohedral intermetallic *β*-SbSn (*R-3m space group*, JCPD No. 00-001-0830) and tetragonal tin (I41/*amd space group*, JCPD No. 01-086-2265), which are in agreement with the phase diagram of Sb-Sn.[53,54] During dealloying, excess Sn reacts with HBr to form hydrogen gas and $SnBr_2$, which is readily soluble in water, leaving only the intermetallic *β*-SbSn behind and breaking the material up into micron scale pieces.[55] Sn in the intermetallic *β*-SbSn phase is also etched, but it does not get etched completely because the alloy composition is close to the percolation threshold of dealloying, which is the miminum geometric criterion required for the non-noble atoms to be connected.[56] With this discontinuity, the etchant cannot readily access the non-noble atoms. As XRD shows, the crystal structure of the as dealloyed NP-SbSn well matches the *β*-SbSn phase found in the parent alloy, *R-3m space group* (JCPD No. 00-001-0830). The reaction scheme for this process is proposed in equation 8.1.

$$\beta\text{-SbSn} + \text{Sn} + 2\text{HBr} \rightarrow \beta\text{-SbSn} + \text{SnBr}_2 + \text{H}_2 \qquad \textbf{\textit{Equation 8.1}}$$

During dealloying, metal clusters of *β*-SbSn and porosity form as the surface rearranges under the absence of Sn. The porous structure of NP-SbSn can be seen in the scanning electron microscopy (SEM) images shown in Figures 8.1b and 8.1c. These NP-SbSn powder are constructed from interconnected micron-sized particles with macropores in between due to their random arrangement. At higher magnification, secondary pores can be found on the surfaces of the particles. These secondary pores (20-50 nm) and the nanoporous structure are also illustrated in the transmission electron microscopy (TEM) image in Figure 8.1d.

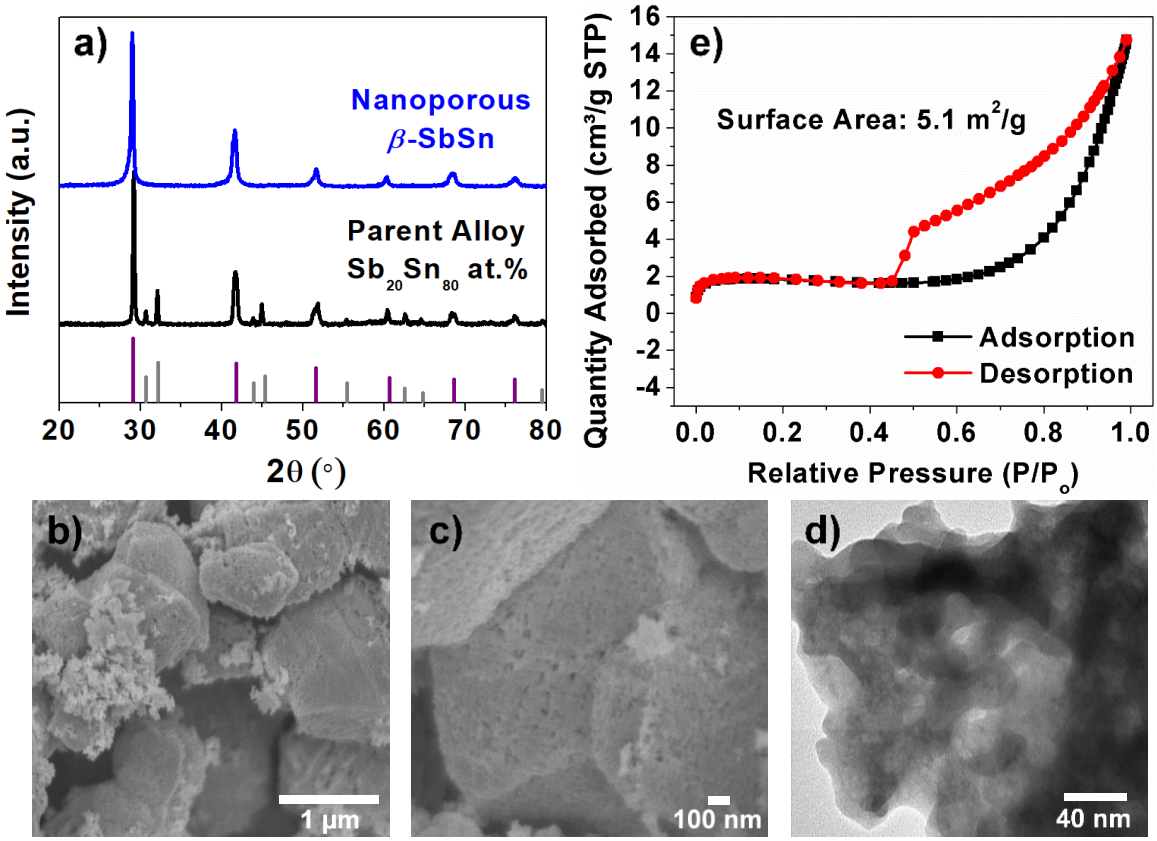

Figure 8.1. a) X-ray diffraction pattern of the parent alloy and the as dealloyed NP-SbSn. b-c) SEM images of the NP-SbSn at low and high magnifications. d) TEM image of the NP-SbSn. e) N_2 porosimetry isotherm of the nanoporous structure.

The total surface area of NP-SbSn iscalculated from the Brunauer-Emmett-Teller (BET) from the N_2 porosimetry measurement. NP-SbSn, with a surface area of 5.1 m^2/g, exhibits a type II adsorption-desorption isotherm (Figure 8.1e), representing materials with both macropores and mesopores. Interestingly, the H4 hysteresis observed in the isotherm suggests that these pores could possibly be slit-like.[57] The pore size distribution is also calculated from the Barret-Joyner-Halenda (BJH) models as shown in Figure ESI1. The average pore size of the mesopores is approximately 30 nm and the calculated fractional porosity from the bulk density and the single point pore volume is 24%. These results are consistent with the porosity observed in the SEM and TEM images.

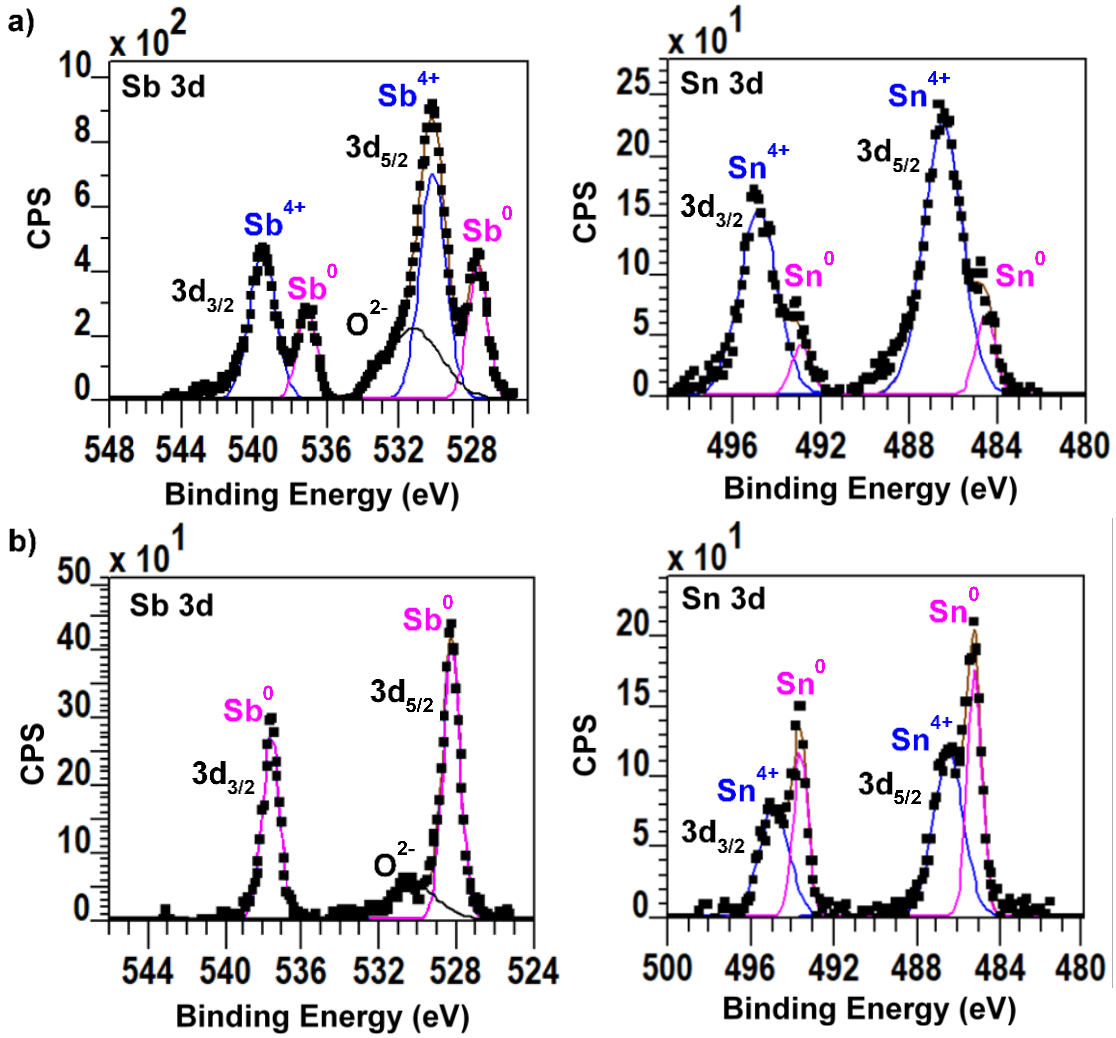

Figure 8.2. X-ray Photoelectron Spectroscopy of np-SbSn a) before Ar^+ etch and b) after etch. Most of the oxide layer was gone after the Ar^+ etch, suggesting that the surface oxide layer is thin.

X-ray photo-electron spectroscopy (XPS) was carried out to characterize the surface chemical composition of the NP-SbSn. The high resolution XPS spectra of Sb 3d/O 1s and Sn 3d signals are shown in Figure 8.2a. The Sb 3d trace is composed of 2 sets of the spin-orbit doublets corresponding to Sb $3d_{3/2}$ and Sb $3d_{5/2}$. The signals are fitted and assigned to two chemical states. The $3d_{3/2}$ peaks at

539.6 eV and 537.2 eV correspond to Sb [58] and SbO_2[59], respectively. Two oxidation states corresponding to Sn and SnO_2 were also fitted in the Sn 3d spectra. The binding energy at 484.7 eV matches metallic Sn [60] while 486.6 eV agrees well with SnO_2.[61] The binding energy of 531 eV in the O 1s spectrum, which overlaps with Sb $3d_{5/2}$, corresponds to the oxygen in SbO_2 and SnO_2.[**Error! Bookmark not defined.,Error! Bookmark not defined.**] This indicates the presence of a thin oxide layer on NP-SbSn surfaces that is likely formed during the DI water washing steps after dealloying. Because zero valent metal can still be observed, despite the low penetration depth of the XPS experiment, we know that the oxide layer is only a nm or two thick. To unravel the chemical composition below the outermost surface, another set of XPS data was collected after an Ar^+ etch (Figure 8.2b). Similar metallic Sb and Sn peaks were observed before and after etch, but the Sb^{4+} peak at 539.6 eV disappears and the Sn^{4+} from SnO_2 at 486.6 eV decreases in intensity in the etched XPS spectrum.

8.2.2. Electrochemistry

The electrochemical performances of NP-SbSn are investigated in half cells against lithium metal using both cyclic voltammetry (CV) and galvanostatic cycling (GV). The CV curves (Figure 8.3a) of the first five cycles were obtained at 0.1 mV/s from 0.05V-1.5V. Due to the native oxide layer (SbO_2/SnO_2) and the formation of solid electrolyte interphase (SEI), a slightly different redox signature is observed in the first cycle..[52,62,63] The reduction peak at 0.75V corresponds to the decomposition of SbO_2 and SnO_2 to Sb and Sn metals. This is immediately followed by a series of lithium intercalation into Sb and Sn to form their alloying phase. The reaction pathway for this process is summarized in Equation 8.2-8.4. Note that the Li-Sb alloying reaction and the electrolyte decomposition also occur around 0.75V, resulting in peak asymmetry and large current response. In the subsequent cycles, a doublet at 0.81V is observed as lithium alloys with Sb to form the intermediate phase Li_2Sb and the lithiated phase Li_3Sb during discharge.[16] Starting around 0.6V, metallic Sn then

alloys with lithium through three major phase transitions, Li_2Sn_5, β-LiSn and finally $Li_{4.4}Sn$.[37,64] During charge, the corresponding peaks can be matched onto the oxidation peaks of Sn (0.6V, 0.73V, 0.8V) and Sb (1.1 V).

$$(SbO_2, SnO_2)_{surface} + xLi + xe^- \rightarrow yLi_2O + (Sb, Sn)_{surface} \qquad \textit{Equation 8.2}$$

$$(Sb, Sn)_{surface} + SnSb + 3Li^+ + 3e^- \leftrightarrow Li_3Sb + Sn \qquad \textit{Equation 8.3}$$

$$Li_3Sb + Sn + yLi + ye^- \leftrightarrow Li_3Sb + LiySn \ (0 \leq y \leq 4.4) \qquad \textit{Equation 8.4}$$

Figure 8.3b shows the galvanostatic charge and discharge curves of NP-SbSn collected at 0.25C from 0.05V to 1.5V. During the first cycle, NP-SbSn delivered 861 mAh/g on discharge and 562 mAh/g on charge. This first cycle irreversibility (65%) can be attributed to the SEI formation and the reduction of the surface oxides on the NP-SbSn. After the formation of a stable SEI on the first cycle, the charge capacity and the coulombic efficiency of the subsequent cycles significantly improved as shown in the GV curves of the 2nd, 5th, 10th and 25th cycle. This stability is further demonstrated in the long-term cycling study (Figure 8.3c) where 595 mAh/g of charge capacity is attained after 100 cycles at 0.25C with 99% capacity retention.

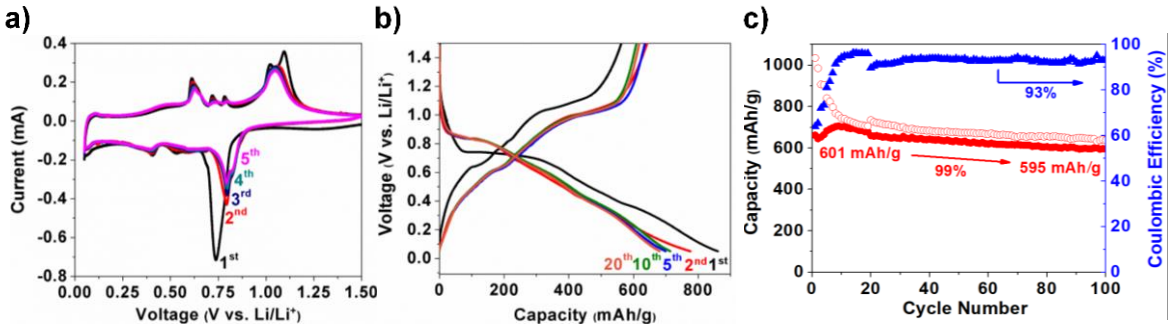

Figure 8.3. a) CV curves of the first five cycles of NP-SbSn at 0.1 mV/s. b) charge and discharge profiles the 1st, 2nd, 5th, 10th, and 20th cycle of NP-SbSn. c) Long term cycle lifetime study of NP-SbSn up to 100 cycles at 0.2C.

8.2.2. *Operando* X-ray Transmission Microscopy Study

To understand the role of Sb in improving the structural stability, *operando* TXM was performed at Stanford Synchrotron Radiation Lightsource (SSRL) beamline 6-2. 2D X-ray images were collected continuously during electrochemical cycling on multiple particles to ensure the changes in the particles and pore sizes are representative of the active material. TXM is a very powerful tool and has been used to study many systems to understand their morphological and chemical changes during electrochemical cycling.[12,65-68]. From our previous *operando* TXM study on NP-Sn, some structural change (particle shape change) was observed due to pore wall degradation during lithium intercalation and deintercalation, despite the fact that NP-Sn demonstrated good cycling capabilities and less volume expansion than bulk tin (Figure 8.4a). This particle shape change was not observed in NP-SbSn during cycling, as seen in Figure 8.4b due to the improved mechanical stability. Even though NP-SbSn experiences similar volume expansion as NP-Sn, 59% and 50% (Figure 8.4c) respectively, the shape of the NP-SbSn particles stayed identical throughout lithiation and delithiation. The presence of a non-reacting component at all times apparently prevents dramatic restructuring of the active material and allows the particle to preserve its shape.

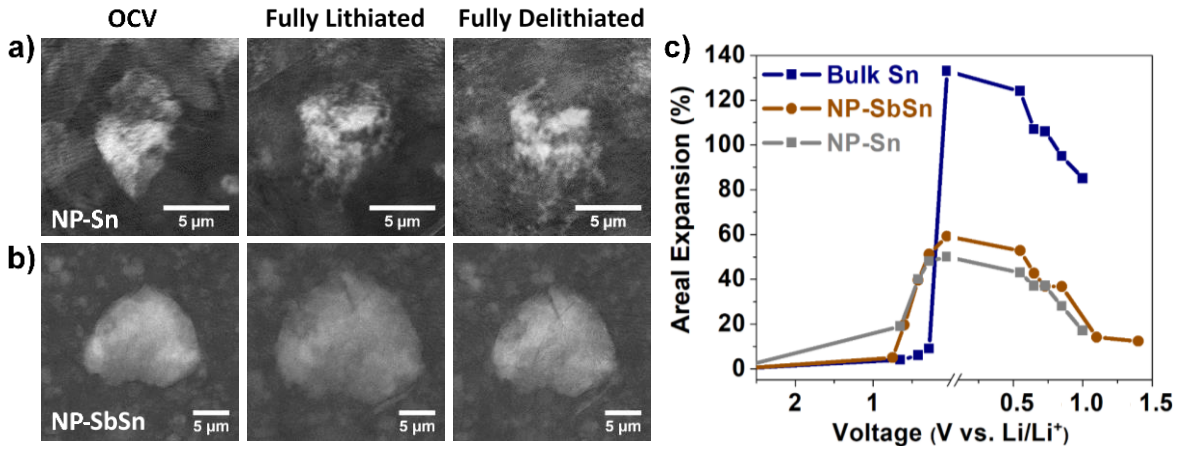

Figure 8.4. Adsorption images of a) NP-Sn and b) NP-SbSn at OCV, fully lithiated and delithiated state c) The areal expansion of bulk and NP-Sn and NP-SbSn throughout the first cycle.

In addition to the shape retention, the improved structural integrity can also be seen in the pore size evolution throughout cycling. With NP-Sn, a significant increase in average pore size was measured by the end of the cycle due to pore wall degradation and the merging of neighboring pores. This process is briefly described here, but a detailed analysis can be found in our previous study.[34] When NP-Sn started to lithiate, the pores size decreased as the pore walls expanded into the void spaces. As lithiation continued, the pore walls eventually brake, causing neighboring pores to merge. This fragmentation unfortunately continued throughout delithiation, resulting in a bimodal pores size distribution by the end of the cycle: a new population of larger pores formed by pore merging is observed in addition to the original small pores that survive the alloying process. This bimodal distribution can be clearly seen in figure 6b after delithiation.

A very different pore size evolution was observed for the NP-SbSn (Figure 8.5a). In NP-SbSn, pores contracted significantly during lithiation due to pore wall expansion as lithium alloys with SbSn to form Li_3Sb and $Li_{4.4}Sn$. Importantly, during delithiation, the pores grow back to their original size

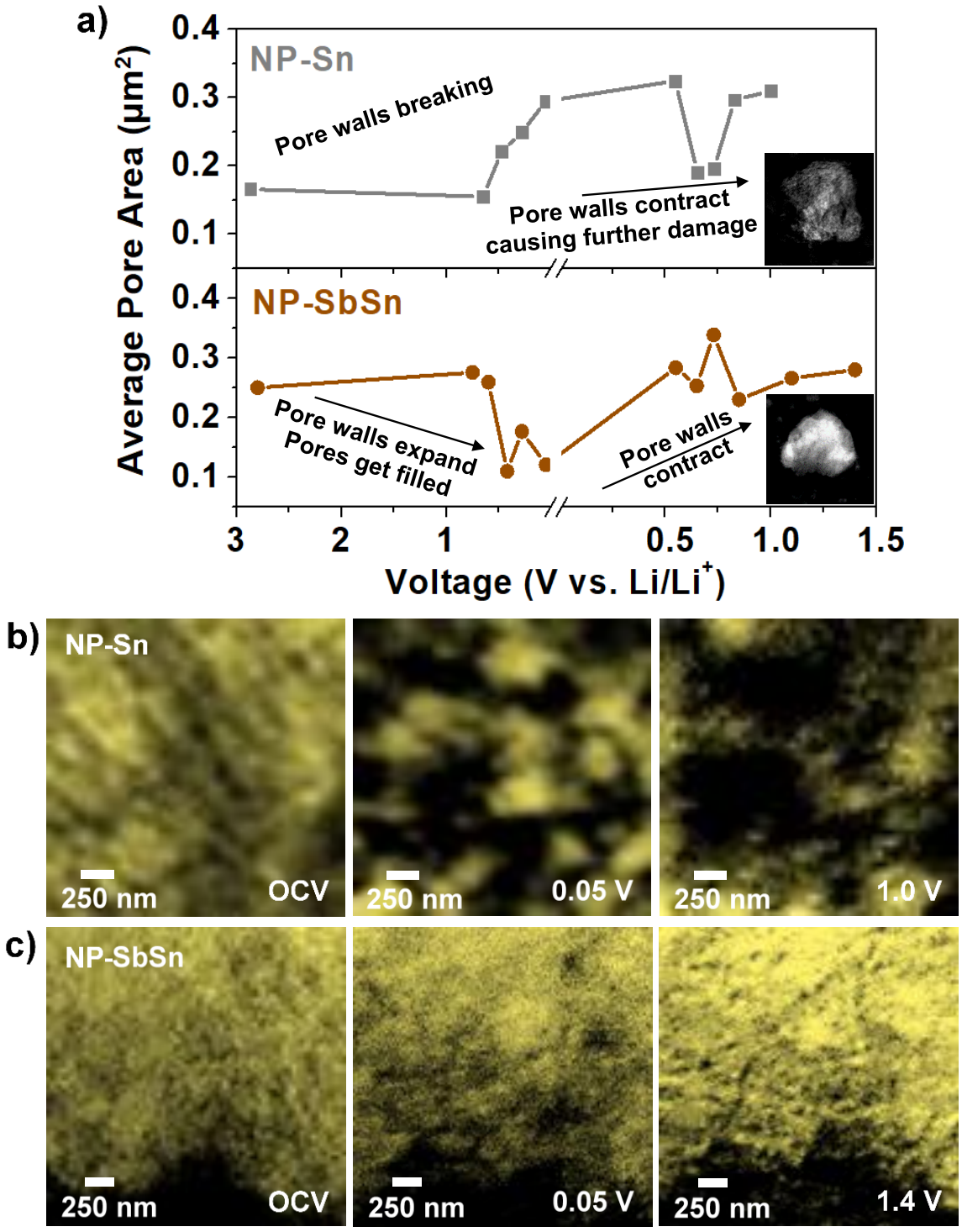

Figure 8.5. a) Pore size evolution of NP-Sn and NP-SbSn throughout the first cycle. High magnification adsorption images of b) NP-Sn and c) NP-SbSn at OCV, lithiated and delithiated state.

without significantly damaging the porous structure. Figures 8.5c show the absorption TXM images of NP-SbSn at OCV, and in the lithiated and the delithiated states. Only one population with an average pore area < 0.5 μm^2 was found in NP-SbSn during lithiation and the average pore are decreases significantly during the lithiation process. After delithiation, most of the pores return to their original < 0.5 μm^2 size. A very small population of slightly larger pores (1-2.25 μm^2) were found, suggesting some degradation in the pore walls, but nothing on the scale of the large scale pore breakage found in the NP-Sn.

It is important to note that even though the pore size decreased during charge, the pores are still opened in the fully lithiated state. This is critical to having a uniform lithiation and delithiation process, which mitigates crack propagation induced by interfacial strain. The homogeneous lithiation/delithiation process can also be confirmed by the even optical density across the particle at each potential. A previous study by Chao and et al. showed that although bulk SbSn experiences a more gradual volume expansion compare to bulk Sn due to the two-step electrochemical process, a core-shell structure was still obtained during cycling due to slow lithium diffusion through the bulk solid. This core-shell structure eventually leads to crack formation in the shell.[12]

The mechanical stability of these NP-SbSn was also examined after 36 cycles. The particle remains completely intact (Figure 8.6a) and the degree of expansion has decreased to only 25% on the 36th cycle, suggesting that the pore structure in NP-SbSn has been partially stabilized (Figure 8.6b). Meanwhile, the same trend in pore size evolution is observed in both the 1st and the 36th cycle. The only difference being the larger initial pore size observed at the start of the 36th cycle (Figure 8.6c) due to the small amount of pore wall degradation occurred over time. The changes in the pore structure after repeated cycling can potentially lead to smaller expansion, partially stabilizing the NP-SbSn.

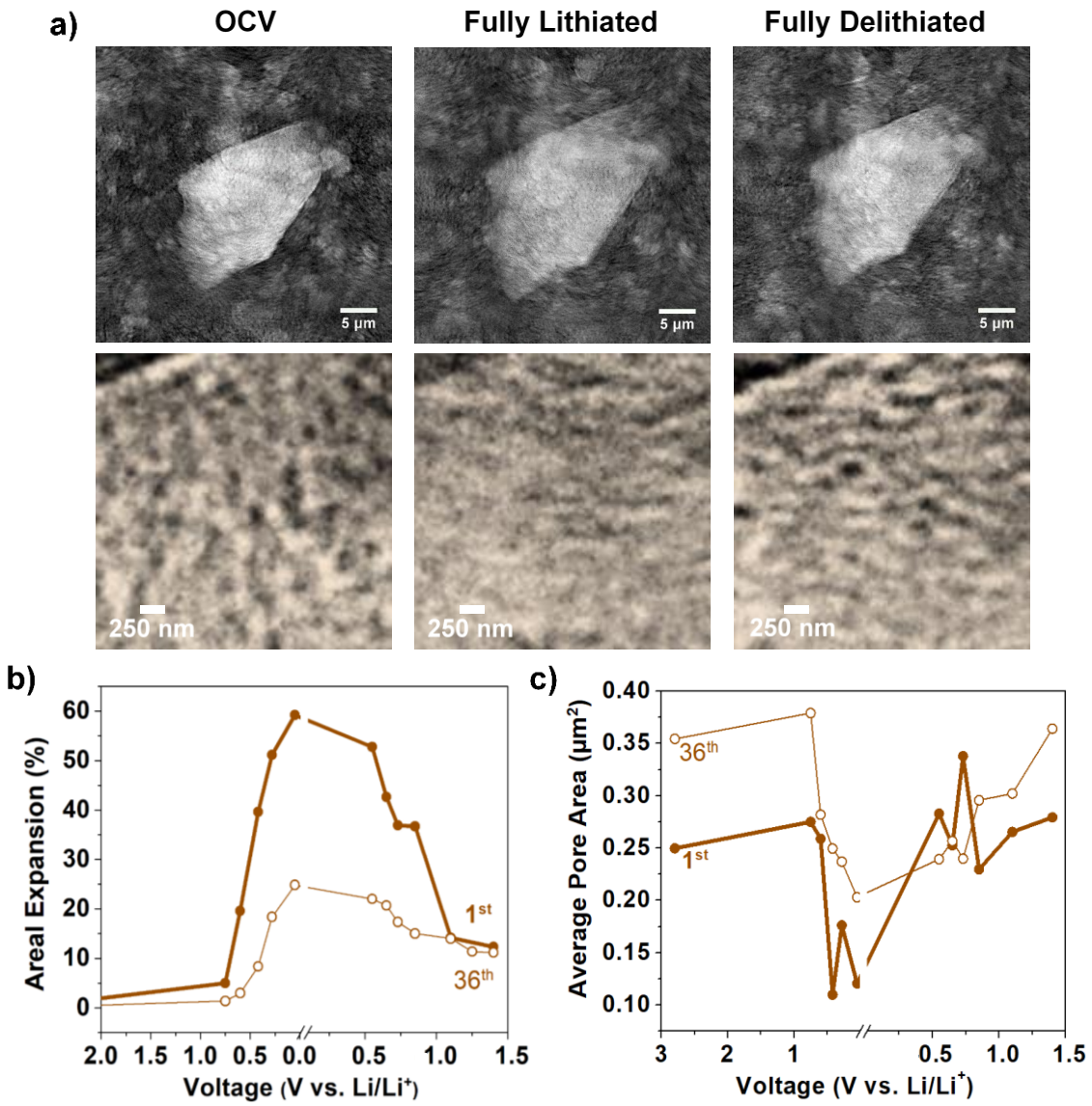

Figure 8.6. a) Low and high magnifications of the adsorption images of NP-SbSn at the 36th cycle at OCV, 0.05 V and 1.5 V. b) The change in areal expansion and c) pore size throughout the

8.3. Conclusion

In this study, we have successfully synthesized a nanoporous NP-SbSn powder with good cycling stability by taking advantage of the structural stability that intermetallic and nanoporous structures provide. These intermetallic 3D conductive materials with open pores synthesized via a

one-step dealloying method showed a reasonable cycle life of 100 cycles with only 1% capacity fade. *Operando* TXM shows that the porous structure of these NP-SbSn are better retained compare to its previous pore Sn analogue, NP-Sn. Very little pore wall degradation is observed. More importantly, the great structural integrity is still observed after 36 cycles. This work provides a direct observation of how intermetallics further stabilizing the structure of alloy anodes during charge and discharge. By having two elements that lithiate and delithiate at different potentials, there is always a non-reactive component stabilizing the structure and, the large volume expansion can be effectively accommodated. This nanoporous intermetallic NP-SbSn with good structural stability, electronic conductivity, and ion/electrolyte diffusion pathways has what appears to be a very favorable architecture to serve as an alloy anode. Given the observed stability with Li^+, these materials can potentially be cycled with even larger ions such as Na^+ and K^+ for alternative energy storage systems.

8.4. Experimental

8.4.1. Synthesis

Nanoporous antimony tin (β-SbSn) was made from a one-step chemical dealloying synthesis. A parent alloy of $Sb_{20}Sn_{80}$ at.% was made by melting the stoichiometric amounts of Sb (Alfa Aesar) and Sn (Sigma Aldrich) in a graphite crucible under Ar flow at 700 °C then cooled to room temperature. To make a homogeneous alloy, the alloy was then heated and cooled several times but at 400 °C. The extra Sn in the parent alloy was then etched away with a 4M HBr (Sigma Aldrich) electrolyte for 21 hr to make the nanoporous structure. After etching, the nanoporous antimony tin powder is washed with water and ethanol several times.

8.4.2. Characterization

Powder X-ray diffraction (XRD) was performed on a D8 diffractometer (Brucker) operating with Cu Kα radiation (λ = 1.5418 Å) with a voltage of 45 kV, and a current of 40 mA. XRD patterns were recorded in the range of $10° < 2\theta < 80°$ using a 0.03° step size. Scanning electron microscopy (SEM) images were obtained using a model JEOL JSM-6700F field emission electron microscope with 5 kV accelerating voltage and secondary electron detector configuration. Transmission electron microscopy (TEM) was performed using a FEI Technai T12 operating at 120 kV. Nitrogen porosimetry was carried out using a Micromeritics TriStar II 3020. The surface area was calculated from the adsorption branch of the isotherm (between 0.04 – 0.30 P/P_0) using the BET model. The pore diameter and pore volume were also calculated from the adsorption branch of the isotherm using the BJH model. XPS analysis was performed using a Kratos Axis Ultra DLD with a monochromatic Al K-α radiation source. The charge neutralizer filament was used to control charging of the sample, a 20 eV pass energy was used with a 0.1 eV step size, and scans were calibrated using the C 1s peak shifted to 284.8 eV. The integrated area of the peaks was found using the CasaXPS software, and atomic ratios were also found using this software. The sample was etched with an Ar beam (raster size 1 mm x 1 mm) at 4 kV for 1 minute.

8.4.3. Electrochemical Testing

Carbon based slurries with 70 wt.% NP-SbSn, 15 wt.% vapor grown carbon fibers (Sigma), and 15 wt.% carboxymethyl cellulose (Mw=250K, Sigma Aldrich) were used for all electrochemical testing. All electrochemical cycling were performed in Swagelok cells with glass fiber separators (Advantec) and 1M $LiPF_6$ (Oakwood Inc) ethylene carbonate: diethylene carbonate (1:1 vol.%) (Sigma) + 5 vol.% fluoroethylene carbonate (TCI America) against lithium.

8.4.4. Operando Transmission X-ray Microscopy

A different set of carbon based slurries and cells were made specifically for imaging purposes. These slurries consist only 25-50 wt.% NP-SbSn, 30-55 wt.% vapor grown carbon fibers, and 20 wt.% carboxymethyl cellulose. Less active material has to be used in order to reduce the probably of the particles overlapping. Pouch cells were used for the TXM measurements, and were sandwiched between two aluminum plates with imaging holes. Components in the pouch cells include 0.5 mm lithium foil as the counter electrode, Celgard (gift from Celgard) soaked in 1 M $LiPF_6$ in a 1:1 ethylene carbonate/dimethylcarbonate solvent (Sigma Aldrich) with 5 vol.% fluoroethylene carbonate (TCI America) as electrolyte. For the *operando* TXM study on later cycles (36th cycle), the electrode was precycled in a Swagelok cell for 35 cycles and disassembled in an Ar glovebox and transferred into a pouch cell for the TXM experiment with everything else the same as previously described.

Transmission X-ray Microscopy of NP-SbSn was performed on beamline 6-2C at the Stanford Synchrotron Radiation Lightsource (SSRL). 8.95 KeV X-rays were used to perform investigations of electrode morphology at the nano/meso scale. The X-ray energy was chosen directly below the Cu Kedge to minimize absorption from the Cu current collector. The spatial resolution of this microscope is ~30 nm, and the field of view at 8.95 KeV is 38.3 μm. Details regarding the *operando* transmission X-ray microscopy of NP-Sn can be found in our previous study.

During operando imaging, the cell was galvanostatically charged and discharged at 0.2C with a VSP potentiostat/galvanostat (Bio-Logic) between 1.4 – 0.05 V *vs.* Li/Li^+. A 3 by 3 mosaic consists of 9 TXM images (38.3 μm x 38.3 μm) were collected at 10-12 regions in the cell. The mosaics were collected continuous during cycling. A camera binning of two (four pixels are averaged into one) was used to further improve the image quality. These parameters result in a pixel size of 34-36 nm.

8.4.5. Data Processing

X-ray micrographs were processed using an in-house developed software package known as TXMWizard. [69] The reference correction was done in TXM-Wizard and the images were further processed using ImageJ. The reference corrected images were first converted to 8 bit images in ImageJ in order to linearly scale all pixels within the image to 255 different grey-levels (0 being white and 255 being black). A threshold was then applied to the image to differentiate the greylevel of the particle and the background. Since TXM is an absorption measurement, all features of interest are light while background is black. The area was then calculated by totaling the number of pixels within the particle after the threshold was applied.

Images used to determine pore size distributions were further processed in ImageJ. The grey scale image described above were threshold again to convert the 255 grey-levels to black and white. Black and white representations of the porous network provides sharp edges and makes the pore more distinguishable. Black regions (i.e. pores) connected by less than 4 pixels were considered individual domains, and the area of each pore was quantified using ImageJ. For this analysis, we magnified the NP-SbSn grain to find a region where pores could be easily distinguished, then counted the number of pores present and the area of each individual pore at each voltage plateau during lithiation and delithiation. Average pore area and the standard deviation of the pore area were also calculated for each voltage plateau. In addition, a series of histograms with 0.25 μm^2 binning were constructed in an effort to study the change in pore size distribution within NP-SbSn upon cycling.

8.5. Reference

[1] E. J. Cairn, P. Albertus, *Annu. Rev. Chem. Eng.* **2010**, *1*, 299.

[2] N. Nitta, G. Yushin, *Part. Part. Syst. Charact.* **2014**, *31*, 317.

[3] W.- J. Zhang, *J. Power Sources* **2011**, *196*, 13.

[4] W.- J. Zhang, *J. Power Sources* **2011**, *196*, 877.

[5] H. Li, *Solid State Ionics* **2002**, *148*, 247.

[6] D. Ma, Z. Cao, A. Hu, *Nano-Micro Lett.* **2014**, *6*, 347.

[7] J. He, Y. Wei, T. Zhai, H. Li, *Mater. Chem. Front.* **2018**, *2*, 437.

[8] D. Larcher, S. Beattie, M. Morcrette, K. Edstrom, J.-C. Jumas, J.-M. Tarascon, *J. Mater. Chem.* **2007**, *17*, 3759.

[9] R. A. Huggins, W. D. Nix, *Ionics* **2000**, *6*, 57.

[10] L. Y. Beaulieu, K. W. Eberman, R. L. Turner, L. J. Krause, J. R. Dahn, *Electrochem. Solid-State Lett.* **2001**, *4*, A137.

[11] C.- M. Park, J.- H. Kim, H. Kim, H.-J. Sohn. *Chem. Soc. Rev.* **2010**, *39*, 3115.

[12] S.-C. Chao, Y.- F. Song, C.-C. Wang, H.-S. Sheu, H.-C. Wu, N.-L. Wu, *J. Phys. Chem. C* **2011**, *115*, 22040.

[13] M. T. McDewell, S. W. Lee, W. D. Nix, Y. Cui, *Adv. Mater.* **2013**, *25*, 4966.

[14] S. J. An, J. Li, C. Daniel, H. M. Meyer, S. E. Trask, B. J. Polzin, D. L. Wood, *ACS Appl. Mater. Interfaces* **2017**, *9*, 18799.

[15] A. J. Louli, J. Li, S. Trussler, C. R. Fell, J. R. Dahn, *J. Electrochem. Soc.* **2017**, *164*, A2689.

[16] M. He, K. Kravchyk, M. Walter, M. V. Kovalenko, *Nano Lett.* **2014**, *14*, 1255.

[17] X. Tang, F. Yan, Y. Wei, M. Zhang, T. Wang, T. Zhang, *ACS Appl. Mater. Interfaces,* **2015**, *7*, 21890.

[18] D. Zhou, W.-L. Song, X. Li, L.-Z. Fan, Y. Deng, *J. Alloy Compd.* **2017**, *699*, 730.

[19] L. Xu, C. Kim, A. K. Shukla, A. Dong, T. M. Mattox, D. J. Milliron, J. Cabana, *Nano Lett.* **2013**, *13*, 1800.

[20] Y. Wang, J. Y. Lee, *Angew. Chem. Int. Ed.* **2006**, *45*, 7039.

[21] S. H. Lee, M. Mathews, H. Toghiani, D. O. Wipf, C. U. Pittman Jr., *Chem. Mater.* **2009**, *21*, 2306.

[22] H. Li, G. Zhu, X. Huang, L. Chen. *J. Mater. Chem.* **2000**, *10*, 693.

[23] C.-M. Park, K. J. Jeon, *Chem. Commun.* **2011**, *47*, 2122.

[24] J. B. Cook, E. Detsi, Y. Liu. Y.-L. Liang, H.-S. Kim, X. Petrissans, B. Dunn, S. H. Tolbert, *ACS Appl. Mater. Interfaces* **2017**, *9*, 293.

[25] J. B. Cook, H.-S. Kim, T. C. Lin, S. Robbennolt, E. Detsi, B. S. Dunn, S. H. Tolbert, ACS *Appl. Mater. Interfaces* **2017**, *9*, 19063.

[26] F. J. Q. Cortes, M. G. Boebinger, M. Xu, A. Ulvestad, M. T. McDowell, *ACS Energy Lett.* **2018**, *3*, 349.

[27] B. Wang, B. Luo, X. Li, L. Zhi, *Mater. Today Chem.* **2012**, *15*, 544.

[28] S. K. Tippabhotla, I. Radchenko, C. V. Stan, N. Tamura, A. S. Budiman, *Procedia Engineering* **2017**, *215*, 263.

[29] H. Wu, Y. Cui, *Nano Today* **2012**, *7*, 414.

[30] N. Obaid, M. T. Kortschot, M. Sain, *Materials* **2017**, *10*, 472.

[31] F. Guiu, P. L. Pratt, *Phys. Stat. Sol.* **1964**, *6*, 111.

[32] H. Ying, W.- Q. Han, *Adv. Sci.* **2017**, *4*, 1700298.

[33] T. Brezesinski, J. Wang, R. Senter, K. Brezensinski, B. Dunn, S. H. Tolbert, *ACS Nano* **2010**, *4*, 967.

[34] J. B. Cook, T. C. Lin, E. Detsi, J. N. Weker, S. H. Tolbert, *Nano Lett.* **2017**, *17*, 870.

[35] H. S. Im, Y. J. Cho, Y. R. Lim, C. S. Jung, D. M. Jang, J. Park, F. Shojaei, H. S. Kang, *ACS Nano* **2013**, *7*, 11103.

[36] X.-L. Wang, W.-Q. Han, J. Chen, J. Graetz, *ACS Appl. Mater. Interfaces* **2010**, *2*, 1548.

[37] M. Winter, J. O. Besenhard, *Electrochim. Acta* **1999**, *45*, 31.

[38] J. Hassoun, S. Panero, P. Simon, P. L. Taberna, B. Scrosati, *Adv. Mater.* **2007**, *19*, 1632.

[39] X.-Z. Liao, Z.-F. Ma, J.-H. Hu, Y.-Z. Sun, X. Yuan, *Electrochemistry Communications* **2003**, *5*, 657.

[40] H. Zhang, T. Shi, D. J. Wetzel, R. G. Nuzzo, P. V. Braun, *Adv. Mater.* **2016**, *28*, 742.

[41] Y. Xia, T. Sakai, T. Fujieda, M. Wada, H. Yoshinaga, *J. Electrochem. Soc.* **2001**, *148*, A471.

[42] J. Chen, L. Yang, S. Fang, S.-I. Hirano, *J. Power Sources* **2012**, *209*, 204.

[43] F.-S. Ke, L. Huang, H.-B. Wei, J.-S. Cai, X.-Y. Fan, F.-Z. Yang, S.-G. Sun, *J. Power Sources* **2007**, *170*, 450.

[44] N. Tamura, M. Fujimoto, M. Kamino, S. Fujitani, *Electrochim. Acta* **2004**, *49*, 1949.

[45] H. Mukaibo, T. Osaka, P. Reale, S. Panero, B. Scrosati, M. Wachtler, *J. Power Sources* **2004**, *132*, 225.

[46] M.-S. Park, S. A. Needham, G.-X. Wang, Y.-M. Kang, J.-S. Park, S.-X. Dou, H.-K. Liu, *Chem. Mater.* **2007**, *19*, 2406.

[47] W. X. Chen, J. Y. Lee, Z. Liu, *Carbon* **2003**, *41*, 959.

[48] X. Tang, F. Yan, Y. Wei, M. Zing, T. Wang, T. Zhang, *ACS Appl. Mater. Interfaces* **2015**, *7*, 21890.

[49] J. Li, Q. Ru, S. Hu, D. Sun, B. Zhang, X. Hou, *Electrochim. Acta* **2013**, *113*, 505.

[50] C.-M. Park, K.-J. Jeon, *Chem. Commun.* **2011**, *47*, 2122.

[51] J. Li, J. Pu, Z. Liu, J. Wang, W. Wu, H. Zhang, H. Ma, *ACS Appl. Mater. Interfaces* **2017**, *9*, 25250.

[52] H. Li, G. Zhu, X. Huang, L. Chen, *J. Mater. Chem.* **2000**, *10*, 693.

[53] H. Okamoto, *J. Phase Equilib.* **1998**, *19*, 292.

[54] B. Legendre, E. Dichi, V. Vassiliev, *Z. Metallkd.* **2001**, *92*, 328.

[55] L. Gmelin, Hand-Book of Chemistry, Cavendish Society, London, United Kingdom, Vol.5, **1851**, p.84.

[56] I. McCue, E. Benn, B. Gaskey, J. Erlebacher, *Annu. Rev. Mater. Res.* **2016**, *46*, 263.

[57] Z. A. ALOthman, *Materials* **2002**, *5*, 2874.

[58] L. Bodenes, A. Darwiche, L. Monconduit, H. Martinez, *J. Power Source* **2015**, *273*, 14.

[59] B. Zhou, E. Sham, T. Machej, P. Bertrand, P. Ruiz, B. Delmon, *J. Catal.* **1991**, *132*, 157.

[60] G. T. Baronetti, S. R. Miguel, O. A. Scelza, A. A. Castro, *Appl. Cata.* **1984**, *24*, 109. [51] J. Li, J. Pu, Z. Liu, J. Wang, W. Wu, H. Zhang, H. Ma, *ACS Appl. Mater. Interfaces* **2017**, *9*, 25250.

[61] S. Süzer, T. Voscoboinikov, K. R. Hallam, G. C. Allen, *Anal. Bioanal. Chem.* **1996**, *355*, 654.

[62] L. Ding, S. He, S. Miao, M. R. Jorgensen, S. Leubner, C. Yan, S. G. Hickey, A. Eychüller, J. Xu, O. G. Schmidt, *Sci. Rep.* **2014**, *4*, 4647.

[63] Z. Yi, Q. Han, X. Li, Y. Wu, Y. Cheng, L. Wang, *Chem. Eng. J.* **2017**, *315*, 101..

[64] K. J. Rhode, R. Meisner, M. Kirkham, n. Dudney, C. Daniel, *J. Electrochem. Soc.* **2012**, *159*, A294.

[65] J. N. Weker, M. F. Toney, *Adv. Funct. Mater.* **2015**, *25*, 1622.

[66] J. N. Weker, N. Liu, S. Misra, J. C. Andrews, Y. Cui, M. F. Toney, *Energy Environ. Sci.* **2014**, *7*, 2771.

[67] S.-C. Chao, Y.-C. Yen, Y.-F. Song, Y.-M. Chen, H.-C. Wu, N.-L. Wu, *Electrochemistry Communications* **2010**, *12*, 234.

[68] J. C. Andrews, B. M. Weckhuysen, *ChemPhysChem.* **2013**, *14*, 3655.

[69] Y. Liu, F. Meirer, P. A. Williams, J. Wang, J. C. Andrews and P. Pianetta, *J. Synchrotron Radiat.* **2012**, *19*, 281.

Chapter 9. Nanoporous Antimony Tin as a Sodium-ion Battery Anode

9.1. Introduction

To extend the technology and application of rechargeable batteries beyond personal electronics to electrical vehicles and grid-scale storage, batteries with lower cost and higher energy density need to be developed. Though lithium-ion batteries (LIBs) are currently the system of choice for many portable power applications, sodium-ion batteries (SIBs) have gained tremendous interest in recent years as an alternative because of sodium's earth abundance and similar alkali chemistry.[1,2] SIBs offer significant cost advantage over LIBs with the possible shortage and associated price increase in lithium and cobalt.[3] Though Li^+ and Na^+ undergo comparable electrochemical processes during cycling, the sodium analogue of many materials established for LIBs cannot readily be used in SIBs.[4] This incompatibility is due to the larger ionic radii of Na^+, causing certain reactions to be thermodynamically unfavorable and making it difficult to find host lattices with adequate capacity.[1,4,5] In addition, it results in slower kinetics, and poor cycling stability as it induces significant structural distortion and rearrangements during charge and discharge.[4,6-10]

Today, significant progress has been made on SIB cathodes while the anode side falls far behind. Graphite, which can readily intercalate Li^+, does not intercalate Na^+ well because it is not energetically favorable and therefore results in Na plating.[11-13] However, in contrary, hard carbon, also known as non-graphitized carbon, has recently demonstrated promising potentials as a SIB anode.[14,15] With the increased defect sites and layer spacing between the randomly oriented graphene sheets in non-graphitized carbon, Na^+ are allowed to intercalate/ deintercalate reversibly into the system.[13,16,17] Though hard carbon is attractive because of its low cost, the specific capacity is still low (300 mAh/g). To increase the energy density of SIBs, alloying anodes with high theoretical capacities are good candidates.[18-20] Similar to alloying anodes used in LIBs, these anodes also undergoes a series of

alloying reactions with Na^+ to form Na-rich phases during cycling. This multi-electron process offers at least two times more energy density than hard carbon. Among all, Sn and Sb have been the most widely studied due to their decent theoretical capacities and high electrical conductivities compare to other metals (Bi, Pb), metalloids (Ge, As) and polyatomic nonmetal compounds (P). Sn and Sb have electrical conductivities of 9 ×104 Scm^{-1} and 2.5 × 104 Scm^{-1} and theoretical capacities of 847 and 660 mAh/g, respectively.[2,21] Unfortunately, due to Na^+'s larger size and much slower kinetics compared to Li^+, these alloying anodes suffer from even more drastic volume changes and shorter lifetimes.[22,23]

In order for alloying anodes to survive this tremendous volume change and repetitive structural rearrangement during Na^+ intercalation and deintercalation, mechanically stable architectures have to be designed. The architecture should include a robust yet flexible conductive scaffold with sufficient empty space to accommodate the volume expansion of the active materials during cycling. This can be achieved by implementing the two of the following strategies. First, by using an intermetallic (e.g., SbSn) instead of a single metal (e.g., Sn or Sb) as the active material. Intermetallics with two active components that alloy with Na^+ at different potentials are more mechanically stable because it allows a more gradual volume expansion and therefore reduce the stress in the material. Moreover, at any given voltage, there is an unreactive component stabilizing the overall structure.[24-26] Another approach is to adopt a 3D nanoporous architecture with void spaces for materials to expand into without inducing and cumulating stress. This can therefore reduce the overall volume expansion and structural damage.[27-32] In addition, porous structures allow for better electrolyte penetration and kinetics, resulting in more uniform sodiation/desodiation process.

In this work, we have synthesized a nanoporous antimony tin powder (np-SbSn) that resembles a dynamical conductive skeleton made of interconnected metallic networks and high porosities. This np-SbSn exhibits long cycle lifetimes (85% capacity retention after 100 cycles), decent capacity (434 mAh/g), and a scalable processing route that involves selective dealloying. In addition

to the electrochemical cycling studies, *operando* transmission X-ray microscopy was performed to correlate the structural changes in micron-sized SbSn (b-SbSn) and np-SbSn during volume expansion to their different cycling performance.

9.2. Results and Discussion

9.2.1. Materials and Characterization

A common method to make homogeneous nanoporous metals and intermetallics is through dealloying. Dealloying occurs when an alloy is immersed in an electrolyte under a driving force such that the more reactive component dissolves and the nobler component remains stable in the metallic and intermetallic form, resulting in the formation of a 3D bicontinuous network of randomly interconnected nanochannels and nanostruts.[33,34] The np-SbSn powder used in this study was dealloyed from a $Sb_{20}Sn_{80}$ at.% parent alloy with strong acid HBr. Meanwhile, the micronsized SbSn particles were synthesized through a solid-state synthesis. The stoichiometric amounts of Sb and Sn metallic powder were melted to make a β-SbSn alloy, which was later ballmilled in liquid nitrogen to break the alloy into powders that consists of micron-sized particles. Figure 9.1a shows the X-ray diffraction pattern of both np-SbSn and b-SbSn synthesized in house. Both patterns well match the JCPD card No.00-033-0118 for rhombohedral (*R-3m*) Stistaite β-SbSn phase with no impurities.

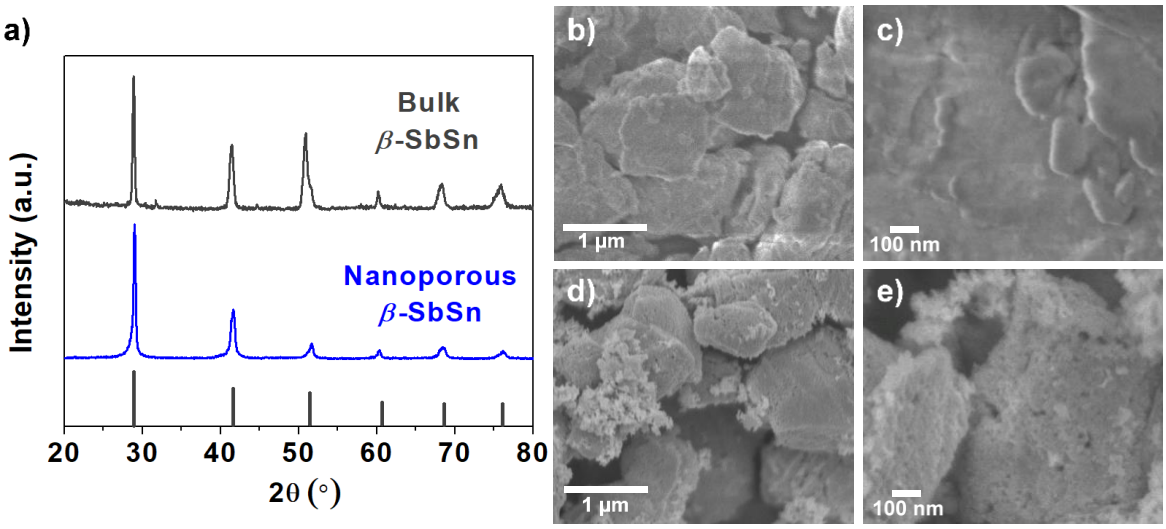

Figure 9.1. Materials Characterization of b- and np-SbSn. a) XRD patterns of b-SbSn in dark gray and np-SbSn in blue. They both match the stick pattern of JCPD card No.00-033-0118 for rhombohedral Stistaite β-SbSn b-c) Low and high magnification SEM images of b-SbSn and d-e) np-SbSn.

The different morphology of b-SbSn and np-SbSn can be seen from the scanning electron microscopy (SEM) images shown in Figures 9.2b-c and 9.2d-e, respectively. Though both b-SbSn and np-SbSn powders are made of micron-size particles, the morphology of the particles are very different. As expected, dense b-SbSn particles have very smooth surfaces whereas pores ~ 20-50 nm can be seen on np-SbSn's texturous surface, resembling their porous structures resulted from dealloying.

The type IV isotherm measured from N_2 porosimetry suggests that np-SbSn consists of both mesopores and macropores.[35] The mesopores represent the intrinsic porosity/nanochannels in the np-SbSn particles while the macropores are originated from the spaces between the randomly arranged micron-size np-SbSn particles as seen from the lower magnification SEM images.

9.2.2. Electrochemistry

To understand the electrochemical reactions occurred during sodiation and desodiation of np-SbSn, cyclic voltammetry (CV) was performed between 0.05 V and 2 V with a scan rate of 0.1 mV/s. The first five cycles are shown in Figure 9.2a. During the first cathodic scan, the broad peak from 0.5 V- 0.05 V corresponds to the reduction of surface oxides (SbO_2 and SnO_2) to metallic Sb and Sn follow by the alloying reactions of Sb and Sn metals with Na^+.[36-38] During the anodic scan, two peaks are observed at 0.71 V and 0.9 V and can be attributed to the desodiation process of $Na_{3.75}Sn$ and Na_3Sb to metallic Sn and Sb, respectively.[39-41] The reaction pathway can be explain by Equation 9.1-9.4. In the subsequent cycles, only redox pairs related to the sodiation and desodiation of Sb and Sn metals can be observed, indicating a stable oxidation/ reduction process with good reversibly.

$$(SbO_2, SnO_2)_{surface} + xNa + xe^- \rightarrow yNa_2O + (Sb, Sn)_{surface} \quad \textit{Equation 9.1}$$

$$(Sb, Sn)_{surface} + SnSb + xNa^+ + xe^- \rightarrow Sn + Na_xSb \quad \textit{Equation 9.2}$$

$$Sn + Na_xSb + (3\text{-}x)Na^+ + (3\text{-}x)e^- \rightarrow Sn + Na3Sb \quad \textit{Equation 9.3}$$

$$Na_3Sb + Sn + 3.75Na + 3.75e^- \rightarrow Na_3Sb + Na_{3.75}Sn \quad \textit{Equation 9.4}$$

Figure 9.2b shows the galvanostatic charge and discharge profiles of the 1st, 2nd, 5th, 10th and 20th cycle of np-SbSn at 0.2C (current density calculated based on theoretical capacity). During the first discharge, a low coulombic efficiency (67%) as well as a lower voltage plateau at 0.5 V is observed compared to the subsequent cycles. This is in good agreement with the surface oxide reduction and SEI formation observed in the CV curves. During the first cycle, the charge capacity is 643 mAh/g and the discharge capacity is 434 mAh/g. After the stable SEI forms, these np-SbSn showed great stability in the subsequent cycle with 92% coulombic efficiency ($Capacity_{discharge}$ = 477 mAh/g and $Capacity_{charge}$ = 442 mAh/g). Even after 100 cycles, 85% of charge capacity was retained. This longterm cycling study performed at a rate of 0.2C can be found in Figure 9.2c. In stark contrast to the performance of np-SbSn, b-SbSn died after three cycles as a result of crack propagation and poor electrical contact. This is one of the few pure SbSn anodes that has demonstrated such stability.[42]

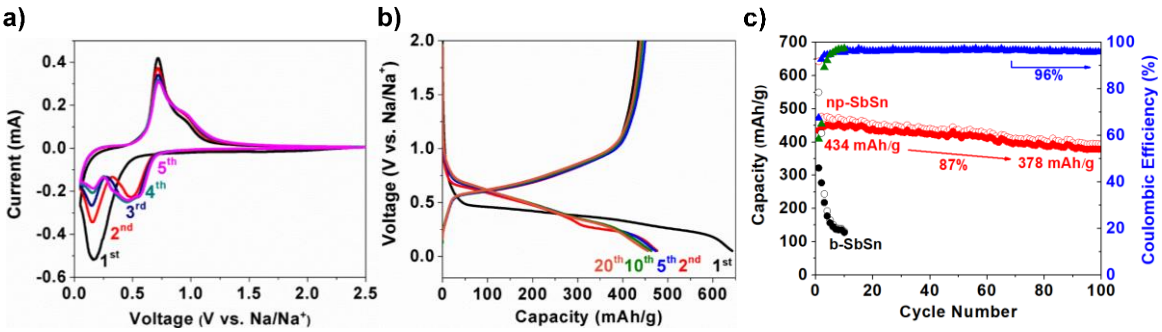

Figure 9.2. Electrochemical cycling of b- and np-SbSn. a) CV curves of the first five cycles of np-SbSn cycled at 0.1 mV/s. b) Galvanostatic charge and discharge profiles of 1st, 2nd, 5th, 10th and 20th cycle of NP-SbSn at 0.2C. c) Longterm cycling of np-SbSn (red) in comparison to the bulk (black). The coulombic efficiency of np- and b- SbSn are plotted in blue and green, respectively.

Most studies still rely on carbon for extra mechanical support and electrical conductivity.[43-45] This conductive bicontinuous scaffold of np-SbSn offers great advantage over other carbon composites as it is flexible to accomodate volume change and favorable for the electron and mass transportation during cycling. These np-SbSn also cycled much better than then the nanoporous tin (np-Sn) demonstrated in our previous study, signifying the enhanced structural stability from the intermetallic.

9.2.3. *Operando* Transmission X-ray Microscopy

To develop a structural understanding on the origins of np- and b-SbSn's markedly different cycling performance with sodium, *operando* transmission X-ray microscopy (TXM) was performed at Stanford Synchrotron Radiation Lightsource (SSRL) beamline 6-2C to monitor the morphological changes in bulk and nanoporous SbSn during cycling. Figures 9.3a and 9.3b show the 2D adsorption images of b-SbSn and np-SbSn, respectively, at open circuit voltage (OCV), 0.05V (sodiated state) and 2V (desodiated state). During cycling, severe crack propagation was observed in b-SbSn while none was found in np-SbSn. Crack propagation is detrimental to the cycling performance as it can cause

the particles to lose electrical contact with the slurry matrix and current collector.[46] Moreover, crack formation introduces unprotected surfaces to the electrolyte. If new SEI continues to grow in every cycle, the amount of available active material and Li^+ will be reduced, leading to capacity lost.[47] As expected, b-SbSn expanded more than np- SbSn as shown in Figure 9.3c. Over a hundred percent (104 %) of areal expansion was calculated for b-SbSn while np-SbSn only expanded 68% with no physical disintegration. The outline of np- SbSn particle stayed nearly identical throughout charge and discharge. At the fully desodiated state, np-SbSn almost contracted back to its original size (24%) and b-SbSn remained expanded (54%). Np-SbSn's good structural stability can be attributed to the nanporous structure, where the diffusion of Na^+ is largely improved and therefore enabling a homogeneous sodiation/desodiation process. This is confirmed from the uniform optical density observed across the particle throughout charge and discharge.

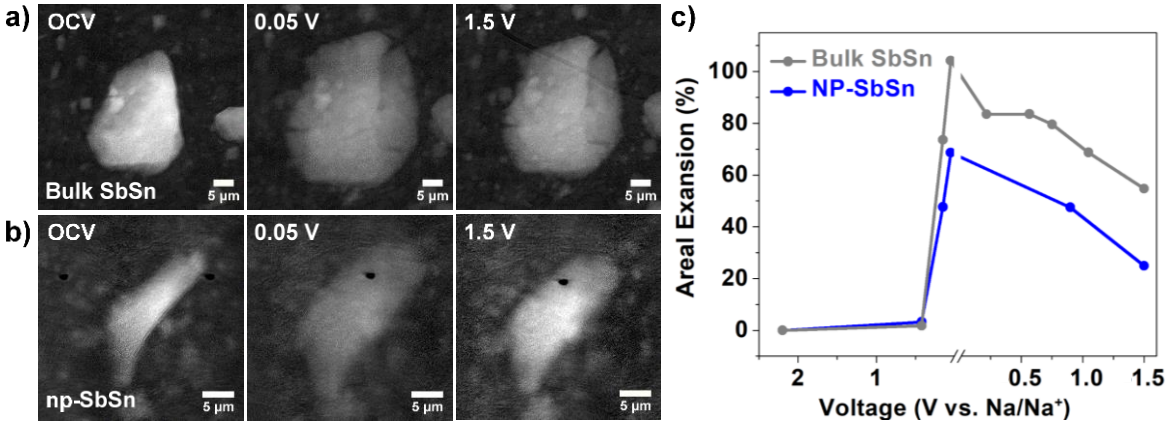

Figure 9.3. Adsorption images of b- and np-SbSn collected during operando TXM study. a) b- and b) np-SbSn collected at OCV, fully sodiated (0.05 V) and desodiated (1.5 V) state. c) Percent areal expansion calculation of b- and np-SbSn throughout the whole cycle.

In addition to the overall structural change, the evolution of porosity in np-SbSn was also studied. Figures 9.4a-c show the high magnification 2D TXM images of np-SbSn at OCV, sodiated

and desodiated state. Throughout discharge, the pores had grown larger compare to the pores in pristine np-SbSn. Even though the pores slightly contracted by the end of the first cycle, they are still larger than at OCV. To quantitatively analyze the change in pore size, a series of high magnification adsorption images and histograms (number of pores versus individual pore area) were constructed. The histograms were used to calculate the average pore area at each voltage plateau shown in Figure 9.4d. The trend depicted in Figure 9.4d is in good agreement with the TXM images and suggests that the pore wall slightly degraded during sodiation as the pore wall expands. This evolution is similar to

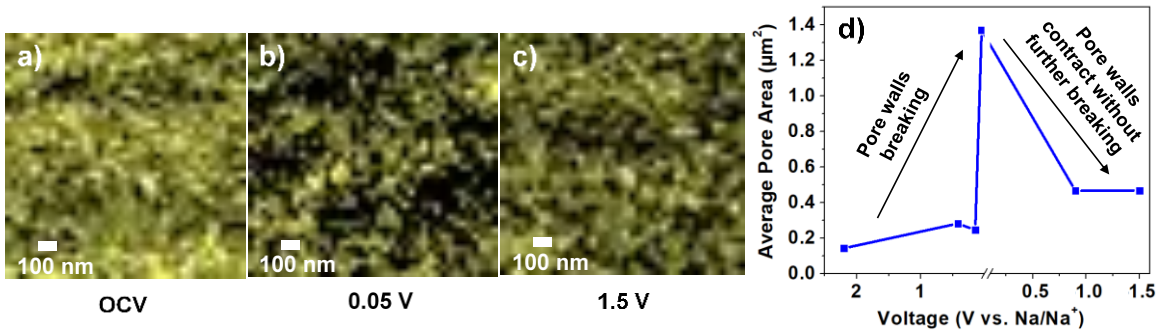

Figure 9.4. Adsorption images of the pores of np-SbSn at a) OCV, b) 0.05 V (sodiated) and c) 1.5 V (desodiated). d) The change in pore size throughout the first cycle.

what we had previously found in our *operando* TXM study on np-Sn during lithiation and delithiation but in a less drastic manner.[29] The reduced amount of damage suggest that np-SbSn is more mechanically stable and can therefore cycle better with Na^+. Despite the degradation in the porous structure, pores remained open throughout cycling. This is critical in allowing for good electrolyte penetration and homogeneous sodiation/desodiation to avoid the formation of a core shell structure and he lattice mismatch between the Li-rich and Li-poor phase that results in interfacial strain and crack formation.

9.3. Conclusion

The good cycling performance of this np-SbSn system compared to the b-SbSn and the np-Sn we have previously synthesized[32] is attributed to the spread out sodiation voltage of intermetallic SbSn and its nanoporous architecture. The unique interconnected granular morphology well accommodates the large volume changes taking place during sodiation, and preserves the electrical contact with the macroporous carbon fiber electrode network even in the sodiated state, allowing for good electrolyte penetration to all active sites. With this np-SbSn, we have successfully delivered 430 $mAhg^{-1}$ with 85% capacity retention after 100 cycles, which outperforms the nanoporous Sn we have previously synthesized (550$mAhg^{-1}$ initial capacity, but only 50% capacity retention after 90 cycles).

9.4. Experimental

9.4.1. Synthesis

Details regarding the synthesis of nanoporous antimony tin (β-SbSn) can be found in the previous chapter. In short, np-SbSn was made from a one-step chemical dealloying synthesis using a parent alloy of $Sb_{20}Sn_{80}$ at% and 4M HBr (Sigma Aldrich) solution as the etchant. Bulk β-SbSn powder was made in house. First, an alloy of $Sb_{50}Sn_{50}$ at% was made by melting stoichiometric amounts of Sb (Alfa Aesar) and Sn (Sigma Aldrich) granules in a graphite crucible under Ar flow at 700 °C then cooled to room temperature. The alloy was then heated and cooled several times but at 400 °C to ensure good mixing. The alloy was then rolled into sheets and broken into small pieces and further grinded into even smaller pieces similar to the size of glitter. To break them into micron-sized particles, the glitter like β-SbSn was then ball milled in liquid nitrogen several times since the alloy is malleable.

9.4.2. Characterization

Powder X-ray diffraction (XRD) was performed on a D8 diffractometer (Brucker) operating with Cu Kα radiation (λ = 1.5418 Å) with a voltage of 45 kV, and a current of 40 mA. XRD patterns were recorded in the range of $10° < 2\theta < 80°$ using a 0.03° step size. Scanning electron microscopy (SEM) images were obtained using a model JEOL JSM-6700F field emission electron microscope with 5 kV accelerating voltage and secondary electron detector configuration. Transmission electron microscopy (TEM) was performed using a FEI Technai T12 operating at 120 kV. Nitrogen porosimetry was carried out using a Micromeritics TriStar II 3020. The surface area was calculated from the adsorption branch of the isotherm (between 0.04 – 0.30 P/P_0) using the BET model. The pore diameter and pore volume were also calculated from the adsorption branch of the isotherm using the BJH model.

9.4.3. Electrochemistry

Carbon based slurries with 70 wt.% NP-SbSn, 7.5 wt.% vapor grown carbon fibers (Sigma Aldrich), 7.5 wt.% multiwall carbon nanotube (Sigma Aldrich), and 15 wt.% carboxymethyl cellulose (M_w=250K, Sigma Aldrich) were used for all electrochemical testing. All electrochemical cycling was performed in Swagelok cells with glass fiber separators (Advantec), 1M $NaPF_6$ ethylene carbonate: diethylene carbonate (1EC:1DEC vol.%, Sigma Aldrich) + 5% fluoroethylene carbonate (FEC, Alfa Aesar) against sodium metal.

9.4.4. *Operando* Transmission X-ray Microscopy

Pouch cells were used for the TXM measurements, and were sandwiched between two aluminum plates with imaging holes. Components in the pouch cells include 0.5 mm sodium foil as the counter electrode, Celgard (gift from Celgard) soaked in 1 M $NaPF_6$ in a 1:1 EC:DEC with 5% (v/v) FEC as electrolyte, and a porous np-SbSn working electrode with a different composition made

only for the imaging study. These slurries consist of only 50 wt.% np-SbSn, 30 wt.% vapor grown carbon fibers, and 20 wt.% carboxymethyl cellulose. Less active material has to be used in order to reduce the probably of the particles overlapping.

Transmission X-ray Microscopy was performed on beamline 6-2C at the Stanford Synchrotron Radiation Lightsource (SSRL). 8.95 KeV X-rays were used to perform investigations of electrode morphology at the nano/meso scale. The X-ray energy was chosen directly below the copper K edge to minimize absorption from the Cu current collector. The spatial resolution of this microscope is ~30 nm, and the field of view at 8.95 KeV is 38.3 μm. Details regarding the *operando* transmission X-ray microscopy of NP-Sn can be found in our previous study.

During in operando imaging, the cell was galvanostatically charged and discharged with a VSP potentiostat/galvanostat (Bio-Logic) between 1.5 – 0.05 V *vs.* Na/Na^+ using a rate of 0.2C. A 3 by 3 mosaic consists of 9 TXM images (38.3 μm x 38.3 μm) were collected at 10-12 regions in the cell. The mosaics were collected continuous during cycling. A camera binning of two (four pixels are averaged into one) was used to further improve the image quality. These parameters result in a pixel size of 34-36 nm.

9.4.5. Data Processing

X-ray micrographs were processed using an in-house developed software package known as TXM-Wizard. The reference correction was done in TXM-Wizard and the images were further processed using ImageJ. The reference corrected images were first converted to 8 bit images in ImageJ in order to linearly scale all pixels within the image to 255 different grey-levels (0 being white and 255 being black). A threshold was then applied to the image to differentiate the grey-level of the particle and the background. Since TXM is an absorption measurement, all features of interest are light while

background is black. The area was then calculated by totaling the number of pixels within the particle after the threshold was applied.

Images used to determine pore size distributions were further processed in ImageJ. The grey scale image described above were threshold again to convert the 255 grey-levels to black and white. Black and white representations of the porous network provides sharp edges and makes the pore more distinguishable. Black regions (i.e. pores) connected by less than 4 pixels were considered individual domains, and the area of each pore was quantified using ImageJ. For this analysis, we magnified the NP-SbSn grain to find a region where pores could be easily distinguished, then counted the number of pores present and the area of each individual pore at each voltage plateau during lithiation and delithiation. Average pore area and the standard deviation of the pore area were also calculated for each voltage plateau. In addition, a series of histograms with 0.5 μm^2 binning were constructed in an effort to study the change in pore size distribution within NP-SbSn upon cycling.

9.5. Reference

[1] J.-Y. Hwang, S.-T. Myung, Y.-K. Sun, *Chem. Soc. Rev.* **2017**, ***46***, 3529.

[2] H. Kang, Y. Liu, K. Cao, Y. Zhao, L. Jiao, Y. Wang, H. Yuan, *J. Mater. Chem. A* **2015**, *3*, 17899.

[3] C. Vaalma, D. Buchholz, M. Weil, S. Passerini, *Nat. Rev. Mater.* **2018**, *3*, 18013.

[4] P. K. Nayak, L. Yang, W. Brehm, P. Adelhelm, *Angew. Chem. Int. Ed.* **2017**, *57*, 102.

[5] M.-S. Balogun, Y. Luo, W. Qiu, P. Liu, Y. Tong, *Carbon* **2016**, *98*, 162.

[6] H. Xie, X. Tan, E. J. Luber, B. C. Olsen, W. P. Kalisvaart, K. L. Jungjohann, D. Mitlin, J. M. Muriak, *ACS Energy Lett.* **2018**, *3*, 1670.

[7] Y. Liang, W.-H. Lai, Z. Miao, S.-L. Chou, *Small* **2018**, *14*, 1702514.

[8] H. Xie, W. P. Kalisvaart, B. C. Olsen, E. J. Luber, D. Mitlin, J. M. Muriak, *J. Mater. Chem. A* **2017**, *5*, 9661.

[9] L. P. Wang, L. Yu, X. Wang, M. Srinivasan, Z. J. Xu, *J. Mater. Chem. A* **2015**, *3*, 9353.

[10] M. D. Slater, D. Kim, E. Lee, C. S. Johnson, *Adv. Funct. Mater.* **2013**, *23*, 947.

[11] P. Ge, M. Fouletier, *Solid State Ionics* **1988**, 28–30, 1172.

[12] M. M. Doeff, Y. Ma, S. J. Visco, L. C. DeJonghe, *J. Electrochem. Soc.* **1993**, *140*, L169.

[13] Y. Wen, K. He, Y. Zhu, F. Han, Y. Xu. I. Matsuda, Y. Ishii, J. Cumings, C. Wang, *Nat. Commun.* **2014**, *5*, 4033.

[14] E. Irisarri, A. Ponrouch, M. R. Palacin, *J. Electrochem. Soc.* **2015**, *162*, A2476.

[15] A. Ponrouch, R. Dedryvere, D. Monti, J. M. Ateba, L. Croguennec, C. Masquelier, P. Johansson, M. R. Palac´ın, *Energy Environ. Sci.* **2013**, *6*, 2361.

[16] D. A. Stevens, J. R. Dahn, *J. Electrochem. Soc.* **2001,** *148*, A803.

[17] Y.-X. Wang, S.-L. Chou, H.-K. Liu, S.-X. Dou, *Carbon* **2013**, *57*, 202.

[18] W. Luo, F. Shen. C. Bommier, H. Zhu, X. Ji, L. Hu, *Acc. Chem. Res.* **2016**, *49*, 231.

[19] H. Ying, W.-Q. Han, *Adv, Sci.* **2017**, *4*,1700298.

[20] Y. Kim, K.-H. Ha, S. M. Oh, K. T. Lee, *Chem. Eur. J.* **2014**, *20*, 11980.

[21] J. He, Y. Wei, T. Zhai, H. Li, *Mater. Chem. Front.* **2018**, *2*, 437.

[22] J. W. Wang, X. H. Liu, S. X. Mao, J. Y. Huang, *Nano Lett.* **2012**, *12*, 5897.

[23] J. Wang, C. Eng, Y.-C. K. Chen-Wiegart, J. Wang, *Nat. Commun.* **2015**, *6*, 7496.

[24] Y. Pan, X.-J. Wu, Z.-Q. Zhang, Z.-W. Fu, Y.-N. Zhou, *J. Alloy Compd.* **2017**, *714*, 348.

[25] Y.-M. Lin, P. R. Abel, A. Gupta, J. B. Goodenough, A. Heller, C. B. Mullins, *ACS Appl. Mater. Interfaces* **2013**, *5*, 8273.

[26] J. Liu, S. Wang, K. Kravchyk, M. Ibáñez, F. Krumeich, R. Widmer, D. Nasiou, M. Meyns, J. Llorca, J. Arbiol, M. V. Kovalenko, A. Cabot, *J. Mater. Chem. A* **2018**, 6, 10958.

[27] J. Liu, Y. Wen, P. A. van Aken, J. Maier, Yan. Yu, *Nano Lett.* **2014**, *4*, 6387.

[28] J. Liu, Z. Yang, J. Wang, L. Gu, J. Maier, Y. Yu, *Nano Energy* **2015**, *16*, 389.

[29] J. B. Cook, T. C. Lin, E. Detsi, J. N. Weker, S. H. Tolbert, *Nano Lett.* **2017**, *17*, 870.

[30] J. B. Cook, H.-S. Kim, T. C. Lin, S. Robbennolt, E. Detsi, B. S. Dunn, S. H. Tolbert, *ACS Appl. Mater. Interfaces* **2017**, *9*, 19063.

[31] J. B. Cook, E. Detsi, Y. Liu, Y.-L. Liang, H.-S. Kim, X. Petrissans, B. Dunn, S. H. Tolbert, *ACS Appl. Mater. Interfaces* **2017**, *9*, 293.

[32] E. Detsi, X. Petrissans, Y. Yan, J. B. Cook, Z. Deng, Y.-L. Liang, B. Dunn, S. H. Tolbert,

Phys. Rev. Materials **2018**, *2*, 055404.

[33] J. R. Hayes, A. M. Hodge, J. Biener, A. V. Hamza, *J. Mater. Res.* **2006**, *21*, 2611.

[34] E. Detsi, S. H. Tolbert, S. Punzhin, J. Th. M. De Hosson, *J. Mat. Sci.* **2016**, ***51***, 615.

[35] M. Thommas, K. Kaneko, A. W. Neimark, J. P. Olivier, F. Rodriguez-Reinoso, J. Rouquerol, K. S. W. Sing, *Pure Appl. Chem.* **2015**, *87*, 1051.

[36] X. Zhou, X. Liu, Y. Xu, Y. Liu, Z. Dai, J. Bao, *J. Phys. Chem. C* **2014**, *118*, 23527.

[37] Q. Sun, Q.-Q. Ren, H. Li, Z.-W. Fu, *Electrochemistry Communications* **2011**, *13*, 1462.

[38] Y. Wang, D. Su, C. Wang, G. Wang, *Electrochemistry Communications* **2013**, *29*, 8.

[39] L. Wu, X. Hu, J. Qian, F. Pei, F. Wu, R. Mao, X. Ai, H. Yang, Y. Cao, *Energy Environ. Sci.* **2014**, *7*. 323.

[40] A. Darwiche, C. Marino, M. T. Sougrati, B. Fraisse, L. Stievano, L. Monconduit, *J. Am. Chem. Soc.* **2012**, *134*, 20805.

[41] C. Kim, K.-Y. Lee, I. Kim, J. Park, G. Cho, K.-W. Kim, J.-H. Ahn, H.-J. Ahn, *J. Power Sources* **2016**, *317*, 153.

[42] A. Darwiche, M. T. Sougrati, B. Fraisse, L. Stievano, L. Monconduit, *Electrochemistry Communications* **2013**, *32*, 18.

[43] C. Chen, K. Fu, Y. Lu, J. Zhu, L. Xue, Y. Hu, X. Zhang, *RSC Adv.* **2015**, *5*, 30793.

[44] L. Xiao, Y. Cao, J. Xiao, W. Wang, L. Kovarik, Z. Nie, J. Liu, *Chem. Commun.* **2012**, *48*, 3321.

[45] L. Ji, W. Zhou, V. Chabot, A. Yu, X. Xiao, *ACS Appl. Mater. Interfaces* **2015**, *7*, 24895.

[46] Y. Liu, A. Palmieri, J. He, Y. Meng, N. Beauregard, S. L. Suib, W. E. Mustain, *Scientific Reports* **2016**, *2*, 25860.

[47] S. Chae, M. Ko, K. Kim, K. Ahn, J. Cho, *Joule* **2017**, *1*, 47.

Chapter 10. Improved Cycling Capabilities of Nanoporous Antimony Tin with Atomic-Layer-Deposition Aluminum Oxide for Sodium Ion Batteries

10.1. Introduction

Rechargeable batteries with high energy densities are critical for the development of renewable energies as the intermittent nature of solar and wind resources produce varying amounts of energy based on the vagaries of weather. In order to store this energy for the grid, economic battery chemistries are required. Sodium-ion batteries with alloying anodes have recently become a promising cheaper alternative to lithium-ion batteries due to the low market price of sodium and the high specific volumetric energy densities of alloying anodes (3-10 times higher than graphite).[1-6]

Though alloying anodes such as Sn and Sb are attractive, the unstable metal/electrolyte interface and the materials degradation resulting from the volume change during alloying reactions with Na+ still hinder their use in practical devices.[1-8] While nanostructuring is an effective method for reducing the volume expansion and crack propagation of alloying anodes,[9,10] the increased surface area leads to increased amounts of electrolyte degradation.[11] Typically, a stable solid electrolyte interphase (SEI) forms on the surface of an active material during the first few cycles as the electrolyte decomposes to form a thin layer of inorganic and organic products.[12-16] Conventional carbonate-based electrolytes with sodium salts (e.g., $NaPF_6$, $NaClO_4$, etc.) readily decompose below ~1.5 V *vs.* Na/Na^+ to a series of carbonates, fluorides, chlorides, and oxides derivatives. A stable SEI that is electronically insulating and ionically conductive is beneficial because it prevents further electrolyte degradation by blocking the electron transport while allowing Na^+ to pass during cycling.[11] However, this can also introduce a high interfacial resistance due to the ionically insulating nature of certain decomposition products and reduce the capacity of the device as the formation of SEI consumes the sodium ions in the electrolyte.[17,18] Particularly with alloying anodes, stable SEIs can be difficult to form due to

repetitive volume changes and crack propagation that expose new surfaces for SEI formation.[17] Certain metals such as Sn, are also known to catalyze electrolyte decomposition.[7,8,19] In order to enable the use of these high-energy-density materials, controlling the stability and properties of electrochemical interfaces while limiting the volume expansion is crucial.

The use of oxides and nitrides as artificial SEIs have recently demonstrated promising results in improved cycling stability and reversibility.[20-25] These thin surface coatings not only prevent the formation of a SEI but also improve the structural integrity of the electrode by anchoring the active material to the current collector.[26-28] Among potential artificial SEI oxides, Al_2O_3 is particularly attractive due to its high ionic conductivity after sodiation (and the formation of a Na-Al-O glass) and its robust ceramic nature.[29-32] Atomic layer deposition (ALD) can be used to deposit a thin coating of materials. Surface coatings deposited through ALD is favorable because of the low deposition temperature, conformality, and tunable thickness.[20,21,33] More importantly, the layer-by-layer atomic scale depositions allow tailoring of the exact stoichiometric composition.

In this study, we demonstrate the improved performance of nanoporous antimony tin (NP-SbSn) with ALD Al_2O_3 during electrochemical cycling with sodium. Intermetallic SbSn is chosen because the two active components alloy with Na^+ at different potentials, allowing for a more gradual volume expansion. This reduces the stress accumulated in the materials and improves the mechanically stablility. Moreover, at any given voltage, there is an unreactive component stabilizing the overall structure.[34-36] NP-SbSn with Al_2O_3 coating can be cycled reversibly with 312 mAh/g after 100 cycles. *Operando* transmission X-ray microscopy (TXM) was performed to understand the stabilization mechanism of these coatings on nanoporous structures. In the first TXM study performed on alloying anodes with ALD coating, NP-SbSn with Al_2O_3 coating is shown to expand less during electrochemical cycling, allowing better retention of the porous structure over 10 cycles. These results

provide a mechanistic understanding of surface coatings on nanostructured materials and indicate the viability of the approach in enabling alloying anodes for high energy density applications.

10.2. Results and Discussion

10.2.1. Materials and Characterization

NP-SbSn was synthesized using a facile selective etching synthesis. In brief, NP-SbSn was etched from a $Sb_{20}Sn_{80}$ at.% parent alloy, consisting of tetragonal Sn and rhombohedral β-SbSn, using HBr acid. As Sn (the less noble metal) dissolves into the etchant, the remaining intermetallic SbSn forms nanoclusters that rearrange into a bicontinuous porous structure. Details regarding this synthesis can be found in our previous studies on NP-SbSn's cycling performances as lithium- and sodium-ion anodes. The X-ray diffraction pattern of NP-SbSn is shown in Figure 10.1a. The XRD pattern matches well with the JCPD pattern (No. 00-001-0830) of β-SbSn with the R-3m space group.

The optimal ALD coating thickness is dependent on the pores size of NP-SbSn. According to the pore size distribution calculated from the Barrett-Joyner-Halenda (BJH) model, the mesopores in NP-SbSn are >20 nm as shown in the inset of Figure 10.1b. Figure 10.1b shows the Type IV isotherm of NP-SbSn measured from N_2 porosimetry, indicating that the structure is bimodal with both macropores and mesopores. The total surface area is 5 m^2/g calculated from the Brunauer-Emmett-Teller (BET) model. A 5 nm thickness of Al2O3 was chosen for this study because it allows the >20 nm pores in NP-SbSn to remain open after deposition of the oxide and previous studies have shown that open pores are crucial for suppressing volume expansion in these nanoporous metals during electrochemical cycling. The voids improve electrolyte penetration and promote a more uniform sodiation/desodiation process without the formation of cores shell structures that lead to the propagation of cracks. Al_2O_3 was deposited onto NP-SbSn powder to demonstrate the conformality of the coatings through ALD. Figures 10.1c and 10.1d show the TEM images of the pristine powder

and Figure 10.1e shows the Al_2O_3-coated NP-SbSn particle. The evenly coated 5 nm artificial SEI on nanoporous particle surface can be observed. While the deposition of Al_2O_3 onto the active material is suitable for imaging, the application of an artificial SEI prior to electrode fabrication can result in slower ion diffusion and the obstruction of electron transport pathways as the oxide layer prohibits direct particle to particle contact within the electrode.[37] Therefore, to study the cycling stability of Al_2O_3-coated NP-SbSn, the ALD coatings were deposited directly onto the composite electrode composed of active material, conductive additive, and binder.

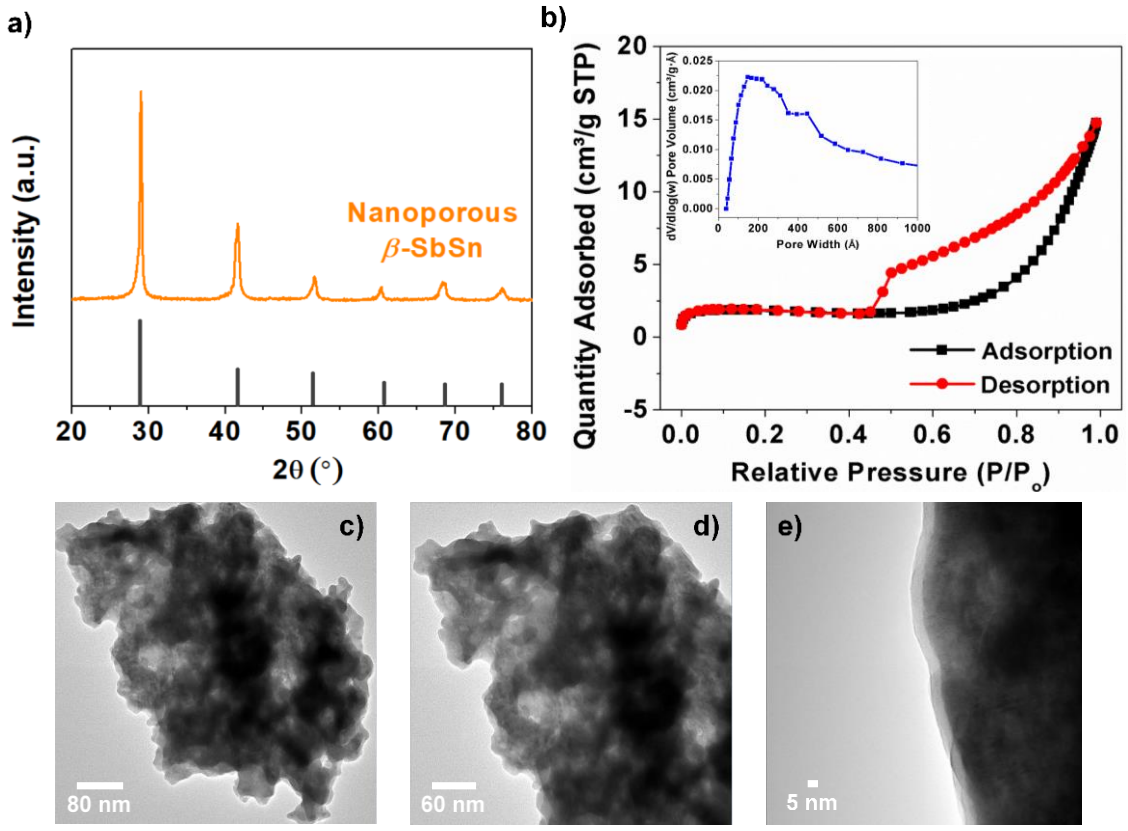

Figure 10.1. a) Powder X-ray diffraction pattern of NP-SbSn. b) Isotherm of N_2 porosimetry. The inset shows the pore size distribution calculated from BJH. c-d) TEM images of pristine and e) Al_2O_3-coated NP-SbSn powder.

10.2.2. Electrochemistry

Figure 10.2a and 10.2b show the cyclic voltammograms (CV) of the bare and Al_2O_3-coated NP-SbSn, respectively. Na^+ first alloys with Sb to form amorphous Na_xSb and hexagonal Na_3Sb then alloys with Sn to $Na_{3.75}Sn$. The electrochemical processes are described in Equation 10.1-10.3. The voltammograms of the bare and Al_2O_3-coated electrodes reveal very similar redox features. On the first cycle NP-SbSn undergoes an activation process in which the native surface oxides reduce to Sb and Sn metal (Equation 10.4).[38-40] The required overpotential for this reaction bypasses the antimony reduction potential (0.7 V *vs.* Na/Na^+), resulting in the presence of a big broad peak starting at 0.6 V (alloying/dealloying SbSn to Na_3Sb and $Na_{3.75}Sn$). On the following cycle, redox peaks of the reversible alloy and dealloy reactions can be observed at their expected potentials and redox pairs at 0.55/0.9 and 0.2 V/0.7 V *vs.* Na/Na^+ represent the conversion of Sb to Na3Sb and Sn to $Na_{3.75}Sn$, respectively.[41-43] An additional peak at 0.81 V *vs.* Na/Na^+ is observed in the anodic scan of the coated sample. The corresponding cathodic peak is present at 0.48 V *vs.* Na/Na^+. This peak corresponds to the intermediate phase, Na_xSb, of the Na and Sb alloying reaction.[41] With the improved ionic conductivity of the coated sample and absence of the SEI, sharper and more refined redox peaks are revealed from the CV curve due to the improved reversibility from the ionically conductive ALD layer.

$$SnSb + xNa^+ + xe^- \rightarrow Sn + Na_xSb \qquad \textit{Equation 10.1}$$

$$Sn + Na_xSb + (3\text{-}x)Na^+ + (3\text{-}x)e^- \rightarrow Sn + Na_3Sb \qquad \textit{Equation 10.2}$$

$$Na_3Sb + Sn + 3.75Na + 3.75e^- \rightarrow Na_3Sb + Na_{3.75}Sn \qquad \textit{Equation 10.3}$$

$$(SbO_2, SnO_2)_{surface} + xNa + xe^- \rightarrow yNa_2O + (Sb, Sn)_{surface} \qquad \textit{Equation 10.4}$$

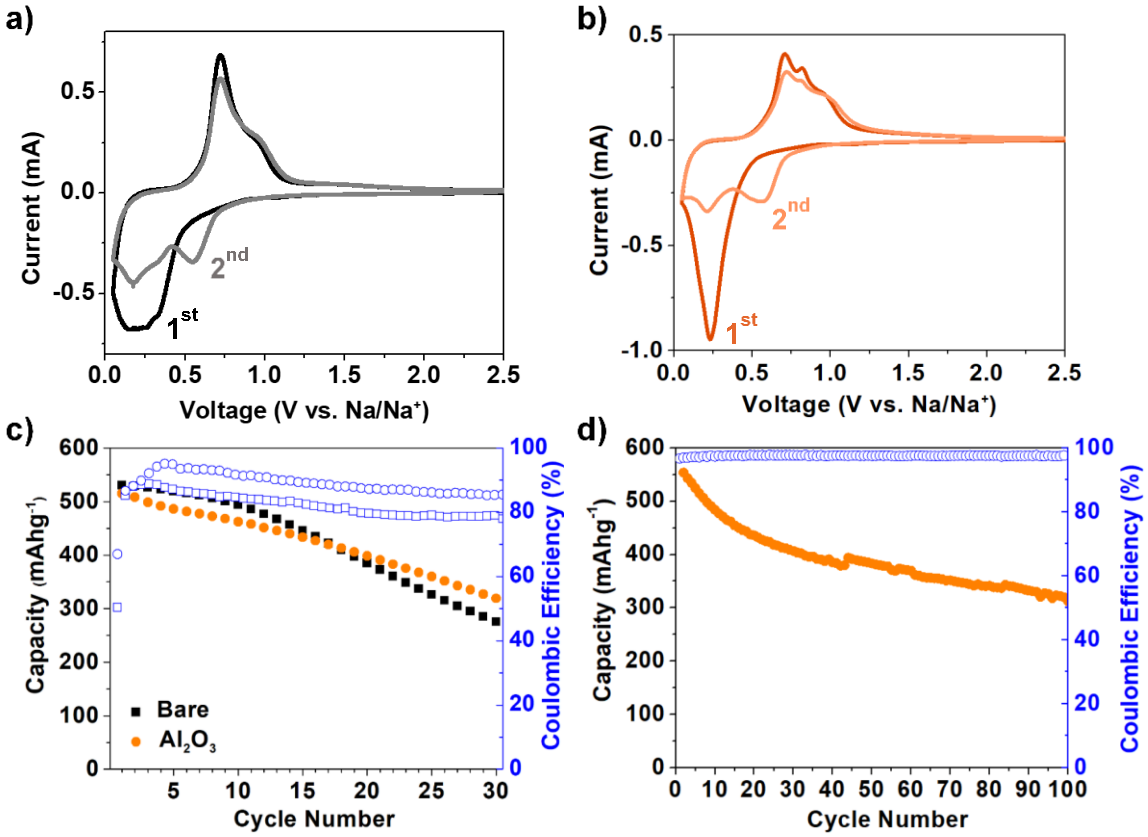

Figure 10.2. Cyclic Voltammogram of the a) bare electrode and the b) Al_2O_3-coated electrode. c) Stability test of the bare and Al_2O_3-coated SbSn in a three-electrode flooded cell. d) Long term cycling of the Al_2O_3-coated SbSn in a two-electrode Swagelok cell.

Galvanostatic charge and discharge profiles of bare and Al_2O_3-coated NP-SbSn electrodes cycled at 0.1C (based on the theoretical capacity of SbSn 725 mAh/g) are shown in Figure 10.2c. This preliminary study was performed in a three-electrode flooded cell before the long-term study to demonstrate the improved cycling capability of the coated electrode in comparison to the bare. The lack of stack pressure in a flooded cell represents a worse-case scenario for the lifetime SbSn electrodes, allowing for the accelerated testing of the coating. The 530 mAh/g capacity of the bare SbSn electrode is close to the theoretical specific capacity of 725 mAh/g. As described previously,

alloying anodes undergo pulverization due to the volume expansion and continuous formation of SEI during electrochemical cycling. This results in a capacity of only 275 mAh/g after 30 cycles. Though the capacity of the coated sample was initially lower than the bare, it demonstrated better capacity retention with 318 mAh/g after 30 cycles. Better columbic efficiency is also found in the ALD NP-SbSn due to the lack of SEI formation on the electrode. The efficiency increased steadily in the first few cycles as the Al_2O_3 layer continues to sodiate with increased cycling, resulting in higher ionic conductivities. Long-term cycling of the Al_2O_3-coated samples in a two-electrode Swagelok cell is shown in Figure 10.2d. With Al_2O_3, NP-SbSn delivered 312 mAh/g after 100 cycles, which is higher than the specific capacity of hard carbon, which is another promising alternative anode for Na-ion batteries.

10.2.2. *Operando* Transmission X-ray Microscopy Study

To understand the role of surface coatings in stabilizing the nanoporous structure during electrochemical cycling, *operando* TXM was performed at beamline 6-2C at Stanford Synchrotron Radiation Lightsource (SSRL). *Operando* TEM studies have been performed in attempt to understand the structural changes of alloying anodes with artificial SEIs,[26,44-46] but are not compatible with the study of composite electrodes used in actual devices due to the limited field of view and the extinction depth of electrons.[47] The use of high flux hard X-ray radiation in TXM offers a large field of view (15−30 μm) and a penetration depth of 100 nm -100 micron with a spatial resolution of 30 nm.[48,49] Because of this, TXM is well suited for studying battery electrodes at the nanoscale under actual operating conditions.[47,50]

Figure 10.3a and 10.3b show the absorption images of NP-SbSn with and without Al_2O_3 coating at OCV, 0.05 V (sodiated), and 1.5 V (desodiated) *vs.* Na/Na^+. The calculated volume change throughout cycling is presented in Figure 10.3c. It is apparent that the coated NP-SbSn expands less

(49%) than the bare NP-SbSn (68%) during charging and the coated NP-SbSn contracts close to its original size (7%) while NP-SbSn does not (25%). This difference in volume change suggests that the coating is physically restraining the volume expansion of NP-SbSn during the sodiation process due to the high bulk modulus of Al_2O_3 compared to the intermetallic.[51,52] The better reversibility of the expansion and contraction of the nanoporous structure can also be attributed to the Na-Al-O layer that allows more uniform sodiation/desodiation of NP-SbSn compared to the SEI present on the bare NP-SbSn.

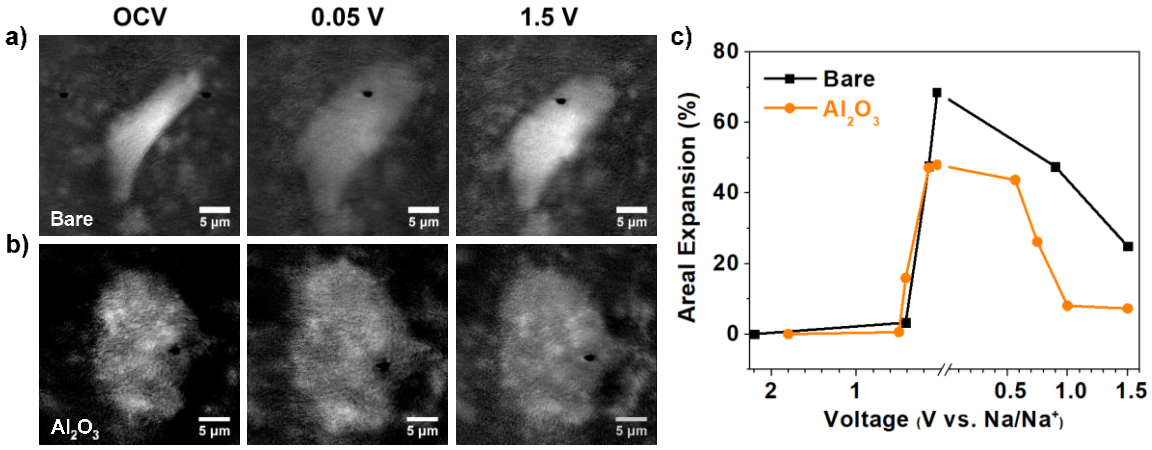

Figure 10.3. Adsorption images of the a) bare and b) Al_2O_3-coated SbSn particle. c) Areal expansion of the two electrodes throughout cycling.

The pore evolution during electrochemical cycling was also analyzed using operando TXM. Figure 10.4a shows the pore evolution throughout charge and discharge while Figure 10.4b shows the absorption images of the pores at OCV, 0.05 V and 1.5 V *vs.* Na/Na^+. In addition to stabilizing the overall particle structure, the conformal Al_2O_3 coating is shown to also stabilize the inner porous structure, particularly the pore walls. A much smaller increase in the pore area due to pore wall degradation is observed in the coated NP-SbSn compared to the bare SbSn. Under ideal conditions,

a decrease in pore area should occur as the particle expands isotropically during sodiation. This small degree of pore wall degradation in the coated sample can potentially result from the expansion of the Al_2O_3 coating during the initial sodiation process. It has been shown that sodiation occurs at the Al_2O_3 layer first before the active material. This causes the Al_2O_3 coating to expand as it sodiates to Na-Al-O.[26,45]

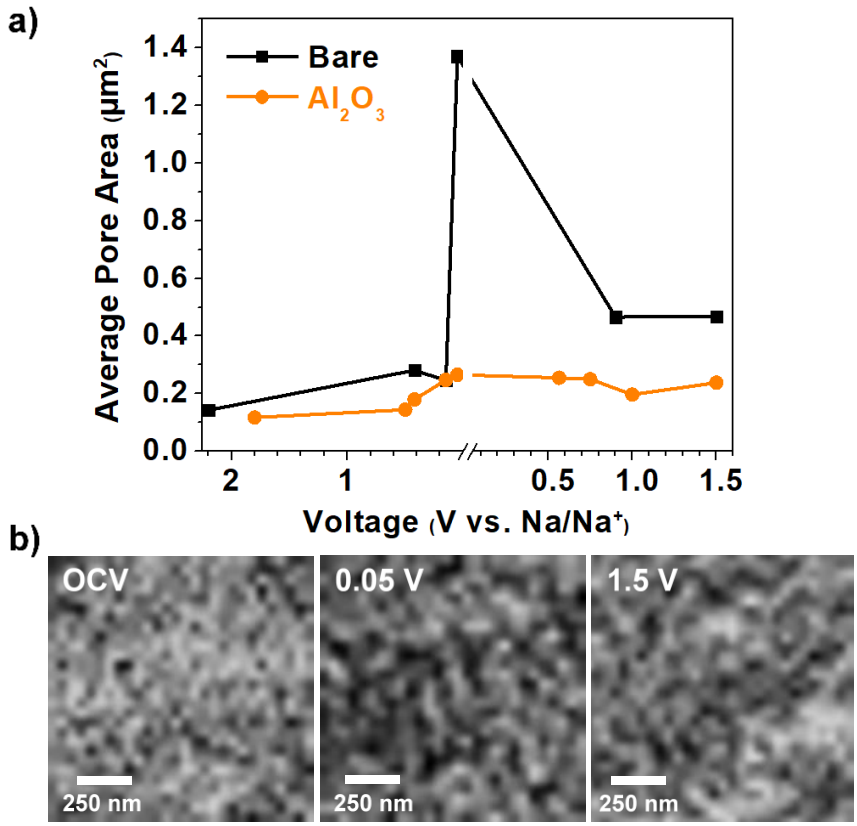

Figure 10.4. a) Pore evolution of bare and coated SbSn throughout cycling b) Absorption images of pores of the Al_2O_3-coated NP-SbSn powder at OCV, 0.05 V (sodiated), and 1.5 V (desodiated) *vs.* Na/Na^+. The black regions resulting from image thresholding correspond to domains of the NP-SbSn.

To study the change in stabilization mechanism over repeated cycling, *operando* TXM was performed on the 10th charge-discharge cycle. During the 10th cycle, negligible volume change is observed throughout cycling. Furthermore, a different evolution in the porosity is observed in the coated NP-SbSn. Interestingly, Na-Al-O has a lower bulk modulus (more elastic) than Al_2O_3.[30] After the initial surface sodiation process, the coating provides a flexible protective layer with good ionic conductivity. This can therefore result in different behaviors in the stabilization mechanism in the first and subsequent cycles. Instead of an increase in pore area during charge, the pore area decreased as expected for an isotropic expansion. This suggests that after the initial pore degradation in the first cycle, the Na-Al-O coating allows the material to expand in all directions. With the particle expanding into the voids of the porous structure, the overall volume expansion decreases significantly. The presence of this elastic artificial SEI is critical in preserving the conduction pathways in the electrode and prolonging the lifetime of alloying anodes. A stretchable SEI layer with high ionic conductivity that can expand and contract with the material without breaking is beneficial as it creates a robust kinetic barrier for electron transfer. This prevents the formation of the traditional SEI with low ionic conductivity. Even though pore wall degradation was observed in the first cycle of our ALD NP-SbSn when the particle and the Al_2O_3 layer expand, a stable pore evolution and minimal volume expansion were observed in later cycles. This suggests that the small amount of traditional SEI introduced during the first cycle is stable with the ALD coating.

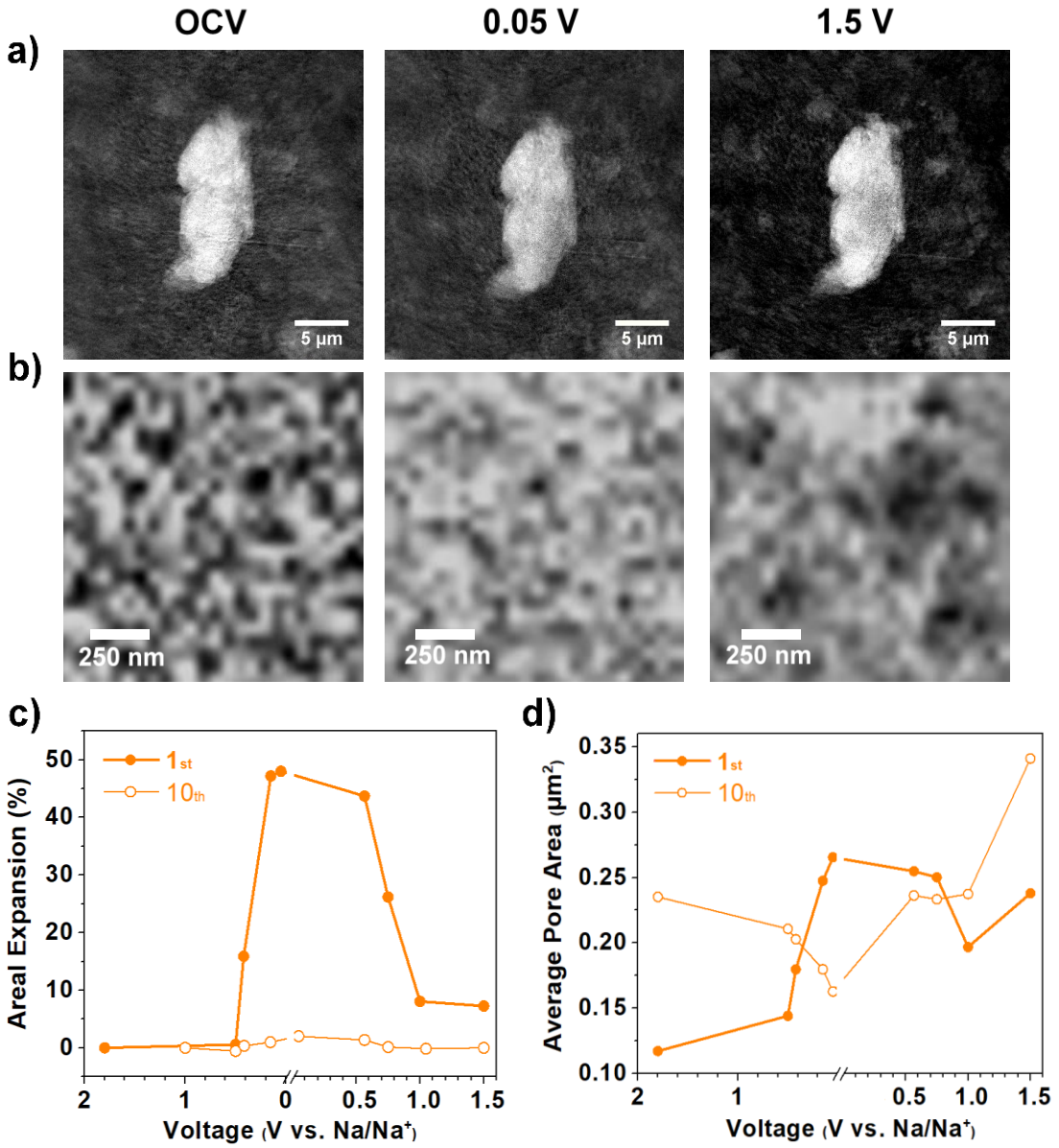

Figure 10.5. a) Adsorption images of the coated NP-SbSn on the 10th cycle. b) High magnification of the adsorption images of the pores. The black regions resulting from image thresholding correspond to domains of the NP-SbSn. c) Areal expansion of the Al_2O_3-coated NP-SbSn powder on first and 10th cycle d) Pore area evolution of the Al_2O_3-coated NP-SbSn powder on the first and 10th cycle.

10.3. Conclusion

In this study we have demonstrated that artificial SEIs are effective in reducing the volume expansion, improving the structural integrity of the porous structure and maintaining good electrical and ionic conductivity of NP-SbSn electrode. This improves the reversibility of the alloying reactions and the longevity of NP-SbSn. These NP-SbSn can be cycled stably over 100 cycles with a capacity of 312 mAh/g. Operando TXM shows that the nanoporous structure was stabilized in later cycles as the Al_2O_3 becomes more flexible to accommodate the volume change. This highly ionically conductive layer prevents the formation a SEI layer and constrains the volume expansion of these alloying anodes. Though this work focuses on the changes in pristine and Al_2O_3-coated NP-SbSn during sodiation/desodiation, this result should be insightful and for many other nanostructured materials with different coatings.

10.4. Experimental

10.4.1. Synthesis

Nanoporous antimony tin (NP-SbSn) was made from a one-step chemical dealloying synthesis. A parent alloy of $Sb_{20}Sn_{80}$ at.% was made by melting stoichiometric amounts of Sb (Alfa Aesar) and Sn (Sigma Aldrich) in a graphite crucible under Ar flow at 700 ° C and cooling to room temperature. The alloy was then heated to 400 °C and cooled several times to ensure homogeneity. The extra Sn in the parent alloy was etched using 4M HBr (Sigma Aldrich) for 21 hr. During this etching, the remaining SbSn reorganizes itself into the nanoporous structure. The nanoporous antimony tin powder was washed with water and ethanol several times to ensure complete removal of the etchant.

10.4.2. Characterization

Powder X-ray diffraction (XRD) was performed on a D8 diffractometer (Brucker) with a Cu Kα source (λ = 1.5418 Å) using a voltage of 45 kV and a current of 40 mA. XRD patterns were recorded in the range of $10° < 2\theta < 80°$ using a 0.03° step size. Transmission electron microscopy (TEM) was performed using a FEI Technai T12 operating at 120 kV. Nitrogen porosimetry was carried out using a Micromeritics TriStar II 3020. The surface area was calculated using the adsorption branch of the isotherm (between 0.04 – 0.30 P/P_0) according to the BET model. The pore diameter and pore volume were also calculated using the adsorption branch of the isotherm according to the BJH model.

10.4.3. Atomic Layer Deposition

Trimethylaluminum (TMA, Sigma-Aldrich, 97%) was used as-received as the Al-source and H_2O vapor was used as the oxidant. ALD of Al_2O_3 was carried out in a hot-wall reactor and the sample stage temperature was maintained at 225 °C with a base pressure of 50 mTorr. Nitrogen gas was used to purge the reactor of unreacted precursor after each ALD half cycle.

10.4.4. Electrochemical Testing

Electrode slurries composed of 70 wt.% NP-SbSn, 15 wt.% vapor grown carbon fibers (Sigma), and 15 wt.% carboxymethyl cellulose (Mw=250K, Sigma Aldrich) were used to fabricate electrodes for electrochemical testing. Slurries were drop-cast onto 316 stainless steel current collectors with a mass loading of 1 mg/cm^2. Initial electrochemical characterization was performed in a three-electrode flooded cell and long-term cycling was performed in Swagelok cells using glass fiber separators (Advantec) and 1M $NaClO_4$ ethylene carbonate:diethylene carbonate (1 EC:1 DEC by vol, Sigma Aldrich) + 5 vol% fluoroethylene carbonate (TCI America) with sodium metal counter/reference electrodes.

10.4.5. *Operando Transmission X-ray Microscopy*

Electrode slurries were modified for imaging studies and were composed of 25-50 wt.% NP-SbSn, 30-55 wt.% vapor grown carbon fibers, and 20 wt.% carboxymethyl cellulose. Lower active material loadings were used to reduce the probably of the overlapping particles that can obscure imaging. Pouch cells were fabricated for the TXM measurements cells using 0.5 mm Na foil as the counter electrode and Celgard separator (gift from Celgard) soaked in 1 M NaClO4 in a 1EC:1DEC (Sigma Aldrich) with 5 vol% FEC. The pouch cells were sandwiched between two aluminum plates with imaging holes to maintain stack pressure. *Operando* TXM was performed on electrodes that were precycled in a Swagelok cell for 9 cycles, disassembled in an Ar glovebox, and fabricated into a pouch cell.

Transmission X-ray Microscopy was performed on beamline 6-2C at the Stanford Synchrotron Radiation Lightsource (SSRL). 8.95 KeV X-rays were used to perform investigations of electrode morphology at the nano/meso scale. The X-ray energy was chosen directly below the copper Kedge to minimize absorption from the Cu current collector. The spatial resolution of this microscope is ~30 nm, and the field of view at 8.95 KeV is 38.3 μm. Details regarding the operando transmission X-ray microscopy of NP-Sn can be found previously reported studies.

During operando imaging, the cell was galvanostatically charged and discharged with a VSP potentiostat/galvanostat (Bio-Logic) between 1.5 – 0.05 V *vs.* Na/Na^+ at a rate of 0.1C. A 3x3 mosaic consisting of 9 TXM images (38.3 μm x 38.3 μm each) were collected at 10-12 regions in the cell during cycling. A camera binning of two (four pixels are averaged into one) was used to improve image quality. These parameters result in a pixel size of 34-36 nm.

10.4.6. Data Processing

X-ray micrographs were processed using an in-house developed software package known as TXMWizard.[53] A reference correction was performed in TXM-Wizard and the images were processed using ImageJ. The reference-corrected images were converted to 8 bit and linearly grey-scaled. A threshold was then applied to the image to differentiate the grey-level of the particle and the black background. The size of individual particles was then calculated by totaling the number of pixels within each threshold border.

Images used to determine pore size distributions were further processed in ImageJ. The grey-scaled image described above were threshold again and converted to black and white. This second threshold provides the sharp contrast needed to distinguish the pores. Regions connected by less than 4 pixels were considered to be individual domains of NP-SbSn, and the area of each pore was quantified. For this analysis, the images of the NP-SbSn grains were enlarged to find a region where pores could be easily distinguished, and the number and area of the pores were measured and monitored at each voltage plateau during sodiation and desodiation. The average pore area and its standard deviation were calculated for each voltage plateau. A series of histograms with 0.2 μm^2 binning were also constructed to study the change in pore size distribution within NPSbSn (both bare and coated) during cycling.

10.5. Reference

[1] C.- M. Park, J.-H. Kim, H. Kim, H.-J. Sohn, *Chem. Soc. Rev.* **2010**, *39*, 3115.

[2] W.-J. Zhang, *J. Power Source* **2011**, *196*, 877.

[3] N. Nitta, G. Yushin, *Part. Part. Syst. Charact.* **2014**, *31*, 317.

[4] Y. Kim, K.-H. Ha, S. M. Oh, K. T. Lee, *Chem. Eur. J.* **2014**, *20*, 11980.

[5] W. Luo, F. Shen, C. Bommier, H. Zhu, X. Ji, L. Hu, *Acc. Chem. Res.* **2016**, *49*, 231.

[6] J.-Y. Hwang, S.-T. Myung, Y.-K. Sun, *Chem. Soc. Rev.* **2017**, ***46***, 3529.

[7] L. Y. Beaulieu, S. D. Beattie, T. D. Hatchard, J. R. Dahn, *J. Electrochem. Soc.* **2003**, *150*, A419.

[8] M. R. Wagner, P. R. Raimann, A. Trifonova, K.-C. Moeller, J. O. Besenhard, M. Winter, *Electrochem. Solid-State Lett.* **2004**, *7*, A201.

[9] H. Wu, Y. Cui, *Nano Today* **2012**, *7*, 414.

[10] H. Zhang, I. Hasa, S. Passerini, *Adv. Energy Mater.* **2018**, *8*, 1702582.

[11] M. Park, X. Zhang, M. Chung, G. B. Less, A. M. Sastry, *J. Power Sources* **2010**, *195,* 7904.

[12] A. Wang, S. Kadam, H. Li, S. Shi, Y. Qi, *npj Computational Materials* **2018**, *4*, 15.

[13] M. D. Slater, D. Kim, E. Lee, C. S. Johnson, *Adv. Funct. Mater.* **2013**, *23*, 947.

[14] I. T. Lucas, E. Pollak, R. Kostecki, *Electrochemistry Communication* **2009**, *11*, 2157.

[15] P. Verma, P. Maire, P. Novák, *Electrochimica Acta* **2010**, *55*, 6332.

[16] S. J. An. J. Li, C. Daniel, D. Mohanty, S. Nagpure, D. L. Wood, *Carbon* **2016**, *105*, 52.

[17] Y. Jin, B. Zhu, Z. Lu, N. Liu, J. Zhu, *Adv. Energy Mater.* **2017**, *7*, 1700715.

[18] S. S. Zhang, *J. Power Sources* **2006**, *162*, 1379.

[19] S. D. Beattie, T. Hatchard, K. C. H. Bonakdarpour, J. R. Dahn, *Journal of The Electrochemical Society* **2003**, *150*, A701.

[20] X. Meng, *J. Mater. Chem. A* **2017**, *5*, 10127.

[21] X. Meng, X.-Q. Yang, X. Sun, *Adv. Mater.* **2012**, *24*, 3589.

[22] Y. He, X. Yu, Y. Wang, H. Li, X. Huang, *Adv. Mater.* **2011**, *23*, 4938.

[23] E. M. Loftabad, P. Kalisvaart, K. Cui, A. Kohandehghan, M. Kupsta, B. Olsen, D. Mitlin, *Phys. Chem. Chem. Phys.* **2013**, *15*, 13646.

[24] A. Kohandehghan, P. Kalisvaart, K. Cui, M. Kupsta, E. Memarzadeh, D. Mitlin, *J. Mater. Chem. A* **2013**, *1*, 12850.

[25] Y.-C. Perng, J. Cho, S. Y. Sun, D. Membreno, N. Cirigliano, B. Dunn, J. P. Chang, *J. Mater. Chem. A* **2014**, *2*, 9566.

[26] X. Han, Y. Liu, Z. Jia, Y.-C. Chen, J. Wan, N. Weadock, K. J. Gaskell, T. Li, L. Hu, *Nano Lett.* **2014**, *14*, 139.

[27] D. Wang, J. Yang, J. Liu, X. Li, R. Li, M. Cai, T.-K. Sham, X. Sun, *J. Mater. Chem. A* **2014**, *2*, 2306.

[28] E. K. Kang, Y. S. Jung, A. S. Cavanagh, G.-H. Kim, S. M. George, A. C. Dillon, J. K. Kim, J. Lee, *Adv. Funct. Mater.* **2011**, *21*, 2430.

[29] E. M. Loftabad, P. Kalisvaart, A. Kohandehghan, K. Cui, M. Kupsta, B. Farbod, D. Mitlin, *J. Mater. Chem. A* **2014**, *2*, 2504.

[30] S. C. Jung, H.-J. Kim, J. W. Choi, Y.-K. Han, *Nano Lett.* **2014**, *14*, 6559.

[31] S. Susman, M. A. Ratner, *Journal of Non-Crystalline Solids* **1988**, *101*, 54.

[32] W. Luo, C.-F. Lin, O. Zhao, M. Noked, Y. Zhang, G. W. Rubloff, L. Hu, *Adv. Energy Mater.* **2017**, *7*, 1601526.

[33] C. Marichy, M. Bechelany, N. Pinna, *Adv. Mater.* **2012**, *24*, 1017.

[34] Y. Pan, X.-J. Wu, Z.-Q. Zhang, Z.-W. Fu, Y.-N. Zhou, *J. Alloy Compd.* **2017**, *714*, 348.

[35] Y.-M. Lin, P. R. Abel, A. Gupta, J. B. Goodenough, A. Heller, C. B. Mullins, *ACS Appl. Mater. Interfaces* **2013**, *5*, 8273.

[36] M. Winter, J. O. Besenhard, *Electrochim. Acta* **1999**, *45*, 31.

[37] Y. S. Jung, A. S. Cavanagh, L. A. Riley, S.-H. Kang, A. C. Dillon, M. D. Groner, S. M. George, S.-H. Lee, *Adv. Mater.* **2010**, *22*, 2172.

[38] X. Zhou, X. Liu, Y. Xu, Y. Liu, Z. Dai, J. Bao, *J. Phys. Chem. C* **2014**, *118*, 23527.

[39] Q. Sun, Q.-Q. Ren, H. Li, Z.-W. Fu, *Electrochemistry Communications* **2011**, *13*, 1462.

[40] Y. Wang, D. Su, C. Wang, G. Wang, *Electrochemistry Communications* **2013**, *29*, 8.

[41] L. Wu, X. Hu, J. Qian, F. Pei, F. Wu, R. Mao, X. Ai, H. Yang, Y. Cao, *Energy Environ. Sci.* **2014**, *7*, 323.

[42] A. Darwiche, C. Marino, M. T. Sougrati, B. Fraisse, L. Stievano, L. Monconduit, *J. Am. Chem. Soc.* **2012**, *134*, 20805.

[43] C. Kim, K.-Y. Lee, I. Kim, J. Park, G. Cho, K.-W. Kim, J.-H. Ahn, H.-J. Ahn, *J. Power Sources* **2016**, *317*, 153.

[44] Y. Liu, N. S. Hudak, D. L. Huber, S. J. Limmer, J. P. Sullivan, J. Y. Huang, *Nano Lett.* **2011**, *11*, 4188.

[45] L. Luo, H. Yang, P. Yan, J. J. Travis, Y. Lee, N. Liu, D. M. Piper, S.-H. Lee, P. Zhao, S. M.

George, J.-G. Zhang, Y. Cui, S. Zhang, C. Ban, C.-M. Wang, **2015**, *9*, 5559.

[46] Y. He, D. M. Piper, M. Gu, J. J. Travis, S. M. George, S.-H. Lee, A. Genc, L. Pullan, J. Liu, S. X. Mao, J.-G. Zhang, C. Ban, C. Wang, *ACS Nano* **2014**, *8,* 11816.

[47] J. B. Cook, T. C. Lin, E. Detsi, J. N. Weker, S. H. Tolbert, *Nano Lett.* **2017**, *17*, 870.

[48] J. C. Andrews, B. M. Weckhuysen, *ChemPhysChem*. **2013**, *14*, 3655.

[49] J. Nelson, S. Misra, Y. Yang, A. Jackson, Y. Liu, H. Wang, H. Dai, J. C. Andrews, Y. Cui, M. F. Toney, *J. Am. Chem. Soc.* **2012**, *134*, 6337.

[50] J. N. Weker, X. Huang, M. F. Toney, *Current Opinion in Chemical Engineering* **2016**, *12*, 14.

[51] O. M. E. Ylivaara, X. Liu, L. Kilpi, J. Lyytinen, D. Schneider, M. Laitinen, J. Julin, S. Ali, S. Sintonen, M. Berdova, E. Haimi, T. Sajavaara, H. Ronkainen, H. Lipsanen, J. Koskinen, S.-P. Hannula, R. L. Puurunen, *Thin Solid Films* **2014**, *552*, 124.

[52] R. M. Shalaby, *Journal of Alloys and Compounds* **2009**, *480*, 334.

[53] Y. Liu, F. Meirer, P. A. Williams, J. Wang, J. C. Andrews, P. Pianetta, *J. Synchrotron Radiat.* **2012**, *19*, 281.

Chapter 11. Conclusion

The first part of this thesis focused on the development of fast charging/pseudocapacitive materials through nanostructuring. Pseudocapacitors, which rely on surface or near-surface Faradaic redox reactions, offer both high energy and power density by combining the storage mechanism of a battery with the kinetics similar to an electrical double-layer capacitor. For most battery materials, the solid-state diffusion of Li^+ (or Na^+) along with the reconstruction of material in order to accommodate the addition or loss of a metal ion and new bonding geometries is intrinsically slow. This results in the reduced power densities of conventional rechargeable batteries. We postulate that pseudocapacitance can occur in nanostructured versions of traditional battery materials when two structural constraints are satisfied. First, solid-state diffusion path lengths must be short and matched to the ion diffusion rate of a given materials to significantly decrease the diffusion time. Second, ion insertion and de-insertion into the material must not induce a first-order phase transition because these transitions limit the kinetics of ion transport.

Using these guidelines we designed new materials for fast-charging energy-storage applications. Through hydrothermal synthesis, we synthesized defective MoS_2 nanocrystals that demonstrate high rate capabilities. Specific capacities over 90 mAh/g were achieved in only 30 seconds of charging with lithium. With sodium, almost 100 mAh/g can be realized in just under 40 seconds. To investigate whether the fast kinetics are due to the suppression of the 1st order phase transition that normally occurs in bulk MoS_2, we performed a series of *operando* X-ray diffraction studies during electrochemical cycling. As expected, during lithium and sodium intercalation, MoS_2 nanocrystals do not show the 1st order phase transition features that are noted in the bulk material.

In addition to this anode system, we also investigated a cathode material, $LiMn_2O_4$ (LMO), and discovered the crystallite size at which its electrochemical behavior crosses over from that of a battery to that of a pseudocapacitor. A significant drop in rate capability was found for crystallite sizes

on the order of 60 nm or larger. *Operando* X-ray also showed that 15 nm LMO does not exhibit any phase transition features while 50 nm LMO shows a discontinuity in both the (311) and (511) peaks. This suggests that there could be a critical size where the barrier to nucleating a new phase becomes too large for phase transitions to occur. Identifying the critical size where phase transition is suppressed and the formation of a deleterious solid-electrolyte interphase (SEI) is not dominant will allow us to find a balance between high rate and high capacity.

Another cathode we had explored was nanostructured $LiVPO_4F$ (LVPF). LVPF is an attractive cathode because it has a relatively high theoretical capacity of 156 $mAh \cdot g^{-1}$ and a high redox potential of 4.3V *vs.* Li/ Li^+. In addition, it shows a relatively high bulk ionic conductivity of $\sim 8 \cdot 10^{-7}$ S/cm due to quasi 1D diffusion paths along the (111) direction. These nanostructured LVPF cycled in 1M $LiPF_6$ 2FEC:8DMC delivered up to 100 mAh/g in two minutes and was stable even after 2000 cycles. By deviating from the traditional electrolytes (1M $LiPF_6$ or $LiClO_4$ in EC: DMC) that begin to decompose at 4.2V, the operating voltage window can be extended to 4.6V and a thinner and more compact SEI layer can be formed. Compared to traditional micron-sized cathode materials for lithium-ion batteries, the short diffusion distances in nanostructured LVPF and stable SEI resulted from FEC/DMC decomposition allow for high capacities even at 30C. We have demonstrated nanostructured LVPF's potential as another promising cathode for high energy fast charging application.

The second part of this thesis focused on extending the lifetime of battery material. Unlike pseudocapacitors, batteries rely on bulk or solid state redox reactions. Though these reactions are slow, they offer much higher energy densities. This is especially true with alloying type anodes that possess specific capacities 3-10 times greater than typical battery electrodes by allowing for multi-electron redox reactions. Unfortunately, these electrochemical reactions are accompanied by severe volume expansion (~400%) that reduce the lifetime of the active material. Three well-recognized approaches to limit the detrimental effects of this expansion include the use of nanoporous structures,

using multiphase composites such as intermetallics, and using artificial SEI coatings. Nanoporous structures accommodate bulk volume expansion using internal void space. By contrast, intermetallics and artificial SEI coatings improve the mechanical properties of the active material and of the composite electrode. The goal of this project is to use TXM to mechanistically understand how each approach accommodates volume expansion and how the approaches can be combined to best advantage for future devices.

Operando TXM shows that NP-Sn and NP-SbSn expand 40 and 60% during lithiation, which is significantly less than in bulk Sn (130%). More importantly, the pore system in NP-SbSn stays completely intact while some degree of fracturing is observed in NP-Sn, suggesting that NP-SbSn is more mechanically stable. This agrees with our observation that NP-SbSn shows better cycle stability than NP-Sn when cycled with sodium. Specifically, we found that NP-Sn and NP-SbSn show comparable performance when cycled with Li^+ (650 mAh/g initial capacity with 98% capacity retention after 200 cycles for NP-Sn and 560 mAh/g initial capacity with 90% capacity retention over 200 cycles for NP-SbSn). By contrast, NP-SbSn demonstrates much better cycle stability than NP-Sn when cycled with Na^+ (430 mAh/g initial capacity with 85% capacity retention after 100 cycles for NP-SbSn compared to 550 mAh/g initial capacity with only 50% capacity retention after 90 cycles for NP-Sn.

Though NP-SbSn is more mechanically stable than NP-Sn and has shown decent cycling stability with Na^+, *operando* TXM shows that the pore wall deteriorates throughout sodiation. To improve the mechanical properties of NP-SbSn further, a thin layer of Al_2O_3 coating was deposited on NP-SbSn using atomic layer deposition. Al_2O_3 coated NP-SbSn showed only ~50% expansion while uncoated NP-SbSn showed over ~70% expansion. In addition, the porous structure was better maintained. After 100 cycles, the coated sample still obtained 312 mAh/g while the bare sample died in 30 cycles.

Overall, this thesis focused on a series of interrelated problems in pseudocapacitive energy storage and high capacity alloying anodes. To be specific, it took aim at understanding the pseudocapacitive behavior and suppression of phase transitions in nanostructured materials. With our better understanding, we were able to develop a series of new materials (MoS_2, $LiMn_2O_4$ and $LiVPO_4F$) for fast charging applications. In terms of high capacity alloying anodes, we were able to precisely control the nanoporous architectures, which had led to significant performance enhancements in these materials in terms of cycle life time. Taken together, these experiments both advance our fundamental understanding of nanostructured pseudocapacitors as well as alloying anodes and provide practical design rules for creating fast charging and long lasting energy storage systems for next generation mobile and automobile power needs.